Theoretical Analysis of Hidden Photon Searches in High-Precision Experiments

Dissertation
zur Erlangung des Grades
„Doktor der Naturwissenschaften "

am Fachbereich Physik, Mathematik und Informatik
der Johannes Gutenberg-Universität Mainz

vorgelegt von

Tobias Beranek

geboren in Datteln

Mainz, 2014

Datum der mündlichen Prüfung: 11.04.2014
D77 (Dissertation Universität Mainz)

Abstract

Although the Standard Model of particle physics provides an extremely successful description of the ordinary matter, one knows from astronomical observations that it accounts only for around 5% of the total energy density of the Universe, whereas around 30% are contributed by the dark matter.

Motivated by anomalies in cosmic ray observations and by attempts to solve questions of the Standard Model like the $(g-2)_\mu$ discrepancy, proposed $U(1)$ extensions of the Standard Model gauge group $SU(3) \times SU(2) \times U(1)$ have raised attention in recent years. In the considered $U(1)$ extensions a new, light messenger particle γ', the hidden photon, couples to the hidden sector as well as to the electromagnetic current of the Standard Model by kinetic mixing. This allows for a search for this particle in laboratory experiments exploring the electromagnetic interaction. Various experimental programs have been started to search for the γ' boson, such as in electron-scattering experiments, which are a versatile tool to explore various physics phenomena. One approach is the dedicated search in fixed-target experiments at modest energies as performed at MAMI or at JLAB. In these experiments the scattering of an electron beam off a hadronic target $e(A,Z) \to e(A,Z)l^+l^-$ is investigated and a search for a very narrow resonance in the invariant mass distribution of the l^+l^- pair is performed. This requires an accurate understanding of the theoretical basis of the underlying processes.

For this purpose it is demonstrated in the first part of this work, in which way the hidden photon can be motivated from existing puzzles encountered at the precision frontier of the Standard Model. The main part of this thesis deals with the analysis of the theoretical framework for electron scattering fixed-target experiments searching for hidden photons. As a first step, the cross section for the bremsstrahlung emission of hidden photons in such experiments is studied. Based on these results, the applicability of the Weizsäcker–Williams approximation to calculate the signal cross section of the process, which is widely used to design such experimental setups, is investigated. In a next step, the reaction $e(A,Z) \to e(A,Z)l^+l^-$ is analyzed as signal and background process in order to describe existing data obtained by the A1 experiment at MAMI with the aim to give accurate predictions of exclusion limits for the γ' parameter space. Finally, the derived methods are used to find predictions for future experiments, e.g., at MESA or at JLAB, allowing for a comprehensive study of the discovery potential of the complementary experiments.

In the last part, a feasibility study for probing the hidden photon model by rare kaon decays is performed. For this purpose, invisible as well as visible decays of the hidden photon are considered within different classes of models. This allows one to find bounds for the parameter space from existing data and to estimate the reach of future experiments.

Zusammenfassung

Auch wenn das Standardmodell der Elementarteilchenphysik eine äußerst erfolgreiche Beschreibung der gewöhnlichen Materie liefert, ist aus astronomischen Beobachtungen bekannt, dass diese nur für 5% der Gesamtenergiedichte unseres Universums verantwortlich ist, wohingegen der Anteil dunkler Materie bei 30% liegt.

Motiviert durch Anomalien in der Beobachtung kosmischer Strahlung und durch Ansätze ungeklärte Fragen des Standardmodells wie die $(g-2)_\mu$-Diskrepanz zu klären, sind in letzter Zeit lange vorgeschlagene $U(1)$-Erweiterungen der $SU(3) \times SU(2) \times U(1)$-Eichgruppe des Standardmodells in den Fokus gerückt. In diesen $U(1)$-Erweiterungen koppelt ein neues, leichtes Austauschteilchen γ', das Hidden Photon, sowohl an den elektromagnetischen Strom des Standardmodells als auch an den Sektor der dunklen Materie, was die Suche nach diesem Teilchen in Laborexperimenten, welche die elektromagnetische Wechselwirkung erforschen, ermöglicht. Aus diesem Grund wurden verschiedene experimentelle Programme zur Suche nach γ'-Bosonen gestartet, wie z.B. Elektronen-Streu-Experimente, die als vielseitiges Hilfsmittel zur Erforschung verschiedenster Phänomene dienen. Ein Ansatz ist dabei die Suche an dedizierten Fixed-Target-Experimenten im Bereich niedriger Energien, wie sie z.B. an MAMI oder am JLAB durchgeführt werden. Bei diesen Experimenten wird die Streuung eines Elektronenstrahls an einem hadronischen Target, d.h. die Reaktion $e(A, Z) \to e(A, Z)l^+l^-$, untersucht, wodurch eine Suche nach einer sehr schmalen Resonanz in der Invarianten-Masse-Verteilung des l^+l^--Paares ermöglicht wird. Notwendige Voraussetzung hierfür ist ein präzises Verständnis der theoretischen Basis des zugrundeliegenden Prozesses, was eine umfassende Studie des Potenzials dieser komplementären Experimente erlaubt.

Im ersten Teil dieser Arbeit wird zu diesem Zweck aufgezeigt, wie sich das Hidden Photon aus existierenden Fragestellungen, auf die man z.B. durch Präzisionsuntersuchungen des Standardmodells trifft, motivieren lässt. Der Hauptteil dieser Dissertation befasst sich daher mit der Analyse des theoretischen Rahmens, der für solche Elektronen-Streu-Experimente zur Suche nach Hidden Photons nötig ist. Als erster Schritt wird dazu der Bremsstrahlungs-Wirkungsquerschnitt eines Hidden Photons an solchen Experimenten untersucht. Basierend darauf wird die Anwendbarkeit der Weizsäcker-Williams-Näherung zur Berechnung des Signal-Wirkungsquerschnitts, die für gewöhnlich zum Design solcher Experimente verwendet wird, überprüft. Ein nächster Schritt widmet sich der theoretischen Studie der Reaktion $e(A, Z) \to e(A, Z)l^+l^-$, welche sowohl als Signal- als auch Untergrundprozess dient, um damit die vom A1-Experiment an MAMI genommenen Daten zu beschreiben und präzise Vorhersagen für Ausschlussgrenzen des γ'-Parameterbereichs zu geben. Schließlich werden die abgeleiteten Methoden verwendet um Vorhersagen für zukünftige Experimente, wie sie an MESA und am JLAB geplant sind, zu erhalten.

Im letzten Teil wird eine Machbarkeitsstudie zur Erforschung des Hidden Photon-Modells unter Verwendung seltener Kaonzerfälle durchführt. Zu diesem Zweck werden sowohl unsichtbare als auch sichtbare Zerfälle des γ' in verschiedenen Modellen betrachtet, wodurch Grenzen für den Parameterbereich aus existierenden Daten abgeleitet und Abschätzungen für die Reichweite der zukünftigen Experimente gefunden werden können.

Contents

List of publications

The results of this thesis are published in parts in the following articles:

Articles published in refereed journals

1. T. Beranek and M. Vanderhaeghen,
   "Constraints on the Dark Photon Parameter Space from Leptonic Rare Kaon Decays,"
   Phys. Rev. D **87**, 015024 (2013).

2. T. Beranek, H. Merkel and M. Vanderhaeghen,
   "Theoretical framework to analyze searches for hidden light gauge bosons in electron scattering fixed target experiments,"
   Phys. Rev. D **88**, 015032 (2013).

3. T. Beranek and M. Vanderhaeghen,
   "Study of the discovery potential for hidden photon emission at future electron scattering fixed target experiments,"
   Accepted for publication in Phys. Rev. D, arXiv:1311.5104 [hep-ph].

Conference proceedings

1. T. Beranek,
   "Light dark gauge boson searches in electroweak processes,"
   Frascati Phys. Ser. **56**, 11 (2012).

2. T. Beranek,
   "A framework to analyze searches for gauge bosons of the hidden light sector in electron scattering fixed target experiments,"
   AIP Conference Proceedings, 1563, 118-121 (2013)

3. T. Beranek,
   "Theoretical Framework for the Analysis of Hidden Light Gauge Boson Searches,"
   Proceedings of the 9th Patras Workshop on Axions, WIMPs and WISPs 2013, DESY-PROC-2013-04.

White paper

1. R. Essig, J. A. Jaros, and W. Wester *et al.* (NLWCP Working Group)
   "Dark Sectors and New, Light, Weakly-Coupled Particles,"
   arXiv:1311.0029 [hep-ph].

Man sieht nur mit dem Herzen gut, das Wesentliche ist für die Augen unsichtbar.

(Der kleine Prinz)

The dark (...) Force is a pathway to many abilities some consider to be unnatural.

(The Emperor, Star Wars)

Preface

Motivation

One of the primary objectives of mankind has always been to understand the world one lives in. Starting in the Stone Age, the discovery how to ignite a fire helped the humans to survive. During the ages, (scientific) research has never lost its importance, although the main objective has changed from ensuring the survival to gain wealth such as by transmuting metal into gold or simply to gather a deeper knowledge of our world.

The particular objectives of research might have changed, nevertheless we are still driven by the desire to understand the basic principles of nature. The publication of the famous work "Philosophiae Naturalis Principia Mathematica" by Isaac Newton in 1687, in which the law of gravitation was formulated for the first time, can be considered as the starting point of modern science. In particular, physics evolved as an interplay between the subjects of theoretical and experimental physics. This is an essential aspect to discover new phenomena and obtain further insight into nature. Theories describe phenomena of physics which are found by experiments and experiments test the predictions of theories.

Even today, it is precisely that interplay which leads to advances in the deeper understanding of our world. Recently, the last missing piece of the "Standard Model of particle physics", the Higgs boson, has been discovered at the Large Hadron Collider at CERN. This particle was postulated by Peter Higgs, François Engler and Robert Brout nearly 50 years ago and now completes the theory of the dynamics of the smallest particles. Even though the Standard Model of particles physics provides an exceedingly successful description of the dynamics at the smallest scales, several hints point to physics beyond the Standard Model.

On the other hand, the dynamics of the very large scales—for example, the evolution of our universe and the galaxies within—can be successfully described by the "Standard Model of cosmology". Within this model based on the mathematical foundations found by Albert Einstein the evolution of our universe from the Big Bang until today is described. One important outcome is that only a small fraction of the energy of the universe, which is around 5%, is contributed by ordinary matter. This is the only building block of our universe, which can be described within the Standard Model of particle physics. As a consequence, 95% of the ingredients of our universe cannot be understood so far. However, observations allow for a slight insight into this field. One can conclude that 27% of the energy result from a kind of matter which has not been observed until today. Thus, one refers to it as "Dark Matter". The remaining 68% arise from an even more mysterious phenomenon known as "Dark Energy". Although most of the ingredients of our universe are still unknown, the cosmological standard model is currently under deep investigation and can be probed to high accuracy.

However, while the physics at the smallest and largest scales can be described successfully within the respective standard model, there is no "Theory of Everything", in which these two models are combined. Thus, the entire physics of the universe is not formulated within one theory, and as an example, dark matter cannot be linked to particle physics within an established framework.

While for physicists it is always satisfying to experience that their predictions could be proven experimentally or their observed phenomena confirm a well-known theory, it is much more interesting, if a discrepancy between theory and experiments arises. This means that a theory which was considered to be valid cannot be reconciled with experimental data, or vice versa. Currently, there exist several of these unsolved puzzles; for example, the discrepancy found in the theoretical and experimental determination of the anomalous magnetic moment of the muon (($g-2$ puzzle). Moreover, the unexpected large rates of positrons observed in the data taken from the study of cosmic rays can neither be explained by astrophysical sources nor by the direct annihilation of dark matter (positron excess puzzle). In consequence of such puzzles, extensive studies from both theoretical and experimental sides are performed to resolve the discrepancies.

In this work one particular extension of the Standard Model of particle physics is studied: the hidden photon model. The hidden photon is a new messenger particle. It has similar properties as the ordinary photon mediating the well-known electromagnetic interaction. The underlying framework attempts to solve the $(g-2)$ puzzle and to explain the positron excess. This means that the hidden photon provides a link between the subjects of particle physics and cosmology by allowing for an interaction between the sectors of ordinary matter within the Standard Model of particle physics and the dark sector in which the dark matter is contained. These studies are examples of how the interplay between theoretical and experimental physics enhances our knowledge of nature. The motivation to have a closer view into this field results from the discrepancy between predictions and observations. Experiments are necessary to probe the theoretical hypothesis this work is based on. This automatically requires that the expected results of these experiments can be predicted precisely.

Currently, a lot of activity is spent to explore this particular realization of physics beyond the Standard Model by experimental as well as theoretical groups. Theorists attempt to obtain accurate predictions which can be probed in experiments to constrain the wide parameter space of the hidden photon model. A large variety of experiments is underway and older data taken for different purposes are re-analyzed. Most of these dedicated experiments are still in the phase of design, whereas a few of them, such as the A1 experiment at Mainz or APEX at the Jefferson Lab already have successfully taken first data. In addition, experiments as HPS at the Jefferson Lab plan to take data within the year.

Therefore, the principal purpose of this work is to provide an accurate theoretical framework for hidden photon searches. The findings of this work allow one to describe data from such existing experiments and to find predictions for the discovery potential of future experiments.

Outline

This thesis is structured as follows:

The fundamental physics of this work is introduced in Chapter 1 and an overview of the current status of hidden photon searches is given. Therefore, the Standard Model of particle physics is introduced and its limitations are pointed out. It is discussed that one can overcome some of the existing puzzles by physics beyond the Standard Model, in particular within the hidden photon model.

Chapter 2 deals with the detailed analysis of the hidden photon production mechanism

$e + (Z, A) \to e + (Z, A) + \gamma'$ at electron-scattering fixed-target experiments. Furthermore, the QED background entering into the search without the detection of the decay products of the hidden photon is studied. In addition, an analysis of the applicability of the Weizsäcker–Williams approximation is presented. This approximation is widely used to calculate the cross sections of such processes. Parts of the results of this chapter are published in Ref. [1].

In Chapter 3 the reaction $e+(Z, A) \to e+(Z, A)+l^+l^-$ is investigated in detail, based on the results obtained in Chapter 2. This processes is studied from the perspective: On the one hand as signal process, where in the intermediate state a hidden photon is emitted decaying into a lepton pair. On the other hand, the study is performed from the point of view as irreducible background with a virtual photon in the intermediate state. It is demonstrated, how the integrated cross sections of the underlying processes can be calculated efficiently. These cross sections are used to obtain a better understanding of the kinematical properties. This allows for a significant reduction of the QED background. Furthermore, investigations for the setups of existing and future experiments are performed and projections of their discovery potential are given. The results of this chapter are published in parts in Refs. [1,2].

In Chapter 4 rare kaon decays are investigated as a probe for new physics. In particular, the decays $K^+ \to \mu^+ + \nu_\mu + \gamma'$ and $K^+ \to \mu^+ + \nu_\mu + l^+l^-$ are analyzed from the viewpoint of invisible and visible hidden photon decays. A feasibility study is made to test a class of models in future experiments, such as the hidden photon model as well as selected other models containing new light gauge bosons, based on the results of 40 years old data. Parts of the results of this chapter are published in Ref. [3].

Finally, the work is summarized and an outlook is given.

Chapter 1

The Standard Model, its Limitations and the Need for New Physics

The foundations for the analysis of hidden photon searches are introduced in this chapter. To classify the topic of this work into the big picture of physics, in Sec. 1.1 an overview of the Standard Models of cosmology and particle physics is given. In Sec. 1.1.1 the cosmological concordance model is introduced as the corresponding standard model. The large-scale evolution of the Universe and the contributions to its energy density can be explained within this model.

A part of the energy of the Universe, namely the visible matter, is investigated in detail in hadron and particle physics. The underlying theory of this subject is the Standard Model of particle physics, which is reviewed in Secs. 1.1.2 and 1.1.3. For this purpose I start with a short historical reflection of the evolution of the subject of particle physics, from the discovery of the proton to the Standard Model. It is emphasized that in many cases the resolution of hitherto unexplained phenomena was accompanied by the postulation and discovery of new particles. In the following, the theoretical basis of the Standard Model and in particular of the gauge theory of the electroweak interaction is illustrated, which allows one to easily understand the fundamentals of the hidden photon model.

In Sec. 1.2 the limitations of the Standard Model are discussed, first and foremost with regard to so-called $U(1)$ extensions. Besides the issues occurring at energies far above the currently accessible scales in experiments, the Standard Model exhibits various puzzles which result from high-precision physics at lower energies. Therefore, an overview of such current puzzles is given, which could be explained by the existence of new, light, weakly coupled gauge bosons.

Finally, in Sec. 1.3 the hidden photon model is introduced. For that purpose, the interaction Lagrangian at low energy is derived based on the discussion of Sec. 1.1.3. From this interaction, basic properties of the hidden photon interaction with particles of the Standard Model can be calculated, such as the decay width in Sec. 1.3.3. Furthermore, possibilities to constrain the hidden photon model are reviewed and an update of the current status is given in Sec. 1.3.4.

1.1 The Standard Models of cosmology and particle physics

1.1.1 The cosmological Standard Model

The evolution of the large-scale structure of our Universe is described within the so-called cosmological concordance model. In this model only a few parameters, e.g., the total energy density, the matter density and the cosmological constant, are necessary to describe the

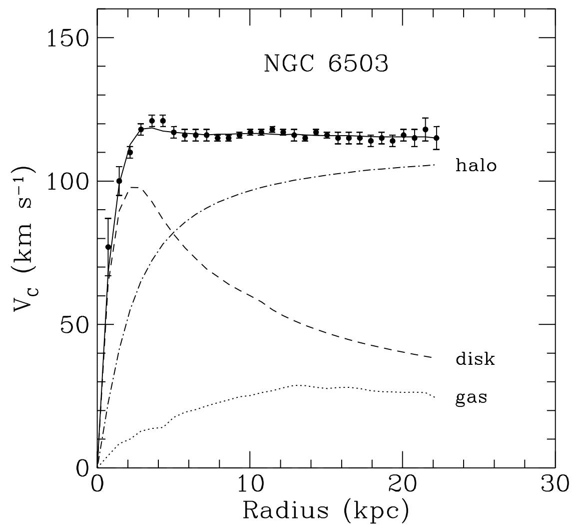

Figure 1.1: Rotation curve of the galaxy NGC 6503. The dotted, dashed, and dashed-dotted curves show the contributions from interstellar gas, the disk of the galaxy, and the dark-matter halo, respectively, as a function of the distance from the galactic center. Obviously, the contribution from the dark matter is needed to reconcile the sum of the contributions (solid curve) with the data points. The figure is taken from Ref. [16].

evolution of the Universe starting from the big bang until today, assuming the validity of general relativity [4, 5]. Mathematically it is based on the Einstein field equations obtained from general relativity, and in particular on a special solution of those, the Friedmann equations. This solution implies that the Universe has a constant curvature and is isotropic which was proven to very high accuracy by the investigation of the cosmic microwave background (CMB) [4–13]. The CMB originates from the big bang and is observed today as an isotropic radiation with a temperature of $\sim 2.7\,\mathrm{K}$. After the recombination phase in which electrons and protons combined to neutral atoms about 380,000 years after the big bang, the Universe was not opaque anymore. The photons emitted at that time are detected today as CMB radiation. Various astrophysical observations, such as the measurement of fluctuations in the CMB, suggest that the Universe is flat. Correspondingly, the curvature is 1, which is related to the total energy density $\Omega_{\text{tot}} = 1$.

The cosmological Standard Model is also referred to as ΛCDM model. This name results from the fact that the parametrization of this model involves the cosmological constant Λ and cold dark matter (CDM). Three important parameters of this model are the energy density of ordinary visible—also named baryonic—matter, dark matter and dark energy. The parameters were recently refined by the data taken by the PLANCK space craft. Already in 1933 the Swiss astronomer F. Zwicky noticed [14] that visible matter cannot be responsible for the observed dynamics of the COMA galaxy cluster. He concluded that invisible matter needs to be responsible for the effects he had found, which he named “dark matter” [14, 15]. Further observations, such as the rotation curves of galaxies [17–21] shown in Fig. 1.1 and the analysis of the large-scale behavior of galaxy clusters and super clusters, suggest the existence of dark matter as well.

Nevertheless, the observed behavior of the large-scale structure of galaxies and galaxy clusters cannot be caused by matter alone. To address this problem, a further ingredient was postulated, namely the "dark energy."

The parameters of the ΛCDM model were accurately determined in various space based experiments such as COBE, WMAP and PLANCK. Deviations from the isotropic CMB were determined to very high accuracy [6–13]. The anisotropies originating from effects when the CMB photons were produced can be expanded in a series of spherical harmonics, which is referred to as the CMB power spectrum. There are 10 free parameters within the ΛCDM model which can be obtained by fitting to the data [4]. The result of the fit is presented in the left panel of Fig. 1.2. It points out that most of the energy of our Universe is contributed by the not-understood sources dark energy and dark matter. The right panel of Fig. 1.2 shows the confidence level contours in the $\Omega_m - \Omega_\Lambda$ plane, where Ω_m and Ω_Λ denote the contributions to the total energy density from matter and dark energy. Besides the contours from CMB and baryonic acoustic oscillations also data from supernovae (SNe) are included.

The recent values determined by PLANCK [12, 13] are around 68.3% and 31.7% for the contributions from dark energy and matter, respectively. Furthermore, it was determined that visible matter only accounts for an energy density of roughly 4.9%, whereas dark matter contributes 26.8%. Assuming the validity of the ΛCDM model means that less than 5% of the energy density of the Universe can be explained by visible matter. Furthermore, no generally accepted theory of the dark energy exists.

Dark matter, as the name implies, needs to have the characteristics of matter and thus of particles with a mass which have to interact at least gravitationally. In general, the dark-matter candidate needs to be non-luminous, i.e., electrically neutral, and stable. Furthermore, dark matter should not be sensitive to the strong interaction. There exist various theories for possible dark-matter candidates. The most promising candidates originate from attempts to solve open questions in the physics of baryonic matter, which is formulated within the Standard Model of particle physics. The interaction via the exchange of the weak gauge bosons is possible in this class of models. These dark-matter candidates are called "weakly interacting massive particles." They can be motivated, e.g., from supersymmetric extensions of the Standard Model and are the best-investigated candidates for dark matter at present. In the following, selected extensions of the Standard Model of particle physics in relation with dark matter are considered in more detail.

1.1.2 From the discovery of the proton to the Standard Model of particle physics

It is worthwhile to look back on the evolution of particle physics from the discovery of the proton to the Standard Model. The discovery of the electron in cathode rays by Thomson in 1897 can be considered as the birth of a new subject of physics—elementary particle physics.[1] Already around 2400 years ago Democritus believed that everything around us is composed of small building blocks which he named "atoms." While we know today that Democritus' imagination of an "atom" is far from being reality, we still believe that all matter can be decomposed into a few building blocks, which are the elementary particles. The idea

[1] In this section no claim is made on presenting the complete history of the Standard Model. Rather, selected steps leading to a theory of the Standard Model are presented. This section is partly based on Ref. [22].

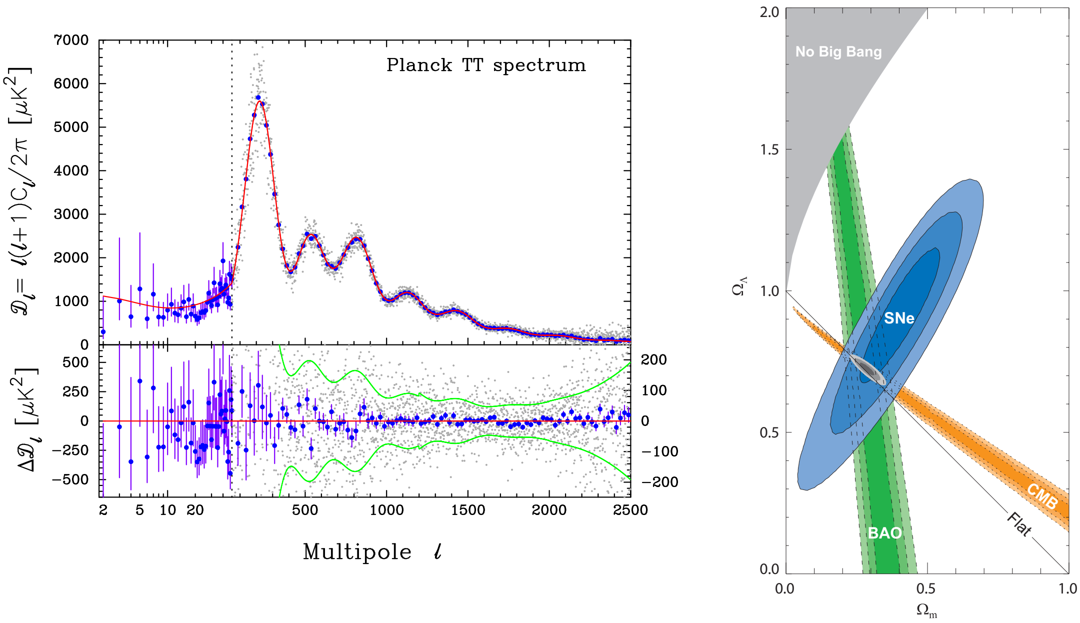

Figure 1.2: Left Panel: Observed power spectrum of PLANCK. Note that the abscissa is plotted logarithmically to $l = 49$. The upper panel shows the coefficients of the temperature power spectrum multipole expansion after subtraction of foreground. The gray data points are the coefficient for each multipole. For $l \geq 50$ the blue points are the averaged results for $\Delta l \simeq 31$ multipoles. The red solid curve represents the best fit to the ΛCDM model parameters. The figure is taken from Ref. [13], where more details can be found. Right Panel: Confidence level contours for the contributions of dark energy and matter to the energy density of the Universe in the $\Omega_m - \Omega_\Lambda$ plane, where Ω_m (Ω_Λ) denotes the energy density originating from matter (dark energy). The confidence levels from baryon acoustic oscillations (BAO), super novae (SNe) and CMB are shown. The figure is adapted from Ref. [4].

of elementary particles had to be adjusted from time to time, when a more fundamental particle was discovered. Up to this point discoveries were related to an increase of the resolution achievable in structure investigations. Enhancing the resolution is directly related to the reduction of the wavelength being equivalent to an increase in energy which can be used to investigate the probe. Therefore, the structure of matter can be probed only to a certain wavelength by optical light. To obtain a better resolution, particle accelerators are used already for several decades. By bombarding a gold foil with α-particles, Ernest Rutherford could show in 1909 that the positive charge of atoms is concentrated around a small area in the center of an atom—the nucleus. In 1917 Rutherford discovered[2] that atomic nuclei are composed of hydrogen nuclei, which he knew as the simplest atomic nucleus. Hence, he considered the hydrogen nucleus as fundamental building block of matter and named it proton—inspired from the ancient Greek word meaning “first.”

[2]Already in 1815 William Proud postulated fundamental particle named “protyle.” He had observed that the masses of investigated atomic nuclei were integer multiples of the mass of the hydrogen atom.

Now one assumed that the atomic nucleus is build up from protons and (nuclear) electrons located in a dense region in the center of the atom. The Russian physicists Ambartsumian and Ivanenko could show from principles of quantum mechanics that this is impossible. However, the model of protons and electrons building up the nucleus was kept. Around 15 years after the discovery of the proton, the neutron was discovered by James Chadwick. The neutron is an electrically neutral particle in contrast to the positively charged proton which was needed to explain the masses and charges of the atomic nuclei. After this discovery, the theory that the nucleus consists of protons and electrons was quickly dropped. However, a theory was needed to explain that a bound object of protons and neutrons could be formed. Yukawa and Stückelberg tried to solve this problem by the introduction of a new force, the nuclear force or also called strong force.[3] The postulation of a new particle mediating an attractive interaction between protons and neutrons—the pion—leads to a new force which binds nuclei together [23]. Yukawa named this new group of particles mesons.[4] The particles involved in the strong interactions are called hadrons. These consist the groups of baryons—such as protons and neutrons—and mesons.

In 1930 Pauli postulated the existence of a new particle in order to explain the continuous energy spectrum of the β-decay observed by Meitner and Hahn in 1911 [25]. The spectrum has to be discrete for the assumed β-decay into two particles. Pauli concluded that a third, invisible particle is involved in the reaction. Today, we know this particle as the electron-neutrino. The first theory of the β-decay was proposed by Fermi [26] in 1934. He introduced a new contact force, which we know today as the weak force.

Independently of the observations of new particles, a covariant quantum field theory of electromagnetism was formulated by Feynman, Schwinger and Tomonaga in the late 1940's. They were awarded with the Nobel Prize in Physics for their fundamental work in Quantum Electrodynamics (QED) in 1965. QED is still used today for the theoretical description of electromagnetic interactions of particles. It is presumed to be the best-understood theory in particle physics and is tested to extremely high precision.

A signature of a particle with the properties postulated by Yukawa could be observed in cosmic radiation and bubble chamber experiments in 1936. These signatures were interpreted to originate from the pion. However, in 1947—with the real discovery of the pion—it turned out that not the pion had been detected eleven years ago. Indeed, the unexplainable muon had been discovered, which was then interpreted as a heavy electron. In the following years, a plethora of new "fundamental" particles could be discovered. Hence, the necessity to find a kind of a periodic table of elements arose. This periodic table of elementary particles was found independently by Gell-Mann [27] and Ne'eman [28] in 1961, which Gell-Mann called "the eightfold way."

Two years later Gell-Mann [29] and Zweig [30] proposed the quark model. Within this model the observed pattern of baryons could be understood qualitatively. They assumed that the mesons and baryons were bound states of two and three constituents, respectively, named "quarks" by Gell-Mann. These should appear in the three different flavors up (u), down (d) and strange (s). The quarks were not treated as real particles within this model, since they could not be observed in experiments.[5]

[3]Note that the term strong force is nowadays used in a different way: the nuclear force is considered as the residual strong force.

[4]Stückelberg did not publish his work on the nuclear forces, since Pauli had the opinion that it was ridiculous [24].

[5]"Quarks were treated like the veal used to prepare a pheasant in the royal French cuisine: the pheasant

An independent view on fundamental particles was given by Feynman within the parton model. Similar to the atomic nucleus, the hadrons constitute of more fundamental particles, the partons. In contrast to Gell-Mann, Feynman treated partons as real particles. It could be proven in deep-inelastic scattering experiments, where a high-energetic electron beam is scattered off a proton target, that point-like partons can be found in the proton. Later, the partons were identified with the quarks. This result had been predicted by Bjorken.

A problem arose from the experimentally observed Δ^{++} baryon, which is made of three up quarks. Since quarks were intended to be fermions, they are sensitive to the Pauli exclusion principle, which states that no two identical fermions may be in the same state. A solution to this problem was found by Han and Nambu [31], who introduced a new degree of freedom named as color. Quarks could be charged under this new quantum number color and interact via the exchange of the gauge bosons of this new force, the gluons. This was the birth of the theory of the strong interaction, which we know as "Quantum Chromo Dynamics (QCD)." QCD exhibits two important properties. The first is that the strong coupling constant becomes weaker with increasing energy and even tends to zero [32, 33]. This phenomenon is called "asymptotic freedom," and was discovered by Gross, Politzer and Wilczek in 1973. They were awarded with the Nobel Prize in Physics for this discovery in 2004. As a consequence of the asymptotic freedom, one can treat the strongly interacting particles within perturbation theory at large energy scales as the coupling is weak. However, at the low energy scales the strong coupling constant is too large to allow for a good perturbative expansion. The other—although unproven—property of QCD is that quarks and gluons cannot exist as single particles. They need to be bound in color neutral states, the hadrons. One refers to this property as "color confinement." This conjecture is driven by the fact that up to now no single quarks could be observed in an experiment.

In the 1960s S. Glashow, A. Salam and S. Weinberg formulated the theory of electroweak unification (GSW theory) in which the massive force carriers of the weak interaction—the $W^{\pm}$ and Z^0 bosons—were predicted. They were awarded with the Nobel Prize of Physics in 1979 for this work. An important contribution was the introduction of weak neutral currents via Z^0 bosons that are similar to the electromagnetic interaction. The particles involved in the reaction do not change their charges but the coupling to electromagnetically neutral states like neutrinos is possible. This type of interaction is contrary to the interactions happening in the nucleon beta decay where a neutron decays into a proton by emitting a W^+ boson. Neutral weak currents were first observed in an experiment at CERN in 1973, where a neutrino beam was scattered off nuclei. Bubble chamber pictures showed few electrons that suddenly start to move, which was understood as exchange of a Z boson. The discovery of neutral weak currents was the manifestation of the GSW theory as unified description of the electromagnetic and weak interactions.

Together with QCD the GSW theory forms the Standard Model of particle physics, which will be explained in detail in the next section.

1.1.3 The Standard Model of particle physics

The fundamental interactions between matter particles are described in terms of a quantum field theory (QFT) within the Standard Model of particle physics (SM). For the construction of a QFT of the Standard Model, the gauge principle formulated by Weyl already in 1929

was baked between two slices of veal, which were then discarded (or left for the less royal members of the court)" H. Leutwyler, found in Ref. [22]

[34] is of crucial importance. Gauge theories are based on the idea that all experimental observables remain unchanged when so-called gauge transformations act on them. These gauge transformations are associated with $U(1)$ or $SU(n)$ gauge groups, with $n > 1$. The number N_G of gauge fields manifesting themselves in the gauge bosons is equal to the number of generators of the gauge group $N_G = n^2 - 1$. Maybe the eventual goal of (particle) physics is to find a QFT based on the gauge principle, which serves as a theory of all fundamental interactions. Although there are four (known) fundamental interactions in nature, i.e., gravitation, electromagnetism, the weak and strong interactions, only three of them are described within the SM.

Electromagnetic Force: The well-known interaction between electrically charged particles as well their interaction with electromagnetic fields can be described within the Quantum Electro Dynamics (QED), which is a $U(1)$ gauge theory. It is the best understood QFT. The messenger particle of the QED is the photon γ. All electrically charged particles interact via the electromagnetic interaction.

Strong Force: The interaction between particles charged under the strong force is described by the Quantum Chromo Dynamics (QCD). The name originates from the fact that one refers to the charge of the strong interaction as "color" charge. Since QCD is a non-abelian $SU(3)$ gauge theory, the eight gluons as the messenger particles of the strong force couple to the color charged quarks and among themselves. The self-interaction of the gluons is a feature of non-abelian gauge theories.

(Electro-) Weak Force: Particles charged under the weak charge, which are all quarks, leptons and the weak gauge bosons $W^{\pm}$, Z, interact via the exchange of heavy, weak gauge bosons. The theory of the weak interaction is not a full QFT. However, the weak interaction is included in the SM by the so-called electroweak (GSW) theory, which unifies the electromagnetic and weak interaction to a $SU(2) \times U(1)$ gauge theory.

The formulation of a QFT including also gravitation is still an open question.

The SM is the theory of fundamental particle physics, in which the interactions of quarks, leptons and gauge bosons are described. The basic building blocks of the SM are QCD and GSW theory. Therefore, the SM is a relativistic gauge theory with the gauge group

$$SU(3)_c \times SU(2)_L \times U(1)_Y, \tag{1.1}$$

where the indices c, L, Y refer to the quantum numbers color, weak isospin and hypercharge, respectively. $SU(3)_c$ is the gauge group of the strong interaction described by QCD.

In the following the construction of the electroweak Lagrangian will be considered in more detail.[6] Before deriving the Lagrangian of the GSW theory, the Lagrangian of QED will be shortly discussed. The corresponding free Lagrangian of fermions and photons reads

$$\begin{aligned}\mathcal{L}_{\text{QED,free}} &= \mathcal{L}_f + \mathcal{L}_\gamma \\ &= \bar{\psi}\left(i\partial\!\!\!/ - m_f\right)\psi - \frac{1}{4}F_{\mu\nu}F^{\mu\nu},\end{aligned} \tag{1.2}$$

where ψ is the fermion field, $F_{\mu\nu} = \partial_\mu A_\nu - \partial_\nu A_\mu$ is the electromagnetic field strength tensor and A denotes the photon field. Since QED is a $U(1)$ gauge theory, its Lagrangian needs

[6] This section is based on Refs. [36, 37]

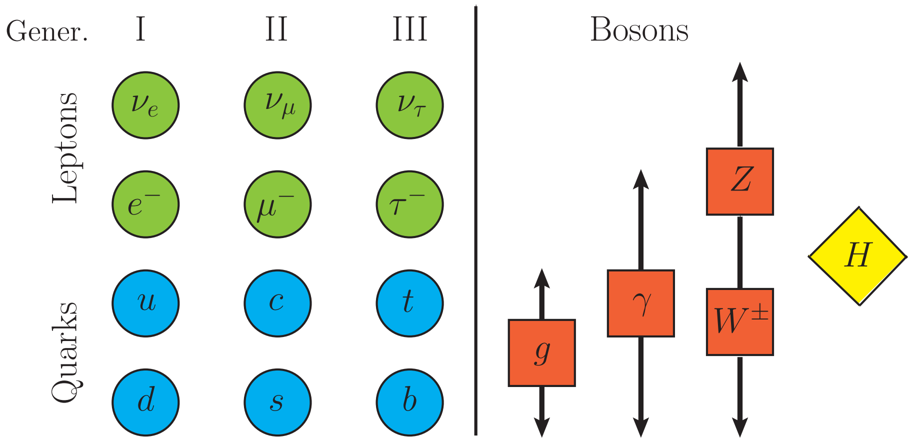

Figure 1.3: Sketch of the particles contained in the SM. The arrows indicate on which particles the forces associated with the gauge bosons act. The figure is adapted from Ref. [35].

to be invariant with respect to local $U(1)$ gauge transformations. One can easily show that the Lagrangian (1.2) is not gauge invariant under these transformations. To restore gauge invariance, the principle of the minimal coupling is used, where an interaction term is introduced. This additional term includes the coupling of a photon to charged fermions into the Lagrangian, which yields

$$\begin{aligned}\mathcal{L}_{\text{QED}} &= \mathcal{L}_f + \mathcal{L}_\gamma + \mathcal{L}_{\text{int}} \\ &= \bar{\psi}\,(i\partial\!\!\!/ - m_f)\,\psi - \frac{1}{4}F_{\mu\nu}F^{\mu\nu} + e\,\bar{\psi}\gamma_\mu\psi\,A^\mu. \end{aligned} \tag{1.3}$$

The combination of the non-abelian gauge group $SU(2)_L$ of the weak isospin and the abelian $U(1)_Y$ hypercharge gauge group forms the symmetry group of the electroweak interaction. The free GSW Lagrangian contains the kinetic terms of the free Lagrangians associated with the fermions underlaying the electroweak force and the gauge bosons associated with the GSW gauge group $SU(2)_L \times U(1)_Y$. However, the free Lagrangian is not invariant under $SU(2)_L \times U(1)_Y$ gauge transformations. Analogously to the discussion for QED, interaction terms are added by means of the principle of the minimal coupling.

The fermions participating in the electroweak interaction are quarks and leptons. These fermions can be grouped into left-handed doublets and right-handed singlets. Moreover, quarks as well as leptons can be arranged into three generations or families. As a first step, the construction for the leptonic sector of the theory will be presented. The leptonic particles are arranged in the doublet $\psi_L^T = (\nu_{eL}, e_L)^T$ and the singlet $\psi_R = (e_R)$. Note that for simplicity e refers to the massive member of each lepton family e, μ, τ, while the ν_e refers to the associated neutrino. The Lagrangian associated with the free gauge bosons contains the three W bosons of the weak isospin and the single hypercharge gauge boson B. The free Lagrangian of the GSW theory can be written as

$$\mathcal{L}_{\text{free}} = \mathcal{L}_W + \mathcal{L}_B + \mathcal{L}_f, \tag{1.4}$$

where

$$\mathcal{L}_W = -\frac{1}{4}\sum_{a=0}^{3} W^a_{\mu\nu} W^{a,\mu\nu}, \quad \mathcal{L}_B = -\frac{1}{4} B_{\mu\nu} B^{\mu\nu}, \quad \mathcal{L}_f = \bar{\psi}(i\partial\!\!\!/ \, \mathbb{1}_{3\times 3})\psi,$$

with the field strength tensors

$$W^a_{\mu\nu} = \partial_\mu W^a_\nu - \partial_\nu W^a_\mu + ig\,\epsilon^{abc} W^b_\mu W^c_\nu, \quad B_{\mu\nu} = \partial_\mu B_\nu - \partial_\nu B_\mu.$$

ψ denotes the combination of the left-handed fermion doublet ψ_L and right-handed fermion singlet ψ_R

$$\psi = \begin{pmatrix} \nu_{eL} \\ e_L \\ e_R \end{pmatrix}.$$

Only the free fields are contained in the Lagrangian (1.4). Analogous to the free QED Lagrangian (1.2), the free GSW Lagrangian (1.4) is not gauge invariant under $SU(2)_L$ gauge transformations of ψ_L and $U(1)_Y$ gauge transformations of both ψ_L and ψ_R. To obtain invariance under $SU(2)_L \times U(1)_Y$ gauge transformations, the ordinary derivative is replaced by the covariant derivative:

$$i\partial_\mu \to iD_\mu = i\partial_\mu - gW^a_\mu T^a - g' B_\mu Y, \tag{1.5}$$

with

$$T^a = \begin{pmatrix} \tau^a/2 & \\ & 0 \end{pmatrix} \quad \text{and} \quad Y = \begin{pmatrix} Y_L\,\mathbb{1}_{2\times 2} & \\ & Y_R \end{pmatrix},$$

where τ^a denotes the Pauli matrices. The massless Lagrangian of the leptonic sector of the GSW theory then reads

$$\mathcal{L} = \mathcal{L}_W + \mathcal{L}_B + \mathcal{L}_f + \mathcal{L}_{\text{int}}, \tag{1.6}$$

with

$$\mathcal{L}_{\text{int}} = -\bar{\psi}\left(gW^a_\mu T^a + g' B_\mu Y\right)\gamma^\mu \psi.$$

The gauge fields in the Lagrangian (1.6) W^a, $a = 1, 2, 3$, and B are not the fields of the corresponding physical states $W^\pm$, Z^0, and γ. After some algebra and with the convention $Y_L = 1/2$ one can identify

$$\begin{aligned} W^\pm_\mu &= \frac{1}{\sqrt{2}}\left(W^1_\mu \mp iW^2_\mu\right), \\ Z_\mu &= \frac{1}{\sqrt{g^2+g'^2}}\left(g\,W^3_\mu - g'\,B_\mu\right) = \cos\theta_W W^3_\mu - \sin\theta_W B_\mu, \\ A_\mu &= \frac{1}{\sqrt{g^2+g'^2}}\left(g'\,W^3_\mu + g\,B_\mu\right) = \sin\theta_W W^3_\mu + \cos\theta_W B_\mu, \end{aligned} \tag{1.7}$$

where θ_W denotes the weak mixing angle with $\cos\theta_W = g/\sqrt{g^2+g'^2}$. Now A_μ can be identified with the photon field and one obtains $Y_R = 1$ and the electromagnetic coupling $e = g\,g'/\sqrt{g^2+g'^2}$. The interaction term of Lagrangian (1.6) is found as

$$\mathcal{L}_{\text{int}} = -e\left(A_\mu j^\mu_{\text{em}} + \frac{1}{\sin\theta_W\,\cos\theta_W} Z_\mu j^\mu_{\text{NC}} + \frac{1}{\sqrt{2}\sin\theta_W}\left(W^+_\mu\, j^\mu_{\text{CC}} + W^-_\mu\,(j^\mu_{\text{CC}})^\dagger\right)\right), \tag{1.8}$$

with

$$
\begin{aligned}
j^{\mu}_{\text{em}} &= -\left(\bar{e}_L,\, \bar{e}_R\right)\gamma^{\mu}\begin{pmatrix} e_L \\ e_R \end{pmatrix}, \\
j^{\mu}_{\text{NC}} &= \frac{1}{2}\bar{\nu}_{eL}\gamma^{\mu}\nu_{eL} - \frac{1}{2}\bar{e}_L\gamma^{\mu}e_L - \sin^2\theta_W j^{\mu}_{\text{em}}, \\
j^{\mu}_{\text{CC}} &= \bar{\nu}_{eL}\gamma^{\mu}e_L,
\end{aligned}
$$

denoting the electromagnetic, neutral weak and charged weak currents, respectively.

No mass terms were included in the Lagrangian (1.6) yet. A naïve introduction of mass terms, as it is possible in the case of QED, would violate gauge invariance. Therefore, another method is used to assign a mass to the particles which is the so-called Higgs mechanism. A new complex, scalar isodoublet field ϕ—the Higgs field—is introduced. This leads to an additional term to the Lagrangian (1.6)

$$
\mathcal{L}_H = \partial_{\mu}\phi^{\dagger}\partial^{\mu}\phi \underbrace{-\mu^2\phi^{\dagger}\phi - \lambda(\phi^{\dagger}\phi)^2}_{\equiv -V(\phi)}, \tag{1.9}
$$

where $\lambda > 0$ and $\mu^2 < 0$ are constants of the potential, which is invariant under $SU(2)$ gauge transformations. The potential $V(\phi)$ is minimized for $(\phi^{\dagger}\phi) = {-\mu^2}/{2\lambda} \equiv {\rho_0^2}/{2}$. Every state of the form $\phi = U(x)\begin{pmatrix} 0 \\ \rho_0/\sqrt{2} \end{pmatrix}$, where $U(x)$ is an arbitrary $SU(2)$ transformation, minimizes the potential $V(\phi)$, but breaks $SU(2)$ gauge invariance. ρ_0 is the vacuum expectation value of the Higgs field. The introduction of this new field provokes that the symmetry of the ground state is less than that of the Lagrangian. Spontaneous symmetry breaking occurs.

An interaction term between fermions, gauge bosons and the Higgs sector is introduced in a way that $SU(2)_L \times U(1)_Y$ invariance is preserved. The Higgs field is coupled to fermions by a $SU(2)_L$ invariant Yukawa coupling

$$
\mathcal{L}_{\text{hff}} = -c_l\bar{\psi}_R\phi^{\dagger}\psi_L - c_l^*\bar{\psi}_L\phi\psi_R. \tag{1.10}
$$

To obtain a coupling between the gauge bosons and the Higgs field, one introduces the covariant derivative for the Higgs field

$$
\partial_{\mu}\phi \rightarrow D_{\mu}\phi = \partial_{\mu}\phi + igW^a_{\mu}\frac{\tau^a}{2}\phi + ig'B_{\mu}Y_H\phi,
$$

with $Y_H = Y_L - Y_R = {1}/{2}$. The ground state of ϕ is not invariant under $SU(2)_L \times U(1)_Y$ transformations. However, it is invariant under $U(1)$ transformations of the form

$$
e^{i\left({\tau^3}/{2} + Y_H\right)\chi(x)}\begin{pmatrix} 0 \\ \rho_0/\sqrt{2} \end{pmatrix} = \begin{pmatrix} 0 \\ \rho_0/\sqrt{2} \end{pmatrix},
$$

where $Q = {\tau^3}/{2} + Y_H$ is the electrical charge. By expanding the kinetic term $(D_{\mu}\phi)^{\dagger}(D^{\mu}\phi)$ of the Lagrangian, expressions appear which have the structure of mass terms. Their coefficients can be identified with the masses of the gauge bosons

$$
m_W^2 = \frac{g^2}{4}\rho_0^2, \quad m_Z^2 = \frac{(g^2 + g'^2)}{4}\rho_0^2.
$$

The W and Z boson masses are related by $m_W^2 = m_Z^2 \cos^2\theta_W$. Fermions acquire a mass in a similar way from expanding Eq. (1.10), where one finds $m_e = c_l(\rho_0/\sqrt{2})$. The photon as well as the neutrinos remain massless.

Hence, by spontaneous symmetry breaking a mass term appears in the Lagrangian which preserves gauge invariance but assigns a mass to the particles. The Higgs field manifests itself by the so-called Higgs particle which is a massive spin-0 boson.

The integration of the quark sector can be performed analogously to the leptonic sector. The left-handed quark fields can be grouped into singlets in the same way. It turned out that grouping the physical mass states of the light, left-handed quarks does not lead to an appropriate description of nature. Instead, the down quark d and the strange quark s mix:

$$\begin{pmatrix} u_L \\ d_L \end{pmatrix} \to \begin{pmatrix} u_L \\ d'_L \end{pmatrix} = \begin{pmatrix} u_L \\ \cos\theta_c d_L + \sin\theta_c s_L \end{pmatrix},$$

where θ_c is the Cabibbo mixing angle. The mixing angle θ_c had been predicted previously by Cabibbo from the analysis of leptonic decays of pions and kaons. The field d' couples with the same strength as leptons. d and s are the physical mass states of the down and strange quarks. The aforementioned kaon decays and the neutron β-decay could be successfully described by this mechanism. However, a term in the weak neutral current $\bar{u}_L\gamma^\mu u_L - \bar{d}'_L\gamma^\mu d'_L$ appears, which leads to a flavor changing between s and d quarks. These flavor changing neutral currents could not be observed in experiments. An explanation to this issue is given by the GIM-mechanism, in which a second generation of quarks is postulated:

$$\begin{pmatrix} c_L \\ s'_L \end{pmatrix} = \begin{pmatrix} c_L \\ -\sin\theta_c d_L + \cos\theta_c s_L \end{pmatrix},$$

where c is the mass state of the charm quark. The flavor changing neutral terms vanish by including this second generation of quarks into the neutral weak quark current.

The procedure was generalized to a third family of quarks, the bottom quark b and the top quark t, where now the states are mixed by the so-called CKM matrix. This concept explains the observed violation of the charge-parity symmetry CP in neutral kaon systems [38].

To conclude, several predictions of the GSW theory could be explored successfully in experiments, e.g.,

Weak neutral currents: Weak neutral currents were predicted from the construction of the GSW Lagrangian. They were observed in 1973 [39].

Weak gauge bosons: The weak gauge bosons were postulated in this theory. They could be observed in 1983. Furthermore, the relation of their masses by the weak mixing angle is probed to high accuracy.

Additional quark flavors: When the GSW theory was formulated only the u, d and s quark were known. From the GIM mechanism another quark flavor, the charm quark c, was postulated to explain the absence of flavor changing, neutral currents [40]. The discovery of its lowest bound state, the J/ψ meson, proved this prediction [41, 42]. Similarly, the top quark was postulated from the CKM mechanism [38] and could be discovered in 1995 [43].

Third lepton family: The last postulated leptons, the τ lepton and its associated neutrino ν_τ could be observed in 1975 [44] and 2000 [45], respectively.

Three lepton and quark families: Up to now there are no hints for more than the three lepton and quark families. In various experiments this prediction was investigated without finding any excess.

Higgs boson: The Higgs field introduces a new particle which is known as the Higgs boson. The discovery of this boson at the Large Hadron Collider at CERN was announced very recently [46, 47].

One obtains the SM Lagrangian from the combination of the GSW Lagrangian and the QCD Lagrangian, where the latter is given by

$$\mathcal{L}_{\mathrm{QCD}} = \sum_f \bar{q}_f \left(i\not{\mathcal{D}} - m_f \right) q_f - \frac{1}{2} \mathrm{Tr}_c \left(\mathcal{G}_{\mu\nu} \mathcal{G}^{\mu\nu} \right). \tag{1.11}$$

The sum runs over the quark flavors $f = u, d, s, c, b, t$. The quark spinor of flavor f is denoted by q_f, which is a triplet with respect to the $SU(3)_c$ color gauge symmetry. The respective current-quark mass is denoted by m_f and

$$\mathcal{G}_{\mu\nu} = \partial_\mu \mathcal{A}_\nu - \partial_\nu \mathcal{A}_\mu + i g_s \left[\mathcal{A}_\mu, \mathcal{A}_\nu \right]$$

is the gluon field strength tensor, where $\mathcal{A}$ is the gluon field. Furthermore,

$$\mathcal{D}_\mu = \left(\partial_\mu + i\, g_s\, \mathcal{A}_\mu \right)$$

is the covariant derivative of QCD, which keeps gauge invariance under local $SU(3)_c$ transformations $U(x) = \exp\left(-i\, \theta_a(x) \lambda_a/2\right)$, where λ_a are the Gell-Mann matrices.

In this section the construction of the SM Lagrangian and the success of the SM in the description of elementary particle physics were illustrated. Many known phenomena can be explained within the SM and observables can be calculated to very high accuracy. The next section will deal with limitations and current issues of the SM, as well as ideas to resolve them.

1.2 Limitations and extensions of the SM

1.2.1 Overview of hints for new physics

Recently a new, scalar boson was observed at the LHC [46,47], which is most likely the Higgs boson—the last missing piece of the SM. The observation of the Higgs boson was predicted from the spontaneous breaking of the electroweak symmetry. This is another important success of the SM. Although a plethora of phenomena can be described within the SM, there are strong hints for physics beyond our known model. As an example, the SM cannot contain a particle which serves as a dark-matter candidate by definition. Thus, around 80% of matter cannot be explained within the SM. Nevertheless, today the SM is the theory of elementary particle physics up to a scale of $\mathcal{O}(1\,\mathrm{TeV})$.

The limitation of the SM as fundamental theory can be pointed out by the famous "gauge hierarchy problem." So far, there is no explanation why the weak interaction, as the weakest of the three forces in the SM, is still 30 orders of magnitude stronger than gravity. Another hierarchy problem is stated by the differences of the particle masses varying over several orders of magnitude [4].

As mentioned before, gravity is not included in the SM. Therefore, the SM cannot serve as a theory of all known forces. The energy scale where (quantum) gravitational effects become important is the Planck scale at $M_P \simeq 1.2 \times 10^{19}\,\text{GeV}$. Hence, there are 15 orders of magnitude between the scale of the SM and the Planck scale of a "theory of everything" unifying the forces of the SM and gravitation. This leaves a large space for possible new physics.

In addition, the Higgs boson mass m_H gains corrections Δm_H from the vacuum polarization. Fermions of the mass m_f and coupling strength λ_f to the Higgs run in a loop, giving rise to

$$\Delta m_H^2 = -\frac{|\lambda_f|^2}{8\pi^2}\, N_{c,f}\, \Lambda_{\text{UV}}^2 + \ldots,$$

where $N_{c,f}$ is the number of colors of the fermion f. Moreover, Λ_{UV} is the cut-off scale to regularize the loop integral. It can be interpreted as the minimal scale at which new physics enters. Terms growing logarithmically with this scale are absorbed in the ellipsis. The largest SM correction to m_H results from the top quark contribution, where $\lambda_f \simeq 1$. For new physics which enters at the Planck scale ($\Lambda_{\text{UV}} \simeq M_P$), the vacuum-polarization correction to the Higgs boson mass exceeds its bare mass by around 30 orders of magnitude. There is no reason, why the correction to the bare mass is that much larger. The removal of the quadratical divergence by renormalization leads to an unnatural fine tuning of 1 part in 10^{30} known as "fine-tuning" and "unnaturalness" problem. Since the scale Λ_{UV} influences the vacuum expectation value of the Higgs boson, which is related to the masses of the fermions and gauge bosons in the SM, the SM is sensitive to this scale. A solution to the gauge hierarchy fine-tuning problem is given by a new symmetry turning fermions into bosons and vice versa, which is known as "Supersymmetry (SUSY)." An additional scalar boson introduced from broken SUSY provokes that the correction to the Higgs boson mass is only logarithmically depending on the scale Λ_{UV}. This strongly reduces the fine-tuning from 1 part in 10^{30} to a $\mathcal{O}(1\%)$ effect, as long as the mass of the scalar superpartner does not exceed m_H too much.

The validity of the SM is not challenged by the fine-tuning problem, rather it points out one more time that the SM can only account for physics up to the weak scale. Questions like the origin of particle masses, in particular the mass of the Higgs boson or the number of its free parameters cannot be answered within the SM. Another issue enters, when the so-called "GUT scale" is reached, at which—predicted by renormalization group equations—the individual gauge couplings of strong, weak, and electromagnetic forces should unify to one coupling constant of a "Grand Unified Theory (GUT)." As illustrated in Fig. 1.4, this does not occur in the SM (left panel). For comparison the evolution of the three inverse couplings with new physics entering at the $\mathcal{O}(1\,\text{TeV})$ scale by means of superpartners in the Minimal Supersymmetric Standard Model (MSSM) is shown in the right panel. Including the supersymmetric contribution gives rise to a unification of the gauge couplings. This is understood as a strong evidence for SUSY at the scale of $1\,\text{TeV}$ [4, 48].

Furthermore, neither dark matter nor dark energy accounting for 95% of the energy density of the Universe are included in the SM. These and many more hints not treated here, motivated to search for physics beyond the SM, which might lead to a more fundamental theory of elementary particle physics.

As a further feature, SUSY can lead to a candidate for a dark-matter particle. This so-called neutralino is consistent with the requirements discussed in Sec. 1.1.1. It is remarkable that the neutralino as dark-matter candidate arises automatically from supersymmetric SM

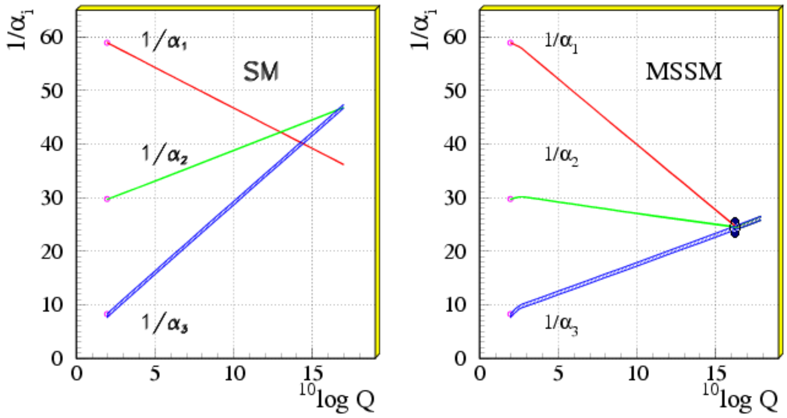

Figure 1.4: Evolution of the inverse gauge coupling constants. Left panel: SM coupling constants. Right panel: Coupling constants with additional superpartners at the $\mathcal{O}(1\,\text{TeV})$ scale in the minimal supersymmetric SM. The figure is taken from Ref. [4] and was first published in Ref. [48].

extensions with R-parity, which is introduced to avoid the proton decay. Since SUSY provides a dark-matter candidate as a byproduct, one often refers to this as "WIMP miracle."

Therefore, supersymmetric extensions of the SM seem to be very promising. If SUSY exists at a mass scale at the TeV scale, its signals are visible in the data taken at the LHC. Thus, constraints on the particular models of SUSY can be derived. As an example, all of the phenomena addressed in this paragraph can be explained within the MSSM. In general, the MSSM has more than 120 free parameters, which makes it very compelling to find constraints on this model. Some versions of the MSSM require only few parameters, such as the constrained MSSM (cMSSM) or the phenomenological MSSM (pMSSM). These models became very popular as benchmark scenarios [4], because several of their free parameters are constrained by measurements of SM processes.

From the up to now existing data taken at the LHC one is already able to draw conclusions. The observation of the Higgs boson at a mass of 125 GeV sets stringent bounds on the models. It is discussed in Ref. [49] that in particular models, such as the cMSSM, the Higgs mass is predicted to be below the observed value. Hence, classes of models are excluded now. Furthermore, the absence of a SUSY signal in the data states further constraints, e.g., on the masses of the SUSY partners of the SM particles. For example, the mass of gluinos, which are the scalar SUSY partners of the gluon, must be above 1 TeV [4, 50]. Since the extraction of bounds for the parameters strongly depends on model assumptions, SUSY below the scale of 1 TeV cannot be considered as excluded. However, one expects that the future runs at the LHC at a center-of-mass energy of 13 TeV or higher will allow one to probe whether or not SUSY exists.

The limitations of the SM mentioned above arise at its high-energy frontier. In addition to these high-energy issues, there are several puzzles existing at the intensity frontier of the SM, where high-precision experiments challenge the theoretical predictions. In the next sections, puzzles from high-precision tests of the SM are introduced and their implications on possible new physics are pointed out.

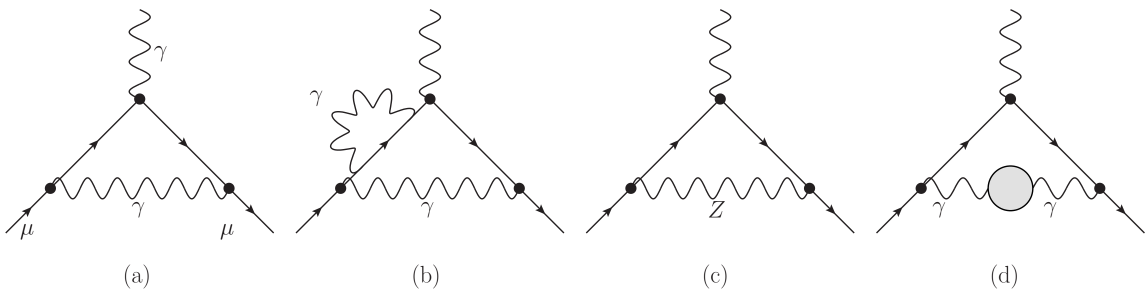

Figure 1.5: Feynman diagrams contributing to the anomalous magnetic moment of a lepton, here in particular for the muon. The Schwinger term, the leading-order correction from QED is represented by diagram (a). Further selected corrections from QED (b), the weak interaction (c) and (hadronic) vacuum polarization (d) are also shown.

1.2.2 The anomalous magnetic moment of the muon

One of the currently most discussed puzzles of the SM is the discrepancy in the theoretical and experimental determination of the anomalous magnetic moment of the muon. Since no significant deviation for the electron anomalous magnetic moment has been found, this section will concentrate on the anomalous magnetic moment of the muon.

The interaction of a massive particle of charge e, mass m and spin s with a magnetic field B leads to a splitting of the levels in the energy spectrum

$$\Delta E = -\underbrace{\left(g\frac{e}{2m}\,\vec{s}\right)}_{=:\vec{\mu}}\cdot\vec{B},$$

where μ is known as the magnetic moment, which is proportional to the gyromagnetic factor g. The gyromagnetic factor g can be calculated in relativistic quantum mechanics, and one finds for fermions in Dirac theory $g = 2$. The anomalous magnetic moment of a fermion $a = {}^{(g-2)}/_{2}$ denotes the relative deviation from this value, which is caused by higher-order corrections. In the first calculation of the Feynman diagram (a) of Fig. 1.5 in QED, Schwinger found a deviation from 2. This so-called Schwinger term is the by far largest contribution to the anomalous magnetic moment.

Measurements of the anomalous magnetic moment of the muon a_μ are performed now for more than 50 years [51]. The anomalous magnetic moment can be investigated in experiments with extremely high accuracy. This serves as a test of the validity of the SM, since a_μ can be precisely predicted within SM calculations. The current average experimental value [52, 53] is

$$a_\mu^{\mathrm{exp}} = 116592089(63) \times 10^{-11}.$$

The anomalous magnetic moments of the electron and muon were calculated to high accuracy in theory. It is convenient to split the SM corrections to the anomalous magnetic moment as

$$a_\mu = a_\mu^{\mathrm{QED}} + a_\mu^{\mathrm{weak}} + a_\mu^{\mathrm{hadronic}}.$$

Selected corrections to the anomalous magnetic moment are illustrated by the Feynman diagrams in Fig. 1.5 from QED (b), the weak interaction (c) and (hadronic) vacuum polarization

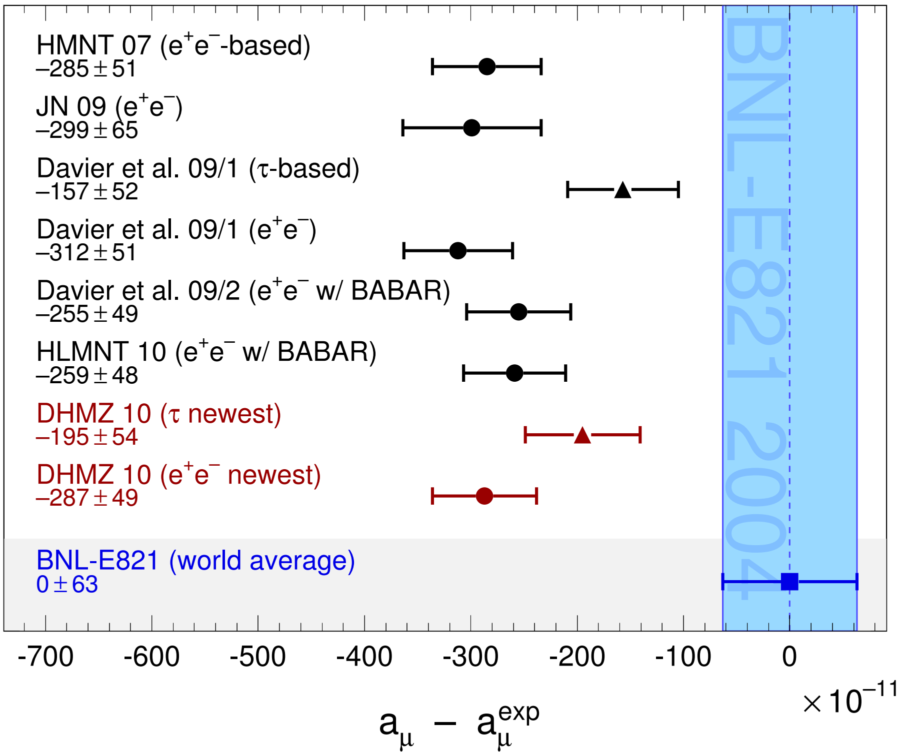

Figure 1.6: Overview over existing SM predictions for the anomalous magnetic moment of the muon a_μ, where the current experimental result [53] was subtracted. The experimental uncertainty is represented by the blue vertical band. The figure is adapted from Ref. [54].

(d). The part contributed by QED is very well known and has been recently calculated to $\mathcal{O}(\alpha_{\text{em}}^5)$ for the electron [55] as well as for the muon [56]. The QED contribution to the muon's anomalous magnetic moment a_μ is given in Ref. [56]

$$a_\mu^{\text{QED}} = 116584718.846(37) \times 10^{-11}. \tag{1.12}$$

The weak contribution calculated up to 2-loop order is found to be [57–60]

$$a_\mu^{\text{weak}} = 154(2) \times 10^{-11}.$$

At present, the largest uncertainty enters from the precise lack of knowledge of the hadronic correction, in particular from the estimates of the hadronic vacuum polarization (HVP) as well as the hadronic light-by-light scattering term (HLbL). Both are currently under investigation by various experimental as well as theoretical groups. The most recent values for the hadronic contribution are given in Ref. [61]

$$\begin{aligned} a_\mu^{\text{HVP, LO}} &= 6886.0(42.4) \times 10^{-11}, \\ a_\mu^{\text{HVP, NLO}} &= -98.4(0.7) \times 10^{-11}, \\ a_\mu^{\text{HLbL}} &= 116(39) \times 10^{-11}, \end{aligned}$$

in the leading order, where of course also higher-order corrections have to be accounted for. Eventually, the prediction of the anomalous magnetic moment of the muon in the SM leads to [61]

$$a_\mu^{\mathrm{SM}} = 116591776.5(56.3) \times 10^{-11},$$

giving rise to a discrepancy between the theoretical and experimental value [54, 61] of

$$a_\mu^{\mathrm{exp}} - a_\mu^{\mathrm{th}} = 312.5(85.4) \times 10^{-11}.$$

This corresponds to a discrepancy of $\simeq 3.7$ standard deviations, which cannot be explained so far. The comparison between the experimental value and some selected predictions is shown in Fig. 1.6.

Several models were motivated to explain this anomaly. In addition, any extension of the SM needs to be in agreement with the high-precision results of a_e and a_μ. Therefore, the accurate determination of a_μ will not only be used as a motivation for SM extensions. Furthermore, it will serve as a test for the models and lead to bounds for the corresponding parameters. A new experiment at the Fermilab and progress in the theoretical calculations, in particular of the hadronic contribution, will clarify in the near future, if this discrepancy results from physics beyond the SM or originates from underestimated SM corrections.

1.2.3 The strong CP problem and axions

The basic properties of QCD, like gauge invariance and Lorentz invariance, allow for an additional term in the Lagrangian which is CP-violating

$$\mathcal{L}_{QCD} \supset \frac{g_s^2}{32\pi^2}\,\theta\,\left(G^a_{\mu\nu}\widetilde{G}^{\mu\nu,\,a}\right), \tag{1.13}$$

where θ is the fundamental, experimentally constrained parameter associated with the strong CP-violation. The existence of such a CP-violating term in the SM Lagrangian would lead to a non-vanishing electric dipole moment of the neutron. It can be estimated to be of the order

$$|d_n| \sim 10^{-16}\,|\bar{\theta}|\,e\,\mathrm{cm},$$

where $\bar{\theta} \equiv \theta + \arg\det M$ is the effective physical CP-violating parameter in the SM and M is the quark mass matrix [62]. As discussed in Refs. [62, 63], the existing upper experimental bound on the electric dipole moment of the neutron is given in Refs. [4, 64] by

$$|d_n| < 0.29 \times 10^{-25} e\,\mathrm{cm},$$

which implies

$$|\bar{\theta}| \simeq 10^{-10}.$$

One expects $|\bar{\theta}| \sim \mathcal{O}(1)$, since $|\bar{\theta}|$ is a dimensionless parameter. This represents another fine-tuning problem in the SM, which is known as the strong CP problem.

The strong CP problem was first resolved by Peccei and Quinn, who introduced a new $U(1)$ symmetry [65]. It was realized that this solution leads to a new light, pseudoscalar particle, the axion [66, 67]. The axion is the (pseudo-) Goldstone boson arising from the spontaneous symmetry breaking of the Peccei-Quinn $U(1)$ symmetry. Due to this symmetry a further term appears in the Lagrangian,

$$\mathcal{L}_{QCD} \supset \frac{g_s^2}{32\pi^2} \frac{a}{f_a} \left(G^a_{\mu\nu} \widetilde{G}^{\mu\nu,\,a} \right), \tag{1.14}$$

where a and f_a denote the axion field and the axion decay constant, respectively. Therefore, the parameter θ is shifted to $\theta + (a/f_a)$, which reestablishes CP conservation.

As discussed in the review articles [62, 63], the axion mass m_a can be calculated from current algebra relations as a function of its dimensionful decay constant f_a [66, 67]

$$m_a \simeq 0.6\,\mathrm{meV} \times \frac{10^{10}\,\mathrm{GeV}}{f_a}.$$

Originally, one assumed that the decay constant of the axion is at the weak scale, $f_a \sim 246\,\mathrm{GeV}$. This conjecture could soon be disproved with the discovery of the J/ψ meson. The "Kim–Shifman–Vainshtein–Zakharov (KSVZ)" model proposed in Refs. [68,69] provides an invisible axion and is consistent with experimental data. The KSVZ model is still today considered as the most promising axion model [62, 63].

Several independent constraints on these parameters exist, which are extensively discussed in Refs. [62, 63]. The fact that axions could not be detected hitherto can be translated into exclusion limits for the mass and coupling parameters according to

$$m_a < 1\,\mathrm{keV} \Leftrightarrow f_a < 10^4\,\mathrm{GeV}.$$

It is obvious from Eq. (1.14) that axions interact with gluons. A similar term, in which the gluon field strength tensor is replaced by the electromagnetic field strength tensor, gives rise to a low-energy effective interaction Lagrangian

$$\mathcal{L}_{a\gamma\gamma} = g_{a\gamma\gamma}\, a\, \vec{E} \cdot \vec{B}, \tag{1.15}$$

describing the Primakoff interaction of the axion with photons. Nevertheless, the interaction of the axion with the gluon as well as the photon is strongly suppressed [62]. The axion can serve as a candidate for a dark-matter particle, although it interacts via the strong as well as the electromagnetic interaction. As a dark-matter candidate, the mass of the axion must be below a few meV. This implies a lifetime longer than that of the Universe.

These possibilities motivated various attempts to search for axions, such as beam-dump experiments [71–73] searching for an anomalous lepton pair abundance behind the beam dumps of high-energy experiments. Another strategy are the so-called Light-shining-through-wall experiments. In these experiments intense laser light is radiated onto a shield behind which a photon detector is placed. In an ideal case, the SM background is complete reduced by the shield. Hence, the photons reaching the detector need to result from the creation and annihilation of an axion as described by the Lagrangian in Eq. (1.15) [70]. Derived bounds for the parameter space of axions can be found in Fig. 1.7.

The generalization of this concept leads to a family of hypothetical particles, the axion-like particles (ALPs). They are widely studied in high-intensity experiments [62, 74]. In the case of ALPs the condition that the decay constant—or correspondingly, the coupling constant—is related with the mass is relaxed. The QCD axion within in the KSVZ model, is a special case of an ALP. One can see that the axion and axion-like particles are further examples, where a puzzle of the SM leads to an extension of the SM, which can be tested by experiments at the precision frontier complementary to direct searches at larger energies.

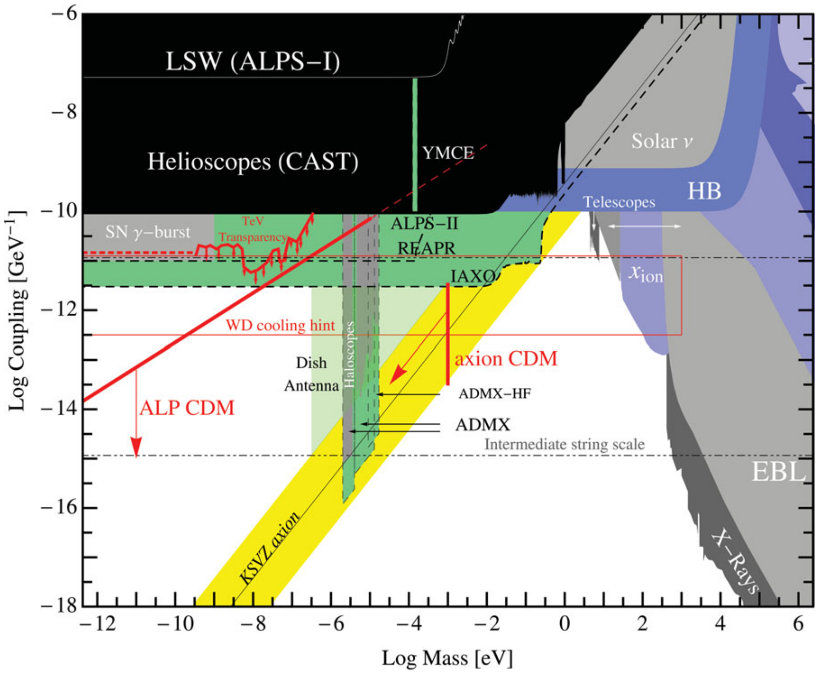

Figure 1.7: Existing constraints for the parameter space of axion-like particles as a function of the mass m_a and the coupling to two photons $g_{a\gamma\gamma}$. The colored regions correspond to existing bounds from astronomical observations (gray), from laboratory experiments (dark-green), and from astrophysical and cosmological arguments (blue). The light-green shaded regions illustrates the projected reach of future experiments. Hints for axions and ALPs from astrophysics are indicated by the red curves. The yellow region labeled as KSVZ axion refers to the QCD axion. This is the region of parameters in which the strong CP problem can be solved. The figure is adapted from Ref. [70].

1.2.4 Hadrons in the Standard Model and the proton radius puzzle

The treatment of hadronic states is not really a limitation of the SM but a generic feature of QCD. Due to the two features named above, asymptotic freedom and confinement, quarks and gluons cannot exist as free particles. Moreover, at low energies their bound states, the hadrons, cannot be treated in terms of a perturbative expansion. The typical scale of momentum transfer at which one assumes that hadrons can be treated perturbatively, is $\sim 3\,\text{GeV}$. The laws of perturbation theory can be applied above this scale to calculate the Feynman amplitudes of the particular processes. Below this scale, which is the case for the processes investigated in this thesis, the structure of the hadrons involved in the reactions must be discussed in a model dependent way parameterizing the hadronic interaction part.

The interaction of photons with hadrons gives rise to the electromagnetic structure of the hadron (see Fig. 1.8). This structure can in general be parametrized by form factors, which would require a very complicated non-perturbative calculation within QCD. Therefore, the present strategy is to determine them in experiments. For a spin-0 hadron the

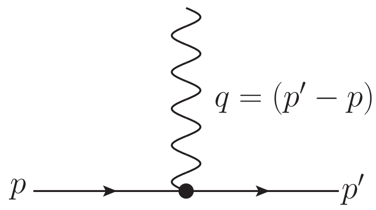

Figure 1.8: Feynman diagram of the QED vertex, describing the coupling of a photon to a charged particle.

electromagnetic current $j_\mu = (p + p')_\mu$ is modified to

$$J_\mu = F((p' - p)^2)\,(p + p')_\mu, \tag{1.16}$$

where F is is the form factor of the spin-0 hadron. In the description of elastic scattering reactions, the parametrization of the electromagnetic structure of spin-0 hadrons involves only the effects from the spatial charge distribution.

As an further example, the electromagnetic structure of a nucleon, as every spin-$1/2$ particle, can be parametrized by two scalar functions, which are the so-called electromagnetic form factors. Compared to the current operator for the scattering off a point-like particle $j_\mu = \bar{u}\gamma_\mu u$, such as the electron, the electromagnetic current can be expressed as

$$J_\mu = \bar{u}(p') \left(F_1(Q^2)\gamma_\mu + \frac{i\,F_2(Q^2)}{2M_N}\,\sigma_{\mu\nu}\,q^\nu \right) u(p), \tag{1.17}$$

where $q = p' - p$, $Q^2 = -q^2 > 0$, and F_1 and F_2 are the Dirac and Pauli form factors, respectively. Moreover, the mass of the proton is $M_N = 938.3\,\mathrm{MeV}$. The Dirac and Pauli form factors can be rewritten in terms of the electric and magnetic Sachs form factors G_E and G_M:

$$G_E(Q^2) = F_1(Q^2) - \frac{Q^2}{2M_N^2} F_2(Q^2), \tag{1.18}$$

$$G_M(Q^2) = F_1(Q^2) + F_2(Q^2), \tag{1.19}$$

which are functions of the momentum transfer Q^2. The Sachs form factors can be related with the distribution of charge and magnetic moments in the so-called Breit frame. Over a wide range of momentum transfer up to $Q^2 \simeq 30\,\mathrm{GeV}$ the form factors can be obtained from experimental data. In the region $Q^2 \lesssim 1\mathrm{GeV}^2$ they can be obtained by fitting the standard dipole

$$G_D(Q^2) = \frac{1}{\left(1 + Q^2/\Lambda^2\right)^2},$$

with $\Lambda = 0.843\,\mathrm{GeV}$. The form factors G_E and G_M in this parametrization are given by

$$G_E(Q^2) = G_D(Q^2), \qquad G_M(Q^2) = \mu_p G_D(Q^2),$$

where $\mu_p \cong 2.793$ is the magnetic moment of the proton. The electric charge radius of the nucleon $r_E = \sqrt{< r_E^2 >}$ is obtained from the slope of the electric Sachs form factor at $Q^2 = 0$

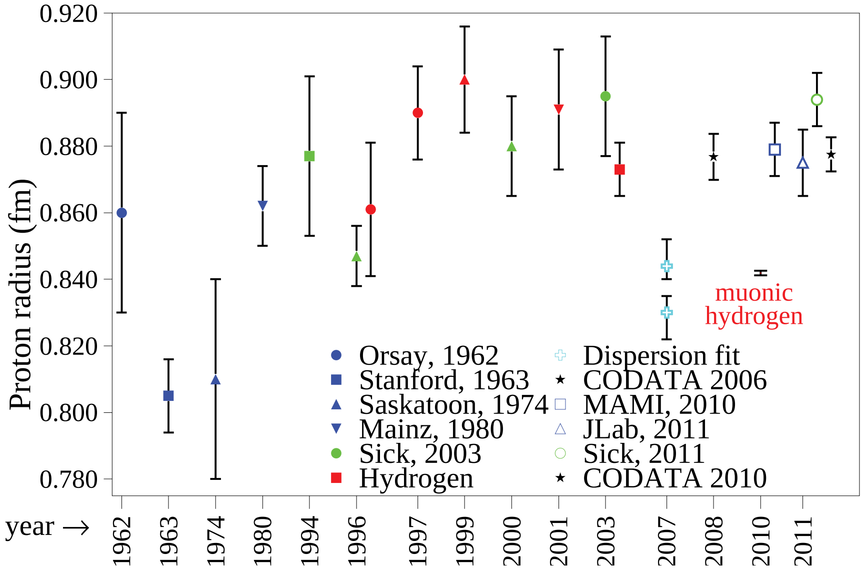

Figure 1.9: Evolution of the values of the proton charge radius from 1962 until today. The figure is adapted from Ref. [75].

according to

$$< r_E^2 >= -6 \frac{dG_E(Q^2)}{dQ^2}\bigg|_{Q^2=0} .$$

This observable was recently determined in several independent ways, such as elastic electron-proton scattering and spectroscopy of electronic and muonic hydrogen.

The electric charge radius is determined as $r_E = 0.879(8)$ fm and $r_E = 0.8768(69)$ fm from elastic electron-proton scattering [76, 77] and electronic hydrogen [78], respectively. From the analysis based on muonic hydrogen [79] $r_E = 0.84184(67)$ fm is found. Recently, the result from muonic hydrogen has been refined to $r_E = 0.84087(39)$ fm [80] with a significantly smaller uncertainty. This corresponds to an uncertainty being one order of magnitude smaller than for the other extractions. The values obtained from muonic hydrogen compared to the ones from electron-proton scattering and electronic hydrogen differ by $\sim 4\%$. Together with the tiny uncertainty, a discrepancy of around 7 standard deviations is found. The different results are presented in Fig. 1.9. Besides the evolution of the values for the electric charge radius of the proton, one can see that the extractions from electronic hydrogen and electron-proton scattering agree within their error bars.

The discrepancy between the muonic and electronic determination of the charge radius has raised a lot of activity on resolving the proton radius puzzle.[7] In this context, several contributions to the Lamb shift in muonic hydrogen were reinvestigated in more detail [81–84]. However, up to now no explanation for the discrepancy could be found. This motivated a number of models which resolve the discrepancy by physics beyond the SM. In some of these models, similar to the hidden photon extension, an additional abelian force is assumed. It was shown in Ref. [85] that the ordinary hidden photon extension cannot explain the discrepancy. Motivated by the fact that the electron experiments are in good agreement

[7] See Ref. [75] for a review.

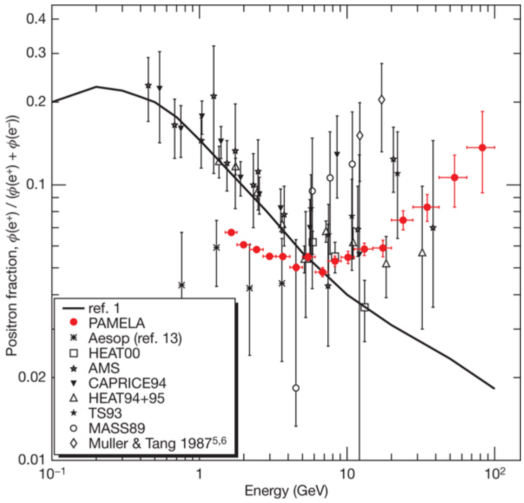

Figure 1.10: Fraction of positrons in the cosmic ray flux observed by the PAMELA experiment. The expected background is indicated by the black solid curve, the red filled circles are the PAMELA data. The figure is adapted from Ref. [92]. Note, that the data taken by ATIC are not shown in this figure.

while they deviate from the muonic determination, some recent works have conjectured a violation of the lepton universality. Using this assumption, the proton radius puzzle can be resolved by an additional light, abelian force carrier [86–90].

1.2.5 The positron excess in cosmic rays

Recent observations from cosmic ray data raised attention to consider models of dark matter which differ from the classical WIMP model mentioned in Secs. 1.1.1 and 1.2.1. In the balloon-borne ATIC experiment [91] an excess of positrons and electrons in the cosmic ray flux above the background was detected at 300–800 GeV with a sharp cut-off in the range 600–800 GeV. It could not be explained by ordinary astrophysical sources. This excess was confirmed by the PAMELA satellite experiment, in which the positron fraction in the cosmic ray flux was measured with a very high accuracy [92]. This was endorsed later by the FERMI satellite [93]. The main result is presented in Fig. 1.10, where the expectation and results for the positron fraction in the flux from cosmic rays are shown. The background expectation illustrated by the black solid curve decreases with growing energy. PAMELA observed a sharp upturn of the positron fraction for energies larger than 10 GeV as indicated by the red data points. A possible explanation of this excess is the annihilation of dark matter into electrons and positrons [94–99]. The dark-matter approach could naturally explain the cut-off seen by ATIC due to its mass scale expected to be at the weak scale [99]. However, the rates from the annihilation of classical WIMPs are predicted to be much below the annihilation cross sections needed to reconcile the large excess seen by PAMELA [100].

A further anomalous production is observed by the INTEGRAL satellite [101–103]. The data of INTEGRAL indicate that $\sim 3 \times 10^{42}$ positrons per second annihilate in the inner 5° of the galactic center, resulting in a very bright 511 keV line. This corresponds to an excess which is far more than expected from sources as supernovae. Furthermore, the data show

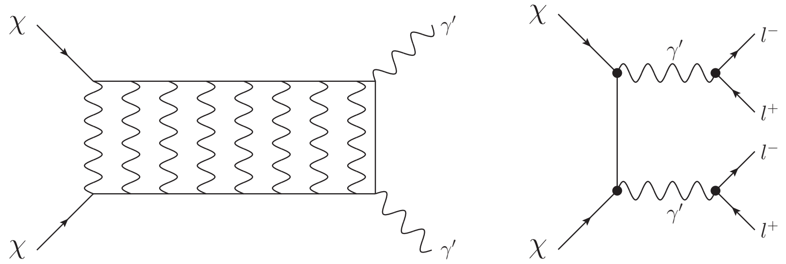

Figure 1.11: Left panel: Ladder diagram with multiple exchange of the new, light gauge boson γ' leading to a strong enhancement of the cross section. Right panel: Feynman diagram describing the annihilation of dark-matter particles into SM leptons by the new, light force carrier γ' in the intermediate state.

that the positrons must be very low-energetic with an energy is near their rest mass. There are several models of dark-matter annihilation existing to explain the INTEGRAL anomaly. Two of them, the Light Dark Matter (LDM) [104, 105] model and the exciting dark matter model (XDM) [106], shall be mentioned here.

Further anomalies in data of WMAP and EGRET [107] as well as the annual modulation of the signal seen in the dark-matter search experiment DAMA/LIBRA [108] motivated numerous attempts to resolve these puzzles. A new "theory of dark matter" was proposed in Ref. [99]. A messenger particle between the dark sector and the visible sector was introduced within this theory. While ordinary astrophysical sources were able to explain a single anomaly, no source allowing one to reconcile all of the mentioned anomalies was known. A prerequisite of such a theory of dark matter is that a large annihilation cross section are obtained without violating further constraint from Big Bang nucleosynthesis. Moreover, the weak-scale annihilation cross section must remain unchanged in agreement with the dark-matter relic abundance. As a consequence, boost factors of more than $\mathcal{O}(100)$ are needed compared to the required WIMP cross section. Furthermore, the data imply an enhancement only for the cross section to leptons, but no excess is seen in the antiproton abundance. It is argued that neither the high lepton rates can be reached nor the shape of the observed spectra can be reconciled by DM annihilation via SM gauge boson exchange. The observations of PAMELA further constrain the cross section to hadrons, which may not be enhanced.

The authors of Ref. [99] have proposed a theory, in which the dark sector is charged under a new $(U(1)_D)$ gauge symmetry. If the new $(U(1)_D)$ gauge boson, denoted here by γ',[8] has a mass at the $\mathcal{O}(1\,GeV)$ scale, the annihilation cross section can be significantly increased by the so-called Sommerfeld enhancement [99, 109]. As described in Ref. [99], the presence of a light mediator can lead to a distortion of the wave function in the initial state. The plane-wave approximation is not accurate for this process anymore. This is accounted for by boost factors to the cross section, which in this case lead to an enhancement. An equivalent picture for this mechanism is the resummation of ladder diagrams as presented in the left panel of Fig. 1.11 leading to the distortion. Furthermore, as long as the associated gauge boson has a mass below the proton production threshold $\lesssim 2\,\mathrm{GeV}$, the annihilation to proton-antiproton pairs is kinematically suppressed. This accounts for the leptophilic character of the new

[8] The reason for the chosen name will become clear in Sec. 1.3.2

gauge boson.

It was shown in Ref. [99] that by the exchange of the additional, light gauge boson DM annihilation as described by the Feynman diagram in the right panel of Fig. 1.11 together with Sommerfeld enhancement can be responsible for the observed anomalies. This model was used with great success to reconcile the theoretical calculation with the data in several subsequent works, e.g., Refs. [110, 111, 114, 115]. Selected results of the mentioned works are illustrated in Fig. 1.12. By a particular choice of the structure in the dark sector in Ref. [99], which was not considered up to this point explicitly, other anomalies can be interpreted as effects resulting from interactions of dark matter. As an example, the 511 keV line can be explained within the XDM model.

Recently, the AMS-02 experiment at the International Space Station, announced first results, which confirm the observations of PAMELA [112]. These results are presented in Fig. 1.13. The data from AMS-02 depicted by the red circles agree with the results of PAMELA (blue squares) [92] and FERMI (green triangles) [93] with a much better accuracy compared to the previous experiments. The expectation for background positrons is indicated by the gray shaded band. In agreement with previous experiments, AMS-02 sees a strong rise of the positron fraction exceeding the background expectation up to an energy of 300 GeV. Currently the AMS-02 data slightly disfavor an explanation of the positron excess from DM annihilation compared to pulsars as sources [98, 116–118]. Unfortunately, the AMS-02 data do not allow for a identification of the source of the excess in this stage. For this determination, precise data at even larger energy are needed, which will be available in the near future.

1.3 U(1) SM extensions and properties of hidden photons

1.3.1 Motivation from dark matter

In this section the special case of $U(1)$ extensions of the SM is considered. This is closely related to the coupling of hidden-sector particles to SM particles, leading to an extension of the SM which incorporates a DM candidate. There are several approaches to motivate $U(1)$ extensions. However, the SM gauge group (before spontaneous symmetry breaking) is always extended to

$$\underbrace{SU(3)_c \times SU(2)_L \times U(1)_Y}_{\text{SM}} \times U'(1). \tag{1.20}$$

Besides the SM gauge symmetry this gauge group contains only one further $U'(1)$ hidden-sector gauge symmetry. Additional gauge groups in a hidden sector, which of course are possible, will not be treated here in detail.

One example of such an additional $U(1)$ gauge symmetry giving rise to a SM extension and leading to a DM candidate was already introduced in Sec. 1.2.3. Axions are a classical example of an additional $U(1)$ symmetry which is broken at a high energy scale giving rise to a light, weakly coupled particle, which is not contained in the SM particle content. As mentioned above, this concept can be generalized to axion-like particles by being less restrictive with respect to the relation between coupling and mass parameters.

A further possibility provoking new, light particles, which are weakly coupled to the SM, is the so-called “hidden photon” extension. Such an extension will be considered in this work.

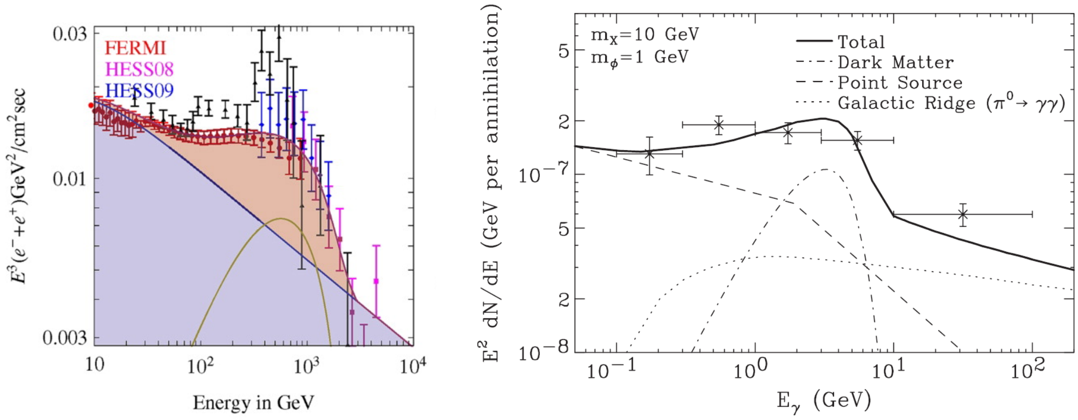

Figure 1.12: Comparison of data from PAMELA and FERMI with predictions from the annihilation of dark matter. Left panel: Gamma ray spectrum obtained from the annihilation of DM particles with $m = 3\,\text{TeV}$ into 4 muons and a mediator mass below 1 GeV, as published in Ref. [110] (red, solid curve). Right panel: Same as left, but DM particles with $m = 10\,\text{GeV}$ a mediator mass of 1 GeV (published in Ref. [111]).

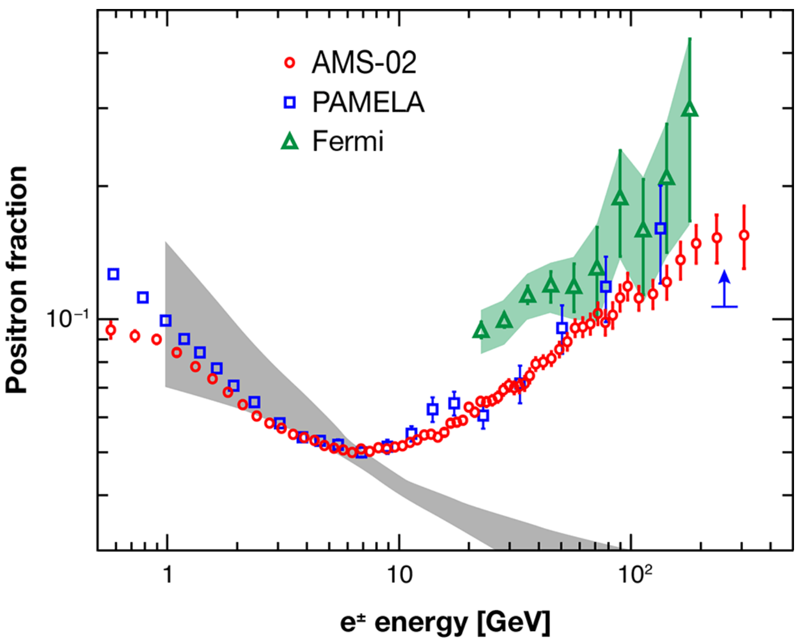

Figure 1.13: Positron fraction observed by the AMS-02 experiment [112] (red circles). The expected background is indicated by the gray band. The data of PAMELA [92] and FERMI [93] are indicated by the blue squares and green triangles, respectively. The figure is taken from Ref. [113].

Hidden photons are extra $U(1)$ gauge bosons, which mediate an interaction between the SM and a hidden sector. In the literature they are also referred to as "heavy," "dark," "para," or "secluded" photons, if they are coupled to the electromagnetic current of the SM. Allowing for further parity-violating interactions, one commonly denotes such particles as U or Z_d bosons.

In top-down extensions of the SM where the SM is embedded in a more fundamental theory appearing as an effective theory at low energies, $U(1)$ extensions are a generic feature. As an example, axions as well as axion-like particles are generic particles of SM extensions. The decay constant f_a can be generated at its natural scale [62]. In the same way as axions and axion-like particles, hidden photons can be motivated from top-down approaches. In Ref. [119] a summary of SM extensions, in which new $U(1)$ gauge groups appear generically, is given. It is argued that at high energy scales the interactions of the SM and of the physics beyond, unify in one gauge group (GUT). For lower energies, our observations of nature imply constraints, requiring that the unified gauge group needs to be broken. $U(1)$ extensions of the SM can be generated from the prediction of additional groups from GUTs [119, 120] as well as from SUSY [121–123]. As a further example, in supergravity string theory, $U(1)$'s appear besides further non-Abelian gauge symmetries of the hidden sector [62].

The opposite way to motivate SM extensions is the so-called bottom-up approach, in which the SM is extended manually to solve existing puzzles. One of the most popular motivations for extensions from bottom-up approaches is dark matter. Recently, hidden photon extensions became popular as a possible solution to the galactic positron excess discussed in Sec. 1.2.5. As an example, a model was proposed in Refs. [124–126], in which the dark matter does not interact directly with the SM particles. This is in contrast to supersymmetric SM extensions mentioned in Sec. 1.2.1. The interaction between SM and hidden-sector particles within this model is realized by a new $U'(1)$ gauge boson coupling through the mechanism of kinetic mixing [127, 128]. This is a special case of the proposed long-range interaction of Ref. [99] to enhance the DM annihilation cross section. In general, the Lagrangian can be written as

$$\mathcal{L} = \mathcal{L}_{\mathrm{SM}} + \mathcal{L}_{\mathrm{D}} + \mathcal{L}_{\mathrm{mediator}},$$

where $\mathcal{L}_{\mathrm{SM}}$ is the SM Lagrangian, $\mathcal{L}_{\mathrm{D}}$ is the Lagrangian describing the dynamics in the hidden sector. Moreover, $\mathcal{L}_{\mathrm{mediator}}$ contains the interaction between the SM sector and the hidden sector, corresponding to the dark-matter sector here. Within this model the dark matter is secluded from the SM particles. It was shown in Ref. [124] that the correct DM relic abundance can be obtained automatically. In addition, neither astrophysical nor laboratory constraints are violated. Numerous more models exist, which incorporate $U(1)$ extensions. They manifest themselves by a new, light gauge boson, coupling weakly to the SM; see for example Refs. [74, 104, 129–132].

However, the interaction between the SM and the hidden sector is strongly constrained. Besides the fact that gauge symmetries and Lorentz invariance may not be violated, a variety of theoretical and experimental constraints needs to be fulfilled [119]. Examples are anomaly cancelation and constraints from searches for physics beyond the SM. One possibility to avoid these strong restrictions, is the mechanism of kinetic mixing [127,128]. This will be discussed in detail in the next section.

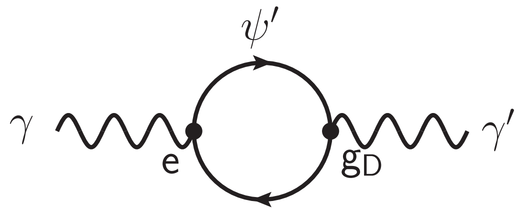

Figure 1.14: Feynman diagram of kinetic mixing. The SM photon γ does not interact directly with the hidden photon γ'. Hidden photon and SM photon are linked by a loop of heavy particles ψ', to which γ and γ' couple with strengths e and g_D, respectively.

1.3.2 The hidden photon model and kinetic mixing

In the previous section hidden photon extensions were motivated from dark-matter models. However, the study of $U(1)$ SM extensions was started independently from the idea of dark matter. It was discussed already 30 years ago [127, 128] that a second $U'(1)$ gauge boson with similar properties as those of the photon could interact with the SM photon.[9] Such an interaction is forbidden at tree-level. An allowed interaction is given within the framework of kinetic mixing.[10] The simplest case is illustrated in Fig. 1.14, where the photon γ does not couple directly to the hidden photon. The two bosons are linked by a loop of heavy particles ψ', which are not contained in the SM. The ψ' particles need to be charged under both the SM $U(1)$ gauge group and the additional $U'(1)$. The photon and the hidden photon couple to them with strengths e and g_D, respectively. Note that these particles, although contained in the hidden sector, cannot be the dark-matter candidate, since they carry electric charge. Therefore, they are sensitive to the electromagnetic interaction. The mass scale of the ψ' particles needs to be above the weak scale. Otherwise they would have been detected in experiments as at the LHC. The mass scale of the ψ' constrains the coupling strength of the hidden photon to the SM photon. For later use, analogously to the electromagnetic fine-structure constant $\alpha_{\text{em}} = e^2/(4\pi)$, it is helpful to define

$$\alpha' = \frac{g_D^2}{4\pi}. \tag{1.21}$$

At lower energies well below the weak scale, the heavy particle ψ' can be integrated out. For two fermions ψ'_1 and ψ'_2 with masses m_1 and m_2, respectively, and $m_1 > m_2$, the strength of the kinetic mixing relative to the electric charge $\varepsilon = g_D/e$ can be obtained as [128]

$$\varepsilon = -\frac{e\, g_D}{12\,\pi^2}\, q_e\, q_D \ln\left(\frac{m_1^2}{m_2^2}\right). \tag{1.22}$$

ψ'_1 and ψ'_2 carry the charges $(q_e,\, q_D)$ and $(q_e,\, -q_D)$ under the gauge groups $U(1)_{\text{em}}$ and $U'(1)$, respectively. Assuming that the charges are 1 and varying the ratio m_1/m_2 from 1.1 to 5, one finds

$$\varepsilon \sim 10^{-4} - 2.5 \times 10^{-3},$$

[9] Note that the SM photon is simply referred to as "photon."

[10] The name kinetic mixing originates from the fact that a mixing between the kinetic terms of the photon and hidden photon occurs in the effective Lagrangian.

where $g_D = e$ was assumed. Smaller values of ε can be reached, when g_D is lowered. It is discussed in Refs. [133, 134] that kinetic mixing is also forbidden at the one-loop level if the SM and hidden photon extension are embedded in a GUT. Due to GUT breaking at the two-loop level one obtains $\varepsilon \simeq 10^{-7} - 10^{-3}$. Although no clear minimal ε can be stated, in Refs. [135–137] values in the range from 10^{-12} to 10^{-3} were predicted.

It is possible to embed the kinetic mixing into the Lagrangian by only mixing with the photon field. However, the more general mixing with the hypercharge associated with the abelian $U(1)_Y$ gauge group of the SM Lagrangian will be demonstrated here, of which the first is only a special case. Let $\widetilde{B}^\mu$ denote the field charged under the $U(1)_Y$ gauge group and $\widetilde{B}^{\mu\nu} = \partial^\mu \widetilde{B}^\nu - \partial^\nu \widetilde{B}^\mu$. Accordingly, the field of the hidden photon γ' is denoted as $\widetilde{A}'^\mu$ and $\widetilde{F}'^{\mu\nu} = \partial^\mu \widetilde{A}'^\nu - \partial^\nu \widetilde{A}'^\mu$. For simplicity, only the relevant terms of the SM Lagrangian are considered:

$$\mathcal{L} \supset -\frac{1}{4}\widetilde{B}_{\mu\nu}\widetilde{B}^{\mu\nu} - \frac{1}{4}\widetilde{F}'_{\mu\nu}\widetilde{F}'^{\mu\nu} + \frac{\varepsilon_Y}{2}\widetilde{B}_{\mu\nu}\widetilde{F}'^{\mu\nu} + \frac{\widetilde{m}^2_{\gamma'}}{2}\widetilde{A}'_\mu\widetilde{A}'^\mu + g_Y j^\mu_B \widetilde{B}^\mu. \tag{1.23}$$

This Lagrangian contains a non-diagonal mixing term proportional to the kinetic mixing parameter $\varepsilon = \cos(\theta_W)\varepsilon_Y$ and the hypercharge gauge coupling g_Y. Thus, the tilde refers to quantities in this non-diagonal basis which have to be rotated in order to transform the fields into those written in the basis of eigenstates with physical masses, as in Eq. (1.7). Furthermore, j_B denotes the SM hypercharge current which is related to the electromagnetic current $j_{\text{em}} = j_A$ and neutral weak current j_Z by $g_Y j^\mu_B = e(\cos\theta_W j^\mu_A - \sin\theta_W j^\mu_Z)$.

In order to diagonalize the Lagrangian one rotates the $\widetilde{B}$ and $\widetilde{A}'$ fields as follows:

$$\widetilde{A}'^\mu = \frac{1}{\sqrt{1-\varepsilon_Y^2}}A'^\mu, \quad \widetilde{B}^\mu = B^\mu + \frac{\varepsilon_Y}{\sqrt{1-\varepsilon_Y^2}}A'^\mu. \tag{1.24}$$

The corresponding field tensors are

$$\widetilde{F}'^{\mu\nu} = \frac{1}{\sqrt{1-\varepsilon_Y^2}}F'^{\mu\nu}, \quad \widetilde{B}^{\mu\nu} = B^{\mu\nu} + \frac{\varepsilon_Y}{\sqrt{1-\varepsilon_Y^2}}F'^{\mu\nu}, \tag{1.25}$$

with $B^{\mu\nu} = \partial^\mu B^\nu - \partial^\nu B^\mu$ and $F'^{\mu\nu} = \partial^\mu A'^\nu - \partial^\nu A'^\mu$.
Inserting Eqs. (1.24) and (1.25) into Eq. (1.23) leads to

$$\begin{aligned}
\mathcal{L} \supset & -\frac{1}{4}B_{\mu\nu}B^{\mu\nu} - \frac{1}{2}\frac{\varepsilon_Y}{\sqrt{1-\varepsilon_Y^2}}B_{\mu\nu}F'^{\mu\nu} - \frac{1}{4}\frac{\varepsilon_Y^2}{1-\varepsilon_Y^2}F'_{\mu\nu}F'^{\mu\nu} - \frac{1}{4}\frac{1}{1-\varepsilon_Y^2}F'_{\mu\nu}F'^{\mu\nu} \\
& + \frac{1}{2}\frac{\varepsilon_Y}{\sqrt{1-\varepsilon_Y^2}}B_{\mu\nu}F'^{\mu\nu} + \frac{1}{2}\frac{\varepsilon_Y^2}{1-\varepsilon_Y^2}F'_{\mu\nu}F'^{\mu\nu} + \frac{\widetilde{m}^2_{\gamma'}}{2(1-\varepsilon_Y^2)}A'_\mu A'^\mu \\
& + g_Y j^\mu_B B_\mu + \frac{g_Y\varepsilon_Y}{\sqrt{1-\varepsilon_Y^2}} j^\mu_B A'_\mu \\
= & -\frac{1}{4}B_{\mu\nu}B^{\mu\nu} - \frac{1}{4}F'_{\mu\nu}F'^{\mu\nu} + \frac{\widetilde{m}^2_{\gamma'}}{2(1-\varepsilon_Y^2)}A'_\mu A'^\mu + g_Y j^\mu_B B_\mu + \frac{g_Y\varepsilon_Y}{\sqrt{1-\varepsilon_Y^2}} j^\mu_B A'_\mu,
\end{aligned} \tag{1.26}$$

where in the last step the non-diagonal terms have canceled and the kinetic terms of the hidden photon field were combined.

Decomposing the hypercharge current into the electromagnetic and weak neutral current yields

$$\begin{aligned}\mathcal{L} \supset &-\frac{1}{4}B_{\mu\nu}B^{\mu\nu} - \frac{1}{4}F'_{\mu\nu}F'^{\mu\nu} + \frac{\widetilde{m}^2_{\gamma'}}{2(1-\varepsilon_Y^2)}A'_\mu A'^\mu \\ &+ g_Y j^\mu_B B_\mu + \frac{e\cos(\theta_W)\varepsilon_Y}{\sqrt{1-\varepsilon_Y^2}} j^\mu_A A'_\mu - \frac{e\sin(\theta_W)\varepsilon_Y}{\sqrt{1-\varepsilon_Y^2}} j^\mu_Z A'_\mu .\end{aligned}$$

With the Taylor expansions around 0 of

$$\frac{\varepsilon_Y}{\sqrt{1-\varepsilon_Y^2}} \simeq \varepsilon_Y + \mathcal{O}(\varepsilon_Y^2), \quad \frac{1}{1-\varepsilon_Y^2} \simeq 1 + \mathcal{O}(\varepsilon_Y^2),$$

and by identifying $m_{\gamma'} = \widetilde{m}_{\gamma'}/\sqrt{1-\varepsilon_Y^2}$, $\varepsilon = \varepsilon_Y \cos(\theta_W)$, one finds

$$\mathcal{L} \supset -\frac{1}{4}B_{\mu\nu}B^{\mu\nu} - \frac{1}{4}F'_{\mu\nu}F'^{\mu\nu} + \frac{m^2_{\gamma'}}{2}A'_\mu A'^\mu + g_Y j^\mu_B B_\mu + \varepsilon e\, j^\mu_A A'_\mu - \varepsilon e\, \tan(\theta_W) j^\mu_Z A'_\mu . \quad (1.27)$$

The last term of Eq. (1.27) is canceled by an equal term entering from the diagonalization of the mass matrix, which is not demonstrated here.

The only parameters of this minimal model are the mass of the hidden photon $m_{\gamma'}$ and the coupling to SM particles parametrized by the kinetic mixing factor $\varepsilon^2 = \alpha'/\alpha$, as one can see from Eq. (1.27). The interaction of the γ' with the electromagnetic current is described by the term

$$\mathcal{L}_{\gamma' ff} = \varepsilon e\, j^\mu_A A'_\mu . \quad (1.28)$$

$\mathcal{L}_{\gamma' ff}$ and the QED interaction term are nearly equal, with the only differences that the hidden photon is massive and couples effectively with a strength reduced by the kinetic mixing factor ε. Furthermore, one can conclude from the γ' interaction Lagrangian (1.28) that the γ' interacts with any particle contained in the SM, which is sensitive to the electromagnetic interaction. This fact became apparent from Fig. 1.14, where the γ' is linked with the photon, which couples to the SM particles. Hence, Eqs. (1.27) and (1.28) are only the effective descriptions of this procedure at low energies. The Feynman rule derived from Eq. (1.27) simply reads

$$i\,\varepsilon e\,\gamma^\mu , \quad (1.29)$$

analogously to the QED interaction.

1.3.3 Decay width and decay length

Since the γ' is not a stable particle, it has a finite decay width $\Gamma_{\gamma'}$, which enters the invariant matrix element in the γ' propagator. For the decay of a γ' into a lepton pair of the species l, the invariant matrix element as read off from Fig. 1.15 is

$$\mathcal{M} = \overline{u}_l(k_1, s_1)\, \varepsilon e\, \not{\epsilon}(q', \lambda)\, v_l(k_2, s_2), \quad (1.30)$$

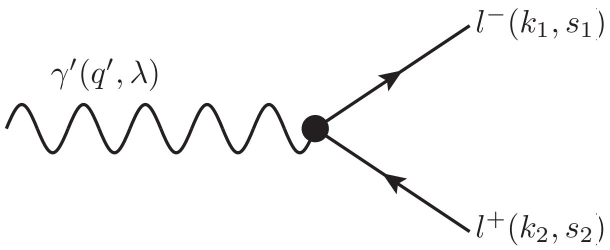

Figure 1.15: Feynman diagram of the γ' decay into a lepton pair.

with m_l denoting the lepton mass. Taking its complex conjugate, squaring and averaging over the γ' polarizations λ and summing over the lepton spins s_1 and s_2 leads to

$$\overline{|\mathcal{M}|^2} = \frac{(\varepsilon e)^2}{3} \left(-g^{\mu\nu} + \frac{q'^{\mu}\, q'^{\nu}}{m_{\gamma'}^2} \right) \mathrm{Tr} \left((\not{k}_1 + m_l)\, \gamma_\mu \, (\not{k}_2 - m_l)\, \gamma_\nu \right).$$

Exploiting four-momentum conservation, the kinematical relations

$$\begin{aligned} q'^2 &= m_{\gamma'}^2, \;\; k_1^2 = k_2^2 = m_l^2, \\ q' \cdot k_1 &= q' \cdot k_2 = \frac{m_{\gamma'}^2}{2}, \\ k_1 \cdot k_2 &= \frac{1}{2} \left(m_{\gamma'}^2 - 2m_l^2 \right), \end{aligned}$$

allow one to evaluate

$$\overline{|\mathcal{M}|^2} = \frac{16\, \pi\, \alpha\, \epsilon^2}{3} \, \left(m_{\gamma'}^2 + 2m_l^2 \right),$$

where in addition $\alpha = e^2/(4\pi)$ has been used. From Eq. (A.4), the general formula for $1 \to 2$ particle decays, the decay width is derived as

$$\Gamma_{\gamma' \to l^+ l^-} = \frac{\alpha \varepsilon^2}{3 m_{\gamma'}^2} \sqrt{m_{\gamma'}^2 - 4m_l^2}\, (m_{\gamma'}^2 + 2m_l^2). \tag{1.31}$$

For the case of a γ' decaying into electrons with $m_{\gamma'} \gg m_e = 0.511\mathrm{MeV}$, Eq. (1.31) simplifies to

$$\Gamma_{\gamma' \to e^+ e^-} = \frac{\alpha \varepsilon^2}{3} \sqrt{s} = \frac{\alpha \varepsilon^2}{3} m_{\gamma'}. \tag{1.32}$$

Above the threshold for pion production, $m_{\gamma'} \geq 2 \times m_{\pi^\pm}$, the hidden photon can also decay into a pair of charged pions. Within scalar QED this decay width can be calculated analogously to the decay into a lepton pair. The Feynman amplitude of the decay reads

$$\mathcal{M} = \varepsilon e \, F_\pi(q'^2) \, (k_1 - k_2)^\mu \varepsilon_\mu(q'),$$

where $F_\pi(q'^2) = F_{\gamma^* \to \pi^+\pi^-}(q'^2)$ is the timelike electromagnetic charged pion form factor, which accounts for the electromagnetic structure of the pion. A parametrization can be

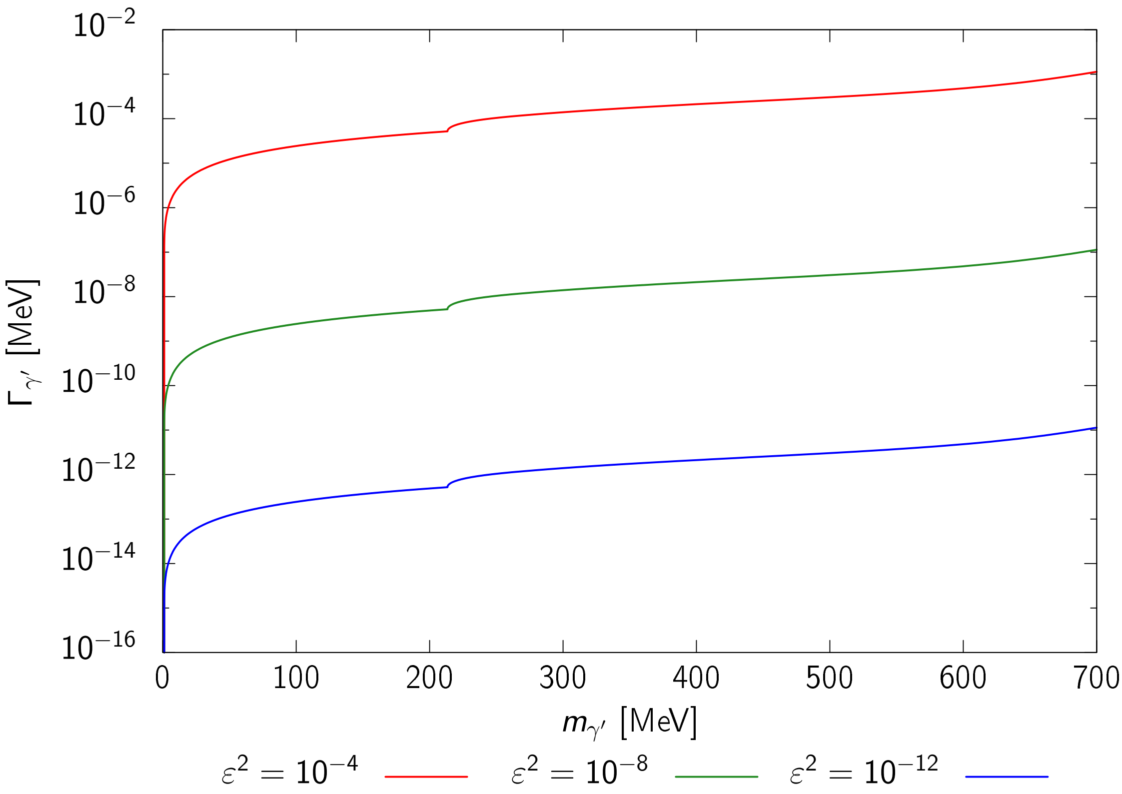

Figure 1.16: Total γ' decay width for $\varepsilon^2 = 10^{-4}, 10^{-8}, 10^{-12}$ with decay channels into electrons, muons and pions. The sharp kink at 212 MeV is due to crossing the threshold for muon production.

found in Appendix A.2, which is valid in the mass range up to 1 GeV. One finds for the partial decay width into a pair of charged pions

$$\Gamma_{\gamma' \to \pi^+\pi^-} = \frac{\alpha\varepsilon^2 \left|F_\pi(q'^2)\right|^2}{12} \frac{\left(m_{\gamma'}^2 - 4m_{\pi^\pm}^2\right)^{3/2}}{m_{\gamma'}^2}. \tag{1.33}$$

Assuming that in a certain mass range, which in the presented work is around $\mathcal{O}$(few GeV), no hidden-sector particles with $m < m_{\gamma'}/2$ exist, γ' decays into other hidden-sector particles are kinematically forbidden. Instead, the γ' has to decay into a visible state. The total width can be expressed as a sum of partial decay rates into SM particles, giving rise to

$$\Gamma_{\gamma'} = \begin{cases} \Gamma_{\gamma' \to e^+e^-} + \Gamma_{\gamma' \to \mu^+\mu^-} + \Gamma_{\gamma' \to \pi^+\pi^-}, & m_{\gamma'} \leq 700\,\text{MeV} \\ \\ \Gamma_{\gamma' \to e^+e^-} + \Gamma_{\gamma' \to \mu^+\mu^-}(1 + R(m_{\gamma'})), & m_{\gamma'} > 700\,\text{MeV} \end{cases} \tag{1.34}$$

where $\Gamma_{\gamma' \to e^+e^-}$, $\Gamma_{\gamma' \to \mu^+\mu^-}$ and $\Gamma_{\gamma' \to \pi^+\pi^-}$ are the partial γ' decay rates into electron-positron, muon and charged pion pairs, respectively. Furthermore, R is the SM ratio $\sigma(e^+e^- \to \text{hadrons})/\sigma(e^+e^- \to \mu^+\mu^-)$ of hadron to muon production cross sections as given in the lower panel of Fig. 46.6 of Ref. [4]. Figure 1.17 shows $\Gamma_{\gamma'}$ as a function of $m_{\gamma'}$ for ε^2.

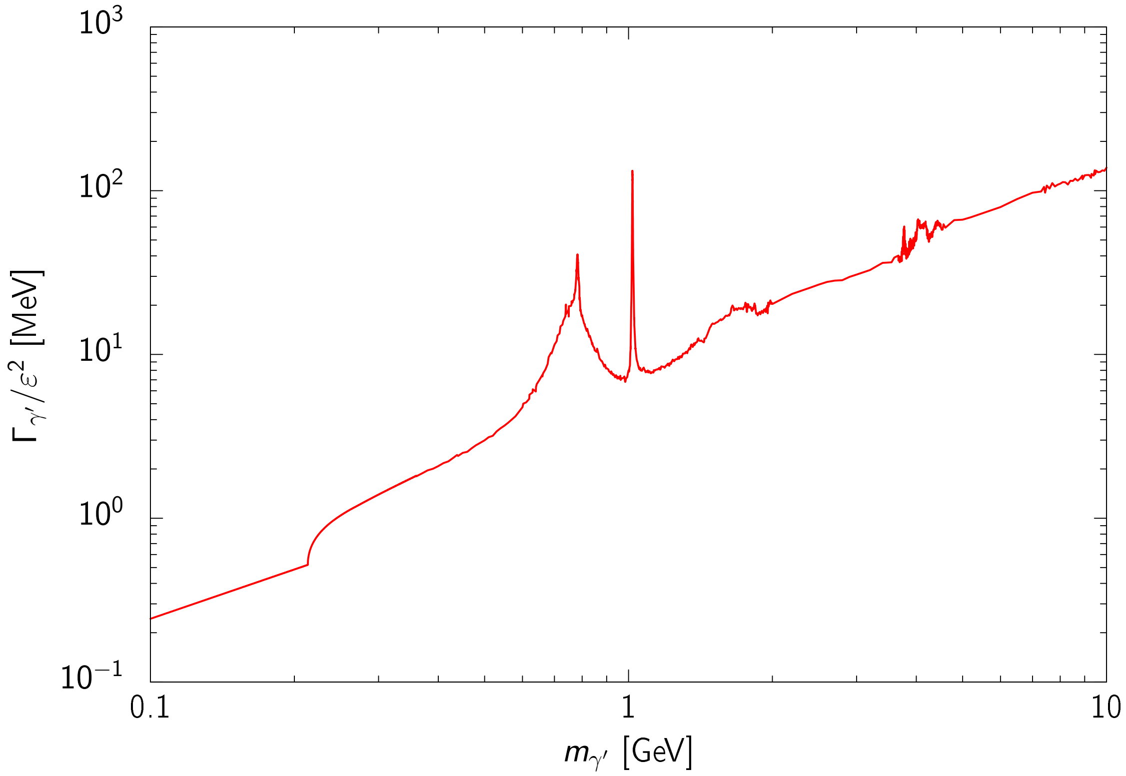

Figure 1.17: Total γ' decay width into the SM particles normalized to $\varepsilon^2 = 1$. $\Gamma_{\gamma'}$ is parametrized by the ratio of the cross sections for electron-positron annihilation to hadrons and muons $\sigma(e^+e^- \to \text{hadrons}, \sqrt{s})/\sigma(e^+e^- \to \mu^+\mu^-, \sqrt{s})$, depending on the energy $\sqrt{s} = m_{\gamma'}$ as published in Ref. [4], in the region $m_{\gamma'} > 700\,\text{MeV}$. Fluctuations are due to the uncertainty in the data for R.

Due to the small coupling strength, one expects only a signal when the γ' is produced on the mass shell. From Eq. (1.34) and Fig. 1.16 one directly recognizes that a hidden photon in an intermediate state will manifest itself by are very narrow peak.

The decay length of the γ' is obtained from

$$l_{\gamma'} = \gamma \frac{1}{\Gamma_{\gamma'}},$$

where $\gamma = {}^{E_{\gamma'}}/_{m_{\gamma'}}$ denotes the Lorentz factor. A calculation of the γ' decay length as a function of $m_{\gamma'}$ and ε^2 can be seen from Fig. 1.18 for energies $E_{\gamma'} = 100\,\text{MeV}$ (upper panel) and $E_{\gamma'} = 1\,\text{GeV}$ (lower panel). The decay length varies in the parameter region of interest from very short distances of around $10^{-6}\,\mu m$ for large masses and couplings to several meters in the case of small $m_{\gamma'}$ and ε^2. This behavior gives rise to several possibilities to search for γ' bosons in the particular regions of the parameter space. In the regions where the decay length is macroscopic, corresponding to the decay vertex shifted by several mm, a search for a displaced vertex can be performed. Such experiments are planned with the HPS experiment and at MAMI. Furthermore, the flight length sets constraints on possible limits from experiments, e.g., beam-dump searches, since the γ' must not evade the detector in

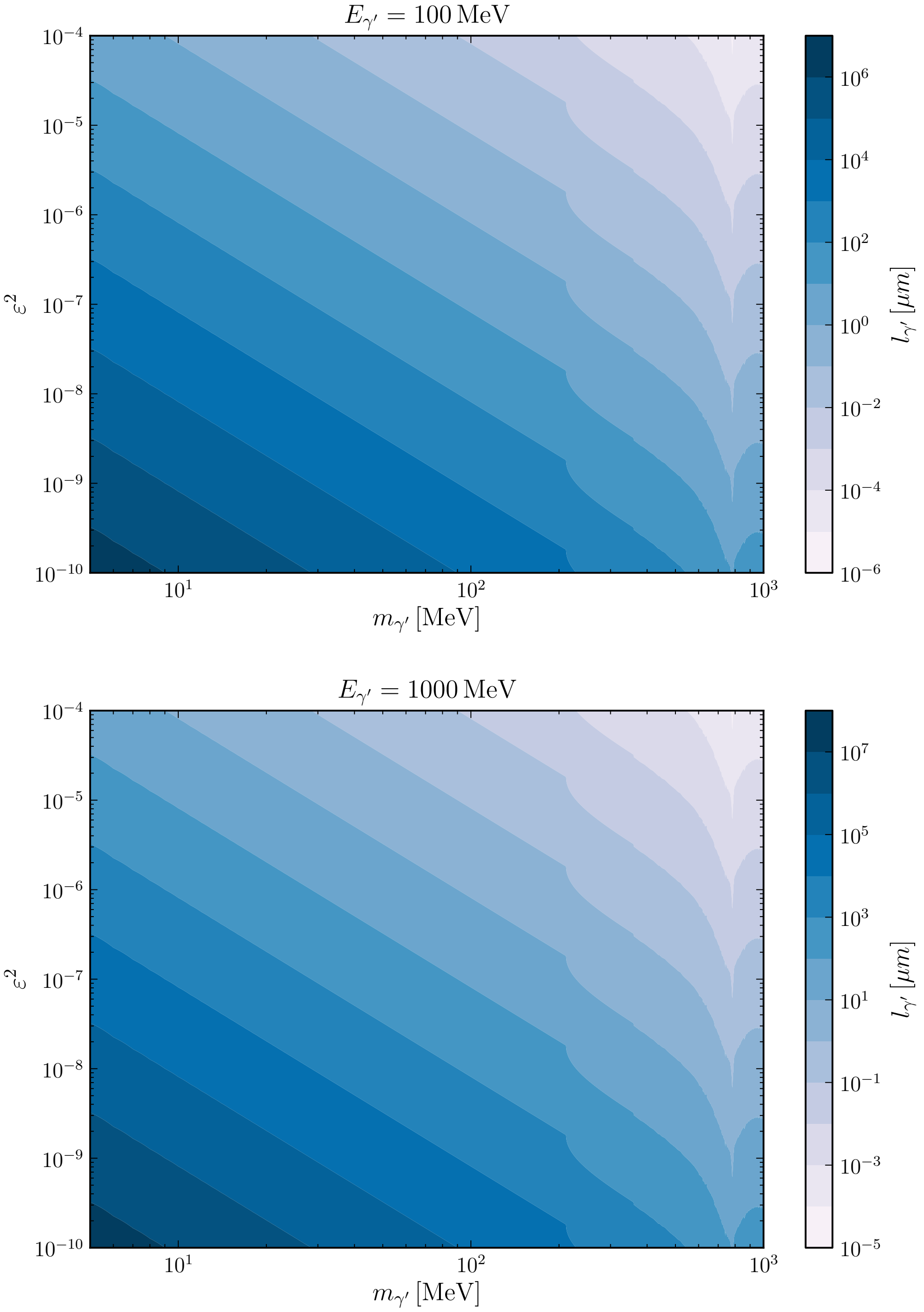

Figure 1.18: Decay length of the γ' for $E_{\gamma'} = 100\,\mathrm{MeV}$ and $E_{\gamma'} = 1\,\mathrm{GeV}$.

order to be able to detect its decay products.

1.3.4 Existing constraints on the hidden photon parameter space

A collection of all currently published limits for the hidden photon parameter space can be found in Fig. 1.19 indicated by the shaded regions. Furthermore, in Table 1.2 the labels of Fig. 1.19 are explained and, in addition, a short description of each bound is given. Note that the limits of Table 1.2 and Fig. 1.19 are only valid for purely visible decays, i.e., the branching ratio to visible SM particles is 1. If a decay into an invisible state is allowed, the bounds requiring the detection of SM particles are significantly worse. Such a decay is possible, if a Light Dark Matter particle χ with $m_{\gamma'} > 2m_\chi$ exists, which couples to the hidden photon. As an example, for a branching ratio to visible SM states of only 0.1, all constraints in Table 1.2 and Fig. 1.19 except the ones from $(g-2)$ would be weakened by this factor.

The light-red shaded band corresponds to the region, where the existing discrepancy in the experimental and theoretical determination of the anomalous magnetic moment of the muon can be explained by the γ' contribution to $(g-2)_\mu$. The limits represented by the colored regions in Fig. 1.19 arise from various experimental and theoretical arguments:

gray: calculation of the anomalous magnetic moment of the electron and muon [126,138,139]

blue: electron beam-dump experiments [140–145]

violet: (e^+e^-) collider experiments [140, 146]

red: meson decays [147–151]

green: fixed-target experiments [152, 153]

Each of these approaches is more appropriate than the others in particular regions of the phase space. In the following the different approaches are explained in more detail.

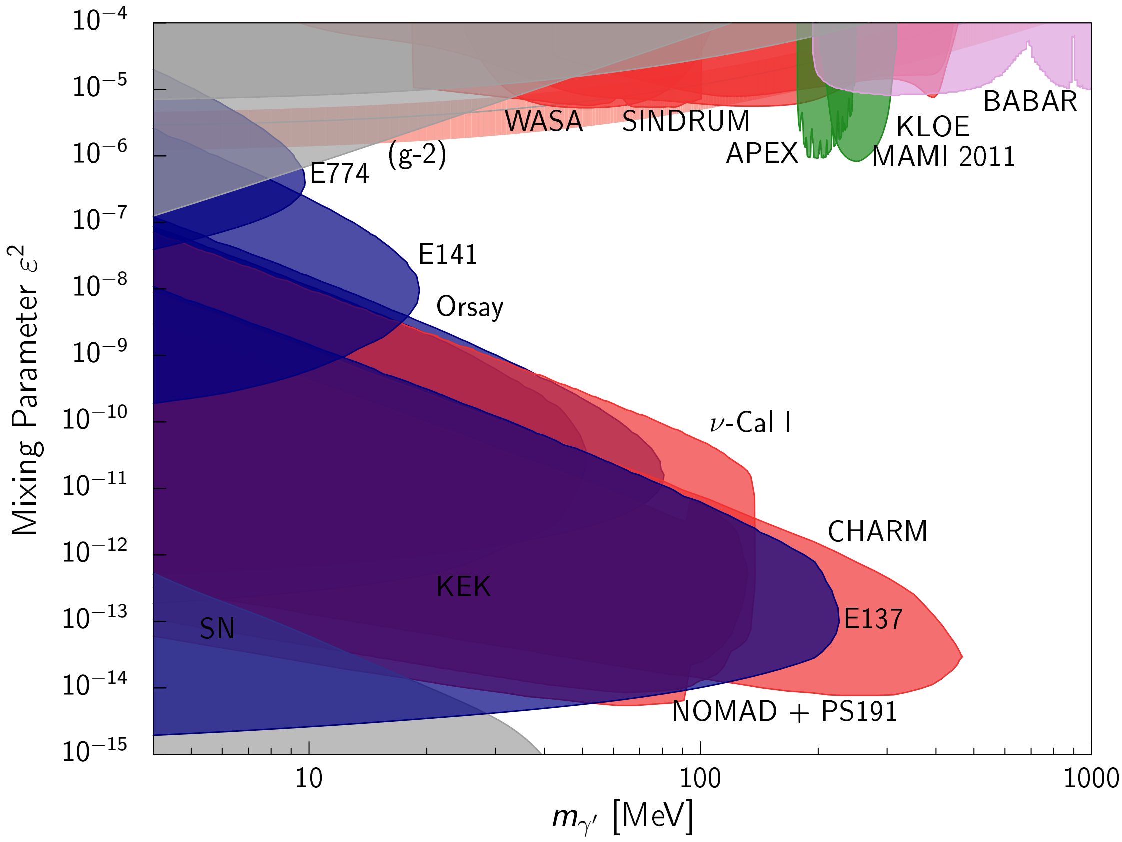

Figure 1.19: Compilation of published exclusion limits for the γ' parameter space. The light-red shaded region represents the $(g-2)_\mu$ welcome band, where the $(g-2)_\mu$ discrepancy can be explained by the γ' contribution to the anomalous magnetic moment of the muon. The other colored regions correspond to existing limits from the calculation of the anomalous magnetic moment of the electron and muon (gray) [126, 138, 139], electron beam-dump experiments (blue) [140–145], e^+e^- collider experiments (violet) [140, 146], meson decays (red) [147–151], and fixed-target experiments (green) [152, 153]. See the text for further details.

Limit name	Type	Reaction	Origin of data	Publication of Limit
$(g-2)_\mu$	(g-2)		[54,61,154]	[126,138,139]
$(g-2)_e$ vs α	(g-2)		[53,55,56,155]	[126,138,139]
E141	e^- beam dump	$e(A,Z) \to e(A,Z)l^+l^-$	E141 [71] (SLAC)	[140,144]
E137	e^- beam dump	$e(A,Z) \to e(A,Z)l^+l^-$	E137 [72] (SLAC)	[140,144]
E774	e^- beam dump	$e(A,Z) \to e(A,Z)l^+l^-$	E774 [73] (Fermilab)	[140,144]
KEK	e^- beam dump	$e(A,Z) \to e(A,Z)l^+l^-$	[156] (KEK)	[144]
SN	Supernova reminiscents		[157]	[140]
BABAR	Collider	$e^+e^- \to \gamma l^+l^-$	[140]	[140]
ν-Cal I	p beam dump	$pp \to \gamma' X$	ν-Cal I [158,159] (IHEP)	[141]
MAMI 2011	e^- fixed-target	$e(A,Z) \to e(A,Z)l^+l^-$	A1 [152] (MAMI)	[152]
APEX Test	e^- fixed-target	$e(A,Z) \to e(A,Z)l^+l^-$	APEX [153] (JLab)	[153]
KLOE 2011	Meson decay	$\phi \to \eta e^+e^-$	KLOE [147] (LNF)	[147]
Orsay	e^- beam dump	$e(A,Z) \to e(A,Z)l^+l^-$	[160] (Orsay)	[144]
BABAR	Meson decay	$e^+e^- \to \gamma l^+l^-$	BABAR [146] (SLAC)	[146]
NOMAD	Meson decay	$\pi^0 \to \gamma l^+l^-$	NOMAD [161–163] (CERN)	[142]
PS191	Meson decay	$\pi^0 \to \gamma l^+l^-$	PS191 [164,165] (CERN)	[142]
CHARM	Meson decay	$\eta/\eta' \to \gamma l^+l^-$	CHARM [166,167] (CERN)	[143]
KLOE 2012	Meson decay	$\phi \to \eta e^+e^-$	KLOE [148] (LNF)	[148]
SINDRUM	Meson decay	$\pi^0 \to e^+e^-$	SINDRUM [168] (PSI)	[149]
WASA	Meson decay	$\pi^0 \to \gamma e^+e^-$	WASA [150] (COSY)	[150]
HADES	Meson decay	$\pi^0/\eta \to \gamma e^+e^-$	HADES [169,169,170] (HADES)	[151]
HADES	Resonance decay	$\Delta \to N e^+e^-$	HADES [171] (HADES)	[151]
ν-Cal I	p beam dump	$pp \to \gamma' X$	ν-Cal I [158,159] (IHEP)	[145]

Table 1.2: Overview of existing limits for the γ' parameter space, sorted after the date of publication.

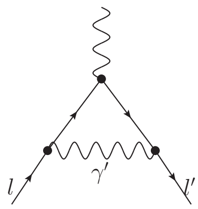

Figure 1.20: Feynman diagram of the one-loop γ' contribution to the anomalous magnetic moment of a lepton l.

1.3.4.1 Anomalous moment of the electron and muon

The anomalous magnetic moment of the electron and muon, $a_l = {}^{(g-2)_l}/_2$, which belong to the quantities known to highest accuracy, can be employed to find limits for the γ' parameter space. The anomalous moment of the electron a_e has been measured [154] as

$$a_e = 1.1596521883(28) \times 10^{-3},$$

and that of the muon [53] as

$$a_\mu = 1.16592089(63) \times 10^{-3}.$$

Compared to the SM predictions of these quantities one finds a very small deviation in the case of a_e,

$$a_e(\mathrm{exp}) - a_e(\mathrm{th, SM}) = (-106 \pm 82) \times 10^{-13},$$

but a deviation of about 3.7σ for the muon as already mentioned in Sec. 1.2.2:

$$a_\mu(\mathrm{exp}) - a_\mu(\mathrm{th, SM}) = (312 \pm 85) \times 10^{-11}.$$

While the knowledge of the anomalous magnetic moment a_e of the electron is limited by the current precision of the experimental result and the uncertainty on the fine structure constant α, the uncertainty for a_μ mainly results from the unknown hadronic contribution. For the theoretical prediction of a_l, effects of physics beyond the Standard Model has not been included in the calculation. Therefore, a possible γ' contribution to a_l must be in agreement with these very accurate studies.

The high accuracy of a_e is due to several reasons. The theoretical prediction of a_e is dominated by the QED contribution, which recently has been evaluated to 5th order in α [55, 56]. In addition, the direct measurement [154] with an uncertainty of the order 10^{-9} and an improved determination of the fine structure constant α [155] from a measurement of the Rubidium mass, minimize its uncertainty. This sets a strong bound on the γ' parameter space for small masses. In the case of the muon the situation is different. The deviation of 3.4σ and the uncertainty are much larger which lowers a possible bound. Furthermore, the γ' can be invoked to explain this discrepancy. Therefore, in Fig. 1.19 besides the bound from a_μ, also the 2σ region is emphasized, where the $(g-2)_\mu$ discrepancy can be explained by the γ' contribution. This region is denoted as "$(g-2)_\mu$ welcome band" in the literature. Due to the accuracy of the determination of anomalous magnetic moments one can find a stringent bound for the coupling strength of a γ' contribution to a_l.

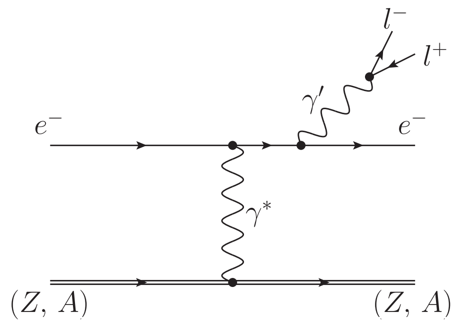

Figure 1.21: Typical Feynman diagram of an investigated process in fixed-target experiments. An electron beam is scattered off a target of atomic number Z and mass number A. A γ' is radiated off by Bremsstrahlung and decays into a lepton pair.

The one-loop γ' contribution $a_l^{\gamma'}$ to the anomalous magnetic moment a_l of the electron or the muon can be found as

$$a_l^{\gamma'} = \frac{(g-2)_l^{\gamma'}}{2} = \frac{\alpha'}{\pi}\int_0^1 dz \frac{z(1-z)^2 m_l^2}{(1-z)^2 m_l^2 + z m_{\gamma'}^2}, \tag{1.35}$$

where m_l denotes the corresponding lepton mass.

Solving the integral for a particular mass $m_{\gamma'}$ allows for finding a bound for the γ' parameter space. To state a conservative bound, where the γ' is ruled out very likely, the 3σ limit is chosen:

$$\begin{aligned} a_e^{\gamma'} &\leq (-106 + 3 \times 82) \times 10^{-13} = 140 \times 10^{-13}, \\ a_\mu^{\gamma'} &\leq (312 + 3 \times 85) \times 10^{-13} = 567 \times 10^{-11}. \end{aligned}$$

In addition, for the $(g-2)_\mu$ welcome band, Eq. (1.35) is solved for the 2σ region around the central value of the discrepancy:

$$142 \times 10^{-11} \leq a_\mu^{\gamma'} \leq 482 \times 10^{-11}.$$

The advantage of invoking the lepton $(g-2)$ as possible limit is the existence of accurate data as well as highly accurate calculations of the SM background, the $a_l(\mathrm{th}, \mathrm{SM})$. Therefore, this bound for the γ' parameter space is a side product from attempts to reconcile the measurements and prediction of $(g-2)_l$.

1.3.4.2 Fixed-target experiments

In Ref. [140, 172] it has been shown that fixed-target experiment can serve as an ideal tool to search for light, hidden particles. The method of such fixed-target experiments is the following: A beam, typically an electron-beam, is scattered off a target at a fixed location. For allowed (effective) interactions of the γ' with the electromagnetic current, the γ' is radiated off by Bremsstrahlung and decays into a lepton pair in the mass range of interest.

The search for a γ' signature is performed by an invariant-mass scan and a displaced-vertex search. For coupling strengths $\varepsilon^2 \lesssim 10^{-8}$ the γ' in the mass range below $m_{\gamma'} \sim 500\,\mathrm{MeV}$ will

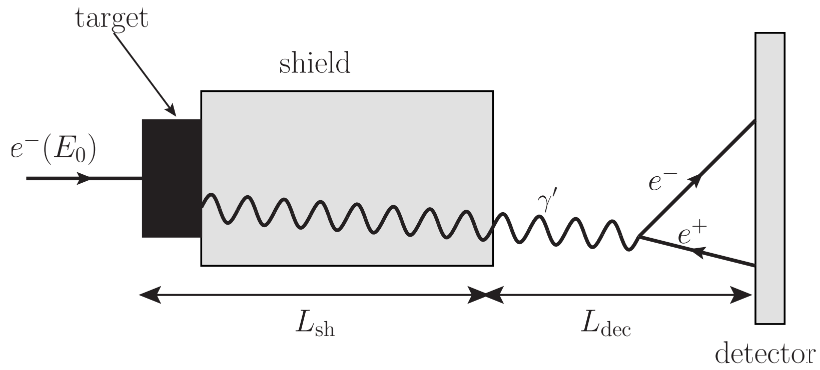

Figure 1.22: Sketch of a typical beam-dump experiment: The electron beam is dumped onto the target, from which as depicted here, a γ' is produced. The γ' passes through the shield and decays outside. The decay products are labeled as $e^{\pm}$. The length of the target plus shield and the length of the decay volume are denoted as L_{sh} and L_{dec}, respectively.

decay inside the detector or target. The invariant mass of the lepton pair can be reconstructed through detection of the corresponding lepton and antilepton. The very narrow decay width of the γ' (see Fig. 1.16) is far below the typical mass resolution of such an experiment. Hence, a γ' signal will appear as a sharp peak in one single mass bin over the smooth background from QED. This type of limits is treated extensively in chapters 2 and 3.

1.3.4.3 Beam-dump experiments

Beam-dump experiments are a special type of fixed-target experiments. Figure 1.22 shows a sketch of such experiments. A beam dump is a basic component of most accelerators. Commonly, a large block of a material with good shielding properties, like lead, is used to absorb the beam. This shielding can be used to search for particles which are not or only very weakly electromagnetically interacting and penetrating through the shield. The installation of a detector behind the shield allows one to search for SM particles which are not expected to appear in that region since they should have been absorbed by the shield. An excess of SM particles must result from particles beyond the SM, which are decaying after passing through the beam dump.

A γ' with appropriate mass and coupling strength (see Fig. 1.17) will not be absorbed by the shield. If furthermore, $m_{\gamma'}$ and ε^2 allow for a decay length larger than the length of the shield but smaller than the distance from the target to the detectors, a lepton pair must be detected as its decay products. An exclusion limit for the γ' parameter space can be derived if no excess is seen. Beam-dump limits for the γ' parameter space have first been found in Ref. [140] by analyzing the E141 [71] and E137 [72] experiments at SLAC and the E774 [73] experiment at the Fermilab, in which a search for axions was performed. In addition, in Ref. [144] these experiments have been re-analyzed and new limits from experiments at KEK [156] and at Orsay [160] have been found. Furthermore, the procedure to derive limits from beam-dump experiments is described in detail in Ref. [144]. For the analysis of these

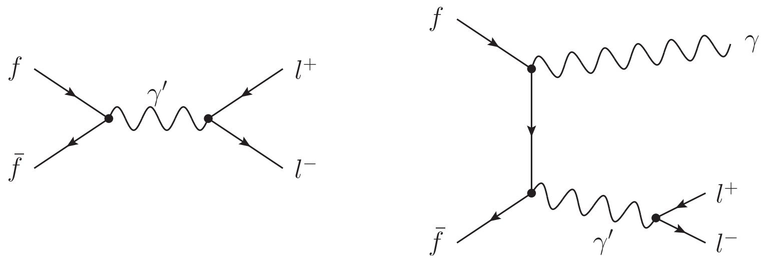

Figure 1.23: Typical Feynman diagrams of processes which can be investigated in collider experiments. Left panel: Direct γ' production at the center of mass energy of the collider decaying into a lepton pair. Right panel: Radiative return method. Besides the hidden photon production with the subsequent decay into a lepton pair, a photon is radiated in the initial state, which allows one to probe a wider $m_{\gamma'}$ range.

data the cross section for the process

$$e(A,Z) \to e(A,Z)\gamma', \quad \gamma' \to e^+e^-$$

has to be calculated to estimate the number of lepton-pair events seen by the detectors. The approximate total number of events from a γ' decay is given by Eq. (13) of Ref. [144]. The cross section of the process $e(A,Z) \to e(A,Z)\gamma'$ is commonly calculated within the Weizsäcker–Williams approximation. The applicability of this approximation is investigated in Sec. 2.3.

The shape of the exclusion limits has an upper bound due to the condition that the γ' must not decay inside the shield. Thus, ε must be small enough that the decay length $l_{\gamma'}$ is larger than the length of target plus shield L_{sh}. The lower limit results from the fact that the γ' decay must happen before the detector is reached and that enough decays take place within this volume.

1.3.4.4 Collider searches

Current limits for the γ' parameter space from collider searches were obtained mostly at e^+e^- machines.

Only e^+e^- machines and low-energy hadron colliders are considered as colliders to search for hidden photons in the mass region of several MeV to GeV. These colliders work at a fixed center of mass energy, which is commonly equal to the mass of a meson resonance in the lower GeV range as in the case of so-called flavor factories like DAϕNE at Frascati or at the Stanford Linear Accelerator Center (SLAC). The LEP collider at CERN was working on the Z boson mass $m_Z \simeq 91\,\text{GeV}$, which is far away from the considered scale of γ' masses.

High energy hadron colliders like the LHC can reach much higher energies. Therefore, they are ideally suited for the search for particles with masses more than $10-100\,\text{GeV}$, but are strongly limited in their precision. Experiments as KLOE at DAϕNE and BABAR at SLAC have already acquired huge datasets, which can be re-analyzed with respect to the search for a small resonance caused by a hidden photon. The feasibility studies for hidden photon searches in low-energy collider experiments were done in Refs. [134, 173]. Typical processes,

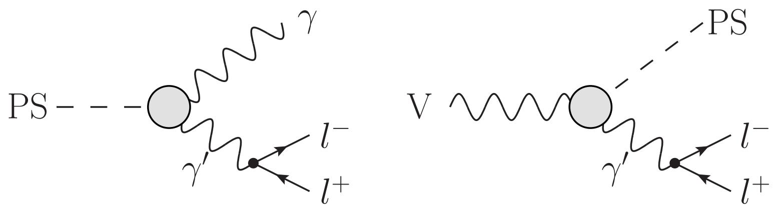

Figure 1.24: Feynman diagrams of typical meson decays which are used to search for hidden photon signatures. Right panel: Radiative pion decay into a photon and a hidden photon subsequently decaying into a lepton pair. Right panel: Decay of a vector meson V into a pseudo scalar meson PS and a hidden photon which decays into a lepton pair.

which can be investigated to search for hidden photon signals are shown in Fig. 1.23. The Feynman diagram in the left panel indicates the direct s-channel exchange of a hidden photon splitting to a lepton pair. Although one receives the highest rates for this process, the use of the s-channel process to search for signals is not feasible. The lepton pair will have an invariant mass equal to the center of mass energy of the collider—usually the mass of a SM resonance. Thus, only one value of $m_{\gamma'}$ can be probed, where a possible hidden photon signal will be covered by the SM resonance.

Therefore, the radiative return method, depicted in the right panel of Fig. 1.23, is used in collider experiments. In addition to the hidden photon, an ordinary photon is radiated from the initial state. On account of this, the invariant mass of the lepton pair and correspondingly the probed hidden photon mass is reduced, which allows one to study a wide range of $m_{\gamma'}$. A background contribution enters from the final-state radiation of the photon, where the hidden photon carries the invariant mass of all three final state particles comparable to the process in the right panel of Fig. 1.23. This background can be strongly reduced by detecting muon-antimuon pairs in the final state, from which the final state radiation due to the larger mass is suppressed.

This method is ideally suited to cover a wide $m_{\gamma'}$ range at kinetic mixing factors down to $\varepsilon^2 \sim 10^{-7}$. Currently, the existing data from BABAR, KLOE and BES-III are under investigation.

1.3.4.5 Meson decays

Meson decays have already been studied for a long time to understand the (electromagnetic) structure of mesons. As a consequence, large data sets of meson decays are existing from various experiments. These experiments were performed at colliders like the mentioned KLOE experiment at DAϕNE or the BABAR experiment at SLAC or at fixed-target facilities like the WASA experiment. For the analysis with respect to hidden photon signals one does not have to take care of the production mechanism of the meson. The achievable statistics of course strongly depends on the meson production mechanism. Nevertheless, the investigated processes are always very similar, independently of the meson production. Feynman diagrams of typical processes are shown in Fig. 1.24. The largest rates are expected from pion-decay experiments. One possibility is to search for a deviation from the SM pion decay. In the SM, the neutral pion π^0 decays dominantly into two photons. The decay into one real and a virtual photon from which an electron-positron pair is produced still gives a large signal. This SM decay will lead to a smooth e^+e^- invariant-mass spectrum on which one can search for a peak by hidden photon production. This process is presented in the left panel of Fig. 1.24. It was used in the SINDRUM and WASA experiments. Another process, which was investigated for instance at KLOE, is the decay of a vector meson into a pseudo-scalar meson and a lepton pair as shown in the right panel of Fig. 1.24. In this case one also searches for a deviation from the SM process due to the hidden photon.

Chapter 2

Production of Hidden Photons from Fixed Target Experiments

The production of a hidden photon γ' may arise as a background process to the elastic electron-hadron scattering $e(Z,A) \to e(Z,A)$. The hadronic state (Z,A) is characterized by the atomic number Z corresponding to the number of protons bound in the nucleus and the mass number A denoting the total number of constituents. In elastic scattering processes with two particles in the final state only one kinematical variable is not fixed. Therefore, it is sufficient to detect only one of the two final state particles to measure the elastic cross section . By detecting both of them, it can be discriminated if an additional particle such as a γ or γ' was produced. The kinematics is not fixed by one variable anymore for a final state involving three or more particles . Hence, the elastic scattering process can be kinematically separated from the γ' production process.

In this chapter the process of hidden photon bremsstrahlung will be studied under two aspects. First of all, the cross section for the production of a hidden photon γ' induced by lepton-hadron scattering is analyzed in general. For this purpose, it is studied for which particular type of kinematical conditions the cross section is largest. Furthermore, scenarios in which the decay products of the hidden photon are not detected or the decay of the hidden photon occurs invisibly are discussed. As a consequence, experiments have to be designed in a way that the peak resulting from the elastic scattering is circumvented in the chosen kinematics. The most important irreducible background arising in the SM results from the production of a real photon: $e(Z,A) \to e(Z,A)\gamma$. In the literature this is often referred to as Bethe–Heitler process.

Therefore, in this section the cross sections of both, the γ' production $e(Z,A) \to e(Z,A)\gamma'$ as well as the Bethe–Heitler process as SM background, will be analyzed. In the following the hadronic state (Z,A) is for simplicity referred to as p, although the analysis is valid for a proton as well as a nucleus. The cross section for the production off heavy nuclei is studied in Sec. 2.1.4. The treatment of nuclear effects such as quasi-elastic scattering are discussed in this section.

The main focus of this chapter is on the understanding of the qualitative behavior of the signal cross section for the process $e(Z,A) \to e(Z,A)\gamma'$. The calculation of signal and background for hidden photon searches with invisible hidden photon states requires a careful investigation of the effects of the applied approximations. In particular, radiative corrections to the signal and background cross sections need to be accounted for.

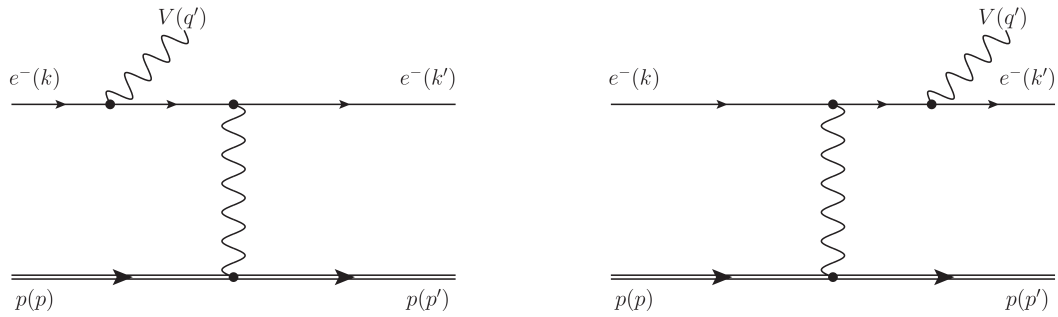

Figure 2.1: Feynman diagrams for the production of a vector boson V from electron fixed-target scattering. The diagrams describe the signal process for $V = \gamma'$ and the background from the Bethe–Heitler process for $V = \gamma$.

2.1 Calculation of the cross section

Since the expressions for the production cross section of a hidden photon γ' and those for the Bethe–Heitler background process are almost equal, the calculation of the cross section is performed in general for a massive vector boson with mass m_V. Due to the gauge invariance required within the kinetic mixing model, which will be shown explicitly for the invariant amplitude in the following, it is possible to take the limit $m_V = 0$ in order to obtain the Bethe–Heitler expressions. Therefore, the process

$$e(k,\, \lambda) + p(p\, s) \to e(k'\, \lambda') + p(p',\, s') + V(q',\, r'), \tag{2.1}$$

with $V = \gamma'$ as hidden photon signal process and $V = \gamma$ as Bethe–Heitler background will be analyzed. The four-momenta of the incoming (outgoing) electron and hadron are named $k\,(k')$ and $p\,(p')$, respectively, and q' is the four-momentum of the vector boson V. The helicities of the incoming (outgoing) electron and hadron are $\lambda\,(\lambda')$ and $s\,(s')$ and r' denotes the polarization of the V.

2.1.1 Amplitude for the process $e(Z, A) \to e(Z, A)\gamma/\gamma'$

The invariant amplitude of the process derived from the Feynman diagrams shown in Fig. 2.1 is

$$\mathcal{M}_V \quad = \frac{i\, e^2\, g_V}{(p' - p)^2}\, \varepsilon^{*\alpha}(q',\, r')\, J_N^\mu\, \mathcal{I}_{\mu\alpha}, \tag{2.2}$$

where $g_V = \varepsilon e$ in the case of γ' production and $g_V = e$ for the Bethe–Heitler process and $\varepsilon^{*\alpha}$ is the polarization vector of the γ' or γ. The leptonic interaction tensor $\mathcal{I}_{\mu\alpha}$ reads

$$\mathcal{I}_{\mu\alpha} = \overline{u}_e(k', s_k') \left(\gamma_\mu \frac{\not{k} - \not{q}' + m}{(k - q')^2 - m^2} \gamma_\alpha + \gamma_\alpha \frac{\not{k}' + \not{q}' + m}{(k' + q')^2 - m^2} \gamma_\mu \right) u_e(k, s_k). \tag{2.3}$$

In the case of a proton target the hadronic current J_N^μ is given by

$$J_N^\mu = \overline{u}_N(p', s_p')\, \Gamma^\mu\, u_N(p, s_p),$$

where for Γ^μ the common parametrization of

$$\Gamma^\mu \equiv \Gamma^\mu(Q_t^2) = F_1(Q_t^2)\,\gamma_\mu + F_2(Q_t^2)\,i\,\sigma_{\mu\nu}q_t^\nu/2M,$$

with the Dirac (F_1) and Pauli (F_2) form factors and $Q_t^2 = -(p-p')^2 > 0$.

To obtain cross sections as large as possible besides protons also heavy nuclei are used as target material in the present and upcoming experiments. For such nuclei the cross section is enhanced by a factor Z^2 compared to the scattering off protons. Hence, nuclei with large enhancement factors are chosen. For fixed-target experiments commonly tantalum (Ta) with $Z = 73$, $A = 181$, and $M \simeq 168\,\mathrm{GeV}$ are utilized. In addition, during the later discussion in Sec. 3.5.3 also xenon (Xe) with $Z = 54$, $A = 132$, and $M \simeq 123\,\mathrm{GeV}$ is considered as possible target.[1]

For a heavy nucleus the hadronic current can be approximately written as

$$J_N^\mu = Z \cdot F_{\mathrm{el}}(Q_t) \cdot (p+p')^\mu, \tag{2.4}$$

where $F_{\mathrm{el}}(Q_t) = \frac{3}{(Q_t\,R)^2} \cdot \left(\frac{\sin Q_t\,R}{Q_t\,R} - \cos Q_t\,R\right)$ is the nuclear charge form factor with $R = 1.21\,\mathrm{fm} \cdot A^{\frac{1}{3}}$. The parametrization of Eq. (2.4) accounts only for coherent scattering off the nucleus. As discussed later in Secs. 2.1.3 and 2.1.4, further effects such as inelastic contributions have an impact on the normalization of the cross section at the level of 5%–10% depending on the kinematics. Since the shape of the cross section is not altered significantly, this approximation can be used to investigate the kinematic dependencies of the signal and background processes.

The squared matrix element after summing and averaging of final and initial spin states, respectively,

$$\overline{|\mathcal{M}_V|^2} = \sum_{s_{k'},s_{p'}} \overline{\sum_{s_k,s_p}} \mathcal{M}_V \mathcal{M}_V^*,$$

where $\overline{\sum}$ indicates the spin averaged sum, can be calculated more conveniently by extracting the polarization vector of the vector boson V out of the matrix element and performing the sum over the spin states separately. One finds

$$\mathcal{M}_V = \mathcal{M}_{V\alpha}\,\varepsilon^{*\alpha}(q',\,r').$$

From the completeness relations for massive spin 1 bosons with $q'^2 = m_V^2$ one has

$$\sum_{r',r''} \varepsilon^{*\alpha}(q',\,r')\varepsilon^{\beta}(q',\,r'') = -g^{\alpha\beta} + \frac{q'^\beta\,q'^\alpha}{q'^2}.$$

In the case of a real photon as in the Bethe–Heitler process the second term does not contribute in the chosen Lorentz gauge. Since the considered process is gauge invariant, the second term must also vanish for the γ' production process. To test the amplitude for gauge invariance one contracts the interaction tensor with the momentum of the final state vector

[1] Therefore, in this thesis the term “heavy nucleus” refers to nuclei such as tantalum and xenon.

particle q':

$$\begin{aligned} q'^{\alpha}\mathcal{I}_{\mu\alpha} &= \overline{u}_e(k',s'_k)\left(\gamma_\mu \frac{\not{k}-\not{q}'+m}{(k-q')^2-m^2}\not{q}' + \not{q}'\frac{\not{k}'+\not{q}'+m}{(k'+q')^2-m^2}\gamma_\mu\right)u_e(k,s_k)\\ &= \overline{u}_e(k',s'_k)\left(\gamma_\mu \frac{2q'\cdot k-\not{q}'\not{k}-\not{q}'\not{q}'+m\not{q}'}{(k-q')^2-m^2} + \frac{2q'\cdot k'-\not{k}'\not{q}'+\not{q}'\not{q}'+\not{q}'m}{(k'+q')^2-m^2}\gamma_\mu\right)u_e(k,s_k)\\ &= \overline{u}_e(k',s'_k)\left(\gamma_\mu \frac{2q'\cdot k-\not{q}'m-q'^2+m\not{q}'}{(k-q')^2-m^2} + \frac{2q'\cdot k'-m\not{q}'+-q'^2+\not{q}'m}{(k'+q')^2-m^2}\gamma_\mu\right)u_e(k,s_k)\\ &= \overline{u}_e(k',s'_k)\left(\gamma_\mu \frac{2q'\cdot k-q'^2}{q'^2-2q'\cdot k} + \frac{2q'\cdot k'+q'^2}{q'^2+2q'\cdot k'}\gamma_\mu\right)u_e(k,s_k)\\ &= \overline{u}_e(k',s'_k)\left(\gamma_\mu(-1)+(1)\gamma_\mu\right)u_e(k,s_k)\\ &= 0. \end{aligned} \tag{2.5}$$

Accordingly, $\overline{|\mathcal{M}_V|^2}$ simply reads

$$\overline{|\mathcal{M}_V|^2} = -\sum_{s_{k'},s_{p'}}\overline{\sum_{s_k,s_p}}\mathcal{M}_V^{\alpha}\mathcal{M}_{V\alpha}^{*}.$$

2.1.2 Calculation of the differential cross section for (quasi-)elastic scattering

In this section the cross section is derived using the assumption that the hadronic reaction happens elastically, where the initial and final state particles are the same. As usual, one starts from the general expression of a cross section for three particles in the final state:

$$\begin{aligned} d\sigma = &\frac{1}{4\sqrt{(p\cdot k)^2-m^2M^2}}\frac{d^3\vec{k}'}{(2\pi)^3 2E_{k'}}\frac{d^3\vec{p}'}{(2\pi)^3 2E_{p'}}\frac{d^3\vec{q}'}{(2\pi)^3 2E_{q'}}\\ &\times(2\pi)^4\delta^{(4)}\left(k+p-k'-p'-q'\right)\overline{|\mathcal{M}|^2}. \end{aligned} \tag{2.6}$$

It is convenient to evaluate this expression within the "recursive phase space" approach.[2] In this approach the phase space is factorized into subprocesses which can be evaluated in the corresponding rest frames. This requires a Lorentz transformation into one common frame if the Feynman amplitude cannot be factorized in the same way.

For this purpose, the $\gamma^*(q)+p(p)\to p(p')+V(q')$ subprocess, $q=(k-k')$, is evaluated in the γ^*p-rest frame, labeled by $*$. One has in this frame:

$$(\vec{q}+\vec{p})^* \;=\; \left(\vec{k}-\vec{k}'+\vec{p}\right)^* \;=\; \vec{0}.$$

For calculations where all quantities are defined in the same reference frame, frame labels are omitted for purposes of clarity. The remaining $e^-(k)\to\gamma^*(q)+e^-(k')$ subprocess is

[2] In textbooks such as Ref. [174] this method is also called "factorization of phase space." Since another phase space parametrization applied (Sec. 3.3.2) also makes use of a factorization of the phase space, instead the name "recursive phase space" approach is used. This name originates from the fact that the phase space of multiparticle final states is generated recursively by this approach.

evaluated in the lab frame (L) where the target is at rest. In this choice of frames, the general cross section reads as

$$\begin{aligned} d\sigma =& \frac{1}{4\sqrt{(p\cdot k)^2 - m^2M^2}} \left(\frac{d^3\vec{k}\,'}{(2\pi)^3 2E_{k'}}\right)^L \\ &\times \left(\frac{d^3\vec{p}\,'}{(2\pi)^3 2E_{p'}}\,\frac{d^3\vec{q}\,'}{(2\pi)^3 2E_V}\,(2\pi)^4\,\delta^{(4)}\left(k+p-k'-p'-q'\right)\right)^* \overline{|\mathcal{M}|^2}, \end{aligned} \tag{2.7}$$

where $E_{q'} \equiv E_V$ has been used. One has the freedom to choose which integration can be eliminated by the Dirac δ function. Here the $d^3|\vec{q}\,'|$ integration is evaluated in this manner.

In the γ^*p-rest frame one finds

$$\begin{aligned} q'^2 &= \left(q+p-p'\right)^2 \\ \Leftrightarrow m_V^2 &= (q+p)^2 + M^2 - 2\,(q+p)\cdot p' \\ \Leftrightarrow m_V^2 &= s^* + M^2 - 2\left(E_q^* + E_p^*\right)E_{p'}^* + 2\left(\vec{q}^{\,*} + \vec{p}^{\,*}\right)\left(\vec{p}\,'\right)^* \\ \Leftrightarrow m_V^2 &= s^* + M^2 - \sqrt{s^*}E_{p'}^* \end{aligned}$$

and thus

$$E_{p'}^* = \frac{s^* + M^2 - m_V^2}{2\sqrt{s^*}}, \tag{2.8}$$

with $\vec{q}^{\,*} + \vec{p}^{\,*} = \vec{0}$ and

$$s^* = (q+p)^2 = \left(\left(q^0\right)^* + E_p^*\right)^2. \tag{2.9}$$

The momentum $|\vec{p}\,|'^*$ results to

$$|\vec{p}\,|'^* = \sqrt{E_{p'}^* - M^2} = \frac{\lambda^{1/2}\left(s^*, M^2, m_V^2\right)}{2\sqrt{s^*}}, \tag{2.10}$$

where λ denotes the kinematical triangle function defined in Eq. (A.1). In the γ^*p-rest frame the three-momenta of the scattered hadron and the outgoing vector boson are equal in magnitude, $|\vec{p}\,|'^* = |\vec{q}\,|'^*$, and opposite in direction, yielding

$$E_V^* = \frac{s^* - M^2 + m_V^2}{2\sqrt{s^*}}.$$

Thus, in the γ^*p-rest frame one has

$$\begin{aligned} &\frac{d^3\vec{p}\,'}{(2\pi)^3\,2E_{p'}}\,\frac{d^3\vec{q}\,'}{(2\pi)^3\,2E_V}\,(2\pi)^4\,\delta^{(4)}\left(k+p-k'-p'-q'\right) \\ &= \frac{d^3\vec{p}\,'}{(2\pi)^2\,4E_{p'}E_V}\,\delta\left(q^0 + E_P - E_{p'} - E_V\right) \\ &= \frac{|\vec{p}\,'|\,dE_{p'}\,d\Omega_{p'}}{(2\pi)^2\,4\left(E_V + E_{p'}\right)}\,\delta\left(E_{p'} - \frac{s^* + M^2 - m_V^2}{2\sqrt{s^*}}\right), \end{aligned}$$

where in the last step a factor from transforming the δ function has entered according to

$$\left|\frac{\partial\left(q^0+E_p-E_{p'}-E_V\right)}{\partial E_{p'}}\right|^{-1} = \left|\frac{\partial\left(\sqrt{s^*}-E_{p'}-\sqrt{|\vec{q}\,'|^2+m_V^2}\right)}{\partial E_{p'}}\right|^{-1}$$
$$= \left|\frac{\partial\left(\sqrt{s^*}-E_{p'}-\sqrt{E_{p'}^2-M^2+m_V^2}\right)}{\partial E_{p'}}\right|^{-1}$$
$$= \left|-1-\frac{E_{p'}}{E_V}\right|^{-1} = \frac{E_V}{E_V+E_{p'}}.$$

Inserting into Eq. (2.7) yields

$$d\sigma = \frac{1}{4\sqrt{(p\cdot k)^2-m^2M^2}}\left(\frac{d^3\vec{k}\,'}{(2\pi)^3 2E_{k'}}\right)^L \frac{|\vec{p}\,'|^*\,d\Omega^*_{p'}}{(2\pi)^2\,4E_V^*}\,\overline{|\mathcal{M}|^2}$$
$$= \frac{1}{32|\vec{k}\,|M}\,\frac{1}{(2\pi)^5}\,\frac{(|\vec{k}\,'|^L)^2\,d|\vec{k}\,'|^L\,d\Omega^L_{k'}}{E_{k'}}\,\frac{|\vec{p}\,'|^*\,d\Omega^*_{p'}}{E_V^*+E^*_{p'}}\,\overline{|\mathcal{M}|^2},$$

and thus

$$\frac{d\sigma}{dE^L_{k'}\,d\Omega^L_{k'}\,d\Omega^*_{p'}} = \frac{|\vec{k}\,'|^L}{32|\vec{k}\,|M}\,\frac{1}{(2\pi)^5}\,\frac{|\vec{p}\,'|^*}{E_V^*+E^*_{p'}}\,\overline{|\mathcal{M}|^2}$$
$$= \frac{|\vec{k}\,'|^L}{64|\vec{k}\,|M}\,\frac{1}{(2\pi)^5}\,\frac{\lambda^{1/2}\left(s^*,M^2,m_V^2\right)}{s^*}\,\overline{|\mathcal{M}|^2}, \tag{2.11}$$

where s^* is given in Eq. (2.9). To evaluate $\overline{|\mathcal{M}|^2}$ the four-vectors need to transformed into one common.

In addition to the approach discussed above, the cross section also has been expressed in terms of lab frame variables. This kind of evaluation is helpful with particular regard to the design of possible experiments. For this reason the cross section is calculated in terms of 3 variables parameterizing the created vector particle, $E_{q'}$, $\theta_{q'}$, $\phi_{q'}$, and two angles for the scattered electron, $\theta_{k'}$, $\phi_{k'}$. Using Eq. (2.6) and integrating over the final state hadron three-momentum, leads to

$$d\sigma = \frac{1}{8|\vec{k}\,|\,M\,E_{p'}}\,\frac{1}{(2\pi)^5}\,\frac{d^3\vec{k}\,'}{2E_{k'}}\,\frac{d^3\vec{q}\,'}{2E_{q'}}\,\delta\left(E_0+M-E_{k'}-E_{q'}-E_{p'}\right)\,\overline{|\mathcal{M}|^2}, \tag{2.12}$$

where $E_{q'}=E_V$ and E_0 is the beam energy. By means of four-momentum conservation one can express the energy of the scattered electron in terms of the remaining 5 quantities as

$$p'^2 = \left(p+k-k'-q'\right)^2$$
$$= \left(p+k-q'\right)^2 + k'^2 - 2\left(p+k-q'\right)\cdot k'$$
$$\Leftrightarrow 0 = \left(\left(p+k-q'\right)^2+k'^2-p'^2\right) - \left(2\,\left(E_0+M-q'^0\right)k'^0\right) + \left(2\left(\vec{k}-\vec{q}\,'\right)\cdot\hat{k}'|\vec{k}\,'|\right),$$

with $q'^0 = E_V$, $k'^0 = E_{k'}$ and the unit direction vector of the scattered electron $\hat{k}' = \left(\vec{k}\,'/|\vec{k}\,'|\right)$. For convenience one assigns

$$\begin{aligned} A &= \left(p + k - q'\right)^2 + k'^2 - p'^2, \\ B &= 2\,\left(E_0 + M - q'^0\right), \\ C &= 2\left(\vec{k} - \vec{q}\,'\right) \cdot \hat{k}', \end{aligned} \tag{2.13}$$

where the mass shell conditions $k'^2 = m^2$ and $p'^2 = M^2$ are applied in the numerical calculation. Therefore, one finds

$$\begin{aligned} 0 &= A - B\sqrt{|\vec{k}\,'|^2 + k'^2} + C\,|\vec{k}\,'| \\ \Rightarrow B^2\left(|\vec{k}\,'|^2 + k'^2\right) &= A^2 + C^2\,|\vec{k}\,'|^2 + 2\,A\,C\,|\vec{k}\,'| \\ \Leftrightarrow 0 &= |\vec{k}\,'|^2 + \frac{2\,A\,C}{C^2 - B^2}\,|\vec{k}\,'| + \frac{A^2 - B^2 m^2}{C^2 - B^2}. \end{aligned}$$

This quadratic equation is solved by

$$|\vec{k}\,'|_\pm = -\frac{A\,C}{C^2 - B^2} \pm \sqrt{\frac{A^2B^2 + B^2C^2m^2 - B^4m^2}{\left(C^2 - B^2\right)^2}}. \tag{2.14}$$

The physical solution of Eq. (2.14) is $|\vec{k}\,'|_+$, as one finds by evaluating Eq. (2.14) for a vanishing electron mass $m^2 = 0$ or by comparing the integrated cross section in the lab frame with that one in the recursive coordinates given in Eq. (2.11). For the integration over the modulus of the three-momentum of the scattered electron $|\vec{k}\,'|$, a transformation of the remaining component of the Dirac δ function has to be performed, which yields

$$\begin{aligned} &\frac{\partial}{\partial|\vec{k}\,'|}\left(E_0 + M - E_{k'} - E_{q'} - E_{p'}\right) \\ &= \frac{\partial}{\partial|\vec{k}\,'|}\left(E_0 + M - \sqrt{|\vec{k}\,'|^2 - k'^2} - q'^0 - \sqrt{(\vec{k} - \vec{k}\,' - \vec{q}\,')^2 - p'^2}\right) \\ &= \left|\frac{|\vec{k}\,'|}{k'^0} - \frac{|\vec{k}\,'| - \left(\vec{k} - \vec{q}\,'\right)\cdot\hat{k}'}{p'^0}\right|, \end{aligned} \tag{2.15}$$

where the notation $k'^0 = E_{k'} = \sqrt{|\vec{k}\,'|^2 - k'^2}$ and $p'^0 = E_{p'} = \sqrt{(\vec{k} - \vec{k}\,' - \vec{q}\,')^2 - p'^2}$ is used. Applying this to Eq. (2.12), one finds

$$\begin{aligned} \frac{d\sigma}{d|\vec{q}\,'|\,d\Omega_{q'}\,d\Omega_{k'}} = &\frac{1}{32|\vec{k}\,|M}\frac{1}{(2\pi)^5}\frac{|\vec{k}\,'|^2\,|\vec{q}\,'|^2}{E_{k'}\,E_{q'}\,E_{p'}}\left|\frac{|\vec{k}\,'|}{E_{k'}} - \frac{|\vec{k}\,'| - \left(\vec{k} - \vec{q}\,'\right)\cdot\hat{k}'}{E_{p'}}\right|^{-1} \\ &\times\delta\left(|\vec{k}\,'| - |\vec{k}\,'|_+\right)\,\overline{|\mathcal{M}|^2}, \end{aligned} \tag{2.16}$$

and thus

$$\frac{d\sigma}{dE_{q'}\,d\Omega_{q'}\,d\Omega_{k'}} = \frac{1}{32|\vec{k}\,|M}\frac{1}{(2\pi)^5}\frac{|\vec{k}\,'|^2\,|\vec{q}\,'|}{E_{k'}\,E_{p'}}\left|\frac{|\vec{k}\,'|}{E_{k'}} - \frac{|\vec{k}\,'| - \left(\vec{k} - \vec{q}\,'\right)\cdot\hat{k}'}{E_{p'}}\right|^{-1}\overline{|\mathcal{M}|^2}, \tag{2.17}$$

where this equation has to be evaluated with $|\vec{k}'| = |\vec{k}'|_+$.

Although Eq. (2.17) has been derived with a certain choice of coordinates, no assumptions on the particular geometry were made. This allows one to easily find a lab frame cross section depending on another set of coordinates. As an example, by replacing the four-vectors

$$q' \to k', \quad k' \to p',$$

Eq. (2.17) can be rewritten depending on 3 quantities associated with the scattered electron and on 2 angles of the final hadron state:

$$\frac{d\sigma}{dE_{k'}\, d\Omega_{k'}\, d\Omega_{p'}} = \frac{1}{32|\vec{k}\,|M} \frac{1}{(2\pi)^5} \frac{|\vec{p}\,'|^2\, |\vec{k}\,'|}{E_{p'}\, E_{q'}} \left| \frac{|\vec{p}\,'|}{E_{p'}} - \frac{|\vec{q}\,'| - \left(\vec{k} - \vec{k}\,'\right) \cdot \hat{q}'}{E_{q'}} \right|^{-1} \overline{|\mathcal{M}|^2},$$

with $|\vec{p}\,'| = |\vec{p}\,'|_+$ and the quantities A, B, C given in Eq. (2.13) changed accordingly. This cross section is commonly used for the study of virtual Compton scattering off the nucleon [175]. These studies were also applied as a cross-check for the calculations.

2.1.3 Discussion and phenomenology of the cross section

For the processes as considered here, it is still possible to determine an analytical expression for the cross section. Nevertheless, there is no practical advantage to find an analytical expression, since the phase space integration needs to be performed numerically. However, for understanding the structure of the amplitude and thus, where the cross section is large, it is worthwhile to have a look at selected terms in more detail.

An example is given in Fig. 2.2, where the calculations of the Bethe–Heitler cross section (solid curve) and of the γ' production cross section are shown for $m_{\gamma'} = 20\,\mathrm{MeV}$ and $\varepsilon^2 = 1$ (dashed curve). The cross sections were evaluated for a kinematical setting with a beam energy of $E_0^L = 855\,\mathrm{MeV}$, a scattered electron with energy $E_{k'}^L = 748\,\mathrm{MeV}$, and a scattering angle $\theta_{k'}^L = 15.1°$ with respect to the incident virtual photon direction as a function of the $\gamma^* p$-rest frame polar angle $\theta_{p'}^*$ in the left panel, where $\phi_{k'}^L = \phi_{p'}^* = 0$. The cross section is varying as a smooth function over several orders of magnitude. It is dominated by two sharp peaks around $\theta_{p'}^* = 60°$ and $90°$ in case of the Bethe–Heitler cross section, whereas no peaks appear in case of the γ' production cross section. The same cross section as a function of the angle $\theta_{q'}^L$ is shown in the right panel. Note that the position of the peaks of course is depending on the particular choice of kinematics.

The cross section displays a peak in general for any propagator in the intermediate state of which the denominator tends to zero. It is obvious from Fig. 2.1 that there are three propagators which can produce a sharp peak: the intermediate electron propagators in the initial and final state and the virtual photon exchange between the lepton and hadron line. Independently of the signal and background process, the cross section will be large, if the momentum transfer carried by the virtual photon exchange between the lepton and hadron line is small,

$$\left(p' - p\right)^2 = \left(q - q'\right)^2 \simeq 0.$$

Hence, in order to enhance the production cross section, it is reasonable to choose the kinematical setting in such a way that the momentum transfer to the hadronic state is small. Unfortunately this automatically implicates that the background process is also enhanced.

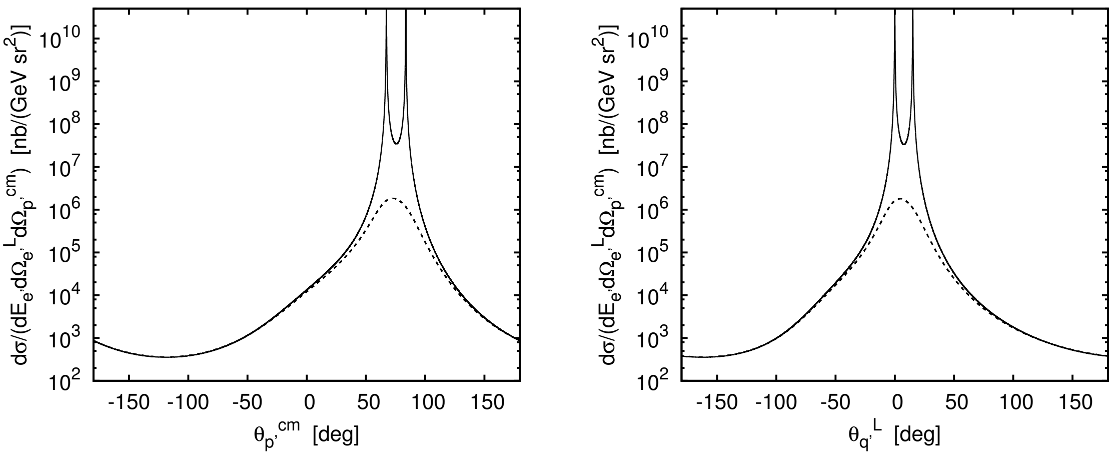

Figure 2.2: Left panel: Differential cross section of the Bethe–Heitler process (solid curve) and of γ' production with $m_{\gamma'} = 20\,\mathrm{MeV}$ and $\varepsilon^2 = 1$ (dashed curve). The plot shows the differential cross section of Eq. (2.11) for a beam energy $E_0^L = 855\,\mathrm{MeV}$, a scattered electron with energy $E_{k'}^L = 748\,\mathrm{MeV}$, and a scattering angle $\theta_{k'}^L = 15.1°$ with respect to the incident virtual photon direction as a function of the $\gamma^* p$-rest frame polar angle $\theta_{p'}^*$, where $\phi_{k'}^L = \phi_{p'}^* = 0$. One notices the two sharp peaks around $\theta_{p'}^* = 60°$ and $90°$ appearing in the case of the Bethe–Heitler cross section which are not present for γ' production. Right panel: Same as in the left panel as a function of the polar angle of the V with respect to the beam-direction.

The arguments are different for the intermediate electron propagators. These are proportional to

$$\frac{1}{m_V^2 - 2q' \cdot k} \quad \text{and} \quad \frac{1}{m_V^2 + 2q' \cdot k'},$$

for the initial and final states, respectively. In the case of a final state photon, one has $1/(-2q'\cdot k)$ and $1/(2q'\cdot k')$, in which the denominator can be approximately zero. If the bremsstrahlung photon is radiated into the direction of the electron and electrons are treated as massless particles, the pole of the propagator can be hit, i.e.

$$\frac{1}{-2|\vec{q}\,'||\vec{k}\,| + 2|\vec{q}\,'||\vec{k}\,|\cos\theta_{e\gamma}} \quad \text{and} \quad \frac{1}{2|\vec{q}\,'||\vec{k}\,'| - 2|\vec{q}\,'||\vec{k}\,'|\cos\theta_{e'\gamma}}.$$

Since one of the angles $\theta_{e\gamma}$ and $\theta_{e'\gamma}$ is zero both terms cancel each other. This explains the typical peak structure of the Bethe–Heitler cross section which can be seen from the solid curve in Fig. 2.2. The angles above are defined as angles between the momenta $\vec{k}$ and $\vec{q}\,'$, and $\vec{k}\,'$ and $\vec{q}\,'$, respectively. The peaks in the left panel of Fig. 2.2 appear at the angles $\theta_{p'}^*$ leading to $\hat{k}\cdot\hat{q}' = 1$ and $\hat{k}'\cdot\hat{q}' = 1$ in the $\gamma^* p$-rest frame. In the right panel the cross section is displayed as a function of the polar angle of the V with respect to the beam axis. Now the Bethe–Heitler peaks are perfectly centered at $0°$ and $15.2°$ for emission of a photon into the direction of the incident and scattered electron.

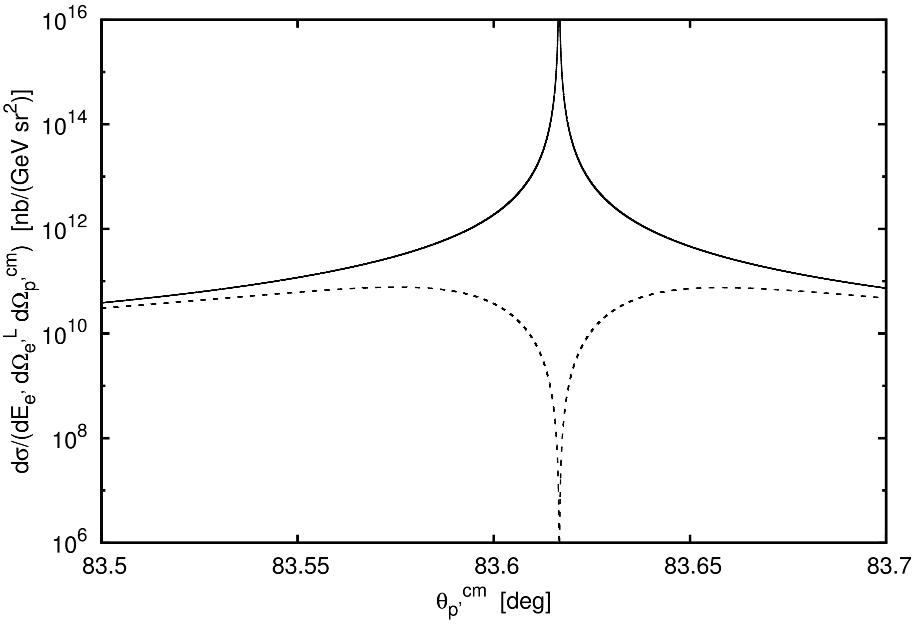

Figure 2.3: Calculation of the Bethe–Heitler cross section as in the left panel of Fig. 2.2 with vanishing (solid curve) and finite (dashed curve) electron mass. To emphasize the influence of a vanishing and finite electron mass, only a very small region around one of the Bethe–Heitler peaks is considered.

Apparently, a finite vector boson mass avoids that the denominator can get close to zero presented by the dashed curve in Fig. 2.2. Note that the electron mass of course is finite, which causes that the above equation must be rewritten as

$$\frac{1}{-2|\vec{q}\,'|E_k + 2|\vec{q}\,'||\vec{k}\,|\cos\theta_{e\gamma}} \quad \text{and} \quad \frac{1}{2|\vec{q}\,'|E_{k'} - 2|\vec{q}\,'||\vec{k}\,'|\cos\theta_{e'\gamma}},$$

where in the first term now the energy instead of the modulus of the three-momentum enters. Due to $E_p = \sqrt{|\vec{p}|^2 + m^2} > |\vec{p}|$ this denominator cannot be zero in any case since the finite electron mass provokes that the pole is unaccessible.

Although a vanishing electron mass simplifies the calculations and is a good approximation for high-energy kinematics, the electron will be treated as a particle with a finite mass in this work. In particular, the finite electron mass has to be taken into account for the calculation of the integrated cross section. Otherwise the amplitude has a singularity leading to a logarithmical divergence $\sim \ln\left(s/m^2\right)$ with $s = (k + p - p')^2$ in the integrated cross section. In Fig. 2.3 the influence of the electron mass on the shape of the 5-fold differential cross section for the same choice of kinematics as in Fig. 2.2 is demonstrated. The solid (dashed) curve in Fig. 2.3 shows the cross section in the region of one of the Bethe–Heitler peaks as a function of the polar angle $\theta^*_{p'}$ in the $\gamma^* p$-rest frame with vanishing (finite) electron mass.

Note that, if the electron is treated as massless this calculation without further modifications leads to a wrong result, since the peaks correspond to the emission of the photon into the direction of the electron. The vector interaction, manifested by the Dirac matrix γ^μ in the electromagnetic current, in general is helicity conserving. Thus, a left-handed state cannot be turned into a right-handed and vice versa. Since the photon is a spin-1 vector particle with helicity ± 1, a helicity flip is necessary in order to fulfill helicity conservation, which has to be preserved in the case of QED. This cannot be realized with a massless electron. Therefore, this infinite peak is forbidden by helicity conservation and in the peaking region the approximation of massless electrons is not valid. In nature of course, the electron has a finite mass, which allows for a small breaking of helicity conservation. This is accurately described by the dashed curve in Fig. 2.3, which drops close to zero for the radiation of the photon into the direction of the electron.

If the decay products are not detected in the investigation of hidden photon production, the kinematics must be chosen in such a way that these so-called "Bethe–Heitler peaks" do not contribute too strongly. In an experiment where the decay products of the γ' are detected, one exploits that the cross section is largest for the emission of the hidden photon into the directions of the initial and final state electron.

Of course, there is also a contribution to the cross section from the Feynman diagrams, where the V couples to the hadronic state. This is known as (true) virtual Compton scattering (VCS) off a hadron. As far as the hadronic state is a nucleus, its contribution is neglected. The emission of a (hidden photon) from the nucleus is suppressed by the large mass and the kinematical features discussed above.

As mentioned, the cross section for bremsstrahlung off the lepton line is largest, if the momentum transfer $Q_t^2 = -(p' - p)^2$ tends to zero. Moreover, the signal cross section is peaked for forward emission of the hidden photon where most of the beam energy is transferred to the γ' (see Sec. 2.2.2). The VCS contribution is suppressed by several orders of magnitudes compared to the radiation off the lepton in this kinematical region.

It is possible to find a simple parametrization of the form factors of the nuclear electromagnetic current, which can describe existing data within an accuracy of around 5% [176, 177] (see the next section). Also inelastic nuclear effects are included in this parametrization.

It was shown that the VCS contribution cannot be neglected for a nucleon target. The VCS amplitude can be decomposed into so-called Born and non-Born parts at low energies. The Born term is the part of the VCS amplitude, in which the interaction is parametrized by a single proton in the intermediate state. The structure dependent effects are absorbed in the non-Born part. Below the pion threshold the non-Born amplitude is of the order of $\mathcal{O}(q')$ [178]. Hence, the contribution due to the non-Born contribution tends to zero for $q'^0 \to 0$. Such effects can be parametrized in terms of generalized polarizabilities of the nucleon which were determined experimentally [179]. The Bethe–Heitler contribution is suppressed in in the kinematics of these experiments. It was found that the non-Born terms contribute up to 10% to the cross section. In the kinematical settings of this work the region is preferred where the Bethe–Heitler cross section is large. Thus, the non-Born contribution is less important and will not contribute more than 5% which is a very conservative estimate.

The nucleon Born amplitude reads

$$\mathcal{M}_{V,\,\mathrm{vcs}} = \frac{-i\, e^2\, g_V}{q^2}\, \varepsilon^{*\alpha}(q',\, r')\, l^\mu\, \mathcal{H}_{\mu\alpha}, \tag{2.18}$$

with the hadronic tensor

$$\mathcal{H}_{\mu\alpha} = \overline{u}_p(p', s_p') \Bigg(\Gamma_\mu(q_t + q') \frac{\not{p} - \not{q}' + M}{(p - q')^2 - M^2} \Gamma_\alpha(-q') + \Gamma_\alpha(-q') \frac{\not{p}' + \not{q}' + M}{(p' + q')^2 - M^2} \Gamma_\mu(q_t + q') \Bigg) u_p(p, s_p),$$

and the leptonic current

$$l^\mu = \overline{u}_e(k', s_k')\, \gamma^\mu\, u_e(k, s_k).$$

The emission of a photon is suppressed by the nucleon mass appearing in the propagators of $\mathcal{H}_{\mu\alpha}$,

$$\frac{1}{-2|\vec{q}\,'|E_p + 2|\vec{q}\,'||\vec{p}\,|\cos\theta_{p\gamma}} \quad \text{and} \quad \frac{1}{2|\vec{q}\,'|E_{p'} - 2|\vec{q}\,'||\vec{p}\,'|\cos\theta_{p'\gamma}},$$

as discussed before for the finite electron mass. Since the mass of the nucleon of $M = m_N \simeq 940$ MeV is much larger than the electron mass $m = 0.511\,\text{MeV}$, the VCS amplitude does not show the peaked structures as the Bethe–Heitler amplitude does.

For a heavy nucleus the propagator structure is very similar, though its mass is much larger than in the case of a nucleon. In addition, the choice of kinematics provokes that the VCS term is suppressed by several orders of magnitude. Hence, the VCS contribution will be neglected for a heavy nucleus in the hadronic current.

Since the VCS contribution has only a very slight effect on the shape of the cross section, this term will be neglected for the following discussion of the kinematical dependencies. However, the normalization of the cross section is typically altered in the range of around 10%. In order to calculate the signal and background cross sections for experiments with invisible hidden photon states, the VCS contribution needs to be accounted for. In addition, to obtain a realistic description of the process at higher energies also the non-Born amplitude parameterizing the nucleon structure-dependent effects has to be included. Therefore, the Born term of the VCS contribution is included in the actual calculations of the signal and background cross sections for the scattering off protons at low energies in Chapter 3.

2.1.4 Cross section for (semi-) inclusive scattering

Up to now the cross section of the process $e(Z, A) \to e(Z, A)\gamma/\gamma'$ has been calculated using the assumption that the scattering off the hadronic state is coherent. In this approximation the hadron does not break up. The break-up of the hadronic state can be included by considering the cross section of the (semi-) inclusive scattering process. The hadronic state breaks up after being struck by the virtual photon,

$$e(Z, A) \to eX\gamma/\gamma',$$

where X denotes any possible final state. The coherent scattering off the hadron will be referred to in the following as elastic contribution.

For the evaluation of the (semi-) inclusive cross section in the lab frame again Eq. (2.6) is used as starting point. The spin averaged matrix element $\overline{|\mathcal{M}|^2}$ can be decomposed for a process as described by the Feynman diagrams of Fig. 2.1 in the 1γ-approximation as

$$\overline{|\mathcal{M}|^2} = \overline{\sum_{s'_e,\, s'_p}} \sum_{s_e,\, s_p} \sum_{\lambda,\, \lambda'} \mathcal{M}\mathcal{M}^* = \overline{\sum_{s'_e,\, s'_p}} \sum_{s_e,\, s_p} \sum_{\lambda,\, \lambda'} L_{\mu\nu} W^{\mu\nu} \tag{2.19}$$

where again s_e (s'_e) and s_e (s'_p) denote the helicity of the initial (final) electron and hadron, λ refers to the (hidden) photon polarization state and $\overline{\sum}$ indicates the spin averaged sum. The squared amplitude $\mathcal{M}\mathcal{M}^*$ in Eq. (2.19) is split into a purely leptonic part $L_{\mu\nu}$ and the hadronic tensor $W^{\mu\nu}$. The leptonic part $L_{\mu\nu}$ of the reaction is exactly known from QED. The corresponding leptonic current $L_\mu = \mathcal{I}_{\mu\alpha}\, \varepsilon^{*\alpha}$ is found by contracting the leptonic tensor $\mathcal{I}_{\mu\alpha}$ of Eq. (2.3) with the (hidden) photon polarization vector $\varepsilon(q',\, \lambda)$. The hadronic tensor $W^{\mu\nu}$ needs to be evaluated in the most general way. This task has been done more than 40 years ago for the first time [180,181].

The lab frame cross section can be rewritten as

$$\begin{aligned} d\sigma =& \frac{1}{4\sqrt{(p\cdot k)^2 - m^2 M^2}} \frac{d^3\vec{k}\,'}{(2\pi)^3 2E_{k'}} \frac{d^3\vec{q}\,'}{(2\pi)^3 2E_V} \\ &\times \frac{d^3\vec{p}\,'}{(2\pi)^3 2E_{p'}} (2\pi)^4\, \delta^{(4)}\left(k + p - k' - p' - q'\right) \overline{|\mathcal{M}|^2} \\ =& \frac{\varepsilon^2 e^6}{4|\vec{k}\,|M} \frac{1}{Q_t^4} \frac{d^3\vec{k}\,'}{(2\pi)^3 2E_{k'}} \frac{d^3\vec{q}\,'}{(2\pi)^3 2E_V} \overline{\sum_{s_e,\, s'_e}} L_\nu L^*_\nu \\ &\times \underbrace{\int \frac{d^3\vec{p}\,'}{(2\pi)^3 2E_{p'}} (2\pi)^4\, \delta^{(4)}\left(q_t + p - p'\right) \overline{\sum_{s_p}} \sum_{X} \langle p|J^\mu|X\rangle\langle X|J^{*\nu}|p\rangle}_{4\pi M^2/p'^0 W^{\mu\nu}}, \end{aligned} \tag{2.20}$$

where $q_t = k - k' - q'$ is the four-momentum transfer onto the hadron and $Q_t^2 = -q_t^2$. J^μ is the hadronic electromagnetic current operator and X is any possible final state. Since only the interaction with the electromagnetic current is considered here, both, the leptonic and hadronic tensors, are entirely symmetric. As shown in several works [180,181], the most general structure of the hadronic tensor is

$$\begin{aligned} W^{\mu\nu} =& A(Q_t^2, q_t\cdot p) g^{\mu\nu} + B(Q_t^2, q_t\cdot p) q_t^\mu q_t^\nu + C(Q_t^2, q_t\cdot p) p^\mu p^\nu \\ &+ D(Q_t^2, q_t\cdot p)(p^\mu q_t^\nu + q_t^\mu p^\nu) + E(Q_t^2, q_t\cdot p)(p^\mu q_t^\nu - q_t^\mu p^\nu), \end{aligned}$$

where A, B, C, D, E are scalar functions and already several constraints were applied. Due to the translation invariance imposed by the δ function, the sum over initial and final states, and Lorentz invariance, $W^{\mu\nu}$ must be a rank 2 tensor and may only depend on two scalar kinematical variables, where Q_t^2 and $q_t \cdot p$ due to $p^2 = M^2$ are the only non-trivial ones. Note that only symmetric structures are taken into account. For a possible electroweak interaction, also an antisymmetric part will contribute. Gauge invariance $q_{t\mu} W^{\mu\nu} = q_{t\nu} W^{\mu\nu} = 0$ leads to

$$\begin{aligned} W^{\mu\nu} =& W_1(Q_t^2, q_t\cdot p)\left(-g^{\mu\nu} + \frac{q_t^\mu q_t^\nu}{Q_t^2}\right) \\ &+ \frac{1}{M^2} W_2(Q_t^2, q_t\cdot p)\left(p^\mu - \frac{q_t\cdot p}{Q_t^2} q_t^\mu\right)\left(p^\nu - \frac{q_t\cdot p}{Q_t^2} q_t^\nu\right), \end{aligned} \tag{2.21}$$

where W_1 and W_2 are the hadronic structure functions. As in the considered process the leptonic current L_μ is also gauge invariant. Thus, $q_t^\mu L_\mu = 0$, $W^{\mu\nu}$ can be reduced to

$$W^{\mu\nu} = -W_1(Q_t^2, q_t \cdot p)\, g^{\mu\nu} + \frac{1}{M^2} W_2(Q_t^2, q_t \cdot p)\, p^\mu p^\nu. \tag{2.22}$$

Inserting the results of Eqs. (2.21) and (2.22), the differential cross section of Eq. (2.20) can be rewritten in terms of the leptonic and hadronic tensors

$$\frac{d\sigma}{dE_k' d\Omega_{k'} dE_V d\Omega_{q'}} = \frac{\varepsilon^2 e^6}{8|\vec{k}\,|\, Q_t^4} \frac{|\vec{k}\,'|\,|\vec{q}\,'|}{(2\pi)^5} \frac{M}{p'^0} \overline{\sum_{s_e,\, s_e'}} L_\nu L_\nu^* W^{\mu\nu}. \tag{2.23}$$

The cross section for elastic scattering can be obtained easily from Eq. (2.23) by using the parametrization with the form factors of elastic scattering and restricting the final state to the same hadron as in the initial state. As an example, for the scattering off a proton target, the structure functions are given by

$$\begin{aligned} W_1(Q_t^2) &= \frac{G_E^2(Q_t^2) + \tau\, G_M^2(Q_t^2)}{1+\tau}\, \delta(E_p + q_t^0 - E_p'), \\ W_2(Q_t^2) &= \tau\, G_M^2(Q_t^2)\, \delta(E_p + q_t^0 - E_p'), \end{aligned}$$

where G_E and G_M are the electric and magnetic Sachs form factors, respectively, and $\tau = {}^{Q_t^2}/_{4\,m_N^2}$. The structure functions for the elastic process only depend on the squared momentum transfer Q_t^2 and the dependence on $q_t \cdot p$ has been dropped due to the additional condition $p'^2 = M^2$. Rewriting the δ function as condition on the energy of the scattered electron and multiplying Eq. (2.23) by the Jacobian of the δ function of Eq. (2.15) and inserting the result of Eq. (2.14), leads to the cross section which was already found in Eq. (2.17).

For a nuclear target the form factors parameterizing the structure function W_1 and W_2 were discussed in e.g. Refs. [177, 181]. The inelastic contribution for a proton can be calculated in theory quite straightforwardly, e.g., within the parton model for large Q_t^2 (see for example Refs. [182, 183]). For a nuclear target the situation is quite different. Since a nucleus is a composite object of many nucleons with a variety of possible energy levels and resonances a general parametrization in terms of electromagnetic structure functions is impossible. Nevertheless, one can estimate the inelastic contribution by exploiting the dominance of quasi-elastic scattering off a nucleon bound in the nucleus, which is sketched in Fig. 2.4. In quasi-elastic scattering the nucleus does not break up and the condition $p'^2 = M^2$ is fulfilled. As shown in Fig. 2.4, the scattering reaction takes places as scattering off a single proton in the nucleus. Quasi-elastic scattering dominates the inelastic reaction for the range of small momentum transfer Q_t^2. As discussed in Sec. 2.1.3, $Q_t^2 \to 0$ corresponds to the region where the cross sections are as large as possible.

A possible parametrization of these structure functions is given in Ref. [177] for a spin-0 nucleus as

$$\begin{aligned} W_1^{\text{el}}(Q_t^2) &= W_1^{\text{inel}}(Q_t^2) = 0, \\ W_2^{\text{el}}(Q_t^2) &= \left(\frac{a^2 Q_t^2}{1 + a^2 Q_t^2}\right)^2 \left(\frac{1}{1 + {}^{Q_t^2}/_d}\right)^2 Z^2, \\ W_2^{\text{inel}}(Q_t^2) &= \left(\frac{a'^2 Q_t^2}{1 + a'^2 Q_t^2}\right)^2 \left(\frac{1 + {}^{Q_t^2}/_{(4m_p^2)}(\mu_p^2 - 1)}{(1 + {}^{Q_t^2}/_{\Lambda^2})^4}\right)^2 Z, \end{aligned} \tag{2.24}$$

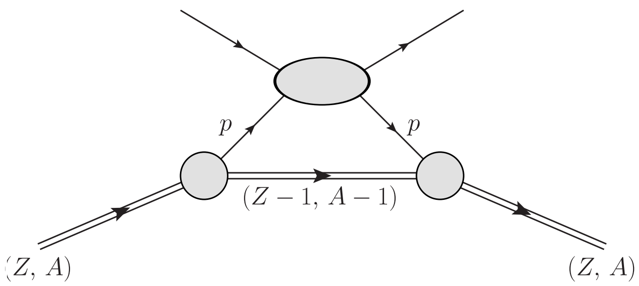

Figure 2.4: Sketch of quasi-elastic scattering: A single proton of the nucleus with atomic number Z and mass number A participates in the scattering reaction, while the remaining $(Z-1)$ protons and $(A-Z)$ neutrons of the nucleus are spectators. In quasi-elastic scattering the nucleus does not break up in the final state.

where $a = 111\,Z^{-1/3}/m$, $a' = 773\,Z^{-2/3}/m$, $d = 0.164\,\mathrm{GeV}^2\,A^{-2/3}$, $\mu_p = 2.793$, and $\Lambda = 0.843\,\mathrm{GeV}$.

As discussed in Refs. [140, 177], the structure function W_1 does not contribute for small momentum transfer Q_t^2. The first term of W_2 is the elastic atomic form factor which was first given in Ref. [176]. The effect of electron screening is parametrized by this expression. The elastic nuclear form factor is presented by the second which accounts for the finite size of the spatial charge of the nucleus [177]. Of course, the dipole parametrization in Eq. (2.24) can be replaced by the more accurate parametrization of Helm [184] applied in Eq. (2.4). Analogously, the first term of the inelastic structure function W_2^{inel} is the inelastic atomic form factor [177]. The second part accounts for the contribution from quasi-elastic scattering off a single proton bound in the nucleus [140]. It is argued in Ref. [177]—based on experimental data [185]—that the quasi-elastic contribution dominates and hardly no other effects are visible. As a consequence, experimental data can be described within an accuracy of around 5% [140, 176, 177]. Note that the cross section obtained using the parametrization of Eq. (2.4) has to be evaluated in the kinematical setting of elastic scattering, since it is assumed that the hadronic final state has an invariant mass M^2.

The different dependencies of the form factors on Z are deduced in Ref. [177]. The inelastic form factor has to converge to Z in the limit of $Q_t^2 \to \infty$, whereas the elastic form factor converges to Z^2 . It follows that the inelastic contribution is suppressed by a factor Z compared to the elastic contribution. For large Z, e.g., for tantalum one has $Z = 73$, the inelastic contribution to the cross section is expected to be around 5%. However, for light nuclear targets the contribution from quasi-elastic scattering may lead to significant effects. A numerical comparison for tantalum is presented in the next section.

2.2 Results for the integrated cross section

2.2.1 Numerical evaluation of the cross section

Only the differential cross sections were determined so far, for which analytical expressions can be found. For the qualitative as well as quantitative study of the phenomenology of the process $e(Z, A) \to e(Z, A)\gamma/\gamma'$ one has to evaluate the cross section within the kinematically allowed range. This corresponds to an integration of the differential cross section over the full phase space, or later on, to an integration with adequately chosen integration limits. For that purpose, the numerical treatment of the cross section will be shortly introduced in this section.

The quantity of interest is the cross section of the process $e(Z,A) \to e(Z,A)\gamma/\gamma'$ expressed as a function of 1 or 2 kinematical variables. Thus, one has to solve the integral over the differential cross section, i.e. for the differential cross sections in Eqs. (2.11) and (2.17) in terms of the recursive coordinates

$$\int dE^L_{k'} \int d\Omega^L_{k'} \int d\Omega^*_{p'} \frac{d\sigma}{dE^L_{k'}\, d\Omega^L_{k'}\, d\Omega^*_{p'}},$$

and expressed by lab frame variables

$$\int dE_{q'} \int d\Omega_{q'} \int d\Omega_{k'} \frac{d\sigma}{dE_{q'}\, d\Omega_{q'}\, d\Omega_{k'}}.$$

Due to Lorentz invariance, the quantity obtained after integration does not depend on the particular choice of the reference frame anymore. It can be related to the count rate observed in an experiment. The result has to yield the same value whichever of the cross sections is evaluated in the corresponding physical limits. Therefore, the differential cross section which allows one to solve the particular problem as conveniently as possible was used. Moreover, a second calculation within the other parametrization was performed as a cross-check. In addition, the calculation of differential cross sections was checked with the numerical results of Ref. [175]. For clarity, in this section the numerical evaluation of the integrated cross section is discussed using the differential cross section of Eq. (2.11) only.

For the numerical calculation, the amplitude

$$\overline{|\mathcal{M}|^2} = -\sum_{s_{k'},s_{p'}} \overline{\sum_{s_k,s_p}} \mathcal{M}^\alpha \mathcal{M}^*_\alpha$$

with $\mathcal{M}^\alpha$ given in Eq. (2.2), has to be calculated for any desired configuration of external momenta. This means that for any space-time point, the necessary matrix multiplications of Eq. (2.2) have to be performed. Such products of Dirac matrices and in particular of their contractions with four-momenta are a large computational effort. To reduce the computation time optimizations and simplifications were applied as described in Appendix C. In addition, one of the final state spin sums can be omitted by means of parity conservation.

The numerical integration was performed in two ways based on Monte Carlo methods:

- use of the VEGAS integration routine [186] and its adaption to graphics processing units (GPUs) [187]
- an event-by-event analysis by use of Sobol random numbers and collection of the results in histograms

These two approaches of course must lead to equal results. Nevertheless, each has its own advantages and disadvantages. By the approach using the VEGAS routine one can calculate only one cross-section distribution at the same time, e.g. the cross section as a function of the energy of the scattered electron $E^L_{e'}$ in the lab frame. An advantage of the VEGAS algorithm is the use of methods of error reducing, such as importance sampling. The integration mesh is dynamically adapted with emphasis on the regions where the uncertainty of the result is large. Furthermore, the time needed for the calculation of the total cross section and the cross section in an arbitrarily small bin are nearly equal. The second method allows one to investigate several observables at the same time. The cross section is calculated from the external momenta and constraints. Afterwards, the results are collected by a binning routine. As an example, the cross section can be calculated as a function of all 5 integration variables at the same time. Correspondingly, one can obtain at least 5 different distributions. In addition, it is possible to find distributions depending on other variables, such as the energy of the scattered proton. A disadvantage of this method is that one always has to calculate the cross section for a large number of random numbers, which is very time-consuming. Hence, this method is not appropriate for the fast calculation of the total cross section.

For the study of the phenomenology of the cross section the large number of available observables is of great help. However, no internal variance reduction mechanism is applied during the calculation leading to larger number of sample points which have to be evaluated. To compensate this quasi-random Sobol numbers were chosen. These are deterministic in the sense that the integration volume is covered much more evenly than in the case of pseudo-random numbers.

2.2.2 Numerical results for the γ' production cross section

In order to design a dedicated experiment for the γ' search as efficiently as possible, one needs to understand the signal cross section as well as the one of the irreducible background. One has to decide between the searches with visible and invisible decays. Visible decays mean that the γ' decays before or within the detector into SM particles, such as lepton-antilepton pairs, which can be detected. This is the strategy of all experiments shown in Fig. 1.19. In the case of invisible decays, the γ' decays into particles which cannot be detected, like the decay into a possible light dark matter candidate, or the decay length of the γ' is larger than the decay volume of the detector.

While in the case of visible decays in which the decay products of the γ' are detected, e.g. $e(Z,A) \to e(Z,A)\gamma'^* \to e(Z,A)l^+l^-$, only the corresponding QED process with an ordinary photon in the intermediate state contributes to the irreducible background, a variety of background contributions for invisible decays have to be taken into account, depending on which particles can be detected. The SM background has to be subtracted completely and must be precisely understood. Therefore, a detector is needed which is able to detect as many particles as possible at the same time to reconstruct the events accurately. Furthermore, radiative corrections have to be performed to a high level of accuracy. This makes a study of invisible decays in such experiments challenging, although not impossible.

For a visible, the cross section for the process $e(Z,A) \to e(Z,A)l^+l^-$ after integrating over the lepton-pair coordinates can be related to the cross section for $e(Z,A) \to e(Z,A)\gamma'$. This is discussed in detail in Appendix B.3. Hence, the results of this section can be used, to understand the dependencies of the γ' production cross section.

Fig. 2.5 shows the γ' production cross section induced from scattering of an electron beam off a fixed proton target for a beam energy $E_0 = 1\,\text{GeV}$. The γ' cross section is evaluated as a function of the γ' lab energy $E_{q'}$ and lab frame polar angle $\theta_{q'}$ in $2\,\text{MeV}$ and $2°$ bins, respectively, for γ' masses $m_{\gamma'} = 200$, 400, $600\,\text{MeV}$. Furthermore, the calculations were performed for $\varepsilon^2 = 1$. From Eq. (2.2) one directly notices that the cross section is proportional to ε^2 and can be easily scaled by this quantity. For completeness, the Bethe–Heitler cross section for the production of a real photon is shown on the upper left panel.

The Bethe–Heitler process is the dominant contribution to the background for an invisible γ' decay besides elastic electron-proton scattering, which can be kinematically separated. The numerical integration of the differential cross section was performed for the full, kinematically allowed phase space.

The Bethe–Heitler cross section dominates, as discussed in Sec. 2.1.3, due to the peaked structures from the electron propagators. It is several orders of magnitude larger than the γ' production cross section, which is suppressed by the finite γ' mass. Note that this is only a crucial issue in the case of invisible decays, where the emitted photon is not detected. For a visible γ' decay, where the l^+l^- pair is detected, a finite mass equal to the invariant mass of the lepton pair is assigned to the virtual photon, leading to a suppression of the background cross section by this factor.

While the Bethe–Heitler cross section is strongly peaked for the emission of a photon in the forward direction and for photons of lower energy, the γ' production cross section shows a different shape. First, due to the finite γ' mass, a smaller region of energy is covered. Furthermore, the cross section is increasing with growing $E_{q'}$ and decreasing $\theta_{q'}$. It has its maximum for $E_{q'} \simeq E_0$ and $\theta_{q'} \simeq 0°$.

The cross section shape as a function of the γ' energy as well as the polar angle of the scattered electron shows a strong dependence on the γ' mass. The γ' is emitted to wider angles if $m_{\gamma'}$ is small compared to the beam energy. Furthermore, if $m_{\gamma'}$ is not much smaller than the beam energy, the cross section is not large for $E_{\gamma'} = E_0$. Instead, the γ' cross section with $m_{\gamma'} = 600\,\mathrm{MeV}$ is approximately zero for $E_{\gamma'} \gtrsim 950\,\mathrm{MeV}$.

It becomes clear from Fig. 2.6 that the cross section peaks for forward scattering of the electron if $m_{\gamma'}$ is small compared to the beam energy (upper left panel). The cross section shows a tail similar to the radiative tail known from the Bethe–Heitler cross section. On the upper right panel of Fig. 2.6 it is illustrated that for $m_{\gamma'} = 600\,\mathrm{MeV}$, which is comparable with the beam energy $E_0 = 1\,\mathrm{GeV}$, the cross section is largest around $E^L_{e'} = 100\,\mathrm{MeV}$. One also clearly sees that $E^L_{e'} \lesssim 200\,\mathrm{MeV}$ is preferred. In addition, the electron is scattered to wider angles, if the $m_{\gamma'}$ is comparable with the beam energy (lower panels), which explains the limits of the $\theta_{q'}$ shape.

This is an important feature which has to be taken care of, when experiments are designed. At MAMI, a beam with an energy around 1 GeV is available, while at JLAB beam energies of $6 - 12\,\mathrm{GeV}$ are provided. The observed shapes can be understood from the discussion of the phenomenology of the cross section in Sec. 2.1.3. For $E_{q'} \gg m_{\gamma'}$ the effect of the finite mass in the kinematics is suppressed, since then $E_{q'} \simeq |\vec{q}\,'|$. Therefore, the kinematical behavior equals that of the Bethe–Heitler cross section, which can be seen from the evolution of the different shapes of the distributions in Fig. 2.5 from $m_V = 0\,\mathrm{MeV}$ to $m_V = 600\,\mathrm{MeV}$. Nevertheless, still the Bethe–Heitler peaks are absent, as the propagators responsible for these peaks are now $1/m^2_{\gamma'}$.

The distinct shapes of the cross section presented in Fig. 2.7 underline the discussed features. In Fig. 2.7, similar to Figs. 2.5 and 2.6, the integrated production cross sections $\Delta\sigma$ for $E_0 = 5\,\mathrm{GeV}$ and a γ' with $m_{\gamma'} = 200\,\mathrm{MeV}$ ($m_{\gamma'} = 600\,\mathrm{MeV}$) are shown on the left (right) panel as a function of $E_{q'}$ and $\theta_{q'}$ (upper panels), $E^L_{e'}$ within 10 MeV bins (central), and $\theta^L_{e'}$ within 1° bins (lower) in the lab frame. Again, the calculations were performed with $\varepsilon^2 = 1$. For the larger beam energy, which corresponds to that available at JLAB, the shapes of the γ' distributions are getting more similar to those of the Bethe–Heitler cross section.

In addition, Fig. 2.8 illustrates the ratio of the cross sections with elastic plus quasi elastic hadron interaction and the purely elastic contribution. The distributions where calculated

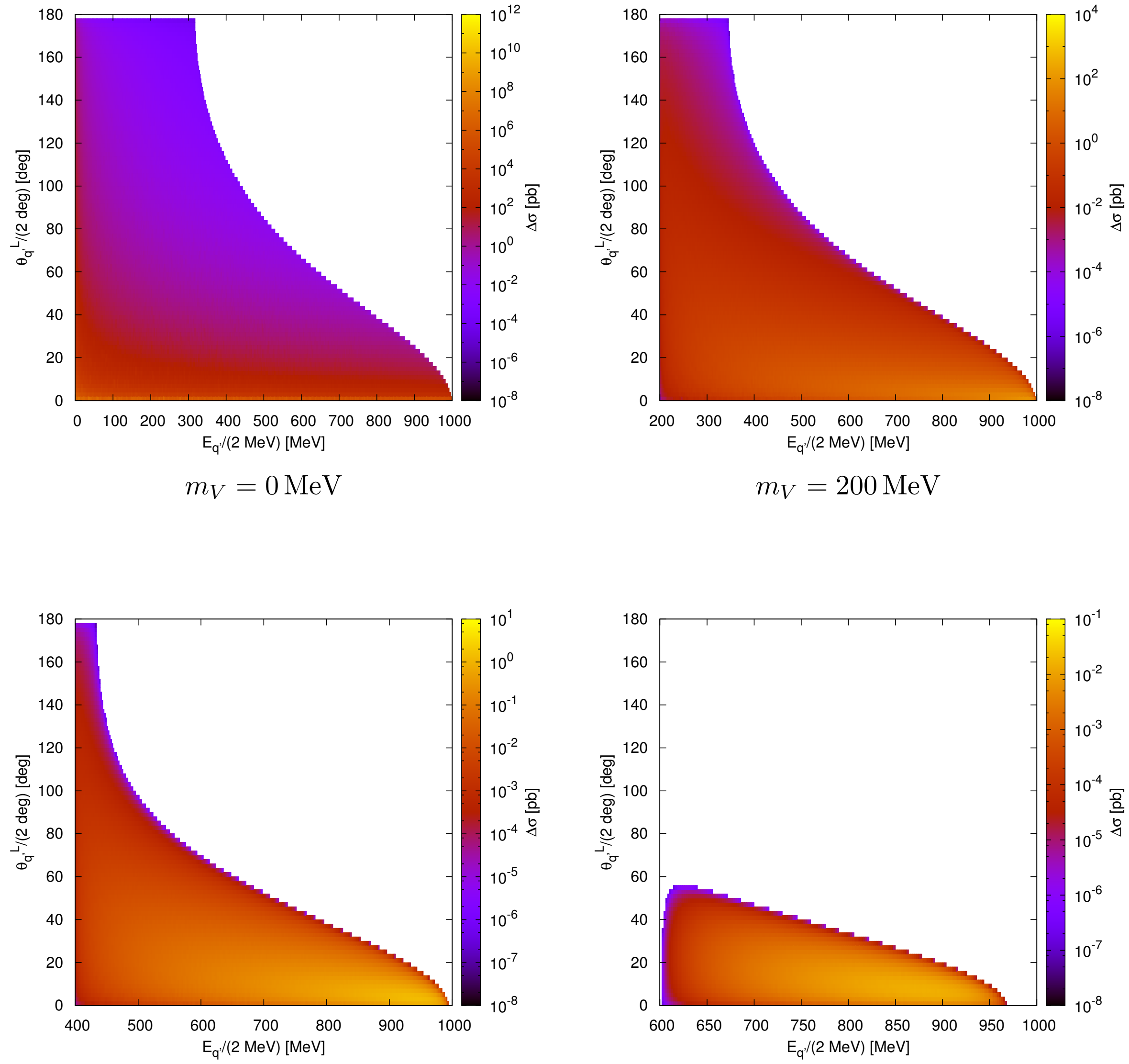

$m_V = 0\,\mathrm{MeV}$ $m_V = 200\,\mathrm{MeV}$

$m_V = 400\,\mathrm{MeV}$ $m_V = 600\,\mathrm{MeV}$

Figure 2.5: Integrated production cross section $\Delta\sigma$ with a beam energy $E_0 = 1\,\mathrm{GeV}$ for a SM photon (upper left panel) and for the γ' with $m_{\gamma'} = 200, 400, 600\,\mathrm{MeV}$, respectively, as a function of the γ' energy $E_{q'}$ and polar angle $\theta_{q'}$ in the Lab frame with $\varepsilon^2 = 1$. For clarity, cross sections smaller than 10^{-8} pb are not shown.

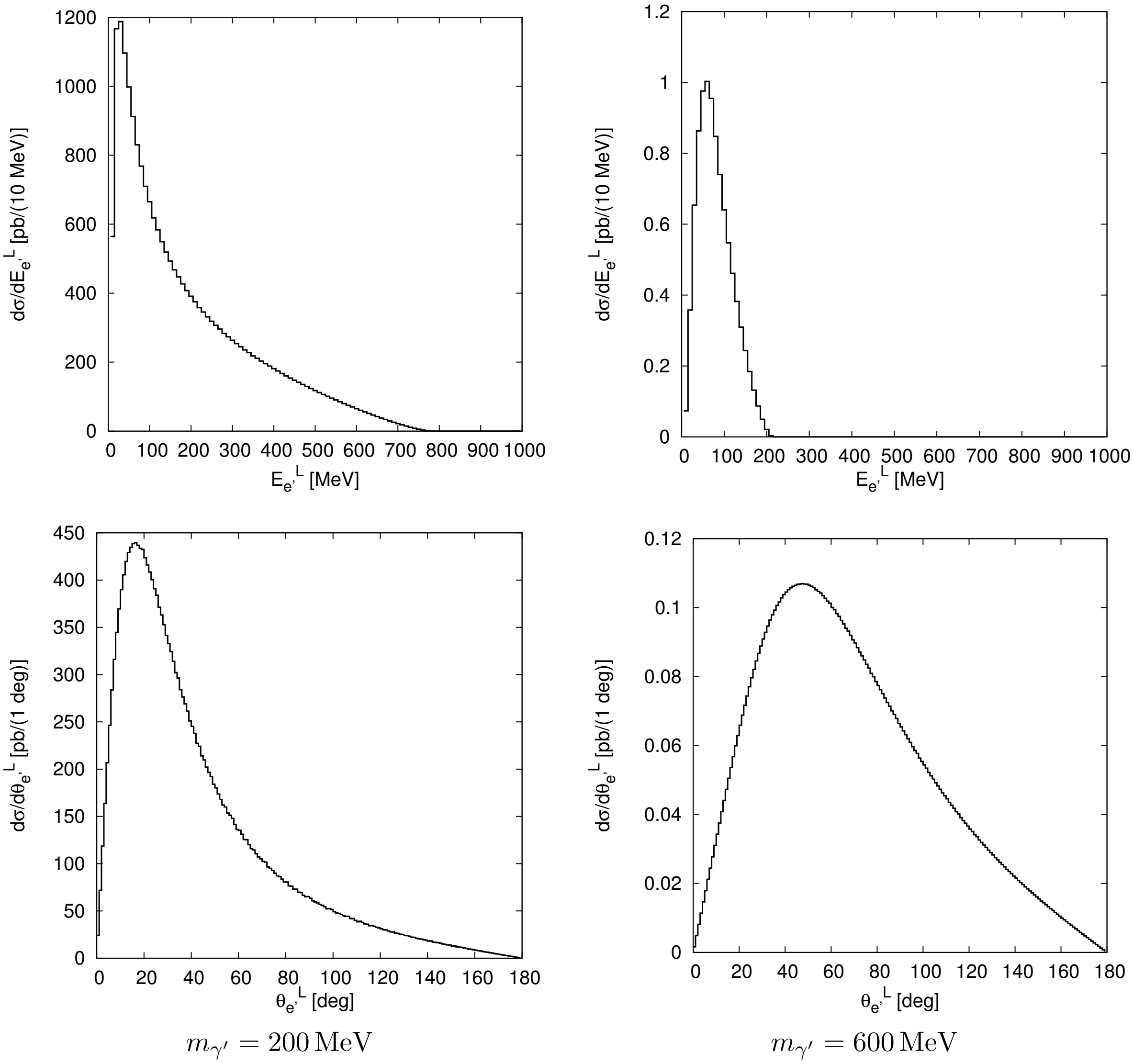

Figure 2.6: γ' production cross section as a function of the energy of the scattered electron $E^L_{e'}$ within $10\,\mathrm{MeV}$ bins (upper panels) and its polar angle $\theta^L_{e'}$ within 1° bins (lower panels) in the lab frame for a beam energy $E_0 = 1\,\mathrm{GeV}$. The left (right) panels correspond to a γ' mass of $m_{\gamma'} = 200\,\mathrm{MeV}$ ($600\,\mathrm{MeV}$).

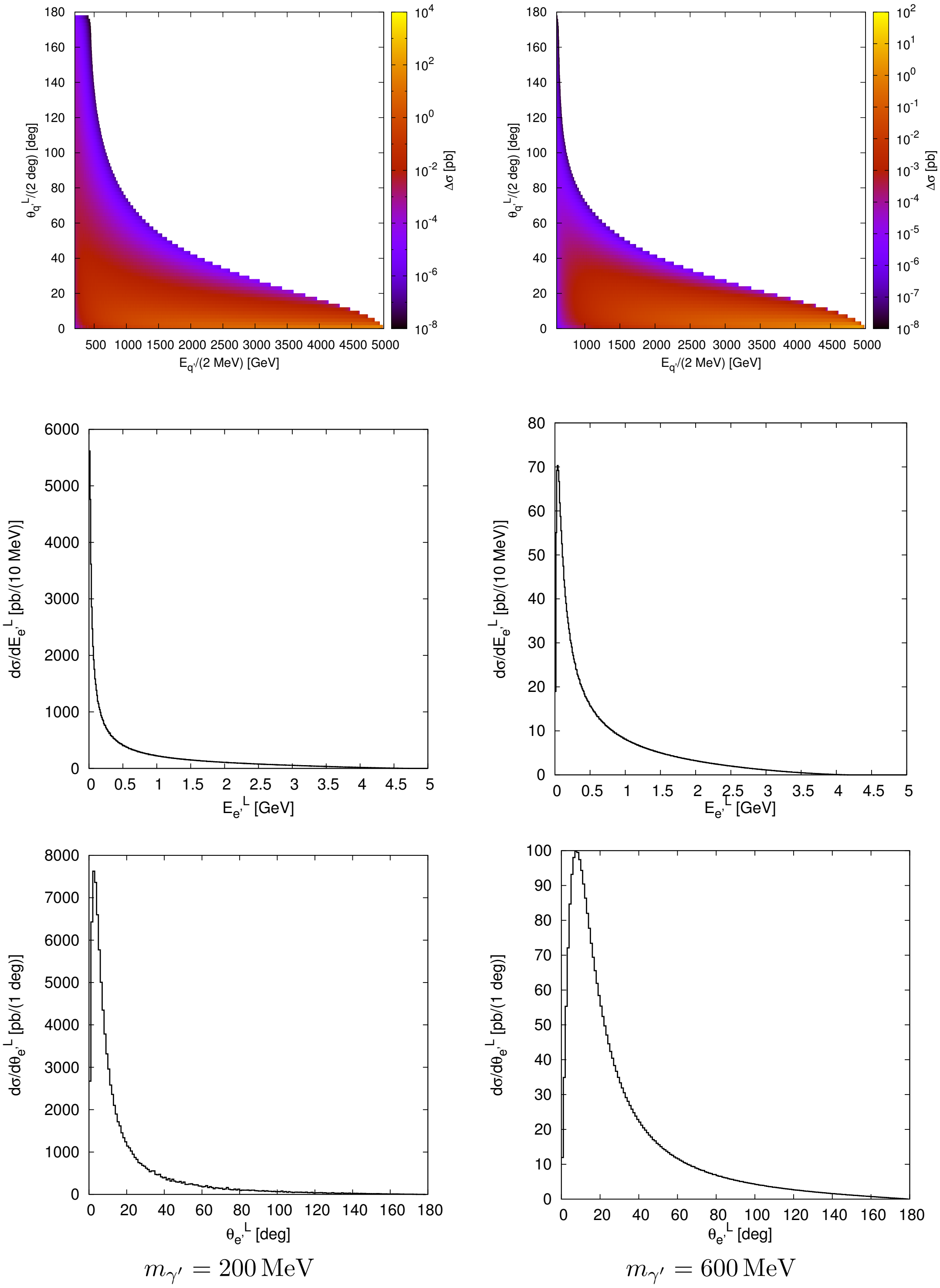

Figure 2.7: Same as in Figs. 2.5 and 2.6, but for a beam energy $E_0 = 5\,\mathrm{GeV}$.

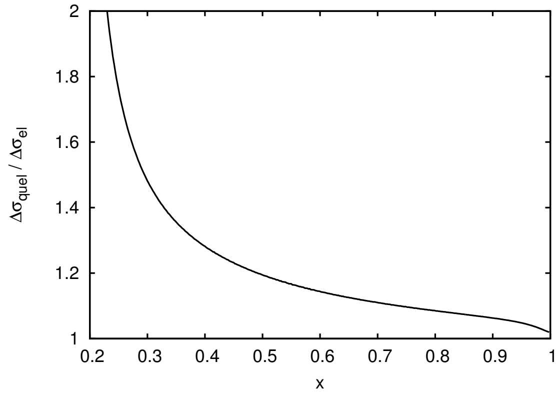

Figure 2.8: Ratio of the inclusive elastic and elastic plus quasi-elastic cross sections off a tantalum target for a typical beam energy $E_0 = 1\,\mathrm{GeV}$, $m_{\gamma'} = 200\,\mathrm{MeV}$ and $\cos\theta_{\gamma'} \leq 0.5$ as a function of the momentum transfer $x = {}^{E_{\gamma'}}\!/_{E_0}$.

for scattering off a tantalum target with a typical beam energy $E_0 = 1\,\mathrm{GeV}$ and $\cos\theta_{\gamma'} \leq 0.5$ as a function of the momentum transfer to the hidden photon $x = {}^{E_{\gamma'}}\!/_{E_0}$.

The influence of the considered inelastic effects is below 5% in the region of interest for γ' production with $x \gtrsim 0.9$. This justifies to focus on coherent scattering off the nucleus only. The influence of the quasi-elastic contribution to the cross section was checked numerically for various beam energies of interest. In particular, the shape of the cross sections is not altered. Thus, inelastic effects do not affect the qualitative discussion of the signal kinematics. It was always found that the quasi-elastic effects are only a small correction below 5% which is in agreement with the findings of Ref. [140].

2.3 Comparison with Weizsäcker–Williams approximation

In Ref. [140] Bjorken et al. discuss the approximation of the γ' production cross section by the so-called Weizsäcker–Williams (WW) approximation. Several proposals for new experiments [188–190] as well as analyses of existing data [140, 144] make use of this approximation. Therefore, the applicability of the WW approximation and in particular its limitations are discussed in this section.

2.3.1 The cross section of hidden photon bremsstrahlung in the Weizsäcker–Williams approximation

Already in 1924 Fermi demonstrated [191] that a rapidly moving electron and a pulse of radiation show an analogous behavior in their influences on an atom. Weizsäcker [192] and Williams [193] independently derived a relation between an incident particle and a corresponding beam of photons, which is in the literature referred to as pseudo-photon beam. The approximation of the effect of such a current by a pseudo-photon beam is known as WW approximation. Furthermore, an approximate treatment of the leptonic part of the reaction and the inclusion of effects from inelastic contributions or thick targets were derived in Ref. [194], which is known as generalized or improved WW approximation.

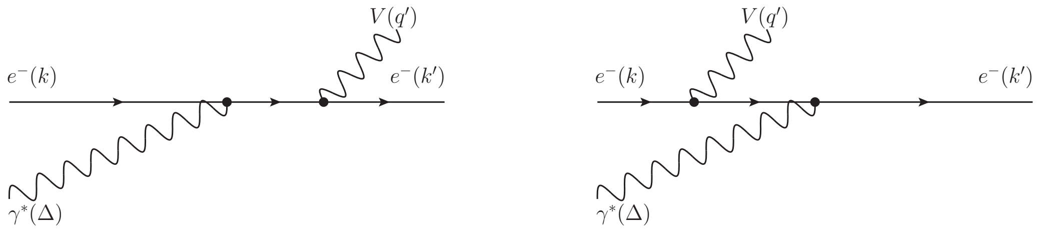

Figure 2.9: Feynman diagrams of Fig. 2.1 in the picture of the WW approximation.

As discussed in Refs. [177, 194, 195], the cross section for lepton-pair production from the interaction of a photon with an atomic nucleus and, correspondingly, bremsstrahlung off a lepton beam as crossed process can be written within the 1γ-exchange approximation as

$$d\sigma \propto L^{\mu\nu} W_{\mu\nu},$$

with $L^{\mu\nu}$ and $W_{\mu\nu}$ denoting the leptonic and hadronic tensors of the interaction, respectively. While the leptonic tensor is exactly known from QED, the hadronic tensor has to be parametrized by two structure functions $W_1(t)$ and $W_2(t)$. They are functions depending on the squared momentum transfer $t = Q_t^2$ carried by the virtual photon connected to the nucleus. It is shown in Ref. [194] that only the transverse part of the hadronic tensor $W_{\mu\nu} \propto g_{\mu\nu}$ contributes. This allows one to rewrite the cross section as a function of a scalar, generalized form factor parameterizing the effective photon flux

$$\chi = \int_{t_{\text{min}}}^{t_{\text{max}}} dt \, \frac{t - t_{\text{min}}}{t^2} G\left(W_1(t),\, W_2(t)\right). \tag{2.25}$$

The form factor G depends on the atomic structure parametrized by $W_1(t)$ and $W_2(t)$. The cross section for axion bremsstrahlung has been derived within the framework of the generalized WW approximation in Ref. [195], which is closely related to the emission of a vector boson [140]. It is discussed that the cross section for

$$eZ \to eaX,$$

where Z and a denote the atomic target and the axion, respectively, and X is an arbitrary final state, can be related to the cross section of the interaction of a pseudo-photon beam with the leptonic part of the reaction given by

$$e\gamma \to ea.$$

Bjorken et al. [140] adopt this method to estimate the cross section for γ' bremsstrahlung emission induced from the interaction of an electron beam with an atomic target. The authors find an approximate expression for the cross section of the process $eZ \to e\gamma' X$ (see Feynman diagrams of Fig. 2.1) within the framework of the generalized WW approximation:

$$d\sigma(eZ \to e\gamma' X)_{\text{WW}} \propto d\sigma(e\gamma \to e\gamma') \times \frac{\alpha}{\pi}\,\chi, \tag{2.26}$$

where $d\sigma(e\gamma \to e\gamma')$ is the cross section of the process depicted by the Feynman diagrams of Fig. 2.9. The factor ${}^{\alpha}/_{\pi}\,\chi$, accounts for the effective pseudo-photon flux for an atomic nucleus of atomic number Z and particle number A with

$$\chi = \chi\left(E_0,\, m_{\gamma'},\, Z,\, A\right) = \int_{t_{\min}}^{t_{\max}} dt \frac{t - t_{\min}}{t^2}\, G_2(t),$$

where $t = Q_t^2 = -(p' - p)^2$ is the negative of the squared momentum transfer, $t_{\min} = ({}^{m_{\gamma'}^2}/_{2E_0})^2$, and $t_{\max} = m_{\gamma'}^2$. The form factor $G_2(t)$ is parametrized by

$$G_2(t) = W_2^{\text{el}}(t) + W_2^{\text{inel}}(t)$$

with $W_2^{\text{el}}(t)$ and $W_2^{\text{inel}}(t)$ as given in Eq. (2.24) corresponding to Ref. [140].

In addition to Ref. [140], the application of the WW approximation of the γ' production cross section was investigated by Andreas et al. in Ref. [144] in order to extract limits for the γ' parameter space from past beam-dump experiments. In these publications the differential cross section for γ' production is given as

$$\frac{d\sigma}{dx\, d\cos\theta_{\gamma'}} = 8\alpha^3\varepsilon^2 E_0^2 x\chi\sqrt{1 - \frac{m_{\gamma'}^2}{E_0^2}}\left(\frac{1 - x + {}^{x^2}/_2}{U^2} + \frac{(1-x)^2\, m_{\gamma'}^2}{U^4} - \frac{(1-x)\, x m_{\gamma'}^2}{U^3}\right). \tag{2.27}$$

$x = {}^{E_{\gamma'}}/_{E_0}$ is the fraction of the energies carried by the γ' and the incident electron and $\theta_{\gamma'}$ is the polar emission angle of the γ' in the lab frame with respect to the z-axis corresponding to the beam axis. The function

$$U = U\left(x,\, E_0,\, m_{\gamma'},\, \theta_{\gamma'}\right) = E_0^2 x\theta_{\gamma'}^2 + m_{\gamma'}^2\frac{1-x}{x} + m^2 x \tag{2.28}$$

parametrizes the virtuality of the electron in the intermediate state in the Feynman diagrams of Figs. 2.1 and 2.9. This approximate expression for the cross section is valid for large beam energies compared to the mass of the γ':

$$m \ll m_{\gamma'} \ll E_0, \tag{2.29}$$

and small γ' emission angles

$$x\theta_{\gamma'}^2 \ll 1. \tag{2.30}$$

Moreover, terms of the order m^2 in the numerator and the t-dependence of the leptonic part of the cross section $d\sigma(e\gamma \to e\gamma')$ were dropped. Neglecting terms of the order m^2 leads to a very small error of less than 0.1%. However, the drop of the dependence on $t = Q_t^2$ leads to a significant overestimate of the cross section for $x \cong 1$. Effects due to the finite momentum transfer Q_t^2 become important for $x \cong 1$. Q_t^2 serves as a cut-off besides the finite mass of the electron. Hence, the cross section within the WW approximation contains a divergence corresponding to the exchange of photons with zero energy which is not present for the calculation within the leading order of QED.

As a further approximation, only leading terms in ${}^{m_{\gamma'}^2}/_{(x^2 E_0^2)}$ were kept. The corresponding error is below 0.1% in the range of interest with $x \geq 0.8$, provided that the condition (2.29) is fulfilled. In addition, the approximation $\cos\theta_{\gamma'} \simeq 1 - {}^{\theta_{\gamma'}^2}/_2 + \mathcal{O}(\theta_{\gamma'}^4)$ is applied. The error entering from this approximation is below 0.5% since the cross section is evaluated for $\theta_{\gamma'} < 0.5\,\mathrm{rad}$.

After the integration of Eq. (2.27) over a small range of the angle $\theta_{\gamma'} < 0.5\,\mathrm{rad}$, in Ref. [144]

$$\frac{d\sigma}{dx} = 4\alpha^3\varepsilon^2\chi\sqrt{1-\frac{m_{\gamma'}^2}{E_0^2}}\,\frac{1-x+{}^{x^2}\!/_3}{m_{\gamma'}^2\,{}^{(1-x)}\!/_x + m^2 x} \tag{2.31}$$

was found.[3]

2.3.2 Comparison of numerical results

In this section the approximate results for the cross section of Eqs. (2.27) and (2.31) within the framework of the WW approximation are compared to the exact calculation of the cross section derived in Sec. 2.1. Although a comparison on the level of the differential cross sections is possible, the acceptance integrated cross sections are considered, since these are the quantities which will be observed in experiments. This allows for taking all of the possible phase space into account. Thus, one avoids influences from kinematical cuts on the result. Furthermore, the integrated cross section can be directly related to experimental data.

For this purpose, the differential cross sections of Eqs. (2.27) and (2.31) are integrated according to

$$\begin{aligned}\Delta\sigma_1(x_0,\,\delta x) &= \int_{x_0}^{x_0+\delta x} dx\frac{d\sigma}{dx},\\ \Delta\sigma_2(x_0,\,\delta x) &= \int_{x_0}^{x_0+\delta x} dx\int_{0\,\mathrm{rad}}^{0.5\,\mathrm{rad}} d\theta_{\gamma'}\sin\theta_{\gamma'}\frac{d\sigma}{dx\,d\theta_{\gamma'}},\end{aligned} \tag{2.32}$$

where the integration over x is performed over an arbitrary small bin with bin width δx. The presented results were calculated with $\delta x = 0.002$. The integrated cross section can simply be related to the differential cross section ${}^{d\sigma}\!/_{dx}$ by

$$\Delta\sigma(x_0,\,\delta x) = \frac{d\sigma}{dx}(x_o)\times\delta x,$$

for most of the x-range (except for $x > 0.99$). It was checked numerically, that the results qualitatively do not depend on the particular choice of δx. Another choice of δx only corresponds to a resummation of the bins with the initial value of δx. The calculations where performed assuming tantalum as nuclear target, which was used in the experiments performed so far [152, 153], i.e., $Z = 73$, $A = 181$, $M \cong 168\,\mathrm{GeV}$. Furthermore, $\theta_{\gamma'} \leq 0.5\,\mathrm{rad}$ was chosen in agreement with Refs. [140, 144]. This corresponds to the γ' forward emission kinematics in which the WW approximation is expected to be valid.

For simplicity, the atomic form factors of Ref. [140] entering in the parametrization in Eq. (2.24) were neglected. The corresponding contribution to the cross section is below 1% and the shape is not altered. In order to compare the results obtained within the WW approximation and the ones of this work, Eq. (2.23) with the parametrization of Eq. (2.24) has been considered. Moreover, the calculation of the cross section by Eq. (2.17) was used

[3] There has been a controversy between Ref. [140] and Ref. [144] about additional factor of 2 in Eq. (2.31) in Ref. [140]. The calculations of this work independently proof Ref. [144] and show that the factor of 2 was placed mistakenly.

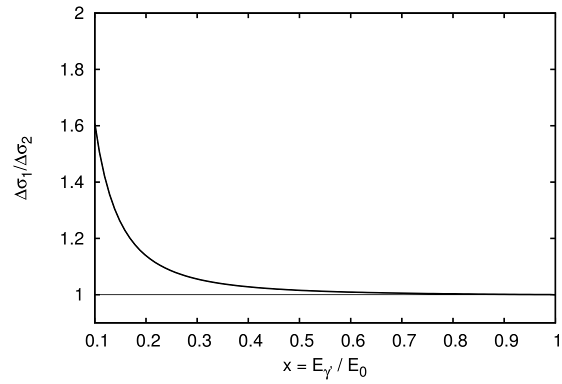

Figure 2.10: Comparison of the cross sections $\Delta\sigma_1$ and $\Delta\sigma_2$ of Eq. (2.32) obtained within the WW approximation for $E_0 = 5\,\mathrm{GeV}$ and $m_{\gamma'} = 200\,\mathrm{MeV}$.

as cross check. In the approximation, in which the nucleus is considered as a scalar particle and the inelastic contribution consists only of the quasi-elastic term, both cross sections lead to the same expressions. Within this approach the square of the single elastic form factor entering Eq. (2.17) is replaced by a linear combination of the elastic and quasi-elastic form factors given in Ref. [140] by

$$Z^2\,F^2(t) \to \underbrace{\left(\frac{1}{1+\frac{t}{d}}\right)^2 Z^2}_{G_{\mathrm{el}}} + \underbrace{\left(\frac{1+\frac{t}{(4M_N^2)}(\mu_p^2-1)}{\left(1+\frac{t^2}{\Lambda^2}\right)^4}\right)^2 Z}_{G_{\mathrm{inel}}}.$$

These form factors were already introduced in Eq. (2.24). As a consequence, for the parametrization of the pseudo-photon flux χ one applies

$$\chi = \int_{t_{\min}}^{t_{\max}} dt\,\frac{t-t_{\min}}{t^2}\,\left(G_{\mathrm{el}}(t) + G_{\mathrm{inel}}(t)\right).$$

Both cross sections of Eq. (2.32) were calculated in order to compare them with the exact calculation. In the graphical illustration of the obtained results only $\Delta\sigma_2$ is shown. The results using $\Delta\sigma_1$ and $\Delta\sigma_2$ agree within a few percent over a wide range of x, which is presented in Fig. 2.10. Only in the very low x region near the γ' production threshold, the results differ significantly. This region is not of interest for the following studies. Hence, this discrepancy can be ignored.

The comparison of the calculation in the leading order of perturbation theory and the result within the WW approximation is in the following done for a light hidden photon with $m_{\gamma'} = 5\,\mathrm{MeV}$ and for $m_{\gamma'} = 200\,\mathrm{MeV}$. This is in the typical range of probed masses at MAMI and JLAB [152, 153, 189]. The calculations for $m_{\gamma'} = 5\,\mathrm{MeV}$ were performed for two different beam energies which were chosen as $E_0 = 100\,\mathrm{MeV}$ and $E_0 = 1\,\mathrm{GeV}$. The results are presented in Fig. 2.11. The solid curve depicts the findings for the exact calculation while the result within the WW approximation is given by the dashed curve. It turns out from the curves in the left panel of Fig. 2.11 that for $m_{\gamma'} = 5\,\mathrm{MeV}$ and $E_0 = 100\,\mathrm{MeV}$ both

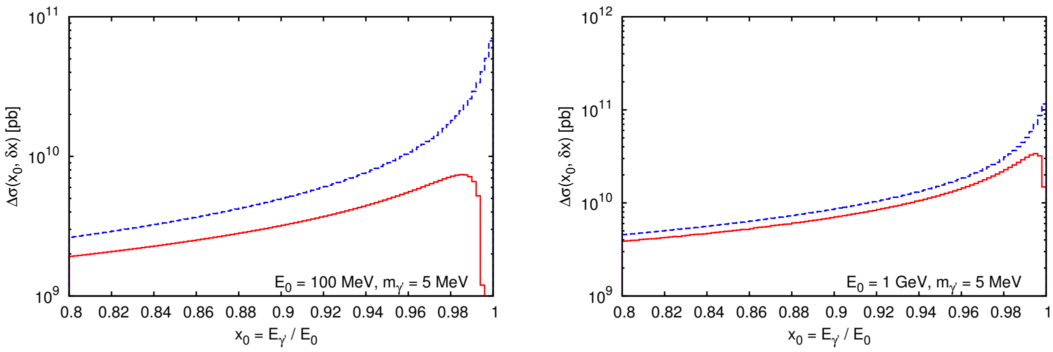

Figure 2.11: Comparison of exact calculation (solid curve) and WW approximation (dashed) for $m_{\gamma'} = 5\,\mathrm{MeV}$. The left (right) panel shows the calculation for a beam energy of $E_0 = 100\,\mathrm{MeV}$ ($1\,\mathrm{GeV}$). For simplicity $\varepsilon^2 = 1$ is used.

calculations differ significantly. While within the WW approximation the cross section is strongly increasing for $x \simeq 1$, the cross section calculated in the leading order of perturbation theory in this work sharply drops. Furthermore, the normalizations of the cross sections differ by a factor of around 2. However, for $E_0 = 1\,\mathrm{GeV}$ both calculations agree within a few percent except for the region around $x \to 1$, which is shown in the right panel of Fig. 2.11.

Figure 2.12 shows this comparison for $m_{\gamma'} = 200\,\mathrm{MeV}$. Both methods are again in agreement for a beam energy which is much larger than $m_{\gamma'}$. For experiments performed at JLAB, beam energies larger than $2\,\mathrm{GeV}$ are possible, whereas at MAMI the beam energy is below $1.6\,\mathrm{GeV}$. Therefore, the settings with $E_0 = 1\,\mathrm{GeV}$ and $E_0 = 2\,\mathrm{GeV}$ correspond to experiments which can be performed at MAMI, whereas $E_0 = 2\,\mathrm{GeV}$ to $E_0 = 10\,\mathrm{GeV}$ refer to possible experiments at JLAB.

For beam energies of $E_0 \geq 5\,\mathrm{GeV}$ or larger the calculation of this work as well as the WW approximation lead to cross sections which agree for x close to 1. However, for a lower beam energy, such as $E_0 = 1\,\mathrm{GeV}$ and $E_0 = 2\,\mathrm{GeV}$, which are presented in the upper panel of Fig. 2.12, the shape of the cross section as well as its normalization differ significantly. Again, while the cross section within the WW approximation is peaking for $x \simeq 1$, the exact calculation shows a sharp fall-off.

Motivated by the overestimate of the cross section within the WW approximation also for large beam energies, the origin of the deviation was investigated in this work. For that purpose the formulas given in Ref. [140] were re-evaluated. It was found that the assumption that the minimal momentum transfer does not depend on x and the emission angle $\theta_{\gamma'}$ [140, 144, 188], leads to the observed overestimate of the cross section.

Therefore, Eq. (A6) of Ref. [140] was used as lower limit of the t-integration given by

$$t_{\min} = t_{\min}\left(x, \cos\theta_{\gamma'}\right) = \left(\frac{U}{2E_0(1-x)}\right)^2 .$$

The dependence on x and $\theta_{\gamma'}$ causes that the t-integral cannot be evaluated independently from the remaining integration over x- and $\cos\theta_{\gamma'}$. Performing this more complicated numerical integration, one is able to find an agreement within a few percent between the WW approximation and the calculation of this work, which is presented in Fig. 2.13. Obviously,

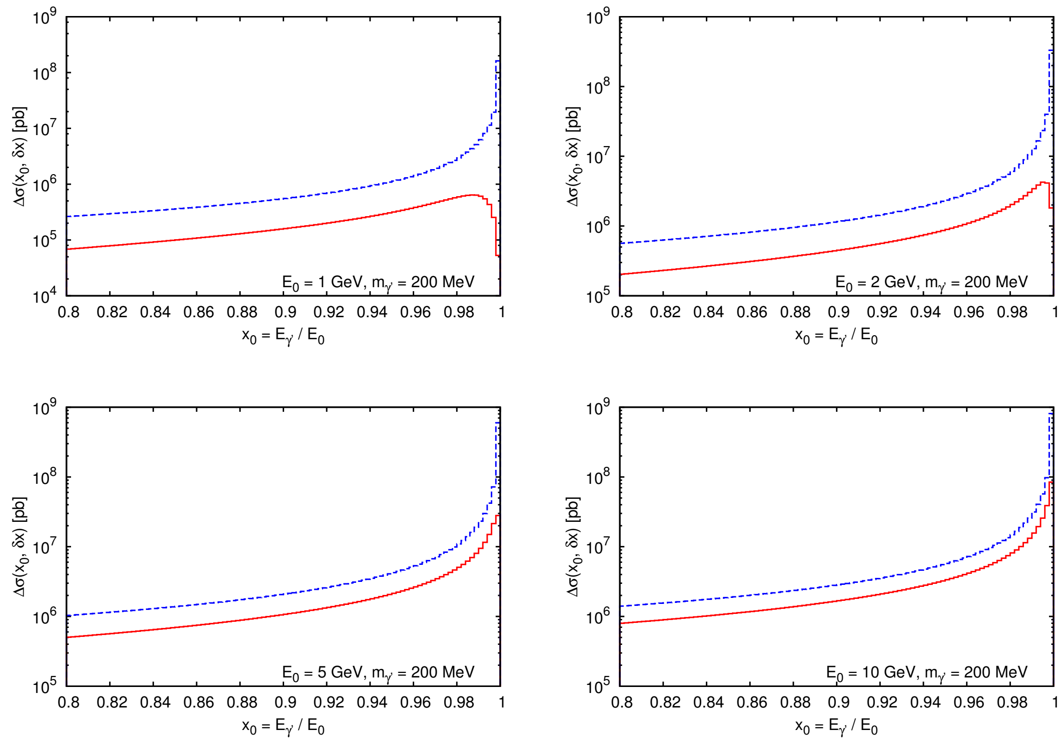

Figure 2.12: Comparison of exact calculation (solid curve) and WW approximation (dashed) for $m_{\gamma'} = 200\,\mathrm{MeV}$. The calculation was performed for beam energies from $E_0 = 1\,\mathrm{GeV}$ (upper left panel) to $E_0 = 10\,\mathrm{GeV}$ (lower right panel). As before, for simplicity $\varepsilon^2 = 1$ is used.

for $E_0 = 10\,\mathrm{GeV}$ both calculations are in very good agreement over the full considered x-range, which can be seen from the right panel. However, for $E_0 = 1\,\mathrm{GeV}$ one still sees a large deviation for $x \to 1$. This effect can be explained by the neglect of the finite momentum transfer to the hadronic state within the WW approximation.

In Fig. 2.14 the ratio of the cross sections calculated with the method of this work and within the WW approximation is plotted as a function of the beam energy at fixed $x = E_{\gamma'}/E_0 = 0.9$. Figure 2.14 illustrates that the deviation between the two calculations which arises from neglecting the x- and $\cos\theta_{\gamma'}$ dependence of the t-integration in case of the WW calculation. It converges to an overestimate of the cross section by the WW method of around 30% in the region, where one expects both calculations to be in good agreement. Taking into account that the lower limit of the t-integral depends on x- and $\theta_{\gamma'}$, both calculations perfectly agree for large beam energies.

This result is of high importance. In optimzing the kind of experiments proposed in Ref. [140] one exploits the fact that nearly all of the beam energy is transferred to the γ^prime. It was discussed in Sec. 2.2.2 that the calculations of this work also show the rise of the cross section for an increasing momentum transfer onto the γ'. However, it was shown in this work that the cross section rapidly drops for beam energies which are not sufficiently larger than the hidden photon mass $m_{\gamma'}$. Therefore, one cannot use the WW approximation for the design of γ'-search experiments in general. Nevertheless, the WW approximation can

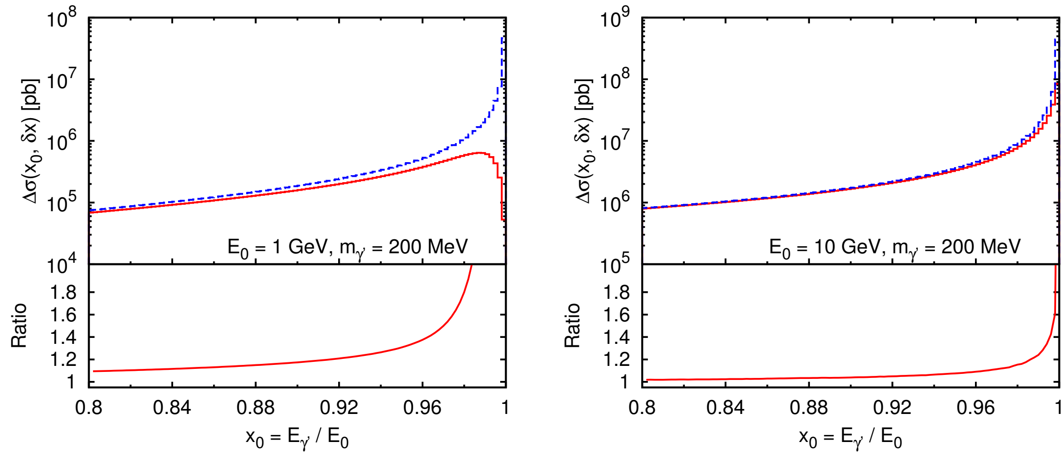

Figure 2.13: Comparison of the calculation in the leading order of perturbation theory (solid curve) and WW approximation, where the dependence of the t-integration on x- and $\cos\theta_{\gamma'}$ is kept (dashed) for $m_{\gamma'} = 200\,\mathrm{MeV}$ and $E_0 = 1\,\mathrm{GeV}$ ($E_0 = 10\,\mathrm{GeV}$) in the left (right) panel. As before, for simplicity $\varepsilon^2 = 1$ is used.

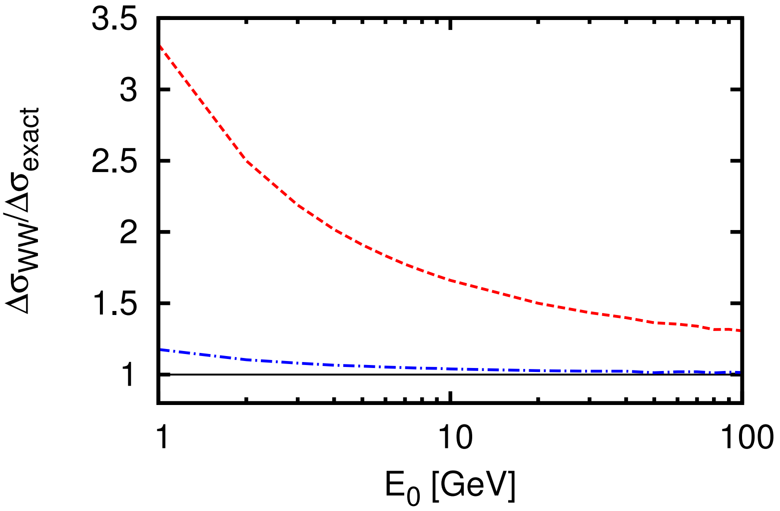

Figure 2.14: Ratio of the cross section obtained within the WW approximation and in the calculation of this work at $x = E_{\gamma'}/E_0 = 0.9$. The dashed (dashed-dotted) curve shows the result obtained without (with) x- and angular dependence of the minimal momentum transfer $t_{\min}$.

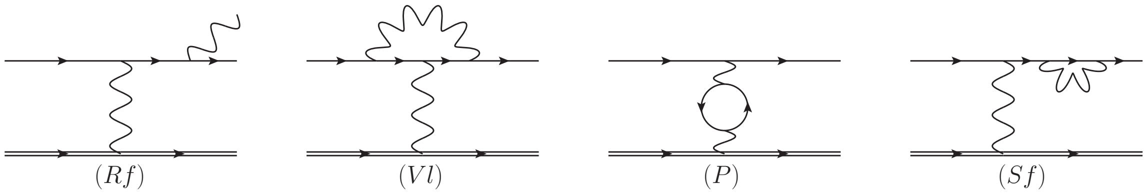

Figure 2.15: Selected diagrams contributing to the radiative corrections for elastic lepton hadron scattering.

be applied in the kinematical range of most experiments at JLAB.

The exclusion limits obtained in beam-dump experiments [140,144] depend on the γ' production cross section to estimate the number of events. The calculations presented in this section show that the estimate of the γ' production cross section within the WW approximation as done in Refs. [140,144] is feasible for this purpose. These beam-dump experiments firstly analyzed with respect to γ' exclusion limits in Ref. [140] were operated at large beam energies with $E_0 \geq 9\,\text{GeV}$, for which the WW approximation is valid over a wide mass range of the γ'. However, the incident beams of the KEK [156] and Orsay [160] experiments, which were additionally analyzed in Ref. [144], have a much lower beam energy of only $E_0 = 2.5\,\text{GeV}$ and $E_0 = 1.6\,\text{GeV}$. As discussed above, the validity of the WW approximation in this energy range must be considered carefully. The probed range of the hidden photon mass $m_{\gamma'}$ is well below 10 MeV in these experiments. Therefore, the WW approximation can be applied to estimate the γ' production cross section. It can be seen from the right panel of Fig. 2.11 that both calculations are in good agreement over a wide range of x. Furthermore, the γ' cross section is slightly underestimated by the WW approximation. This can be interpreted as treating the limit as a more conservative one.

2.4 Radiative corrections

Up to this stage all cross sections were calculated in the leading order of perturbation theory. However, these cross sections cannot be measured directly in experiments. The experimentally accessible cross sections always contain radiative corrections from higher orders of the perturbative expansion. One can relate the leading-order cross section $d\sigma_0$ with the observed one $d\sigma_{\text{exp}}$ by

$$d\sigma_{\text{exp}} = d\sigma_0 \times (1 + \delta_1), \tag{2.33}$$

where the leading-order radiative corrections are contained in δ_1.

2.4.1 Radiative corrections to elastic electron-proton scattering

In this section the leptonic leading-order corrections to elastic electron-proton (ep) scattering are discussed, whereas the corrections from the proton side are not discussed. In Fig. 2.15 selected Feynman diagrams contributing to the radiative corrections for elastic ep-scattering are shown. In general, these corrections can be grouped into real corrections where a (soft) photon is emitted (diagram Rf) and virtual corrections. The virtual corrections account for the exchange of virtual particles such as virtual photons in the vertex (Vl) and lepton self-energy (Sf) diagrams or virtual lepton-antilepton pairs in the vacuum-polarization (V) diagram. The corrections on the proton side such as emission of a soft photon from the proton are suppressed by the large proton mass compared to the corrections on the electron lines. The proton side corrections are typically at the level of below 10% compared to the electron-side corrections in the kinematics of interest for this work. Thus, they will not be discussed in the following.

The correction illustrated by the Feynman diagram (Rf) in Fig. 2.15 accounts for the emission of very low-energetic soft photons which avoid detection. The corresponding amplitude can be factorized into the amplitude at tree-level and a factor from the soft photon emission. The cross section can be written as

$$d\sigma_R = d\sigma_0 \times (-e^2) \int \frac{d^3\vec{l}}{(2\pi)^3 2l^0} \left(\frac{k'_\mu}{k'\cdot l} - \frac{k_\mu}{k\cdot l}\right)\left(\frac{k'^\mu}{k'\cdot l} - \frac{k^\mu}{k\cdot l}\right), \tag{2.34}$$

where as before the initial- and final-state electrons carry the momenta k and k', respectively, and the four-momentum of the soft photon is l. By performing the l-integration one finds that Eq. (2.34) contains a logarithmic divergence in the soft-photon limit where l^0 tends towards zero. The infrared (IR) divergent integral can be made finite by assigning a finite, unphysical mass μ to the soft photon. One finds for the divergent part in the limit $Q^2 = (k-k')^2 \gg m^2$

$$d\sigma_R \simeq d\sigma_0 \times \frac{\alpha}{\pi}\ln\left(\frac{Q^2}{\mu^2}\right)\ln\left(\frac{Q^2}{m^2}\right) + \mathcal{O}(\alpha^2), \tag{2.35}$$

where m is the electron mass. Nature does not depend on the mass scale μ in the logarithm.

The electron-vertex correction (Vl) for on-shell leptons can be parametrized by

$$\bar{u}(k')\Gamma^\mu u(k) = \bar{u}(k')\left\{\left(1+F(Q^2)\right)\gamma^\mu + G(Q^2) i\sigma^{\mu\nu}\frac{q_\nu}{2m}\right\}u(k), \tag{2.36}$$

where analogously to the $pp\gamma$-vertex the form factors F and G are scalar functions of Q^2. One obtains analytic expressions for the form factors by solving the corresponding loop integral and regularizing the ultraviolet (UV) divergence for $l \to \infty$. At $Q^2 = 0$ the form factor G yields the leading-order correction to the anomalous magnetic moment of a lepton. The cross section accounting for the leading-order vertex correction in the limit $Q^2 \gg m^2$ can be written as

$$d\sigma_{vertex} = d\sigma_0 \times (1 + F(Q^2)).$$

However, the form factor F still contains an IR divergence. The divergent part can be written as

$$F(Q^2 \gg m^2) \simeq -\frac{\alpha}{\pi}\ln\left(\frac{Q^2}{m^2}\right)\ln\left(\frac{Q^2}{\mu^2}\right) + \mathcal{O}(\alpha^2).$$

The measured cross section $d\sigma_{\text{exp}}$ always contains both the virtual and real corrections,

$$d\sigma_{\text{exp}} = d\sigma_R + d\sigma_{virtual}.$$

The divergent part in the limit $Q^2 \gg m^2$ reads $d\sigma_{\text{exp}} = d\sigma_{vertex} + d\sigma_R$. Since detectors can only detect a photon with a minimal energy $E_{l,\text{min}}$ one has to evaluate $d\sigma_R$ at this minimal value. This calculation yields

$$
\begin{aligned}
d\sigma_{\text{exp}} &= d\sigma_0 \times \left\{ 1 - \frac{\alpha}{\pi} \ln\left(\frac{Q^2}{m^2}\right) \ln\left(\frac{Q^2}{\mu^2}\right) + \frac{\alpha}{\pi} \ln\left(\frac{E^2_{l,\min}}{\mu^2}\right) \ln\left(\frac{Q^2}{m^2}\right) + \mathcal{O}(\alpha^2) \right\} \\
&= d\sigma_0 \times \left\{ 1 - \frac{\alpha}{\pi} \ln\left(\frac{Q^2}{m^2}\right) \ln\left(\frac{Q^2}{E^2_{l,\min}}\right) + \mathcal{O}(\alpha^2) \right\} .
\end{aligned}
\tag{2.37}
$$

Obviously, this expression does not depend on the unphysical quantity μ anymore and the IR divergence is canceled.

The Feynman diagram (P) of Fig. 2.15 indicates that the virtual-photon propagator is affected by this contribution. The actual calculation of this term will not be demonstrated here. Qualitatively, the vacuum polarization correction can be understood as screening of the electric charge by virtual e^+e^- pairs. After the regularization of the arising UV divergence and renormalization, the effect of the vacuum polarization can be written as a modification of the electromagnetic coupling constant.

The calculation of the lepton self-energy (diagram Sf) will not be studied here in detail. One can show that this correction does not contribute for on-shell leptons after renormalization. Hence, these diagrams do not lead to a correction for the elastic scattering process.

In this work the leading-order radiative corrections calculated in Ref. [175] are used. The contribution originating from vacuum polarization (P) is found as

$$
\delta_{vac} = \frac{\alpha}{\pi} \left[\left(v^2 - \frac{8}{3} + v \frac{3 - v^2}{2} \ln\left(\frac{v+1}{v-1}\right) \right) \right] ,
\tag{2.38}
$$

where $v^2 = 1 + {}^{4m_l^2}/_{Q^2}$, and in the limit $Q^2 \to \infty$

$$
\delta_{vac} \cong \frac{\alpha}{\pi} \left[-\frac{5}{3} + \ln\left(\frac{Q^2}{m^2}\right) \right] .
\tag{2.39}
$$

The vertex correction (see diagram (Vl)) in the ultrarelativistic limit $Q^2 \gg m^2 \to \infty$ reads

$$
\delta_{vertex} \cong \frac{\alpha}{\pi} \left[\frac{3}{2} \ln\left(\frac{Q^2}{m^2}\right) - 2 - \frac{1}{2} \ln^2\left(\frac{Q^2}{m^2}\right) + \frac{\pi}{6} \right] .
\tag{2.40}
$$

The soft photon correction in the limit $Q^2 \gg m^2$ is found as

$$
\begin{aligned}
\delta_R \cong \frac{\alpha}{\pi} \Bigg[& \ln\left(\frac{(\Delta E_s)^2}{E_0\, E_{e'}}\right) \left(\ln\left(\frac{Q^2}{m^2}\right) - 1 \right) \\
& - \frac{1}{2} \ln^2\left(\frac{E_0}{E_{e'}}\right) + \frac{1}{2} \ln^2\left(\frac{Q^2}{m^2}\right) - \frac{\pi^2}{3} + Sp\left(\cos^2 \frac{\theta_e}{2} \right) \Bigg] ,
\end{aligned}
\tag{2.41}
$$

where $\Delta E_s = {}^{E_0}/_{E_e'^{el}} \times \Delta E'$, $\Delta E' = \left(E_e'^{el} - E_{e'} \right)$ and $E_e'^{el}$ is the energy of an electron scattered elastically by an angle θ_e in the lab frame. In addition, $Sp(x)$ denotes the Spence function.

The actual value of ΔE_s has to be determined from the experiment, in particular from the detector properties. The cut-off energy $\Delta E' = \left(E_e'^{el} - E_{e'} \right)$ is the maximum difference between the energies of an elastically scattered electron and of the measured final state

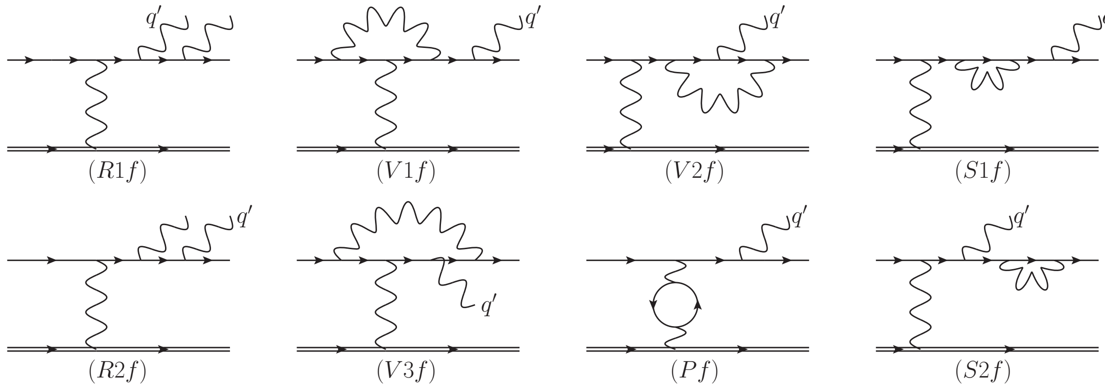

Figure 2.16: Selected diagrams contributing to the radiative corrections for the process $ep \to ep\gamma$. To distinguish the two real photon the photon of the reaction $ep \to epV$ is labeled by q'. The label "f" refers to the fact that the photon with momentum q' is emitted from the final state.

electron. An energy difference larger than $\Delta E'$ leads to a change of the cross section $d\sigma_0$. Hence, corrections with an energy difference larger than $\Delta E'$ are absorbed in the radiative tail. On the one hand, $\Delta E'$ must be larger than the resolution of the detector to ensure that no detectable events are excluded. On the other hand, the cut-off energy must be below the pion threshold where the procedure breaks down. A consistency check for the chosen value of $\Delta E'$ can be performed by plotting the ratio of the experimental cross section $d\sigma_{\text{exp}}$ and $(1 + \delta_1)$ as a function of $\Delta E'$. For a valid choice of $\Delta E'$ the ratio shows a plateau behavior. A convenient and mostly appropriate choice resulting from these arguments is $\Delta E' = 0.01\, E_0$ [175,196]. This value was used for the calculation of the radiative corrections.

However, the quantity $\ln\!\left(\frac{(\Delta E_s)^2}{E_0\, E_{e'}}\right)$ in Eq. (2.41) reveals, that δ_R tends towards $-\infty$ for $\Delta E_s \to 0$. For such small values of the cut-off energy $\Delta E'$ the interpretation of δ_R as emission of a single, very low-energetic photon is not correct anymore. It is discussed in Refs. [183, 197] that indeed numerous low-energetic photons are radiated. Hence, one has to perform the calculation with the full set of diagrams describing the emission of an arbitrary number of soft photons. It was shown in Ref. [197] that the anomaly cancelation discussed above occurs in each order. By iteration one finds [197]

$$1 + \delta + \frac{\delta^2}{2} + \ldots = e^{\delta}.$$

Setting $\delta = \delta_1$ leads to the behavior $e^{\delta_1} \to 0$ for $\Delta E_s \to 0$. Of course, one does not obtain the radiative corrections to all orders by this procedure. Instead, one finds an estimate for the uncertainty of the radiative corrections. In Ref. [175] the uncertainty for the second order $\delta_2 = \delta_1^2/2$ is found to be around 2% for the investigated kinematics.

2.4.2 Radiative corrections to the Bethe–Heitler process

Also for the reaction $e(Z,\, A) \to e(Z,\, A)V$ radiative corrections need to be applied to obtain realistic cross sections which can be related with experimental count rates. For the purpose of studying the dependencies of the signal process $e(Z, A) \to e(Z, A)\gamma'$ qualitatively it is not necessary to apply these corrections. The reason is that the cross section is not altered significantly. Although the normalizations of the leading-order and corrected cross sections will typically differ within the range of around 10%–20%, the shape of the cross section is not altered. Hence, in this case the corrections can be neglected.

The radiative corrections cannot be neglected of course for the case that a signal from the invisible hidden photon production is searched. In this case it is crucial to calculate the signal and background cross section as accurately as possible.

The corrections to the reaction $e(Z, A) \to e(Z, A)V$ can be divided into virtual and soft-photon contributions as done for the elastic ep-scattering. The Feynman diagrams (R1f) and (R2f) of Fig. 2.16 represent two selected amplitudes contributing to the soft-photon corrections. The remaining diagrams are examples for contributions to the virtual corrections. As in the previous section only the lepton side corrections are discussed.

The virtual radiative corrections consist of the contributions from the vertex corrections (diagrams (V1f)–(V3f)), vacuum polarization (Pf), and the lepton self-energy ((S1f), (S2f)). To distinguish the two real photons, the photon of the reaction $ep \to ep\gamma$ is labeled by q'. The label "f" refers to the fact that the photon with momentum q' is emitted from the final state in the shown diagrams. The actual calculation of the corrections is very similar to the elastic ep-scattering process since the building blocks of the one-loop amplitudes are the same. The calculation is presented in detail in Ref. [175].

The analytical calculation of the vertex correction is very involved and will not be discussed here in detail. Therefore, in Ref. [175] the UV-divergent parts are evaluated analytically, whereas the finite parts are determined only numerically. However, the resulting correction is logarithmically divergent in the infrared limit $l \to 0$.

As discussed for ep-scattering, the diagram (S2f) of Fig. 2.16 where the loop is on the final electron line does not contribute. The corresponding contribution is absorbed by renormalization. Hence, only diagrams with a loop on an internal line as (S1f) lead to a finite correction. Note that also these contributions are logarithmically infrared divergent.

The correction for the vacuum polarization is found to be of the same structure as for elastic ep-scattering. For the correction originating from lepton side diagrams as (Pf) one has to replace the momentum transfer Q^2 in Eq. (2.39) by $Q_t^2 = -(p' - p)^2$.

The calculation of the real soft-photon corrections is done in a similar way as in the previous section. The diagrams (R1f) and (R2f) of Fig. 2.16 show examples of such contributions. These two diagrams differ in the way that in one of them (R1f) the soft photon is emitted from an external electron line whereas it is emitted from an internal line in the other one (R2f). Since the amplitudes of the types (R1f) and (R2f) are proportional to $1/l$ and are finite in the soft photon limit $l \to 0$ only diagrams where the soft photon is coupled to the external electron line lead to a logarithmic divergence. As in the case of elastic scattering these infrared divergent term and the ones originating from the virtual corrections cancel each other [175].

The finite part of the real radiative corrections is given by Eq. (2.41) where the lab frame quantities (E_0, $E_{e'}$, θ_e) have to be replaced by quantities of a corresponding center-of-mass frame. If the final state electron and the photon are detected in an experiment, this frame is chosen as the one where $\vec{p}+\vec{q}-\vec{q}\,' = \vec{0}$. In an experiment searching for invisible hidden photon decays one would detect the electron and the hadron. Thus, the frame with $\vec{p}+\vec{q}-\vec{p}\,' = \vec{0}$ needs to be chosen.

2.5 Summary and conclusions of the section

In this section the process of bremsstrahlung emission of a hidden photon induced by lepton-hadron scattering was discussed. This analysis was performed under the aspects to study the signal process in general, and in particular from the point of view, to search for invisible hidden photons. For this purpose, the dynamics of the process was studied qualitatively at the level of the amplitudes, as derived from the Feynman diagrams of the process. The phase space was investigated in order to isolate regions in which the signal cross section is largest, and in addition, the QED background from the Bethe–Heitler process is small. Furthermore, a study of invisible hidden photon signals, e.g., from displaced decays or decays to particles, which cannot be detected, requires an accurate understanding of the background processes.

To find quantitative results, the cross section integrated over the allowed phase space was calculated. For this analysis, the differential cross section of the process was computed in different ways, which leads to results in excellent agreement for the integrated cross sections. It was found that the signal cross section is dominated by the region of phase space where nearly all of the beam energy is carried by the hidden photon and its emission occurs into the forward or beam direction.

Based on these calculations, the applicability of the Weizsäcker–Williams approximation to evaluate cross sections relevant for low-energy fixed-target experiments searching for hidden photons was investigated. It was found that for beam energies above 5 GeV the shape of the cross section is well reproduced within the WW approximation, whereas for lower beam energies, it differs significantly. While from the WW approximation a steep rise of the cross section for $x \to 1$ is predicted, it is found in the cross section calculations of this work that the cross section sharply drops. This result has a great impact for the actual configuration of experiments, since current experiments are designed such that the cross section for the emission of a hidden photon is largest, which is in the region $x \to 1$. However, the formulas for the WW approximation found in Ref. [140] overestimate the cross section calculated in the leading order of QED by 30% or more, also for large beam energies. This is not an issue of the WW approximation itself but results from a too simplistic treatment of the hadronic current. By a more sophisticated treatment, taking the angular dependence of the momentum transfer carried by the virtual photon into account, the calculation in the leading order of QED and within the WW approximation agree within a few percent also for $x \to 1$, as long as the beam energy is sufficiently large.

Chapter 3

Theoretical Framework for Hidden Photon Searches at Electron Scattering Fixed-Target Experiments

3.1 Introduction to this chapter

The phenomenology of the production of a hidden photon γ' via Bremsstrahlung induced by electron scattering off a fixed target with the subsequent γ' decay into a lepton pair,

$$e + (Z, A) \to e + (Z, A) + l^+ l^-,$$

is discussed in this chapter. The γ' emission in fixed-target experiments was studied in the previous chapter. These findings are applied to investigate the process extended by the decay of the hidden photon into a lepton pair. This process is extensively studied in experiments which makes a qualitative as well as quantitative understanding of the cross section to high accuracy crucial.

For this purpose, the cross section is derived from the contributing Feynman diagrams in Secs. 3.2 and 3.3. In Sec. 3.3.3, the cross section is decomposed into contributions, which can be identified with groups of Feynman diagrams allowing one to discriminate between the kinematical behavior of the signal and the background. In order to verify the simulation of the considered process, in Sec. 3.4 the integrated cross section is calculated and compared to data taken at MAMI. This allows for the calculation of the discovery potential of selected experiments, where setups for MAMI (Sec. 3.5.2), MESA (Sec. 3.5.3), DarkLight (Sec. 3.5.4), and HPS (Sec. 3.5.5) are investigated. Finally, the findings of this chapter are compared to the existing limits presented in Sec. 1.3.4.

In this chapter the following notation is used: The four-momenta of the initial and recoiled electrons in the Feynman diagrams of Fig. 3.1 are denoted by $k = (E_0, \vec{k})$ and $k' = (E'_e, \vec{k}\,')$; the four-momenta of the initial and final target state by $p = (E_p, \vec{p})$ and $p' = (E'_p, \vec{p}\,')$, and the lepton pair four-momenta by $l_- = (E_-, \vec{l}_-)$ and $l_+ = (E_+, \vec{l}_+)$, for the lepton and antilepton, respectively. The initial and final electron spins are s_k and s'_k; the spins of the initial and final proton are s_p and s'_p, and the spins of the created lepton and antilepton are s_- and s_+. Furthermore, the conventions of Bjorken and Drell [198] are followed.

3.2 Amplitude of the process

One obtains the direct amplitude of the process in which the leptons are initially treated as distinguishable particles from the Feynman diagrams of Fig. 3.1. In order to distinguish

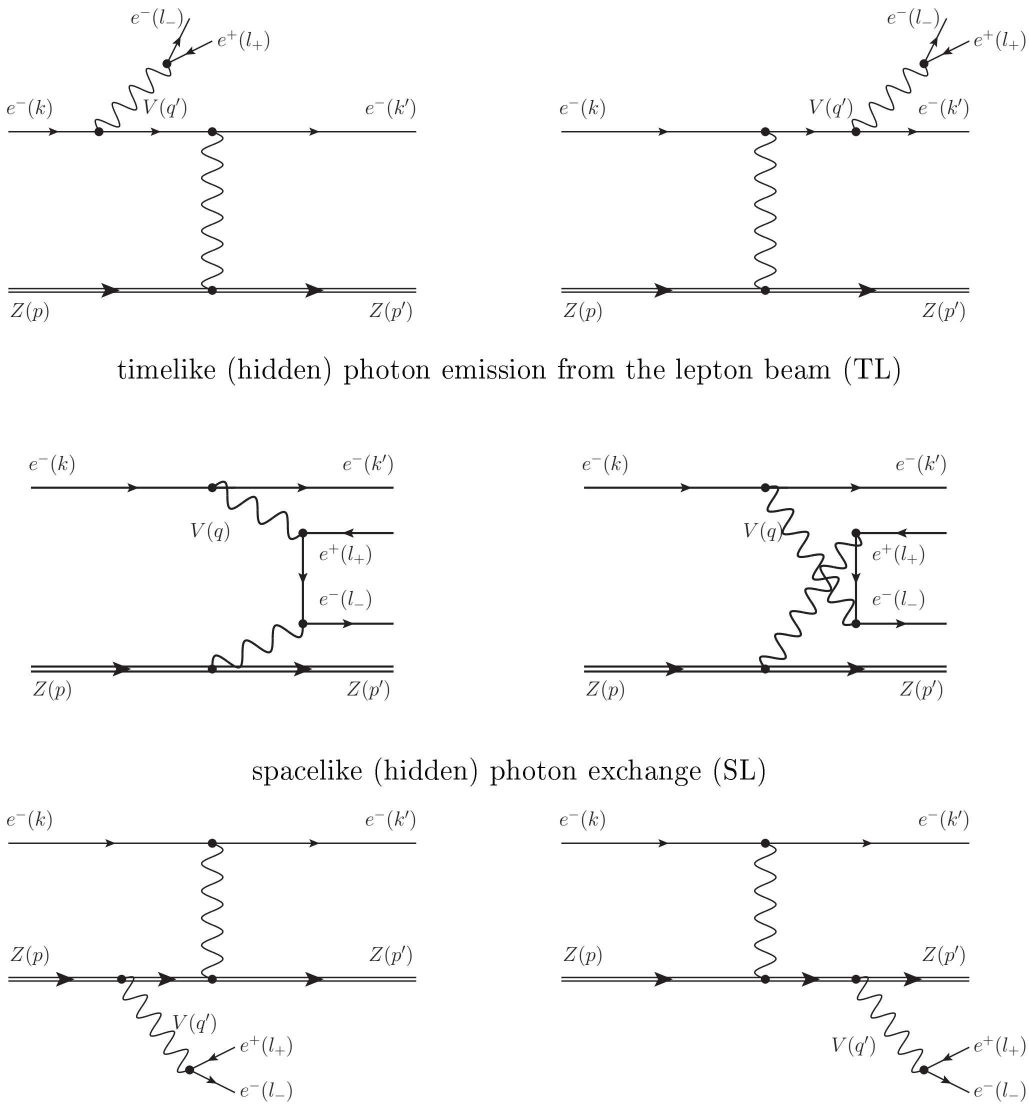

timelike (hidden) photon emission from the lepton beam (TL)

spacelike (hidden) photon exchange (SL)

timelike (hidden) photon emission from the hadronic state (VVCS)

Figure 3.1: Direct (D) tree level Feynman diagrams contributing to the amplitude of the process $e(Z, A) \to e(Z, A)l^+l^-$. Upper panel: exchange of the timelike boson V and a spacelike γ (TL). Central panel: the spacelike boson V and a spacelike γ (SL). Lower panel: doubly virtual Compton scattering (VVCS)

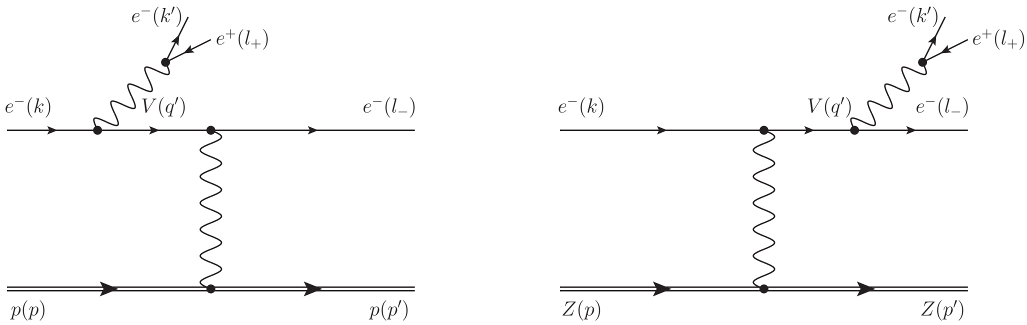

timelike (hidden) photon emission from the lepton beam (TL)

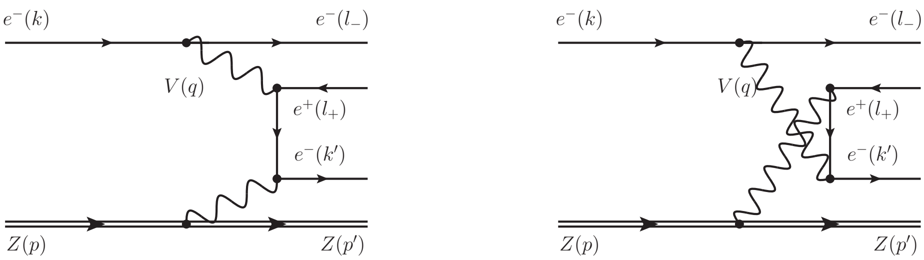

spacelike (hidden) photon exchange (SL)

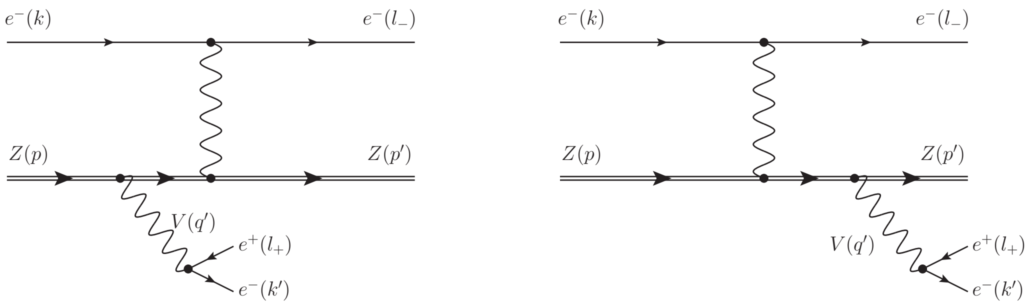

timelike (hidden) photon emission from the hadronic state (VVCS)

Figure 3.2: Exchanged (X) tree level Feynman diagrams contributing to the amplitude of the process $e(Z, A) \to e(Z, A)l^+l^-$. Same as in Fig. 3.1, but the final-state beam lepton $e^-(k')$ and the negatively charged pair lepton $(e^-(l_-))$ are exchanged.

between the contributions from the individually gauge invariant sets of diagrams, they are denoted by the character of the exchanged vector boson V. As in Chapter 2, V either denotes the hidden photon or the photon. For this reason the amplitudes from the set of diagrams in the upper panel of Fig. 3.1 where the V is timelike are referred to as "TL" and for the center as "SL" due to the spacelike V. In the lower panel, a timelike V is radiated off the hadronic state, which is known as doubly virtual Compton scattering. The corresponding amplitude is labeled by "VVCS." The study will be restricted to the Born diagrams of the VVCS contribution drawn in the lower panel of Fig. 3.1.

The signal cross section is described by the Feynman diagrams of Fig. 3.1 in which the boson V is timelike. For the production from a heavy nucleus, the radiation off the target is suppressed by its large mass and the typical choice of kinematics where most of the beam energy is transferred to the lepton pair. Therefore, the VVCS contribution is suppressed by several orders of magnitude and only the TL diagrams contribute. The emission of a spacelike hidden photon can be safely neglected since the γ' propagator in the central panel of Fig. 3.1 can be written as

$$\frac{-g^{\alpha\beta}}{q^2 - m_{\gamma'}^2}.$$

Due to the spacelike momentum transfer $q^2 < 0$ for scattering processes, the denominator always implies a suppression of this contribution. The propagator in the case of a timelike γ' leads to a peak in the signal and a cancelation of a factor ε^2 occurs. It was checked numerically that the contribution from the interference of the SL amplitude with the other amplitudes does not alter the cross section by more than 0.1% - 1%, which is less than the experimental and numerical uncertainty.

It was already discussed in Sec. 2.1.3 that the VVCS contribution is not suppressed that strongly for a proton target compared to a heavy-nucleus target. Therefore, in the case of a proton target also the VVCS diagrams are included into the amplitude of the signal cross section. In this thesis, experiments with a proton target are considered only for beam energies up to 100 MeV. Hence, the VVCS contribution is restricted to the nucleon Born amplitude below the pion threshold, as discussed in Sec. 2.1.3. This approximation is valid at the level of better than 5%. However, for beam energies above 140 MeV a larger uncertainty is expected.

Hence, the isolated γ' production process is obtained

$$\mathcal{M}_{\gamma'}^{\mathrm{TL}} = \frac{i\, e^4\, \varepsilon^2}{(p'-p)^2} \frac{-g^{\alpha\beta} + q'^{\alpha} q'^{\beta}/m_{\gamma'}^2}{q'^2 - m_{\gamma'}^2 + i\, m_{\gamma'}\, \Gamma_{\gamma'}}\, J_N^{\mu}\, \mathcal{I}_{\mu\alpha}\, j_{\beta}^{\mathrm{pair}}, \tag{3.1}$$

and

$$\mathcal{M}_{\gamma'}^{\mathrm{VVCS}} = \frac{-i\, e^4\, \varepsilon^2}{q^2} \frac{-g^{\alpha\beta} + q'^{\alpha} q'^{\beta}/m_{\gamma'}^2}{q'^2 - m_{\gamma'}^2 + i\, m_{\gamma'}\, \Gamma_{\gamma'}}\, j_{\mathrm{beam}}^{\mu}\, \mathcal{H}_{\mu\alpha}\, j_{\beta}^{\mathrm{pair}}, \tag{3.2}$$

where $\Gamma_{\gamma'}$ denotes the total γ' decay width given in Eq. (1.34). The leptonic and hadronic tensors are given by

$$\mathcal{I}_{\mu\alpha} = \overline{u}_e(k', s'_k) \Bigg(\gamma_\mu \frac{\not{k} - \not{q}' + m}{(k - q')^2 - m^2} \gamma_\alpha + \gamma_\alpha \frac{\not{k}' + \not{q}' + m}{(k' + q')^2 - m^2} \gamma_\mu \Bigg) u_e(k, s_k), \tag{3.3}$$

and

$$\mathcal{H}_{\mu\alpha} = \overline{u}_p(p', s'_p) \Bigg(\Gamma_\mu(q_t + q') \frac{\not{p} - \not{q}' + M}{(p - q')^2 - M^2} \Gamma_\alpha(-q') + \Gamma_\alpha(-q') \frac{\not{p}' + \not{q}' + M}{(p' + q')^2 - M^2} \Gamma_\mu(q_t + q') \Bigg) u_p(p, s_p), \tag{3.4}$$

with m (M) denoting the mass of the electron (hadron). The leptonic currents read

$$j_\beta^{\text{pair}} = \overline{u}_l(l_-, s_-)\, \gamma_\beta\, v_l(l_+, s_+),$$
$$j_\beta^{\text{beam}} = \overline{u}_e(k', s'_k)\, \gamma_\beta\, u_e(k, s_k).$$

In the case of a proton target the hadronic current J_N^μ is parametrized by

$$J_N^\mu = \overline{u}_N(p', s'_p)\, \Gamma^\mu\, u_N(p, s_p),$$

with $\Gamma_\mu(Q_t^2) \equiv F_1(Q_t^2)\, \gamma_\mu + F_2(Q_t^2)\, i\, \sigma_{\mu\nu} q_t^\nu / 2M$ using the Dirac (F_1) and Pauli (F_2) form factors and $Q_t^2 = -(p' - p)^2 > 0$. Furthermore, the form factors F_1 and F_2 are parametrized by a linear combination of the electric and magnetic Sachs form factors given in Eq. (1.19). A standard dipole fit is used in the spacelike as well as timelike regions for low momentum transfer $\left|Q_t^2\right| \lesssim 1\,\text{GeV}^2$, which is the region of interest in this work. For a heavy nucleus the hadronic current can be written as

$$J_N^\mu = Z \cdot F_{\text{el}}(Q_t) \cdot (p + p')^\mu,$$

where

$$F_{\text{el}}(Q_t) = 3/(Q_t\, R)^3 \cdot \left(\sin\left(Q_t\, R\right) - Q_t R\, \cos\left(Q_t\, R\right)\right),$$

is the nuclear charge form factor with $R = 1.21\,\text{fm} \cdot A^{\frac{1}{3}}$ [184]. This parametrization accounts only for the coherent scattering of the nucleus. Of course, the parametrization of Ref. [140] can be applied. Since the form factor enters the cross section only quadratically one can simply replace

$$F_{\text{el}}^2 \to W_2^{\text{el}} + W_2^{\text{inel}},$$

where the structure functions W_2^{el} and W_2^{inel} are given in Eq. (2.24). For the experimental setups at MAMI (Sec. 3.4.3) the resulting uncertainty due to the different parametrizations and the inelastic contributions was found to be less than 5%.

The amplitude of the QED background is given by the coherent sum over all diagrams shown in Fig. 3.1 with a corresponding virtual photon $V = \gamma^*$ in the intermediate state, where each amplitude reads

$$\mathcal{M}_{\gamma^*}^{\mathrm{TL}} = \frac{i\,e^4}{(p'-p)^2}\,\frac{-g^{\alpha\beta}}{q'^2}\,J_N^\mu\,\mathcal{I}_{\mu\alpha}\,j_\beta^{\mathrm{pair}}, \tag{3.5}$$

$$\mathcal{M}_{\gamma^*}^{SL} = \frac{i\,e^4}{(p'-p)^2}\,\frac{-g^{\alpha\beta}}{q^2}\,J_N^\mu\,\tilde{\mathcal{I}}_{\mu\alpha}\,j_\beta^{\mathrm{beam}}, \tag{3.6}$$

$$\mathcal{M}_{\gamma^*}^{\mathrm{VCS}} = \frac{-i\,e^4}{q^2}\,\frac{-g^{\alpha\beta}}{q'^2}\,j_{\mathrm{beam}}^\mu\,\mathcal{H}_{\mu\alpha}\,j_\beta^{\mathrm{pair}}, \tag{3.7}$$

with the leptonic tensor

$$\tilde{\mathcal{I}}_{\mu\alpha} = \overline{u}_l(l_-,s_-)\left(\gamma_\mu\frac{\not{q}-\not{l}_+ + m_l}{(q-l_+)^2-m_l^2}\gamma_\alpha + \gamma_\alpha\frac{\not{l}_- - \not{q} + m_l}{(l_- - q)^2 - m_l^2}\gamma_\mu\right) v_l(l_+,s_+),$$

where m_l denotes the mass of the leptons from the pair.

In the case of identical species of the beam lepton and of the lepton pair, besides the direct contribution denoted by D one also has to account for the exchange term (X). The total amplitude must be antisymmetric under the interchange of these two final-state leptons. Thus, the structure of the exchange term is obtained by interchanging the two negatively charged leptons. The Feynman diagrams of the exchange term X are shown in Fig. 3.2.

The full amplitude of the process is found as

$$\mathcal{M}_{\gamma'+\gamma^*} = \left(\mathcal{M}_{\mathrm{D},\gamma'}^{\mathrm{TL}} + \mathcal{M}_{\mathrm{D},\gamma^*}^{\mathrm{TL}} + \mathcal{M}_{\mathrm{D},\gamma^*}^{\mathrm{SL}}\right) - \left(\mathcal{M}_{\mathrm{X},\gamma'}^{\mathrm{TL}} + \mathcal{M}_{\mathrm{X},\gamma^*}^{\mathrm{TL}} + \mathcal{M}_{\mathrm{X},\gamma^*}^{\mathrm{SL}}\right), \tag{3.8}$$

for a heavy nucleus target and

$$\begin{aligned}\mathcal{M}_{\gamma'+\gamma^*} = &\left(\mathcal{M}_{\mathrm{D},\gamma'}^{\mathrm{TL}} + \mathcal{M}_{\mathrm{D},\gamma^*}^{\mathrm{TL}} + \mathcal{M}_{\mathrm{D},\gamma^*}^{\mathrm{SL}} + \mathcal{M}_{\mathrm{D},\gamma^*}^{\mathrm{VCS}}\right)\\ &- \left(\mathcal{M}_{\mathrm{X},\gamma'}^{\mathrm{TL}} + \mathcal{M}_{\mathrm{X},\gamma^*}^{\mathrm{TL}} + \mathcal{M}_{\mathrm{X},\gamma^*}^{\mathrm{SL}} + \mathcal{M}_{\mathrm{X},\gamma^*}^{\mathrm{VCS}}\right),\end{aligned} \tag{3.9}$$

for a proton target.

For the further discussion, it is convenient to assign

$$\begin{aligned}\mathcal{M}_{\gamma^*} &= M_{\mathrm{D},\gamma^*} + M_{\mathrm{X},\gamma^*},\\ \mathcal{M}_{\gamma'} &= M_{\mathrm{D},\gamma'} + M_{\mathrm{X},\gamma'},\end{aligned}$$

where each of these amplitudes contains all of the SL, TL, and VVCS amplitudes which contribute depending on the kind of target state.

3.3 Cross sections in terms of recursive phase space and detector coordinates

As in the case of the hidden photon production process $e(Z,A) \to e(Z,A)\gamma'$ discussed in Chapter 2, the cross section of the process $e(Z,A) \to e(Z,A)l^+l^-$ will be calculated within two different approaches. As a first step, the cross section is calculated in the "recursive phase space" approach in which the phase spaced is factorized into three subprocesses. Furthermore, as a second step the cross section is expressed in terms of detector coordinates, which parametrize the geometric acceptance of the detectors used in the investigated experimental setups. Since the first method is commonly applied to calculate cross sections, it will mostly serve as a cross check of the results obtained in the second approach. Expressing the cross section in terms of detector coordinates allows one to perform a highly efficient numerical study of the process. Only the part of the phase space covered by the experimental acceptance needs to be considered. This clear discrimination between geometrically allowed and forbidden parts of phase space is not always possible within the first approach.

The calculation of the differential cross section for the process $e(Z,A) \to e(Z,A)l^+l^-$ is very similar to the calculation of the hidden photon bremsstrahlung cross section presented in Sec. 2.1.2. Starting point is the general cross section of a $2 \to 4$ particle reaction:

$$\begin{aligned} d\sigma = & \frac{1}{4\sqrt{(p\cdot k)^2 - m^2M^2}} \frac{d^3\vec{k}'}{(2\pi)^3 2E_{k'}} \frac{d^3\vec{p}'}{(2\pi)^3 2E_{p'}} \frac{d^3\vec{l}_+}{(2\pi)^3 2E_+} \frac{d^3\vec{l}_-}{(2\pi)^3 2E_-} \\ & \times (2\pi)^4\, \delta^{(4)}\left(k + p - k' - p' - l_+ - l_-\right) \overline{|\mathcal{M}|^2}. \end{aligned} \tag{3.10}$$

3.3.1 Cross section expressed within the recursive phase space approach

The phase space of the basic process $e(Z,A) \to e(Z,A)l^+l^-$ is decomposed into individual subprocesses within the recursive phase space approach. As a first step, the creation of the lepton pair from a vector boson V with momentum q', which is either the photon γ^* or the hidden photon γ', is separated. This reaction is evaluated in the V-rest frame $(**)$. Furthermore, as in Sec. 2.1.2, the leptonic part related to the lepton beam is separated from the hadronic reaction $\gamma^* p \to p'V$. The latter one is evaluated in the $\gamma^* p$-rest frame, where one has as before

$$(\vec{q} + \vec{p})^* = \left(\vec{k} - \vec{k}' + \vec{p}\right)^* = \vec{0}.$$

Hence, the cross section reads

$$\begin{aligned} d\sigma = & \frac{1}{4\sqrt{(p\cdot k)^2 - m^2M^2}} \left(\frac{d^3\vec{k}'}{(2\pi)^3 2E_{k'}}\right)^L \left(\frac{d^3\vec{p}'}{(2\pi)^3 2E_{p'}}\right)^* \\ & \times \left(\frac{d^3\vec{l}_+}{(2\pi)^3 2E_+} \frac{d^3\vec{l}_-}{(2\pi)^3 2E_-} (2\pi)^4\, \delta^{(4)}\left(k + p - k' - p' - l_+ - l_-\right)\right)^{**} \overline{|\mathcal{M}|^2}. \end{aligned} \tag{3.11}$$

In the V-rest frame the three-momenta satisfy the relation

$$(\vec{q}')^{**} = (\vec{l}_+ + \vec{l}_-) = \vec{0},$$

with $q' = l_+ + l_- = k + p - k' - p'$, and $|\vec{l}|_+ = |\vec{l}|_-$ and $E_+ = E_-$. Since the invariant mass of the lepton pair $q'^2 = m_{ll}^2$ is commonly reconstructed in experiments, this quantity is ideally suited as a frame independent variable of the process. In this frame one has $q'^0 = E_+ + E_- = m_{ll}$. Thus, the energy of the leptons can be written as

$$E_\pm^{**} = \frac{m_{ll}}{2},$$

and

$$|\vec{l}_\pm|^{**} = \frac{\lambda^{1/2}\left(m_{ll}^2, m_l^2, m_l^2\right)}{2m_{ll}} = \frac{\sqrt{m_{ll}^2 - 4m_l^2}}{2}$$

is the modulus of the three-momenta of the leptons from the pair. Plugging these expressions into the term in the parentheses evaluated in the V-rest frame in Eq. (3.11) yields

$$\begin{aligned}\left(\dots\right)^{**} &= \left(\frac{|\vec{l_+}|^2}{4E_+^2}\frac{E_+}{|\vec{l_+}|}\,dE_+\,d\Omega_+\delta\left(m_{ll}-2E_+\right)\right)^{**}\\ &= \left(\frac{1}{4}\frac{|\vec{l_+}|}{E_+}\,dE_+\,d\Omega_+\frac{1}{2}\delta\left(E_+-\frac{1}{2}m_{ll}\right)\right)^{**}\\ &= \frac{1}{8}\frac{\sqrt{m_{ll}^2-4m_l^2}}{m_{ll}}d\Omega_+^{**}.\end{aligned}$$

Equation (3.11) can be rewritten as

$$d\sigma = \frac{1}{4|\vec{k}\,|^L M}\frac{1}{(2\pi)^8}\left(\frac{d^3\vec{k}\,'}{2E_{k'}}\right)^L\left(\frac{d^3\vec{p}\,'}{2E_{p'}}\right)^*\frac{1}{8}\frac{\sqrt{m_{ll}^2-4m_l^2}}{m_{ll}}\,d\Omega_+^{**}\,\overline{|\mathcal{M}|^2}. \tag{3.12}$$

As before in Sec. 2.1.2, the hadronic subprocess can be conveniently calculated in the rest frame of the combined target and initial virtual photon state with momentum $q = k - k'$. In this frame one has $(\vec{q}+\vec{p})^* = (\vec{q}\,'+\vec{p}\,')^* = \vec{0}$. The center-of-mass energy of the subprocess is expressed by the corresponding Mandelstam variable

$$s = (q+p)^2.$$

The invariant mass of the lepton pair results to

$$\begin{aligned}m_{ll}^2 = q'^2 &= \left(q+p-p'\right)^2\\ &= (q+p)^2 + M^2 - 2\,(q+p)\cdot p'\\ &= s + M^2 - 2\underbrace{\left(q^0+p^0\right)^*}_{=\sqrt{s}}(p'^0)^* + 2\underbrace{(\vec{q}+\vec{p})^*}_{=\vec{0}}(\vec{p}\,')^*\\ &= s + M^2 - 2\sqrt{s}E_{p'}^*,\end{aligned}$$

Thus, the energy of the scattered hadron reads

$$E_{p'}^* = \frac{s+M^2-m_{ll}^2}{2\sqrt{s}}.$$

The corresponding modulus of the three-momentum is

$$|\vec{p}\,'|^* = \frac{\lambda^{1/2}\left(s,\,M^2,\,m_{ll}^2\right)}{2\sqrt{s}}.$$

It is convenient, to integrate over quantities associated with the emitted (hidden) photon instead of those of the final-state hadron. Therefore, the integration measure has to be transformed according to

$$\begin{aligned}\frac{dm_{ll}}{d|\vec{p}\,'|} &= \frac{d}{d|\vec{p}\,'|}\sqrt{s+M^2-2\sqrt{s}\sqrt{(|\vec{p}\,'|^*)^2+M^2}}\\ &= \frac{-2\sqrt{s}}{2m_{ll}}\frac{|\vec{p}\,'|^*}{E_{p'}^*}\\ \Rightarrow d|\vec{p}\,'|^* &= -\frac{m_{ll}}{\sqrt{s}}\frac{E_{p'}^*}{|\vec{p}\,'|^*}dm_{ll},\end{aligned}$$

and

$$d\Omega^*_{p'} = d\Phi^*\, d\cos\theta^*_{p'} = -d\Phi^*\, d\cos\left(\theta^*_{p'} - \pi\right) = -d\Phi^*\, d\cos\theta^*_{q'} = -d\Omega^*_{q'}.$$

Due to ${d\Omega^*_{p'}}/{dm_{ll}} = 0$ and ${d|\vec{p}\,'|^*}/{d\Omega^*_{q'}} = 0$ one finds

$$\begin{aligned}
\left(\frac{d^3\vec{p}\,'}{2E_{p'}}\right)^* &= \left(\frac{|\vec{p}\,'|^2\, d|\vec{p}\,'|\, d\Omega_{p'}}{2E_{p'}}\right)^* \\
&= \frac{1}{2}|\vec{p}\,'|^* \frac{|\vec{p}\,'|^*}{E^*_{p'}} \frac{m_{ll}}{\sqrt{s}} \frac{E^*_{p'}}{|\vec{p}\,'|^*}\, dm_{ll}\, d\Omega^*_{q'} \\
&= \frac{1}{2}|\vec{p}\,'|^* \frac{m_{ll}}{\sqrt{s}}\, dm_{ll}\, d\Omega^*_{q'}.
\end{aligned}$$

Inserting this into Eq. (3.12), one finally obtains

$$\frac{d\sigma}{dE^L_{e'}\, d\Omega^L_{e'}\, dm_{ll}\, d\Omega^*_{q'} d\Omega^{**}_{+}} = \frac{|\vec{k}\,'|^L}{128|\vec{k}\,|^L M} \frac{1}{(2\pi)^8} \frac{|\vec{p}\,'|^* \sqrt{m^2_{ll} - 4m^2_l}}{\sqrt{s}} \overline{|\mathcal{M}|^2}. \tag{3.13}$$

To evaluate the matrix element $\mathcal{M}$, all four-vectors need to be obtained in the lab frame. Therefore, q' and p' are evaluated in the $(q+p)$-rest frame $(*)$ and are transformed along $(q+p)^L$ into the Lab frame. Furthermore, the four-vectors $l_\pm$ first are determined in the q'-rest frame $(**)$ and subsequently are boosted and rotated along q'^L into the lab frame.

3.3.2 Cross section expressed by detector coordinates

As discussed, it can be helpful to evaluate the cross section in terms of the quantities which are directly measured in the experiments.

It was described in Sec. 1.3.4.2 that in the considered type of experiments a search for a resonance from an intermediate particle above the smooth QED background is performed. For this purpose, the cross section of the process $e(Z,A) \to e(Z,A)l^+l^-$ is evaluated in terms of lab frame variables of the detected particles. If no other particles are detected, which is usually the case, the quantities associated with these unobserved particles must be integrated out. Hence, it is straightforward to calculate the cross section depending on the invariant mass $m^2_{ll} = q'^2 = (l_+ + l_-)^2$ and on the other measured quantities corresponding to the four-momenta of the leptons of the pair. Furthermore, it is convenient to parametrize the three-momentum vectors of the detected particles in terms of detector coordinates. This allows one to restrict the integration limits to the geometrical acceptances of the used detectors. The parametrization in detector coordinates is derived in Appendix B.2. Since the four-momenta of the lepton pair are over-constrained by the momentum vectors and the invariant mass, the three-momentum norm of the created electron $|\vec{l_-}|$ will be expressed by q'^2 and $\vec{l_+}$.

A parametrization of the 8-fold differential cross section containing most of the directly measured quantities is

$$\frac{d^8\sigma}{d\Omega_{e'}\, d|\vec{l_+}|\, d\Omega_+\, d\Omega_- dq'^2}. \tag{3.14}$$

If not explicitly mentioned, all quantities are chosen to be in the lab frame. In this particular kinematical setting the scattered hadron is not detected. Consequently, the associated three-momentum will be integrated out by means of the Dirac δ function. Moreover, the scattered electron is not detected in most experiments. Thus, energy conservation is used to eliminate the three-momentum modulus of the scattered electron and the cross section needs be integrated over its solid angle. However, if the scattered electron is detected as well, the integration has to be performed over the corresponding experimental acceptances.

By inserting an identity into Eq. (3.11)

$$1 = \int d^4q' \, \delta^{(4)}\big(q' - l_+ - l_-\big)\,,$$

the cross section in terms of the favored quantities can be easily found. This corresponds to a factorization of the phase space into a γ' production and a decay part. Since no approximations or assumptions need to be applied here, this factorization is valid in general. Following Eq. (3.10), one finds

$$\begin{aligned} d\sigma = &\frac{1}{4\sqrt{(k\cdot p)^2 - m^2M^2}} \frac{d^3\vec{k}\,'}{(2\pi)^3\, 2\, E_e'} \frac{d^3\vec{p}\,'}{(2\pi)^3\, 2\, E_p'} \frac{d^3\vec{q}\,'}{(2\pi)^3\, 2\, E_{q'}} (2\pi)^4\, \delta^{(4)}\left(k + p - k' - p' - q'\right) \\ &\times \underbrace{\frac{2E_{q'}\, dE_{q'}}{2\pi}}_{dq'^{\,2}/(2\pi)} \frac{d^3\vec{l_-}}{(2\pi)^3\, 2\, E_-} \frac{d^3\vec{l_+}}{(2\pi)^3\, 2\, E_+} (2\pi)^4\, \delta^{(4)}\big(q' - l_+ - l_-\big)\, \overline{|\mathcal{M}|^2} \end{aligned}$$

The beam axis corresponding to the momentum of the incident electron is chosen to be parallel to the z-axis and the target is at rest $\left(\vec{p} = \vec{0}\right)$. Since the detectors are commonly centered in the same plane as the incident beam, no further conditions for the kinematical quantities will be used in the following. Note that the derivation of the cross section and the formula itself does not depend on the particular choice of quantities in the lab frame, but only on scalar products of three-momenta. The δ functions constrain the three-momenta

$$\vec{q} = \vec{l_-} + \vec{l_+} \quad \text{and} \quad \vec{p}\,' = \vec{k} - \vec{k}\,' - \vec{q}\,',$$

which leads to

$$\begin{aligned} d\sigma &= \frac{1}{128\,|\vec{k}\,|\, M} \frac{1}{(2\pi)^8} \frac{1}{E_{p'} E_{k'} E_{q'} E_+ E_-} d^3\vec{k}\,'\, \delta\left(E_0 + M - E_{e'} - E_{p'} - E_{q'}\right) \\ &\quad \times d^3\vec{l_+}\, d^3\vec{l_-}\, dq'^{\,2}\, \delta\left(E_{q'} - E_+ - E_-\right) \overline{|\mathcal{M}|^2} \\ &= \frac{1}{128\,|\vec{k}\,|\, M} \frac{1}{(2\pi)^8} \frac{|\vec{k}\,'|^2 |\vec{l_+}\,|^2 |\vec{l_-}\,|^2}{E_{p'} E_{k'} E_{q'} E_+ E_-} d|\vec{k}\,'|\, d\Omega_{e'}\, \delta\, \underbrace{\left(E_0 + M - E_{e'} - E_{p'} - E_{q'}\right)}_{=:\delta_1} \\ &\quad \times d|\vec{l_+}\,|\, d\Omega_+\, d|\vec{l_-}\,|\, d\Omega_-\, dq'^{\,2}\, \delta\, \underbrace{\left(E_{q'} - E_+ - E_-\right)}_{=:\delta_2} \overline{|\mathcal{M}|^2}. \end{aligned} \tag{3.15}$$

The remaining two delta functions can be used to compute the zero-components of the four-momenta k' and l_- and thus to perform the integration over their three-momentum moduli. Therefore, expressions for $|\vec{k}\,'|$ and $|\vec{l_-}\,|$ in terms of the remaining quantities have to be found.

To express $|\vec{l_-}\,|$ in terms of the non-constrained variables, the equation

$$q'^2 = (l_+ + l_-)^2$$

has to be solved, giving rise to

$$
\begin{aligned}
q'^2 &= 2m_l^2 + 2E_+E_- - 2|\vec{l_-}|\vec{l_+}\cdot\hat{l}_- \\
\Rightarrow 0 &= -q'^2 + 2m_l^2 + 2E_+E_- - 2|\vec{l_-}|\vec{l_+}\cdot\hat{l}_- \\
\Leftrightarrow 0 &= \underbrace{\left(-\frac{q'^2}{2} + m_l^2\right)}_{=:A} + E_+E_- - |\vec{l_-}|.\underbrace{\vec{l_+}\cdot\hat{l}_-}_{=:B}.
\end{aligned} \tag{3.16}
$$

This equation can be rewritten as a quadratic equation for $|\vec{l_-}|$, which can be solved easily. After adding $(B|\vec{l_-}| - A)$ on both sides of Eq. (3.16), squaring the result and using $E_-^2 = |\vec{l_-}|^2 + m_l^2$ one finds the two solutions

$$
\begin{aligned}
B^2|\vec{l_-}|^2 + A^2 - 2AB|\vec{l_-}| &= E_+^2|\vec{l_-}|^2 + E_+^2 m_l^2 \\
\Leftrightarrow 0 &= |\vec{l_-}|^2 - \frac{2AB}{B^2 - E_+^2}|\vec{l_-}| + \frac{A^2 - E_+^2 m_l^2}{B^2 - E_+^2} \\
\Rightarrow |\vec{l_-}|_{1,2} &= \frac{AB}{B^2 - E_+^2} \pm \sqrt{\frac{(AE_+)^2 + (E_+ m_l B)^2 - (E_+^2 m_l)^2}{(B^2 - E_+^2)^2}}.
\end{aligned} \tag{3.17}
$$

As in Sec. 2.1.2, the physical solution can be determined by considering the particles as massless. In this case the calculation simplifies to

$$
\begin{aligned}
q'^2 &= \underbrace{l_+^2 + l_-^2}_{=0} + 2|\vec{l_-}||\vec{l_+}|(1 - \hat{l}_+\cdot\hat{l}_-) \\
\Leftrightarrow |\vec{l_-}| &= \frac{q'^2}{2|\vec{l_+}|(1 - \hat{l}_+\cdot\hat{l}_-)}.
\end{aligned} \tag{3.18}
$$

Comparing Eqs. (3.17) and (3.18) (numerically), one finds that the solution corresponding to the physical one is

$$
|\vec{l_-}| = \frac{AB}{B^2 - E_+^2} + \sqrt{\frac{(AE_+)^2 + (E_+ m_l B)^2 - (E_+^2 m_l)^2}{(B^2 - E_+^2)^2}}, \tag{3.19}
$$

with $A = -\frac{q'^2}{2} + m^2$ and $B = \vec{l_+}\cdot\hat{l}_-$.

The calculation of $|\vec{k}'|$ is performed in a similar way. Since it is not necessary that the four-vectors l_+ and l_- appear explicitly in the following, the sum $q'^2 = (l_+ + l_-)^2$ is used, where $|\vec{l_-}|$ is symbolic for the result of Eq. (3.19). Starting again from four-momentum conservation one finds

$$
\begin{aligned}
p'^2 = M^2 &= (p + k - k' - q')^2 \\
\Leftrightarrow M^2 &= (p + k - q')^2 + \underbrace{k'^2}_{m^2} - 2(p + k - q')\cdot k' \\
\Leftrightarrow 0 &= \underbrace{(p + k - q')^2 + m^2 - M^2}_{=:D} - \underbrace{2(E_0 + M - E_{q'})}_{=:F} E_{e'} + \underbrace{2(\vec{k} - \vec{q}')\cdot\hat{k}'}_{=:G}|\vec{k}'|
\end{aligned}
$$

An analogous calculation as for $|\vec{l_-}|$ leads to

$$|\vec{k}'| = -\frac{DG}{G^2 - F^2} + \sqrt{\frac{(mFG)^2 + (DF)^2 - (mF^2)^2}{(G^2 - F^2)^2}}. \tag{3.20}$$

To find an appropriate form of the argument in the δ function, one has to apply the transformation

$$\delta(f(x_o)) = \left|\frac{1}{\frac{\partial f}{\partial x}(x_0)}\right| \cdot \delta(x_0).$$

Hence, one obtains

$$\begin{aligned}
\frac{\partial \delta_1}{\partial |\vec{k}'|} &= \frac{\partial}{\partial |\vec{k}'|}\left(E_0 + M - E_{e'} - E_{p'} - E_{q'}\right) \\
&= \frac{\partial}{\partial |\vec{k}'|}\left(-\sqrt{|\vec{k}'|^2 + m^2} - \sqrt{\left(\vec{k} - \vec{q}'\right)^2 + |\vec{k}'|^2 - 2|\vec{k}'|\,\hat{k}' \cdot \left(\vec{k} - \vec{q}'\right) + M^2}\right) \\
&= -\frac{|\vec{k}'|}{E_{k'}} - \frac{|\vec{k}'| - \hat{k}' \cdot \left(\vec{k} - \vec{q}'\right)}{E_{p'}}
\end{aligned} \tag{3.21}$$

and

$$\begin{aligned}
\frac{\partial \delta_2}{\partial |\vec{l_-}|} &= \frac{\partial}{\partial |\vec{l_-}|}\left(E_{q'} - E_+ - E_-\right) \\
&= \frac{\partial}{\partial |\vec{l_-}|}\left(\sqrt{|\vec{l_+}|^2 + |\vec{l_-}|^2 + 2|\vec{l_-}|\,\vec{l_+} \cdot \hat{l}_- + q'^2} - E_+ - \sqrt{|\vec{l_-}|^2 + m_l^2}\right) \\
&= -\frac{|\vec{l_-}|}{E_-} + \frac{|\vec{l_-}| + \vec{l_+} \cdot \hat{l}_-}{E_{q'}}.
\end{aligned} \tag{3.22}$$

Inserting the quantities of Eqs. (3.19) to (3.22) into Eq. (3.15) leads to the 8-fold differential cross section

$$\frac{d\sigma}{d|\vec{l_+}|\, d\Omega_+\, d\Omega_-\, d\Omega_{e'}\, dq'^2} = \frac{1}{128\,|\vec{k}|\,M}\,\frac{1}{(2\pi)^8}\,\frac{|\vec{k}'|^2 |\vec{l_+}|^2 |\vec{l_-}|^2}{E_{p'} E_{k'} E_{q'} E_+ E_-}\left(\left|\frac{\partial \delta_1}{\partial |\vec{k}'|}\right| \left|\frac{\partial \delta_2}{\partial |\vec{l_-}|}\right|\right)^{-1} \overline{|\mathcal{M}|^2}, \tag{3.23}$$

where this equation is understood to be evaluated with $|\vec{l_-}|$ and $|\vec{k}'|$ given in Eqs. (3.19) and (3.20), respectively.

Of course, one has to ensure that in the numerical calculation only physically allowed solutions are found. For this purpose, several checks are applied. As implied by the Dirac δ function, four-momentum conservation must be fulfilled. Furthermore, the components of the external four-momenta need to be real valued numbers. Hence, it is checked during the calculation that the arguments of the square roots in Eqs. (3.17) and (3.19) are positive numbers. In addition, it is tested that the energies of the four-vectors are larger than the corresponding rest masses.

Equation (3.23) is applied to calculate integrated cross sections within the acceptances of detectors. The integrations over the angular acceptances are performed within a small range of few mrad. Moreover, the momentum acceptance corresponds to a relatively small range. As an example, for the A1 experiment at MAMI, momentum moduli deviating up to 10% from the central value are allowed and the angular acceptance is up to 21 msr. In addition, the central values are chosen in such a way that the kinematical setting is physically allowed. Hence, it is not necessary to calculate the lower and upper bounds of each integration variable as a function of the other ones.

3.3.3 Decomposition of the cross section

The dynamics of the cross section which can be observed experimentally is described by the Feynman amplitudes given in Eq. (3.8) for a nuclear target and in Eq. (3.9) for a proton target. Although only the cross section containing all interference terms can be observed, it is useful to decompose it into isolated contributions originating from the amplitudes in Eqs. (3.1), (3.2) and (3.5) to (3.7). Therefore, as a first step, the differential cross section in general can be rewritten as

$$d\sigma_{\gamma^*+\gamma'} = d\sigma_{\gamma^*} + d\sigma_{\gamma'} + d\sigma_{\gamma^*\gamma'}, \tag{3.24}$$

where

$$d\sigma_{\gamma^*} \propto \overline{|\mathcal{M}_{\gamma^*}|^2} \quad \text{and} \quad d\sigma_{\gamma'} \propto \overline{|\mathcal{M}_{\gamma'}|^2}$$

denote the QED background cross section and the cross section for pair production from hidden photon emission, respectively. The quantity

$$d\sigma_{\gamma^*\gamma'} \propto \overline{|\mathcal{M}_{\gamma^*+\gamma'}|^2} - \overline{|\mathcal{M}_{\gamma^*}|^2} - \overline{|\mathcal{M}_{\gamma'}|^2}$$

is the interference term between those two contributions.

As discussed in Sec. 3.2, the contribution of a spacelike hidden photon to the signal cross section is negligible. Because of the very narrow width entering in the propagators of Eqs. (3.1) and (3.2), the dependence of the signal cross section on the invariant mass of the lepton pair can be approximated by a Dirac δ function. A detailed discussion is given in Appendices B.1 and B.3. It was found numerically for $\varepsilon^2 \leq 10^{-4}$ that the approximation agrees within the numerical precision of around 0.5% for a wide range of configurations. As a consequence, the contribution of the exchange term (X) to the cross section is vanishingly small and can be neglected as well. Thus, one can rewrite the signal cross section as

$$d\sigma_{\gamma'} = d\sigma^{\mathrm{SL+TL+VVCS}}_{\mathrm{D+X},\gamma\gamma'} = d\sigma^{\mathrm{TL+VVCS}}_{\mathrm{D},\gamma'} \propto \overline{\left|\mathcal{M}^{\mathrm{TL}}_{\mathrm{D},\gamma'} + \mathcal{M}^{\mathrm{VVCS}}_{\mathrm{D},\gamma'}\right|^2}, \tag{3.25}$$

for a proton target and

$$d\sigma_{\gamma'} = d\sigma^{\mathrm{SL+TL}}_{\mathrm{D+X},\gamma'} = d\sigma^{\mathrm{TL}}_{\mathrm{D},\gamma'} \propto \overline{\left|\mathcal{M}^{\mathrm{TL}}_{\mathrm{D},\gamma'}\right|^2}. \tag{3.26}$$

for a heavy nuclear target.

In addition, the interference term $d\sigma_{\gamma^*\gamma'}$ between virtual photon and hidden photon emission in case of a bump search can be neglected. The very narrow decay width of the hidden photon causes that this contribution is vanishingly small compared to $d\sigma_{\gamma'}$. It was checked that $d\sigma_{\gamma^*\gamma'}$ is well below the numerical accuracy.

For convenience, one defines the following quantities to understand the kinematical dependence of the QED background in more detail:

$$d\sigma^{\mathrm{TL}}_{\mathrm{D/X},\,\gamma^*} \propto \overline{\left|\mathcal{M}^{\mathrm{TL}}_{\mathrm{D/X},\,\gamma^*}\right|^2}, \tag{3.27a}$$

$$d\sigma^{\mathrm{SL}}_{\mathrm{D/X},\,\gamma^*} \propto \overline{\left|\mathcal{M}^{\mathrm{SL}}_{\mathrm{D/X},\,\gamma^*}\right|^2}, \tag{3.27b}$$

$$d\sigma^{\mathrm{VVCS}}_{\mathrm{D/X},\,\gamma^*} \propto \overline{\left|\mathcal{M}^{\mathrm{VVCS}}_{\mathrm{D/X},\,\gamma^*}\right|^2}. \tag{3.27c}$$

Furthermore,

$$d\sigma_{\mathrm{D/X},\,\gamma^*} \propto \overline{\left|\mathcal{M}^{\mathrm{SL+TL}}_{\mathrm{D/X},\,\gamma^*}\right|^2},$$

and

$$d\sigma_{\mathrm{D/X},\,\gamma^*} \propto \overline{\left|\mathcal{M}^{\mathrm{SL+TL+VVCS}}_{\mathrm{D/X},\,\gamma^*}\right|^2},$$

denote the isolated direct and exchange contributions to the background cross sections for a nuclear target and a proton target, respectively. By means of these quantities, the background cross section can be split as

$$d\sigma_{\gamma^*} = d\sigma_{\mathrm{D},\,\gamma^*} + d\sigma_{\mathrm{X},\,\gamma^*} + d\sigma_{\mathrm{DX},\,\gamma^*}, \tag{3.28}$$

where $d\sigma_{\mathrm{DX},\,\gamma^*}$ is the interference term between the direct and exchanged contributions $d\sigma_{\mathrm{D},\,\gamma^*}$ and $d\sigma_{\mathrm{X},\,\gamma^*}$. In addition, $d\sigma_{\mathrm{D},\,\gamma^*}$ and $d\sigma_{\mathrm{X},\,\gamma^*}$ can be further decomposed as

$$d\sigma_{\mathrm{D/X},\,\gamma^*} = d\sigma^{\mathrm{TL}}_{\mathrm{D/X},\,\gamma^*} + d\sigma^{\mathrm{SL}}_{\mathrm{D/X},\,\gamma^*} + d\sigma^{\mathrm{TLSL}}_{\mathrm{D/X},\,\gamma^*}, \tag{3.29}$$

where $d\sigma^{\mathrm{TLSL}}_{\mathrm{D/X},\,\gamma^*}$ corresponds to the interference contribution. Although none of these isolated contribution can be accessed directly in experiments, it is crucial to understand their individual kinematical behavior in order to improve the signal to background ratio.

3.4 Discussion of the integrated cross sections and comparison with experimental data

3.4.1 Calculation of acceptance integrated cross sections

To describe experimental data and to obtain realistic predictions one has to integrate the differential cross sections within the particular experimental acceptances. Hence, the differential cross sections of Eqs. (3.13) and (3.23) have to be integrated over the part of phase space which can be investigated in the particular experimental settings. The resulting integral can only be solved numerically. As an example, in the lab frame one has to evaluate the integral of Eq. (3.23) which yields

$$\begin{aligned}\Delta\sigma = \int_{|\vec{l_+}|_0-\Delta|\vec{l_+}|}^{|\vec{l_+}|_0+\Delta|\vec{l_+}|} d|\vec{l_+}| \int_{4\pi} d\Omega_{e'} \int_{\Delta\Omega_+} d\Omega_+ \int_{\Delta\Omega_-} d\Omega_- \int_{m_{\gamma'}-\delta m/2}^{m_{\gamma'}+\delta m/2} dm_{ll} \\ J(\delta\phi_-,\,\delta\theta_-)\,J(\delta\phi_+,\,\delta\theta_+)\;\frac{d^8\sigma}{d|\vec{l_+}|\,d\Omega_+\,d\Omega_-\,d\Omega_{e'}\,dq'^2}\Bigg|_{|\vec{l_-}|_0-\Delta|\vec{l_-}|}^{|\vec{l_-}|_0+\Delta|\vec{l_-}|}.\end{aligned} \tag{3.30}$$

The acceptance integrated cross section $\Delta\sigma$ determined in Eq. (3.30) corresponds to an experiment in which only the lepton pair is detected. The detector coordinates discussed in Appendix B.2 are used for the momenta of the lepton pair $l_\pm$ in Eq. (3.30). This allows one to calculate the integral only over the phase space region which is covered by the detectors, e.g., in an experiment at MAMI. The integration region associated with the solid angle $\Delta\Omega_\pm$ corresponds to the angular acceptance of the detector in these coordinates. The momentum integration is restricted to the range resulting from the detector acceptance $|\vec{l_\pm}|_0 - \Delta|\vec{l_\pm}| \leq |\vec{l_\pm}| \leq |\vec{l_\pm}|_0 + \Delta|\vec{l_\pm}|$, where $|\vec{l_\pm}|_0$ is the central momentum of the setup. The δ function was used to eliminate the dependence of the cross section on the energy E_- during the derivation of Eq. (3.23). The cross section has to be computed on condition that the modulus of the momentum of the created negatively charged lepton is within the range allowed experimentally. Since the scattered lepton from the beam in the direct Feynman diagrams is not detected, one has to integrate over the full solid angle for this particle. In addition, an integration over the invariant mass of the lepton pair m_{ll} has to be performed. In Eq. (3.30) this is done in the range $m_{\gamma'} - \delta m/2 \leq m_{ll} \leq m_{\gamma'} + \delta m/2$, where $m_{\gamma'}$ corresponds to the central value of this mass bin.

Numerous peaked structures originate from the propagators in the amplitudes derived in Sec. 3.2. To deal with these and the complicated phase space with four particles in the final state, the integration was performed on graphics processing units (GPUs). For this purpose the NVIDIA CUDA framework [199] and the implementation of the VEGAS algorithm [186] on GPUs published in Ref. [187] were used. The common way to integrate over the phase space of an reaction involving n particles in the final state is by means the recursive approach leading to Eq. (3.13). For the numerical calculations on GPUs the integral of Eq. (3.23) is used. This is due to the particular structure which programs should have for best performance when run on GPUs.

GPUs are designed to perform a large number of common operations in parallel at the same. To reduce the idle time it is crucial that as many parts of the integration region as possible are allowed. In the approach by means of Eq. (3.13) this is not the case, even after optimizing the variables. The integral in the parametrization of Eq. (3.23), on the contrary, automatically contains nearly only the region of the phase space accepted by the experimental cuts. Since the method using Eq. (3.13) is well understood, this approach was used as a cross check for the method solving the integral in Eq. (3.30). The methods to prepare programming code for the execution on GPUs are discussed in more details in Appendix C.

3.4.2 Discussion of the acceptance integrated cross section

In this section the dependence of the acceptance integrated cross section on the actual kinematics is discussed in more detail for the signal and the background process. An understanding of these dependencies is crucial to perform experiments in the setup, which is best suited to search for signatures of hidden photons. A similar analysis was done in Ref. [140], where the Weizsäcker–Williams approximation and further simplifications were applied for the cross section. In the present discussion, no further approximations than those for the hadronic state are applied (see Sec. 3.2). As discussed, the dominating contribution results from coherent scattering off the nucleus. The inelastic contribution leads to slightly different cross sections. However, the shape of the cross section is not altered. While these effects do not play a role in this section, they cannot be neglected in the next section where the simu-

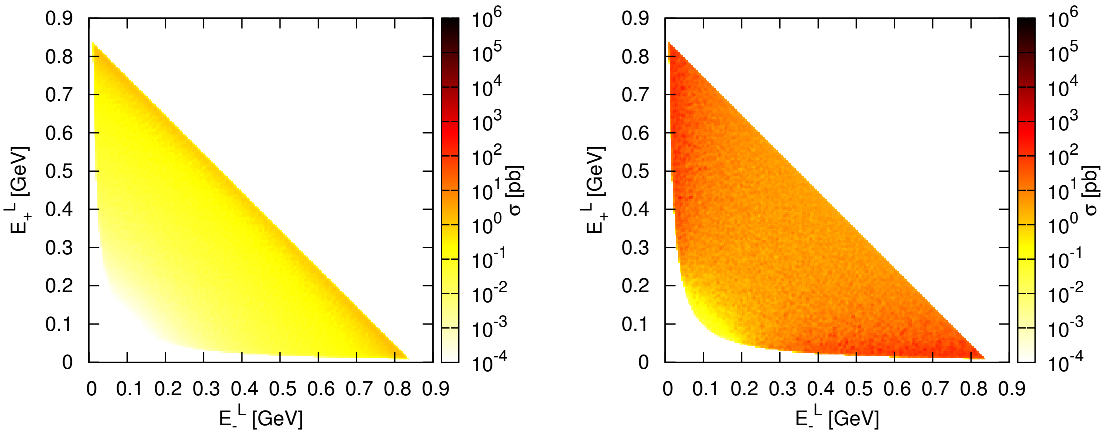

Figure 3.3: Integrated cross section as a function of the energy carried by the detected leptons for a beam energy of $E_0 = 855\,\mathrm{MeV}$ in the mass range $200\,\mathrm{MeV} \leq m_{ll} \leq 300\,\mathrm{MeV}$ and hidden photon emission along the beam axis, i.e. for a polar angle of the hidden photon of $\theta_{\gamma'} \leq 0.5\,\mathrm{rad}$, in $(0.4275\,\mathrm{MeV} \times 0.4275\,\mathrm{MeV})$ bins. Left (right) panel: Timelike (spacelike), direct contribution $\Delta\sigma^{\mathrm{TL}}_{\mathrm{D},\gamma^*}$ ($\Delta\sigma^{\mathrm{SL}}_{\mathrm{D},\gamma^*}$) to the QED background cross section.

lation is compared to data taken at MAMI. It was found by comparison that the uncertainty due to different parametrizations of the form factors and from inelastic effects is below 5% for the studied setup at MAMI.

Furthermore, the analysis of the kinematical dependencies is extended to the exchange contribution originating from the indistinguishability of the final-state leptons of equal charge and species compared to the studies in the literature.

The cross section for the creation of a hidden photon from the reaction $e(A, Z) \to e(A, Z)\gamma'$ was discussed in Secs. 2.1.3 and 2.2.2. It was found that the signal cross section is largest, when the hidden photon is emitted along the beam axis and nearly all of the beam energy is transferred to it, corresponding to $\theta^L_{q'} \simeq 0°$ and $x = E_{q'}/E_0 \simeq 1$. Obviously, this has to be taken into account for the arrangement of kinematical settings.

A possible γ' signal results from the exchange of a timelike hidden photon as described by Eqs. (3.1) and (3.2). Equation (3.34) indicates that the signal is proportional the background contribution $\Delta\sigma^{\mathrm{TL}}_{\gamma^*,D}$. Hence, this background cannot be reduced. The photon and off-shell hidden photons are timelike particles in this contribution . This provokes that the Bethe-Heitler peaks are not present and a suppression by the virtuality occurs. Therefore, the discussion of the kinematical dependence of $\Delta\sigma^{\mathrm{TL}}_{\gamma^*,D}$ can be directly translated into the kinematics of $\Delta\sigma_{\gamma'}$. However, because of the different structure of the amplitudes in Eqs. (3.5) and (3.6), the $\Delta\sigma^{\mathrm{SL}}_{\gamma^*,D}$ background contribution can be reduced by an appropriate choice of the kinematics.

The integrated cross section $\Delta\sigma^{\mathrm{TL}}_{\mathrm{D},\gamma^*}$ ($\Delta\sigma^{\mathrm{SL}}_{\mathrm{D},\gamma^*}$) is shown as a function of the energies of the detected leptons in the left (right) panel of Fig. 3.3. The calculation was performed for a beam energy of $E_0 = 855\,\mathrm{MeV}$ and an invariant mass of the lepton pair in the range

$200\,\text{MeV} \leq m_{ll} \leq 300\,\text{MeV}$. In addition, the hidden photon shall be emitted along the beam axis with $\theta_{\gamma'} \leq 0.5\,\text{rad}$. The timelike contribution $\Delta\sigma^{\text{TL}}_{\text{D},\gamma^*}$ is largest when the detected leptons carry most of the beam energy ($x \simeq 1$). This was expected from the discussion in Secs. 2.1.3 and 2.2.2. Therefore, in the following the condition $x = 1 \Leftrightarrow E_- = E_0 - E_+$ will be used. Furthermore, no strong dependence on the distribution of the energy onto the two leptons can be found.

The situation is completely different for the spacelike contribution to the background cross section. As can be seen from the right panel of Fig. 3.3, this contribution is largest, if $x \simeq 1$ and nearly all energy is carried by only one of the detected leptons. This can be easily understood. In this case one of the lepton propagators in Eq. (3.6) peaks and the SL contribution dominates the cross section. Experimental setups are chosen in such a way that the energy is shared symmetrically between the leptons to reduce the SL contribution [152,153]. However, the spacelike contribution $\Delta\sigma^{\text{SL}}_{\text{D},\gamma^*}$ strongly dominates over $\Delta\sigma^{\text{TL}}_{\text{D},\gamma^*}$ also in the optimized kinematics. Thus, one always has to deal with a large irreducible QED background.

Neglecting the lepton mass, the polar angle of the hidden photon with respect to the beam axis can be calculated from the three-momenta of the detected leptons:

$$\begin{aligned}\theta_{\gamma'} &= \cos^{-1}\left(\frac{|\vec{l_+}\,|\cos\theta_+ + |\vec{l_-}\,|\cos\theta_-}{|\vec{l_+}\,| + |\vec{l_-}\,|}\right)\\ &\simeq \cos^{-1}\left(\frac{1}{2}\left(\frac{E_+}{E_0}\cos\theta_+ + (1-\frac{E_+}{E_0})\cos\theta_-\right)\right).\end{aligned}$$

Furthermore, if $E_- \simeq E_+$ is chosen, one directly sees that the emission angle of the hidden photon simplifies to

$$\theta_{\gamma'} = \cos^{-1}\left(\frac{\cos\theta_+ + \cos\theta_-}{2}\right).$$

For a symmetrical setup one finds

$$\theta_{\gamma'} = \theta_\pm.$$

As a consequence, the expected signal cross section is largest for the setup in which the detectors are placed as close as possible to the beam axis.

If the beam lepton and the leptons of the pair are of the same species, one has to account for the exchange term (X) given by the Feynman diagrams in Fig. 3.2. This contribution results from the fact that the two negatively charged leptons cannot be distinguished. Unfortunately, a clear separation between the signal process and the background is not possible for this contribution. The corresponding amplitudes contain the same structures the signal cross section, which can be easily seen from the Feynman diagrams in Fig. 3.2. Because of the exchange of the final-state lepton momenta, the amplitude describing the signal $\mathcal{M}^{\text{TL}}_{\text{D},\gamma'}$ as well as the background contributions $\mathcal{M}^{\text{TL}}_{\text{D},\gamma^*}$ and $\mathcal{M}^{\text{SL}}_{\text{X},\gamma^*}$ include a structure

$$\frac{\not{k} - \not{l}_- - \not{l}_+ + m}{(k - l_- - l_+)^2 - m^2},$$

contributing to the irreducible background. This gives rise to a large contribution from $\mathcal{M}^{\text{SL}}_{\text{X},\gamma^*}$ in the case of forward γ' production, since the denominator of the propagator is close to zero. As mentioned in Sec. 3.3.3, the signal cross section is not enhanced. In Fig. 3.4

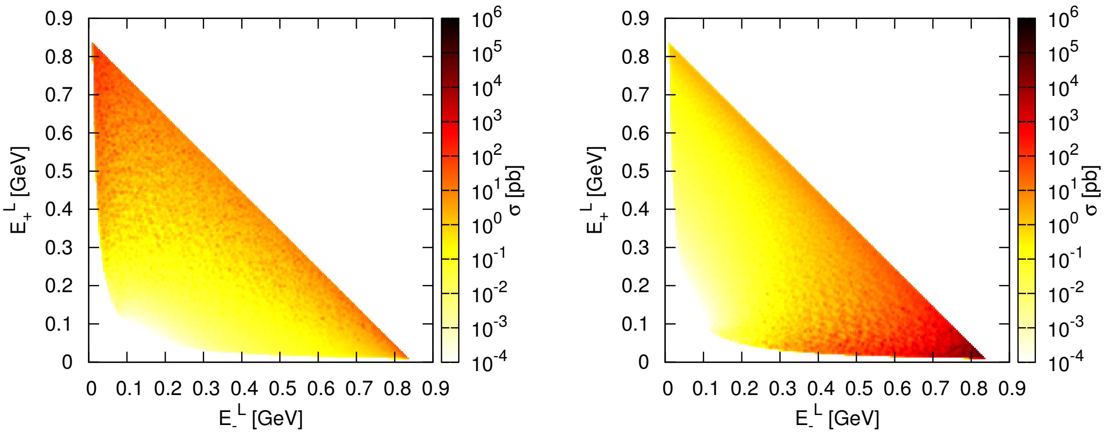

Figure 3.4: Same as in Fig. 3.3 for the TL and SL exchange term X.

	Spec. A (e^-)		Spec. B (e^+)	
	$\lvert\vec{l_-}\rvert$ (MeV)	ϕ_0	$\lvert\vec{l_+}\rvert$ (MeV)	ϕ_0
setup 1	346.3	22.8°	507.9	15.2°
setup 2	338.0	22.8°	469.9	15.2°

Table 3.1: Kinematical settings of the MAMI test run in 2010. The beam energy was $E_0 = 855\,\mathrm{MeV}$, and the settings are roughly centered around $E_{e^+} + E_{e^-} = E_0$ and $m_{\gamma'} = 250\,\mathrm{MeV}$. The values are taken from Ref. [152]

the integrated cross sections $\Delta\sigma^{\mathrm{TL}}_{\mathrm{X},\gamma^*}$ and $\Delta\sigma^{\mathrm{SL}}_{\mathrm{X},\gamma^*}$ are shown for the same setting as used for Fig. 3.3. These quantities are large for both the symmetric as well as the asymmetric production of the lepton pair. This illustrates that these contributions cannot be separated by an appropriate choice of the kinematical setting from the signal as in the case of $\Delta\sigma^{\mathrm{SL}}_{\mathrm{D},\gamma^*}$. Accordingly, it is impossible to reduce the background from the exchange term.

3.4.3 Comparison of the theory calculation with experimental data from MAMI

Spec.	momentum	horizontal angle	vertical angle	$d\Omega$
A	±10%	±75 mrad	±70 mrad	21 msr
B	±7.5%	±20 mrad	±70 mrad	5.6 msr

Table 3.2: Acceptances of the spectrometers A and B at MAMI [200].

A first test run to investigate the feasibility of a dedicated γ' search fixed-target experiment

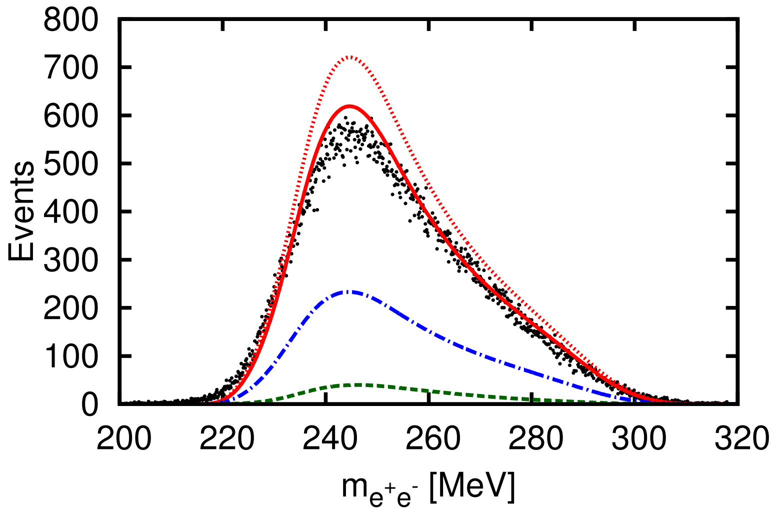

Figure 3.5: Comparison of theory calculations and experimental data for a $m_{e^+e^-}$ bin width of 0.125 MeV. Black points: Data taken in a particular run of the MAMI 2010 experiment [152] in setup 1. Red solid curve: Theory calculation of the background cross section. Red dotted curve: Theory calculation of the background cross section without radiative corrections. Blue dashed-dotted curve: Theory calculation of the direct SL + TL cross section. Green dashed curve: Theory calculation of the direct TL cross section.

was performed at MAMI by the A1 Collaboration in 2010. No evidence for the existence of the γ' could be found in this experiment. Hence, an exclusion limit for the γ' parameter space was evaluated [152]. The heavy nucleus tantalum with $Z = 73$, $A = 181$, and $M \cong 168\,\text{GeV}$ served as a target for this experiment. The spectrometers A and B [200] were used to detect the lepton pair in the settings of Table 3.1. Therefore, the integral of Eq. (3.30) was evaluated within the limits given in Table 3.2 to calculate the acceptance integrated cross section $\Delta\sigma$.

To cross-check the simulation, experimental data were provided by the A1 Collaboration. In addition, the corresponding event generator for this experiment applied by A1 is based on the results of this work. Since the simulations were performed by two independent programs, this serves as a further cross check.

In order to reproduce the data more accurately, one has to account for radiative corrections. The calculation of the full radiative corrections to the process $e(A, Z) \to e(A, Z)l^+l^-$ is beyond the scope of this work. Hence, the radiative corrections of the corresponding elastic scattering process were applied to obtain a crude estimate of the expected effects. The following discussion will focus on the kinematics of the MAMI 2010 test run.

The leading-order radiative corrections for the elastic electron-proton (ep) scattering were discussed in Sec. 2.4.1. To summarize, the corrections can be grouped into the virtual corrections including self-energy diagrams and vacuum polarization, vertex corrections, and the correction from soft-photon emission (see Fig. 2.15). The resulting finite corrections found in Ref. [175] were given in Eqs. (2.39) to (2.41). Hence, the differential cross sections

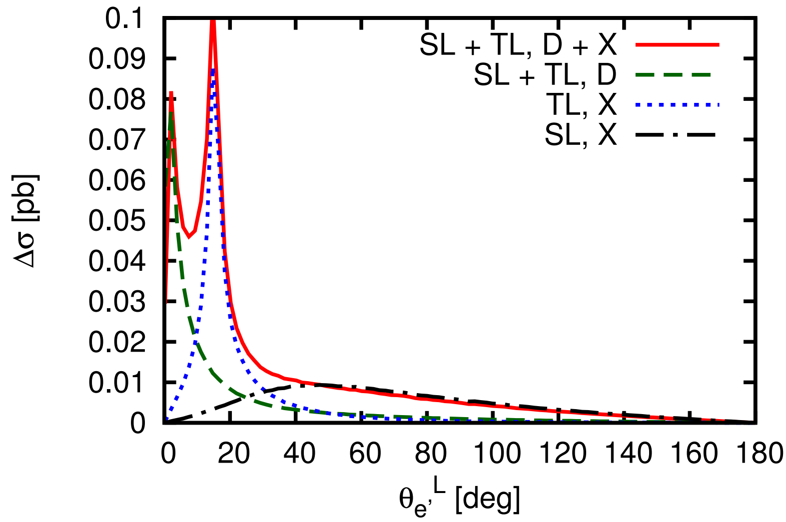

Figure 3.6: Angular distribution per 0.5° with respect to the polar angle of the scattered electron for the MAMI 2010 experiment.

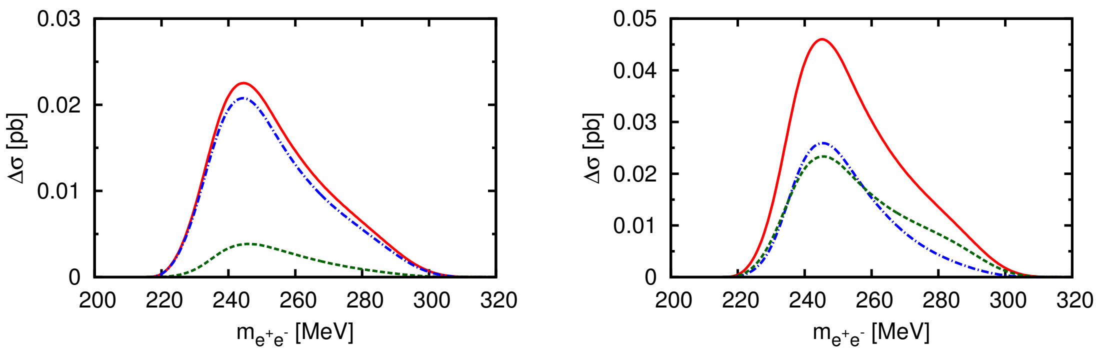

Figure 3.7: Calculated direct (left panel) and exchange (right panel) term of the cross section assuming distinguishable electrons in the final state. Solid curve: SL + TL cross section. Dashed curve: TL. Dashed-dotted curve: SL

(see Eqs. (3.13) and (3.23)) are multiplied by

$$(1+\delta_1) = 1 + \delta_{vac} + \delta_{vertex} + \delta_R.$$

As discussed in Sec. 2.4.1, δ_R depends on the actual choice of the cut-off energy $\Delta E'$. An appropriate choice for this experimental setup is $\Delta E' = 0.01 \times E_0$. The cross check with the experimental data is passed for this value. Furthermore, the energy resolution of the detectors is better than this value and it is well below the pion threshold [175, 196]. Of course, the normalization of the cross section depends on the particular choice of $\Delta E'$. It is important to mention that the value of $\Delta E'$ was chosen in advance motivated from the existing calculations for VCS experiments [175] and elastic scattering [196]. In particular, no fit to the data was performed to adjust $\Delta E'$.

As can be seen from Table 3.1, in the chosen kinematics nearly all of the beam energy is transferred onto the e^+e^- pair. Because of the particular choice of kinematics, the moduli of the logarithms in entering in Eqs. (2.39) to (2.41) are large. Therefore, a large contribution results from the soft-photon emission where the logarithms enter quadratically.

As discussed in Sec. 2.4.2, the corresponding corrections to the process $ep \to ep\gamma$ contain the same basic building blocks. The same building blocks occur in the process $e(A, Z) \to e(A, Z)l^+l^-$ at the lepton side. Due to the choice of a symmetrical setup, the l^+l^- pair can be considered as a neutral object which does not radiate in a first crude approximation. Hence, one expects that the largest soft photon corrections arise from the emission off the beam. Moreover, the emission of soft photons from the nucleus was neglected. The recoil onto the nucleus is small compared to the mass ($Q_t^2/M^2 < 10^{-6}$). Thus, the target will stay at rest and does not radiate.

For ep-scattering, such radiative corrections typically lead to a reduction of the cross section in the range of 10%–20% for $\Delta E' = 0.01 \times E_0$ in the investigated kinematics [175, 201]. However, for a more accurate description of the data one has to calculate the full radiative corrections. The approximate treatment discussed above needs to be understood as a semiclassical estimate. As an example, quantum effects such as the antisymmetrization of the amplitude are not accounted for in this approach.

A sample of the data taken in this experiment compared to the results of this work can be seen in Fig. 3.5. The data were provided by the A1 Collaboration. Setup 1 as given in Ref. [152] was chosen, since for this setup a luminosity measurement was performed, finding an integrated luminosity of $\mathcal{L} = 41.4\,\mathrm{fb}^{-1}$ for the selected sample of events. A background contribution of around 5% was already subtracted from the data points in this sample. The systematic uncertainty in the luminosity from the knowledge of the thickness of the target foil is below 5% [152].

As seen in Fig. 3.5, the calculation (solid curve) of the radiative background given by $\Delta\sigma^{\mathrm{TL+SL}}_{\mathrm{D+X},\gamma^*}$ and the experimental data (points) are in good agreement. Because of the estimate of the radiative corrections and the nuclear current the discrepancy between theory and data was expected. The influence of the radiative corrections is displayed by the red solid and dotted curves in Fig. 3.5 which have been calculated with and without radiative corrections, respectively. One notices from Fig. 3.5 that the applied radiative corrections lower the result of the theory calculation by an amount of around 10%. As mentioned before, this value is strongly depending on the actual choice of the energy cut off ΔE_s.

One can see from Fig. 3.5 that the approximate treatment of the radiative corrections already provides a good approximation, as theory and data already are in good agreement.

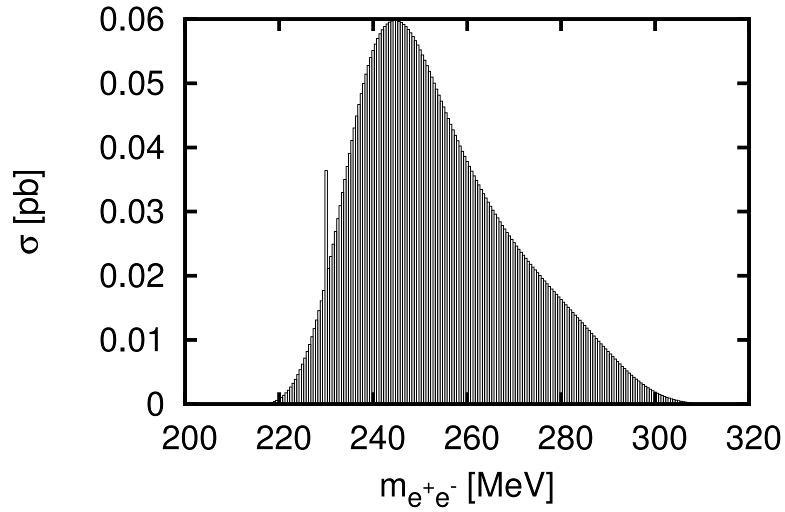

Figure 3.8: Simulation of a signal from a hidden photon with $m_{\gamma'} = 230\,\mathrm{MeV}$ and $\varepsilon^2 = 10^{-4}$ in the kinematics of the MAMI 2010 test run.

The data and the simulation agree within 15% or less for the largest part of the invariant mass range ($220\,\mathrm{MeV} \leq m_{e^+e^-} \leq 300\,\mathrm{MeV}$) with $\delta m = 0.5\,\mathrm{MeV}$.

The dashed (dashed-dotted) curve shows the direct TL (SL + TL) cross section $\Delta^{\mathrm{TL}}_{\mathrm{D},\gamma^*}$ ($\Delta^{\mathrm{TL+SL}}_{\mathrm{D},\gamma^*}$). One clearly sees the expected large contribution to the cross section originating from the antisymmetrization due to the indistinguishability of the scattered beam electron and the pair electron. The kinematical setting was optimized to reduce the SL background [152] relying on the expressions given in App. C of Ref. [140]. These expressions were derived within the framework of the WW approximation, and do not account for the exchange term contribution. Hence, the setup of the test run was not the best one for probing a region of parameter space as large as possible.

The angular distribution with respect to the polar angle of the scattered electron is presented in Fig. 3.6. For the 2010 A1 experiment the crossed TL amplitude is responsible for a second peak in the background cross section compared to the direct amplitude (dashed curve), which only peaks at very forward scattering followed by a rapidly dropping tail. The exchange SL term enhances the tail of the angular distribution significantly. Fig. 3.7 reveals that in the chosen kinematical setting the exchange term contribution is about twice as large as the direct SL part, which initially should be minimized.

3.5 Exclusion limits from fixed-target experiments: Results and predictions

3.5.1 Calculation of exclusion limits

Figure 3.8 illustrates the signature expected from a hidden photon with $m_{\gamma'} = 230\,\mathrm{MeV}$ and $\varepsilon^2 = 10^{-4}$ in the kinematics of the MAMI 2010 test run. Due to the very narrow decay width of the hidden photon the caused excess is restricted to one mass bin. Furthermore, the background can be described by a smooth, slowly varying function. Note that the parameters used for this simulation are already excluded, as can be seen from Fig. 1.19.

If no such signature is found in the invariant mass distribution of the lepton pair, one can calculate an exclusion limit for the parameter space. In this thesis two different ways are applied to find an upper bound on the kinetic mixing factor ε^2 as a function of $m_{\gamma'}$:

- Approximation of $\Delta\sigma_{\gamma'}$ by an analytical integration over a small mass window, which was first demonstrated in Eq. (19) of Ref. [140]. One exploits that, due to the narrow decay width of the hidden photon, the Breit-Wigner resonance curve can be approximated by a Dirac δ function.

- Evaluation of $\Delta\sigma_{\gamma'}$ for a fixed value of ε^2 and re-weighting the signal cross section, which utilizes that the hidden photon peak is described by a Breit-Wigner resonance.

Of course, both approaches must lead to the same result. In the following, the expressions for the upper limits for ε^2 are derived.

In a first step one decomposes the cross section which can be accessed experimentally analogously to Eq. (3.24),

$$\Delta\sigma_{\gamma^*+\gamma'} = \Delta\sigma_{\gamma^*} + \Delta\sigma_{\gamma'} + \Delta\sigma_{\gamma^*\gamma'}, \tag{3.31}$$

into a contribution from the QED background $\Delta\sigma_{\gamma^*}$, the isolated signal cross section $\Delta\sigma_{\gamma'}$ and the interference term $\Delta\sigma_{\gamma^*\gamma'}$. As discussed in Sec. 3.3.3, the interference contribution can be safely neglected. Dividing Eq. (3.31) by the background cross section $\Delta\sigma_{\gamma^*}$ gives

$$\begin{aligned} \frac{\Delta\sigma_{\gamma^*+\gamma'}}{\Delta\sigma_{\gamma^*}} &= \frac{\Delta\sigma_{\gamma^*}}{\Delta\sigma_{\gamma^*}} + \frac{\Delta\sigma_{\gamma'}}{\Delta\sigma_{\gamma^*}} \\ \Leftrightarrow \quad \frac{\Delta\sigma_{\gamma'}}{\Delta\sigma_{\gamma^*}} &= \frac{\Delta\sigma_{\gamma^*+\gamma'}}{\Delta\sigma_{\gamma^*}} - 1. \end{aligned} \tag{3.32}$$

The term $S := {}^{\Delta\sigma_{\gamma^*+\gamma'}}/_{\Delta\sigma_{\gamma^*}} - 1$ describes the magnitude of an excess above the QED background which corresponds to the sensitivity of an experiment. This quantity must be determined from the experimental data. In order to obtain predictions, the sensitivity can be estimated by the background cross section, the luminosity L, and the number of standard deviations N_σ which fixes whether or not a fluctuation is considered as a signal. The aimed sensitivity can be expressed as the number of expected signal events over the number of background events. The minimal number of signal events which allows one to observe a peak over the smooth background corresponds to one standard deviation of the background distribution. This quantity is commonly estimated by the square root of background events in a mass bin [152, 188, 202]. Hence, one finds for the aimed sensitivity:

$$S = \frac{N_\sigma \times \Delta\sigma_{\gamma^*} \times L}{\sqrt{\Delta\sigma_{\gamma^*} \times L}} = \frac{N_\sigma}{\sqrt{\Delta\sigma_{\gamma^*} \times L}}. \tag{3.33}$$

Up to this point, the discussion for both approaches to calculate exclusion limits is equal. In the following, an expression for an upper limit of ε^2 using the concept of Ref. [140] is derived. In this approach, the signal cross section is estimated by the timelike contribution

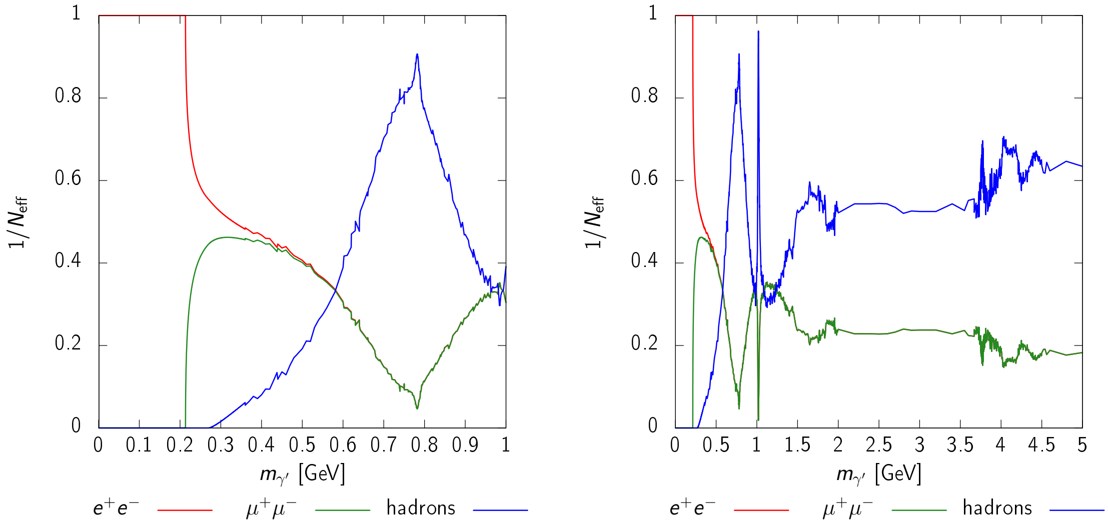

Figure 3.9: Dependence of the inverse effective degrees of freedom $1/N_{\text{eff}}$ for e^+e^- pairs (red curve), $\mu^+\mu^-$ pairs (green), and hadrons (blue) on the hidden photon mass. The signal cross section $\Delta\sigma_{\gamma'}$ depends linearly on this quantity after integration over the variables of the lepton pair and the invariant mass m_{ll}. The irregular shape for large masses originates from the uncertainty in R.

to the direct term of the background cross section $\Delta\sigma^{\text{TL}}_{D,\gamma^*}$, which is given by Eq. (19) of Ref. [140]:

$$\frac{d\sigma_{\gamma'}}{d\sigma^{\text{TL}}_{D,\gamma^*}} \simeq \frac{3\pi}{2N_{\text{eff}}}\frac{\varepsilon^2}{\alpha}\frac{m_{\gamma'}}{\delta m}. \tag{3.34}$$

δm is the mass resolution of an experiment and N_{eff} accounts for additional degrees of freedom in the decay of the hidden photon into SM particles.

For this treatment it is required that the background cross section does not vary too strongly in the considered invariant-mass range. The remaining variables are treated as constants. Thus, the considered approximation is valid for sufficient small intervals of the invariant mass of the lepton pair m_{ll}. The range of these intervals corresponds to the mass resolution of an experiment. Typically, this is at the level of 1 MeV to 5 MeV. Furthermore, one demands that the total decay width of the hidden photon is much smaller than its mass, $\Gamma_{\gamma'} \ll m_{\gamma'}$. This condition is automatically fulfilled in the considered minimal model, as the discussion of the decay width in Sec. 1.3.3 and in particular Fig. 1.17 shows. As one can see from Fig. 1.19, a lower limit for the hidden photon mass in the non-excluded regions of parameter space is $m_{\gamma'} \lesssim 5\,\text{MeV}$. For this value only $\varepsilon^2 \lesssim 10^{-5}$ is still allowed. Since the decay width is growing only linearly with the hidden photon $m_{\gamma'}$ and $\varepsilon^2 \gtrsim 10^{-4}$ is excluded in the full considered parameter space, the condition $\Gamma_{\gamma'} \ll m_{\gamma'}$ is always matched in the mass range of interest. Conveniently, N_{eff} can be parametrized by

$$N_{\text{eff}} = \begin{cases} \Gamma_{\gamma'}/\Gamma_{\gamma' \to e^+e^-} & \text{for } e^+e^- \text{ pairs,} \\ \Gamma_{\gamma'}/\Gamma_{\gamma' \to \mu^+\mu^-} & \text{for } \mu^+\mu^- \text{ pairs,} \\ \Gamma_{\gamma'}/\Gamma_{\gamma' \to \text{had.}} & \text{for hadrons,} \end{cases}$$

where $\Gamma_{\gamma' \to l^+l^-}$ and $\Gamma_{\gamma'}$ are given in Eqs. (1.31) and (1.34) and the decay width to hadrons is parametrized by

$$\Gamma_{\gamma' \to \text{had.}} = \Gamma_{\gamma' \to \mu^+\mu^-} \times R(m_{\gamma'}).$$

Figure 3.9 illustrates the dependence of $1/N_{\text{eff}}$ on the hidden photon mass $m_{\gamma'}$. The effective degrees of freedom for the decay channel into electron-positron pairs are illustrated by the red curve. The green and blue curves depict $1/N_{\text{eff}}$ for decays of the hidden photon into $\mu^+\mu^-$ pairs and hadrons, respectively.

In the following, the discussion will focus on hidden photon decays into e^+e^- pairs. All studied experimental setups will investigate electrons and positrons in the final state. In addition, the HPS experiment will also search for $\mu^+\mu^-$ pairs.

The derivation of relation (3.34) is presented in Appendix B.1 in detail. Using Eq. (3.34), one can rewrite Eq. (3.32) as

$$S = \frac{\Delta\sigma_{\gamma'}}{\Delta\sigma_{\gamma^*}} = \frac{\Delta\sigma_{\gamma'}}{\Delta\sigma^{\text{TL}}_{D,\gamma^*}} \frac{\Delta\sigma^{\text{TL}}_{D,\gamma^*}}{\Delta\sigma_{\gamma^*}} = \frac{3\pi}{2N_{\text{eff}}} \frac{\varepsilon^2}{\alpha} \frac{m_{\gamma'}}{\delta m} \frac{\Delta\sigma^{\text{TL}}_{D,\gamma^*}}{\Delta\sigma_{\gamma^*}},$$

and thus

$$\varepsilon^2 = S \frac{\Delta\sigma_{\gamma^*}}{\Delta\sigma^{\text{TL}}_{D,\gamma^*}} \frac{2N_{\text{eff}}\alpha}{3\pi} \frac{\delta m}{m_{\gamma'}}. \tag{3.35}$$

This expression is only valid, if the conditions $m_{\gamma'} \gg m_e$ and $\delta m \ll m_{\gamma'}$ apply. If these conditions are not fulfilled, Eq. (3.35) can be improved to

$$\varepsilon^2 = S \frac{\Delta\sigma_{\gamma^*}}{\Delta\sigma^{\text{TL}}_{D,\gamma^*}} \frac{2N_{\text{eff}}\alpha}{3\pi} \frac{\delta m \,(m_{\gamma'}^2 + 2m_e^2)\sqrt{m_{\gamma'}^2 - 4m_e^2}}{\left(m_{\gamma'}^2 - \delta m^2/4\right)^2}. \tag{3.36}$$

Instead of Eq. (B.8) to approximate the signal cross section Eq. (B.7) was used, where the aforementioned conditions are not required. However, it is still required that the background cross section remains constant in the considered invariant-mass interval.

In the second approach only the requirement $\Gamma_{\gamma'} \ll m_{\gamma'}$ is needed. Although the squared amplitude of the signal cross section scales with ε^4 at the first view, after the integration over the invariant mass of the lepton pair within a range δm and the phase space of the lepton pair variables, a factor of ε^2 is canceled. Therefore, the signal cross section indeed scales with ε^2. This can be understood from the discussion in Appendix B.3 and can be shown analytically. One exploits that the narrow width of the γ' allows for an approximation of the hidden photon propagator appearing in Eqs. (3.1) and (3.2) as a Dirac δ function in the squared amplitude. After integrating over the variables associated with the lepton pair and its invariant mass m_{ll} one finds that the cross sections of the processes $e + (A,\, Z) \to e + (A,\, Z) + (\gamma' \to l^+l^-)$ and $e + (A,\, Z) \to e + (A,\, Z) + \gamma'$ are related by

$$\Delta\sigma_{\gamma'}(e(A,\, Z) \to e(A,\, Z)\gamma') = N_{\text{eff}} \times \Delta\sigma_{\gamma'}(e(A,\, Z) \to e(A,\, Z)l^+l^-).$$

This is the finding of Eq. (B.18). Both cross sections need to show the same linear dependence on ε^2, as can be seen from, e.g., Eq. (2.3). Moreover, one utilizes that the resonance caused by the exchange of a hidden photon is described by a Breit-Wigner distribution. Hence, the integral over this resonance curve is independent of the width of the resonance which is depending on ε^2. To perform the numerical integration in case of the cross section $\Delta\sigma_{\gamma'}(e(A, Z) \to e(A, Z)l^+l^-)$ one has to choose a value of ε^2. This fixed value used for the calculation is in the following denoted by $\widetilde{\varepsilon}^2$. Dividing the cross section calculated with $\widetilde{\varepsilon}^2$ by this value corresponds to the quantity from which the ε^2-dependence is removed. One can write

$$\Delta\sigma_{\gamma'}(\varepsilon^2) = \frac{\Delta\sigma_{\gamma'}(\widetilde{\varepsilon}^2)}{\widetilde{\varepsilon}^2} \times \varepsilon^2.$$

By substituting this into Eq. (3.32), one obtains

$$\varepsilon^2 = S\,\frac{\widetilde{\varepsilon}^2 \times \Delta\sigma_{\gamma^*}}{\Delta\sigma_{\gamma'}(\widetilde{\varepsilon}^2)}. \tag{3.37}$$

In this approach, the dependence on N_{eff} is entering in terms of the total decay width $\Gamma_{\gamma'}$ into the cross section $\Delta\sigma_{\gamma'}$. A parameter $\widetilde{\varepsilon}^2 = 10^{-4}$ was used for the calculation of exclusion limits for fixed-target experiments. With this parameter one ensures that the decay width is also of a realistic magnitude. An issue, which may enter, is that the caused peak is too narrow and is ignored in the numerical integration. One has to verify, of course, that the result of this calculation is accurate. Such a check can be performed by the linear scaling of the signal cross section with ε^2, which was already discussed above. With the chosen value of $\widetilde{\varepsilon}^2 = 10^{-4}$ no problems with the accuracy of the numerical integration of the narrow structure over m_{ll} were found.

Within this work it was proven numerically that both methods, using Eqs. (3.35) and (3.37), lead to the same results. To determine or predict exclusion limits both methods have their respective merits. On the one hand, the approach proposed in Ref. [140] (Eq. (3.35)) allows for reading off the dependencies on parameters such as the mass resolution δm or the hidden photon mass $m_{\gamma'}$ directly. On the other hand, the method using Eq. (3.37) does not rely on any more assumptions than $\Gamma_{\gamma'} \ll m_{\gamma'}$ which is fulfilled in the kinematical region of interest. From Eq. (3.35) one can see that predictions for limits with a sensitivity estimated in Eq. (3.33) can be written as

$$\begin{aligned}\varepsilon^2 =& \frac{N_\sigma}{\sqrt{\Delta\sigma_{\gamma^*} \times L}}\,\frac{\Delta\sigma_{\gamma^*}}{\Delta\sigma^{\mathrm{TL}}_{D,\gamma^*}}\,\frac{2N_{\mathrm{eff}}\alpha}{3\pi}\,\frac{\delta m}{m_{\gamma'}} \\ =& \sqrt{\frac{\Delta\sigma_{\gamma^*}}{L}}\,\frac{N_\sigma}{\Delta\sigma^{\mathrm{TL}}_{D,\gamma^*}}\,\frac{2N_{\mathrm{eff}}\alpha}{3\pi}\,\frac{\delta m}{m_{\gamma'}}.\end{aligned}$$

Thus, reducing the background cross section or improving the luminosity will only lead to an “square-root” enhancement of the exclusion limit.

3.5.2 Exclusion limits for experiments at MAMI

3.5.2.1 Exclusion limit for the MAMI 2010 test run

The necessary cross sections to find an exclusion limit for the test run of the hidden photon search experiment at MAMI in 2010 [152] were already discussed in Sec. 3.4.3. Plots of these

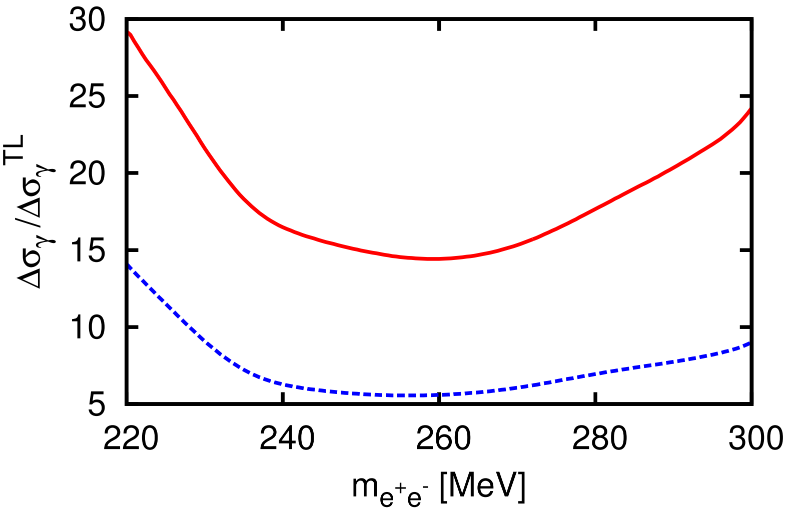

Figure 3.10: Red solid (blue dashed) curve: Ratio of the background cross section $\Delta\sigma^{\mathrm{TL+SL}}_{\mathrm{D+X},\gamma^*}$ ($\Delta\sigma^{\mathrm{TL+SL}}_{\mathrm{D},\gamma^*}$) to the direct TL cross section $\Delta\sigma^{\mathrm{TL}}_{\gamma}$.

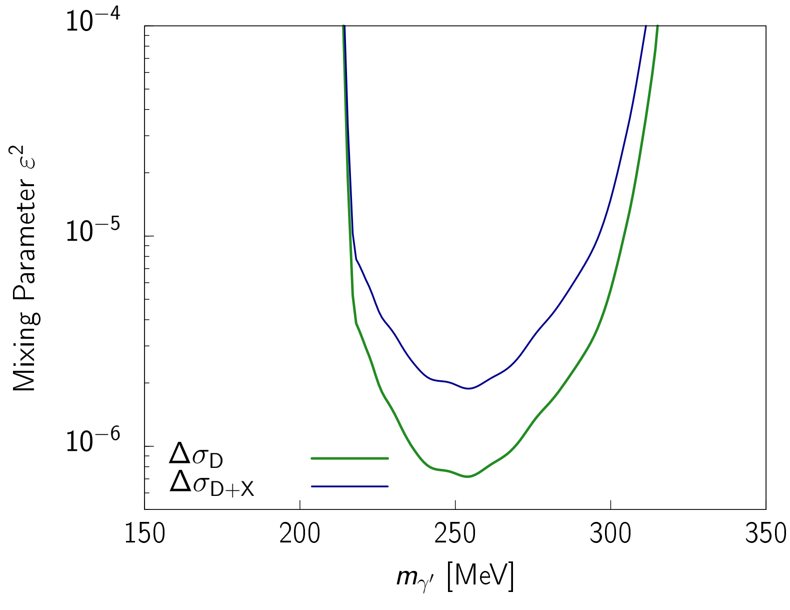

Figure 3.11: Green (blue) curve: Exclusion limit determined from the experimental data of the MAMI 2010 test run using the cross section $\Delta\sigma^{\mathrm{TL+SL}}_{\mathrm{D},\gamma^*}$ ($\Delta\sigma^{\mathrm{TL+SL}}_{\mathrm{D+X},\gamma^*}$) to describe the irreducible QED background.

cross sections are shown in Fig. 3.5. The calculations were performed for setup 1 of the MAMI 2010 test run. The corresponding kinematical quantities are given in Table 3.1.

To calculate an exclusion limit for ε^2 in this section Eq. (3.35) is applied. Hence, the background cross section $\Delta\sigma^{\mathrm{TL+SL}}_{\mathrm{D+X},\gamma^*}$ and the direct TL cross section $\Delta\sigma^{\mathrm{TL}}_{\mathrm{D},\gamma^*}$ are needed in order to find a bound on ε^2. The ratio of these two quantities entering in Eq. (3.35) is presented in Fig. 3.10. In this figure, the red solid curve is the ratio of the background cross section $\Delta\sigma^{\mathrm{TL+SL}}_{\mathrm{D+X},\gamma^*}$ to the direct TL cross section $\Delta\sigma^{\mathrm{TL}}_{\gamma}$. Moreover, the blue dashed curve is the ratio of the direct background cross section $\Delta\sigma^{\mathrm{TL+SL}}_{\mathrm{D},\gamma^*}$, where the final-state electrons were treated distinguishable, to the direct TL cross section $\Delta\sigma^{\mathrm{TL}}_{\gamma}$. As mentioned in Sec. 3.4.3, this setting was optimized to reduce the direct SL contribution. This can be seen from the relatively small value of the ratio $\Delta\sigma^{\mathrm{TL+SL}}_{\mathrm{D},\gamma^*}/\Delta\sigma^{\mathrm{TL}}_{\gamma}$. Taking the exchange term into account, the ratio of the background cross section increases by a factor of 2 to 3 which leads to a weaker exclusion limit.

Because the contribution of the exchange term was not yet included in the background calculation used to determine the exclusion limit of the MAMI 2010 test run, the actual limit is lower by this factor. The limit found within this work using the cross section $\Delta\sigma^{\mathrm{TL+SL}}_{\mathrm{D+X},\gamma^*}$ for the irreducible QED background is indicated by the blue curve in Fig. 3.11. The limit represented by the green curve corresponds to the one where the exchange term $\Delta\sigma^{\mathrm{TL+SL}}_{\mathrm{X},\gamma^*}$ was neglected.

3.5.2.2 Predictions for exclusion limits for the investigated settings at MAMI 2012/2013

The A1 Collaboration started a γ' search run at MAMI in 2012 which was continued by a second beam time in 2013. In these experiments the kinematics given in Tables 3.3 and 3.4 were probed. No narrow peak in the invariant-mass spectrum as a hidden photon signal could be found. The obtained invariant-mass distributions are displayed in Figs. 3.12 and 3.13. The following distributions arising from the different cross sections are compared: background (red solid curve), SL + TL exchange term (blue dotted), SL exchange term (yellow double-dashed), SL + TL direct term (green dashed), and TL direct term (magenta dashed-dotted). It turns out that the SL exchange process is the largest contribution to the radiative background. Figures 3.12 and 3.13 illustrate the dependence of the separated background contributions on the invariant mass $m_{e^+e^-}$. The SL exchange term dominates the cross section at low invariant masses. Although the SL direct and the TL exchange terms become more important for increasing $m_{e^+e^-}$, the SL exchange term still remains the largest contribution. The ratio between the TL direct term and the SL exchange term has a similar behavior, retaining nearly the same maximum value in each of the considered settings. Furthermore, Figs. 3.12 and 3.13 show the importance of the interference terms in order to describe the data correctly.

In Fig. 3.14 a combined plot of the results for the ratio $\Delta\sigma_{\gamma}/\Delta\sigma^{\mathrm{TL}}_{\gamma}$ for each setting given in Tables 3.3 and 3.4 is presented. As discussed, this ratio as a function of the invariant mass $m_{e^+e^-}$ is crucial to obtain the exclusion limits for the γ' parameter space following Eq. (3.35). Due to the particular choice of kinematics in these experiments, the ratio $\Delta\sigma_{\gamma}/\Delta\sigma^{\mathrm{TL}}_{\gamma}$ has a value between $10-15$ and $10-30$ in the mass ranges of the setups probed in the runs in 2012 and 2013, respectively. In Fig. 3.15 the predictions for the exclusion limits on ε^2 for the set of kinematics probed in the 2012 (2013) beam time are indicated by the green

	E_0 [MeV]	$\lvert\vec{l}\rvert_+$ [MeV]	$\lvert\vec{l}\rvert_-$ [MeV]
kin057	180	78.7	98
kin072	240	103.6	132.0
kin077	255	110.1	140.4
kin091	300	129.5	164.5
kin109	360	155.4	197.6
kin138	435	190.7	247.7
kin150	495	213.7	271.6
kin177	585	250.0	317.3
kin218	720	309.2	392.7

Table 3.3: Kinematics of the MAMI 2012 γ' search. Electron scattering angle: $\phi_- = 20.01°$ (spectrometer A). Positron scattering angle: $\phi_+ = -15.63°$ (spectrometer B). The number in the label of the kinematics refers to the invariant mass around which a setting is centered.

	E_0 [MeV]	$\lvert\vec{l}\rvert_+$ [MeV]	$\lvert\vec{l}\rvert_-$ [MeV]
kin054	180	97.1	73.9
kin076	255	137.5	104.7
kin103	345	186.0	141.7
kin135	450	242.6	184.8
kin170	570	307.3	234.1
kin206	690	372.1	283.4
kin256	855	461.0	351.2

Table 3.4: Kinematics of the MAMI 2013 beam time. Electron scattering angle: $\phi_- = 20.01°$ (spectrometer A). Positron scattering angle: $\phi_+ = -15.11°$ (spectrometer B). Note that for the setup “kin256” the spectrometers A and B were exchanged. Hence, one has to exchange the momenta, angles, and acceptances from Table 3.2.

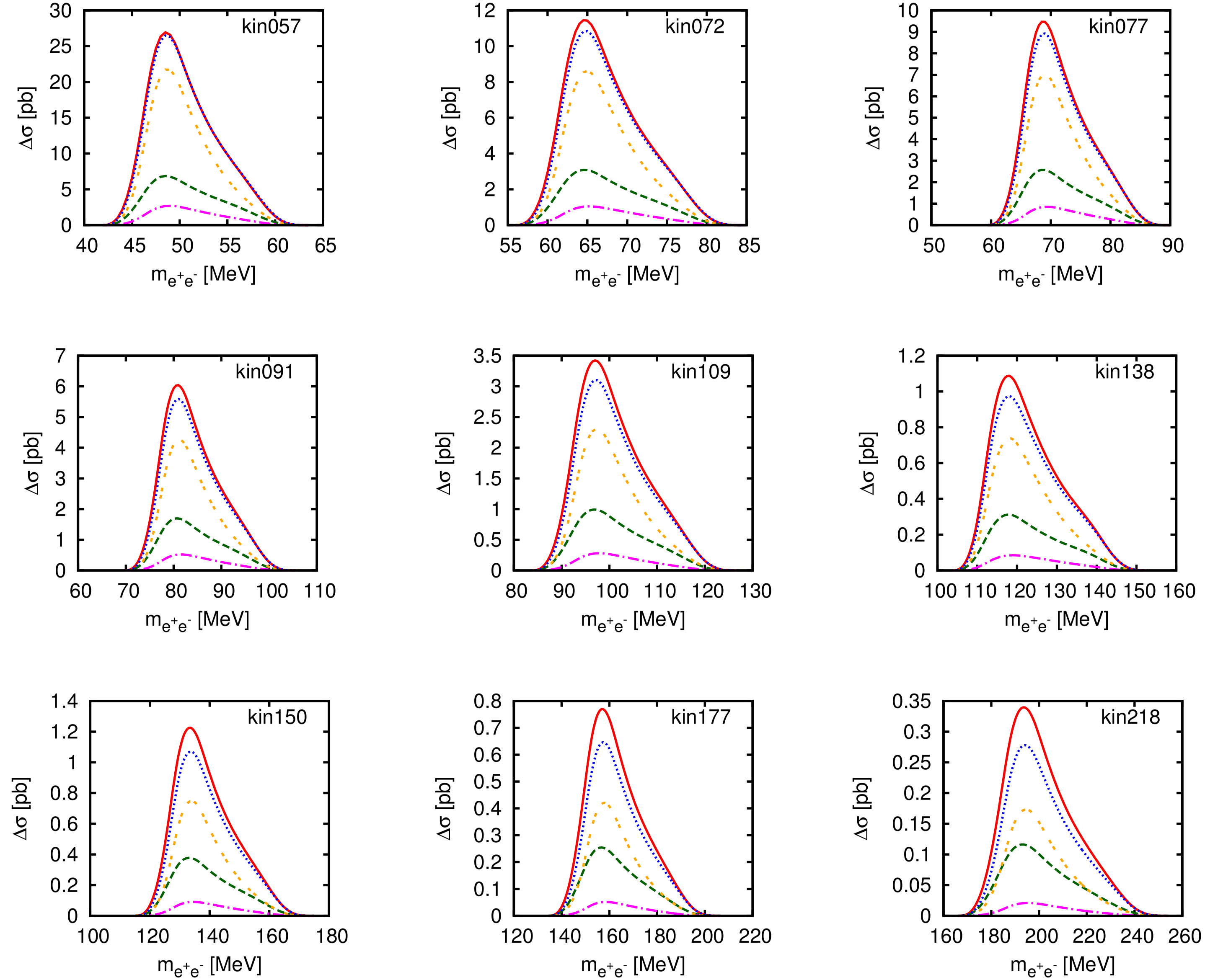

Figure 3.12: Simulation of the invariant-mass distributions calculated from the different cross sections for the kinematics probed at MAMI in 2012: background (red solid curve), SL + TL exchange term (blue dotted), SL exchange term (yellow double-dashed), SL + TL direct term (green dashed), and TL direct term (magenta dashed-dotted).

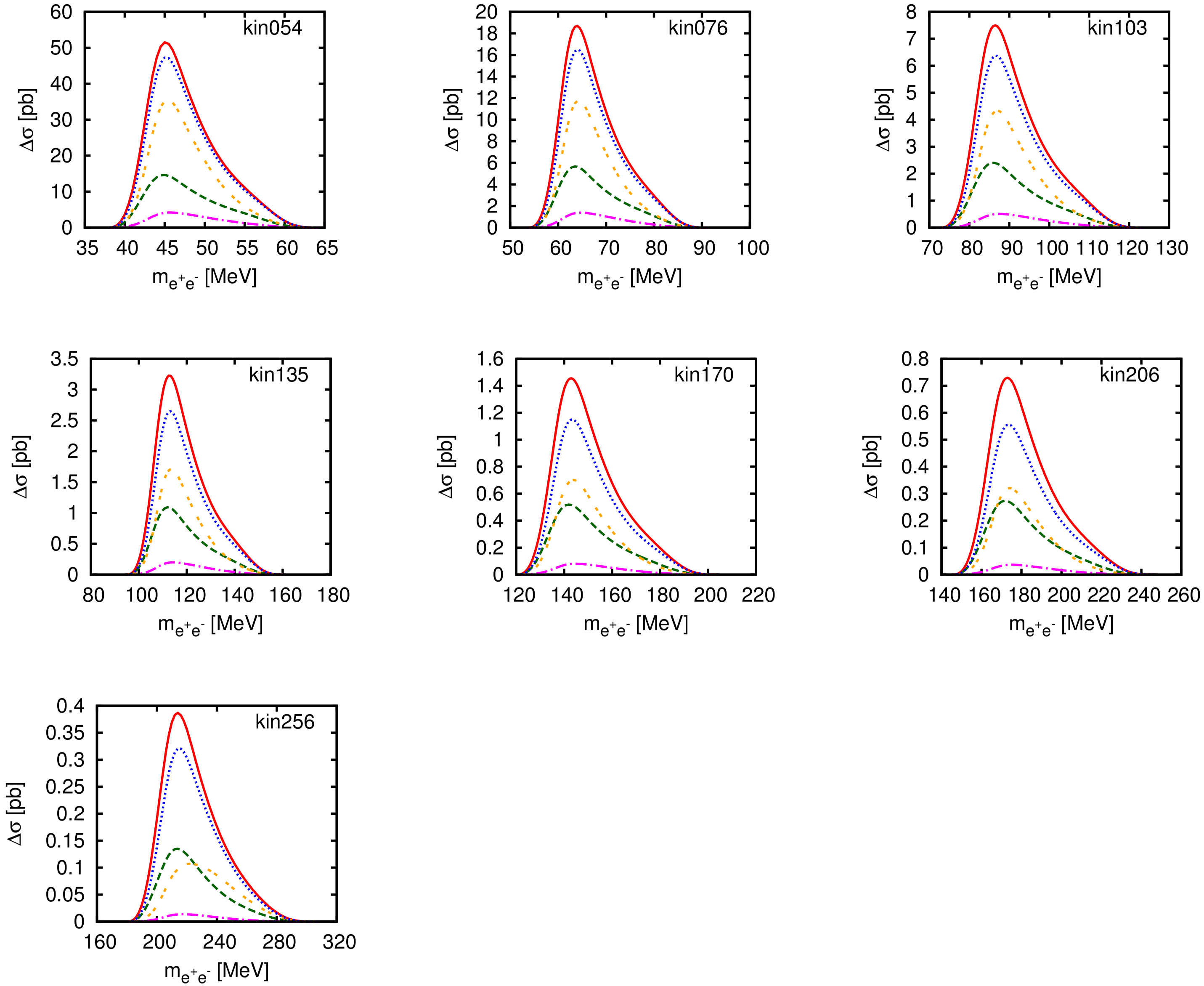

Figure 3.13: Same as Fig. 3.12 for the settings in Table 3.4 probed in the MAMI 2013 beam time.

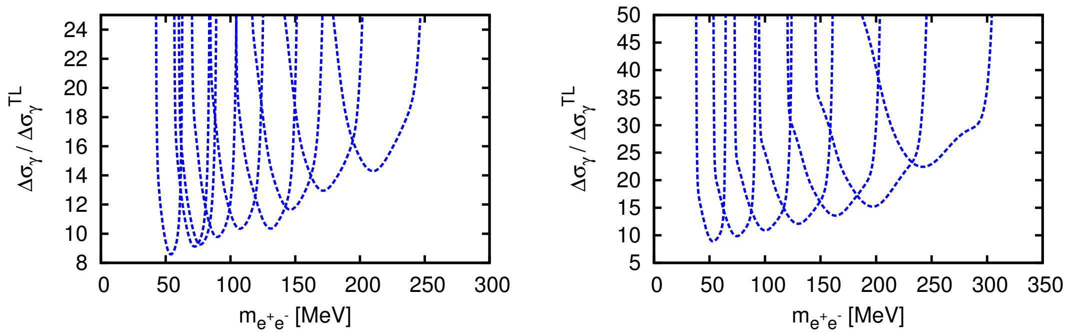

Figure 3.14: Left (right) panel: Combined plot of the result for the ratios $\Delta\sigma_\gamma/\Delta\sigma_\gamma^{\mathrm{TL}}$ of each setting investigated in the MAMI 2012 (2013) beam time, starting with the lowest beam energy on the left.

(blue) curves. An integrated luminosity of around $10\,\mathrm{fb}^{-1}$ for each setting of the 2012 run was estimated. In addition, a value of $25\,\mathrm{fb}^{-1}$ for the 2013 settings corresponding to 3 days of beam time per setting was assumed.

3.5.3 Predictions for the experimental reach of a hidden photon experiment at MESA

In this section a feasibility study to search for hidden photons at the future "Mainz Energy-recovering Superconducting Accelerator (MESA)" is performed. The construction of MESA at the University of Mainz was approved in 2013. It is planned to provide the first beam for experiments in 2017. MESA is designed as a small, multi-turn accelerator providing a high intensity electron beam up to beam energies of around 160 MeV. Thus, MESA should be ideally suited to probe the γ' parameter space in the low mass region [203, 204].

In this thesis it was investigated whether or not it is possible to carry out such hidden photon search experiments by using two small spectrometers similar to the experiments at MAMI discussed in Secs. 3.4.3 and 3.5.2. A realistic assumption is that each of these spectrometers has a horizontal and vertical angular acceptance of $\pm 50\,\mathrm{mrad}$, and a momentum acceptance of $\pm 5\%$. Since the beam energy is low compared to experiments at MAMI, such detectors for MESA will be significantly smaller. This allows one to reach smaller scattering angles. Therefore, one has access to the region of phase space where the cross section for hidden photon production is largest (see. Secs. 2.2.2 and 3.4.2).

It was assumed that such a future experiment at MESA will be performed by making use of a gas target to minimize the multiple scattering in the target material. This will improve the mass resolution compared to solid target. The same methods and program code as for the MAMI experiments discussed in Sec. 3.4 were used for the calculation of the cross sections.

In order to obtain as large cross sections as possible, xenon is considered as target material. For comparison, the calculations were also performed for a proton target in one setup. Furthermore, the integration over the invariant mass $m_{e^+e^-}$ is performed for a 0.125 MeV interval, which is the aimed mass resolution in this experiment. To obtain the projected reach of the experiment a beam time of about 3 months and a luminosity of $10^{34}\,\mathrm{cm}^{-2}\mathrm{s}^{-1}$ were assumed, which is a conservative choice.

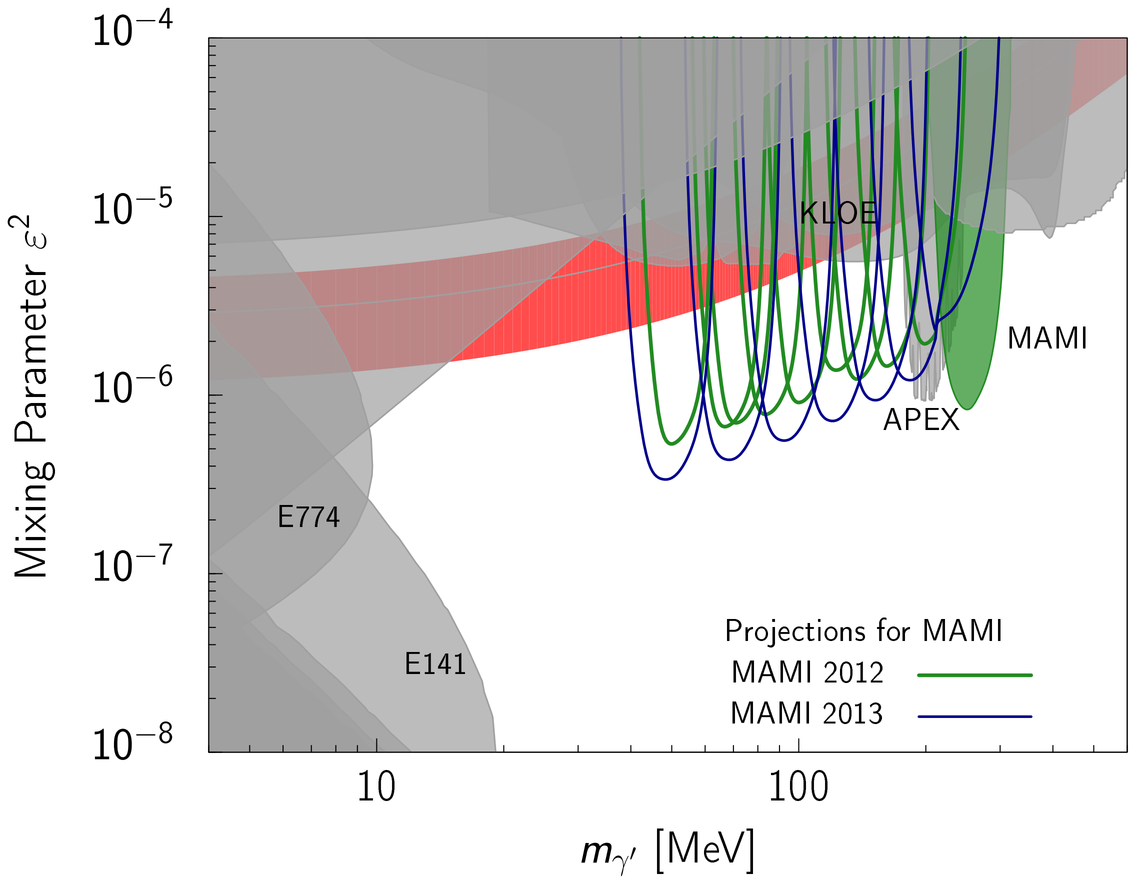

Figure 3.15: Projection of exclusion limits from the MAMI beam-time in 2012 (green curves) and 2013 (blue). Note that only the individual bands are shown. Summing the individual bands will lead to an improved result.

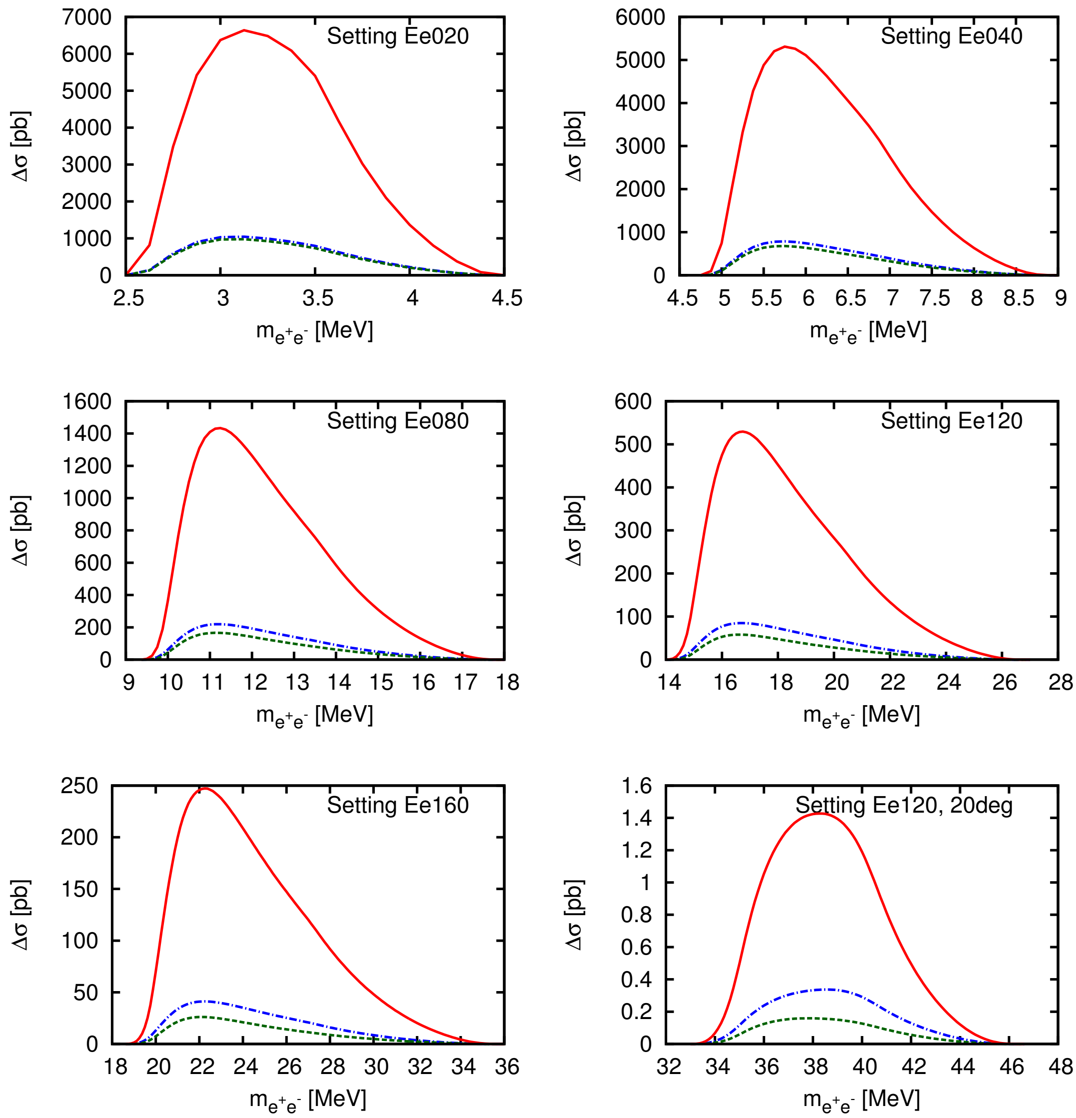

Figure 3.16: Invariant mass distributions from the feasibility study for the MESA experiment. Solid curve: SL+TL (direct + exchange term), dashed curve: direct TL, dashed-dotted curve: direct SL+TL.

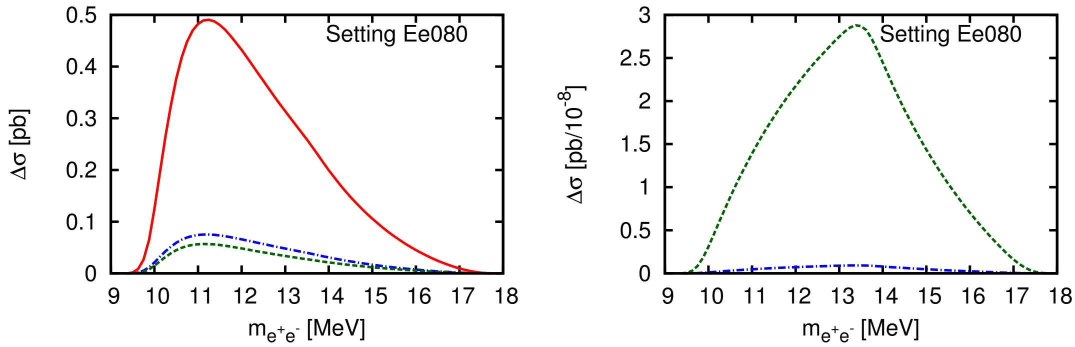

Figure 3.17: Left panel: Invariant mass distributions from the feasibility study for the MESA experiment for a proton target. Solid curve: SL+TL (direct + exchange term), dashed curve: direct TL, dashed-dotted curve: direct SL+TL. Right panel: Isolated VVCS cross section. Dashed curve: exchange term contribution, dashed-dotted curve: direct contribution.

The results for the invariant-mass distributions for beam energies E_0 of 20, 40, 80, 120, and 160 MeV are shown on Fig. 3.16. The kinematics was chosen in such a way that the central scattering angle ϕ of the e^- (e^+) is $+10°$ ($-10°$). The central momentum is $|\vec{l}\,|_\pm = 0.98 \times E_0/2$. Furthermore, one setting for $E_0 = 120\,\mathrm{MeV}$ and $\phi_\mp = \pm 20°$ was calculated in order to cover the full so-called $(g-2)_\mu$ welcome band together with the settings probed in the MAMI beam times in 2012 and 2013, of which the projected reach is shown in Fig. 3.15.

Since the low mass region $m_{\gamma'} \lesssim 10\,\mathrm{MeV}$ in the $(g-2)_\mu$ discrepancy is already excluded by the electron anomalous magnetic moment $(g-2)_e$, the settings for beam energies of 20 and 40 MeV were not included in the exclusion limit calculation. Therefore, one does not have to deal with the difficulties in the low mass regime.

For comparison, the acceptance integrated cross sections depending on $m_{e^+e^-}$ for a proton target with a beam energy of $E_0 = 80\,\mathrm{MeV}$ are shown in Fig. 3.17. The same curves as in Fig. 3.16 are plotted in the left panel. In the right panel of Fig. 3.17 it is demonstrated that the VVCS contribution originating from those Feynman diagrams of Fig. 3.1, in which the hidden photon is radiated off the proton line, is suppressed by more than 6 orders of magnitude in the chosen kinematical setting. Thus, this contribution can be neglected. As indicated by the shape of the curves for $\Delta\sigma^{SL+TL}_{\gamma^*,\mathrm{D+X}}$ and $\Delta\sigma^{TL}_{\gamma^*,\mathrm{D}}$ in Figs. 3.16 and 3.17, the ratio of these two quantities is equal. Hence, the kind of target does not affect the ratio of the cross sections entering in the calculation of exclusion limits using Eq. (3.35).

The left panel of Fig. 3.18 shows the calculated ratio $\Delta\sigma_\gamma/\Delta\sigma^{\mathrm{TL}}_\gamma$ which reaches a value around 8–10 for the proposed settings. The expected exclusion limit on ε^2 as obtained from Eq. (3.35) corresponding to the invariant-mass spectra of Fig. 3.16 is presented in the right panel of Fig. 3.18. A mass resolution of 0.125 MeV was assumed. The blue (red) curve in the right panel of Fig. 3.18 represents the settings with central angle of 10° (20°). At very low masses below 10 MeV Eq. (3.35) does not serve as a good approximation for the exclusion limit anymore, since Eq. (19) of Ref. [140] overestimates the γ' signal cross section by up to 50%. In summary, one finds that such experiments at MESA will be able to probe the low mass region of the parameter space down to $\varepsilon^2 = 10^{-7}$.

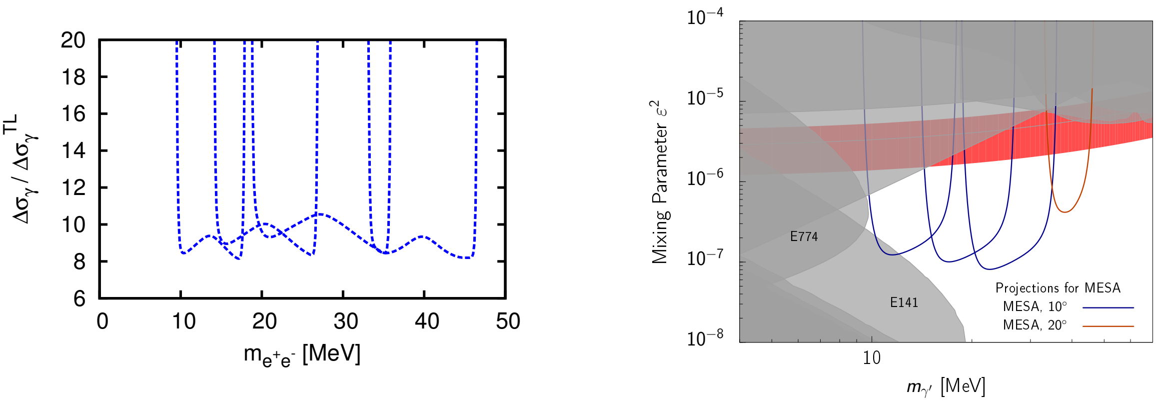

Figure 3.18: Left Panel: Combined plot of the result for the ratio $\Delta\sigma_\gamma/\Delta\sigma_\gamma^{\mathrm{TL}}$ of each setting for the MESA experiment. The settings correspond with the following beam energies and scattering angles (from left to right): $E_0 = 80$, 120, 160 MeV with $\phi_\mp = \pm 10°$, $E_0 = 120$ MeV with $\phi_\mp = \pm 20°$. Right Panel: Projected reach of the experiment in the investigated setups.

3.5.4 Predictions for the reach of DarkLight experiment

The DarkLight experiment at JLAB plans to investigate the low mass γ' parameter region. The experiment is planned at the JLAB Free Electron Laser, which allows for a beam energy of $E_0 = 100$ MeV with a very high intensity. As target a hydrogen gas target will be used. The goal is to acquire an integrated luminosity of $1\,\mathrm{ab}^{-1}$.

In the previous Sec. 3.5.3 a possible experiment using two high-resolution spectrometers detecting the lepton pair in the forward direction at the new MESA facility at Mainz was investigated. The DarkLight detector, covering nearly the full solid angle, is intended to detect all particles involved in the reaction. Due to the similar energy range, both experimental setups are complementary. The discussion of this section can also be understood as the investigation of a possible experiment using a 4π-detector at MESA. Since the beam energy $E_0 = 100$ MeV is below the pion threshold, the differential cross sections of the signal and background process are described by Eqs. (3.25) and (3.28) without any further modifications.

The applied kinematical limits accounting for the detector geometry are written in Table 3.5. The simulations were performed with two slightly different settings: Setting I corresponds to the one discussed in the proposal of the DarkLight experiment [190]. In setting II the range of the polar angles of the final-state proton and leptons is slightly extended. This allows for the acceptance of leptons emitted more closely to the beam axis.

The cross sections to predict the reach of the experiment were calculated in the kinematical settings of Table 3.5. The results of the simulation of the QED background and the signal are shown in the left and right panel of Fig. 3.19, respectively. The distributions depending on the lepton pair invariant mass $m_{e^+e^-}$ using a bin width $\delta m = 1$ MeV are presented. As discussed in Sec. 3.2, one has to account for the VVCS contribution for the production off a proton. In the following study this was done for both the background and the signal cross sections. It was shown in the literature that the Born terms dominate the VVCS contribution up to the pion threshold. Hence, for $E_0 = 100$ MeV one can neglect the non-Born terms for

Quantity	Setting I	Setting II
$\lvert\vec{l}\rvert = \lvert\vec{k}'\rvert,\ \lvert\vec{l_-}\rvert,\ \lvert\vec{l_+}\rvert$	$\lvert\vec{l}\rvert \geq 5\,\mathrm{MeV}$	$\lvert\vec{l}\rvert \geq 5\,\mathrm{MeV}$
$\theta_l = \theta_{k'},\ \theta_{l_-},\ \theta_{l_+}$	$25^\circ \leq \theta_l \leq 155^\circ$	$20^\circ \leq \theta_l \leq 160^\circ$
$\phi_l = \phi_{k'},\ \phi_{l_-},\ \phi_{l_+}$	$0^\circ \leq \phi_l \leq 360^\circ$	$0^\circ \leq \phi_l \leq 360^\circ$
$\lvert\vec{p}'\rvert$	$\lvert\vec{p}'\rvert \geq 2\,\mathrm{MeV}$	$\lvert\vec{p}'\rvert \geq 2\,\mathrm{MeV}$
$\theta_{p'}$	$5^\circ \leq \theta_{p'} \leq 175^\circ$	$4^\circ \leq \theta_{p'} \leq 176^\circ$
$\phi_{p'}$	$0^\circ \leq \phi_{p'} \leq 360^\circ$	$0^\circ \leq \phi_{p'} \leq 360^\circ$

Table 3.5: Choice of kinematical limits used within the calculations for DarkLight.

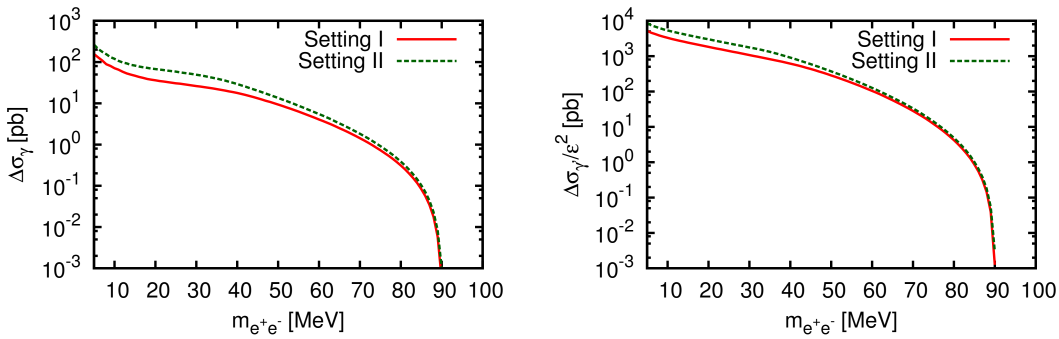

Figure 3.19: Invariant mass distributions of the background (left) and signal normalized by ε^2 (right) cross section for DarkLight kinematics. The solid (dashed) curve represents the calculation in setting I (II) with values given in Table 3.5.

which one expects an effect less than 5%.

Obviously, the cross section calculated in setting II is slightly larger than the one in setting I, as expected due to the larger allowed phase space. In order to illustrate the signal cross section over the full experimental mass range, the corresponding curves in the right panel were calculated for a hidden photon mass equal to the central value of each invariant-mass bin. The expected signal in the experiment, of course, is not a smooth distribution as shown in the right panel of Fig. 3.19. Instead, a signal in only one mass bin corresponding to the hidden photon mass is expected.

Figure 3.20 shows the ratio of the signal cross section with γ' production from the lepton and proton ($\Delta\sigma_{\gamma'}(TL+VVCS)$) and only from the lepton ($\Delta\sigma_{\gamma'}(TL)$) for $E_0 = 100\,\mathrm{MeV}$ (left panel) and $E_0 = 300\,\mathrm{MeV}$ (right panel). It turns out that the VVCS contribution leads to an enhancement of the signal cross section for the full considered mass range, which is mostly in the range from 10% to 20%. For a larger hidden photon mass $m_{\gamma'}$, the enhancement of the cross section grows and leads to a twice larger value. Compared to studies of virtual Compton scattering off the proton [175], where the process $ep \to ep\gamma$ is investigated, this effect appears unnaturally large. It can be understood from the fact that the cross section is suppressed by the mass of the radiated particle and the fermion mass in the propagator. In the process $ep \to ep\gamma$ the cross section for bremsstrahlung radiation of a photon from the

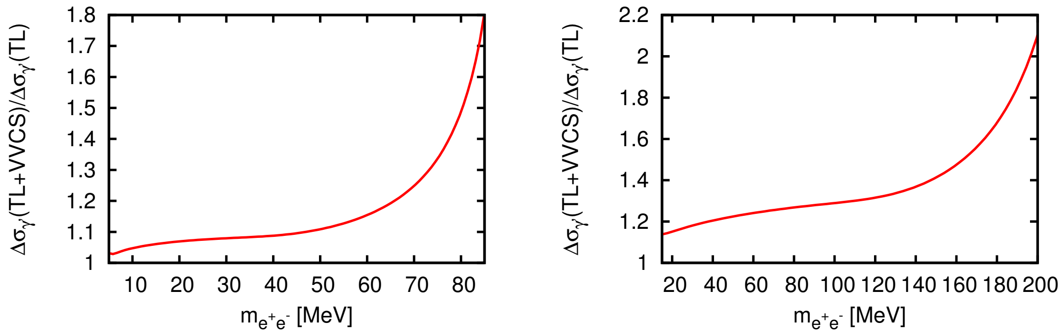

Figure 3.20: Ratio of the signal cross sections for γ' production from the lepton, $\Delta\sigma_{\gamma'}(TL)$, and additionally taking the VVCS contribution into account, $\Delta\sigma_{\gamma'}(TL + VVCS)$, calculated in setting I. Left panel: Beam energy $E_0 = 100\,\mathrm{MeV}$ as planned for the DarkLight experiment. Right panel: $E_0 = 300\,\mathrm{MeV}$.

electron is strongly peaked, if the photon is emitted into the direction of the electron. The radiation from the proton, on the contrary, is relatively suppressed by the comparatively large mass of the proton. On the other hand, the VVCS contribution is relatively enhanced for the $ep \to epe^+e^-$ process compared with the emission off the electron due to the finite virtuality of the photon or hidden photon. As a consequence, in particular for a large hidden photon mass, the VVCS contribution appears larger compared to the other contributions. Furthermore, it is shown in the right panel of Fig. 3.20 that the sharp upturn in the cross section ratio is caused by the particular choice of kinematics. To illustrate this, the cross section ratio for the same allowed angular acceptance but with a beam energy $E_0 = 300\,\mathrm{MeV}$ was calculated. The upturn in the ratio starts for a much larger invariant mass of the lepton pair than in the case $E_0 = 100\,\mathrm{MeV}$.

Using Eq. (3.37) and the calculated cross sections shown in Fig. 3.19 one obtains predictions for the reach of the DarkLight experiment. Following Ref. [202], it is assumed that a perfect detector efficiency, a mass resolution $\delta m = 1\,\mathrm{MeV}$, and a luminosity $L = 1\,\mathrm{ab}^{-1}$ can be reached. The results of these calculations are presented in Fig. 3.21. Besides the prediction of the exclusion limit using the TL + VVCS signal cross section $\Delta\sigma_{\gamma'}(TL{+}VVCS)$ illustrated by the solid (dashed) curve for setting I (II), for comparison the exclusion limit derived from $\Delta\sigma_{\gamma'}(TL)$ calculated in setting I (dashed-dotted curve) is shown. While the cross section is significantly altered by the VVCS process, the effect on the exclusion limit is minimal. The small effect can be explained by the smallness of the cross section itself where the VVCS effect becomes large. Furthermore, one can see that the exclusion limit is also only slightly affected by the choice of the two kinematical settings.

This calculation leads to a similar projected reach as the one given in Ref. [202]. The reach found in Ref. [202] is weaker by a constant factor of roughly 3. This is due to the different choice of N_σ in Eq. (3.37). While in Ref. [202] $N_\sigma = 5$ was applied, in this work $N_\sigma = 2$ was used for reasons of comparability with the results obtained in Secs. 3.5.2, 3.5.2.2 and 3.5.3. The two results agree when they are normalized with the same value of N_σ. Due to the larger cross section of setting II, the projected exclusion limit can be improved by around 10 to 30 % in the considered mass range. Moreover, the enhancement of the signal

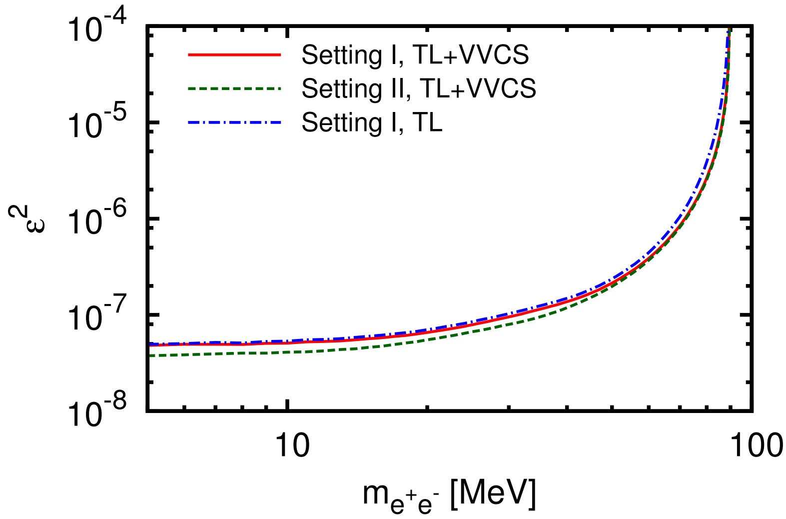

Figure 3.21: Projected reach of the DarkLight experiment assuming that a luminosity $L = 1\,\mathrm{ab}^{-1}$, a mass resolution $\delta m = 1\,\mathrm{MeV}$ and a perfect detector efficiency can be reached. The area above the curves can be excluded. The predictions obtained in settings I (solid and dashed dotted curve) and II (dashed) are shown. In setting I the exclusion limit was calculated using the TL + VVCS (solid) and the TL (dashed-dotted) signal cross section. In setting II only the limit using the TL + VVCS signal cross section is presented.

cross section by accounting for the VVCS contribution only leads to a small effect for the projected bound.

3.5.5 Predictions for the reach of HPS-type experiments

In this section experiments of the same type as the future "Heavy Photon Search (HPS)" experiment at JLAB [189] are studied. Since the more complicated actual setup of the HPS experiment is not treated in total, these setups are referred to as "HPS-type." Like in the A1 and APEX experiments, HPS is designed to detect the created lepton and antilepton. This is not done by two large spectrometers in contrast to A1 and APEX. Instead a rather small detector array aligned directly at the beam is used. This allows for the investigation of very small scattering angles for which the hidden photon signal is largest. The resulting cuts for the horizontal scattering angles are $|\Theta| \leq 50\,\mathrm{mrad}$. The vertical out-of-plane angle is restricted to $-60\,\mathrm{mrad} \leq \alpha \leq -15\,\mathrm{mrad}$ and $+15\,\mathrm{mrad} \leq \alpha \leq +60\,\mathrm{mrad}$, respectively. These numbers are given in the proposal of the HPS experiment [189]. Furthermore, it is required that the sum of the energies of the detected leptons exceeds 80% of the beam energy, $(E_+ + E_-)/E_0 > 0.8$, and that energy of each detected lepton is larger than 500 MeV. It is further demanded that the two leptons may not be in the same half of the detector. Hence, the associated vertical scattering angles need to have opposite signs. A sketch of the setting is presented in Fig. 3.22.

Since the energy range allowed for $E_+ + E_-$ is comparably large, the cross section was cal-

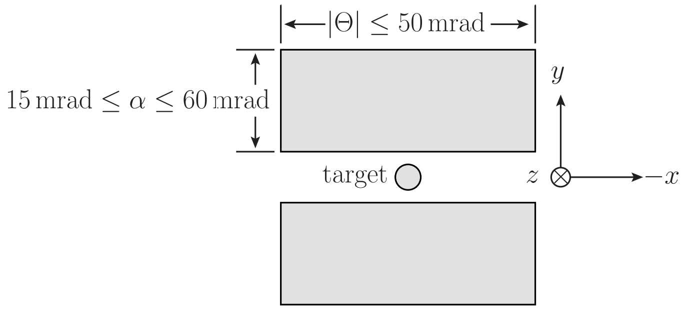

Figure 3.22: Sketch of the setup of HPS-type experiments.

culated with the form factors given in Eq. (2.24). This parametrization accounts for inelastic effects. These effects cannot be neglected the kinematical range of HPS-type experiments.

Following the proposal of the HPS collaboration [189], the cross sections are calculated for beam energies $E_0 = 1.1\,\mathrm{GeV}$, $2.2\,\mathrm{GeV}$, and $6.6\,\mathrm{GeV}$. The results of the simulation for HPS-type experiments can be found in Fig. 3.23. In this figure the background cross section $\Delta\sigma_\gamma^{\mathrm{TL+SL,D+X}}$ ($\Delta\sigma_\gamma^{\mathrm{TL+SL,D}}$) is drawn by the solid (dashed) curve. For comparison with other simulations the contribution to lepton-pair production from a timelike virtual photon $\Delta\sigma_\gamma^{\mathrm{TL,D}}$ (dotted curve) is also shown, which is related to the signal cross section. The largest part of the irreducible QED background originates from the contribution due to the indistinguishability of the final-state electrons, as one can easily see by comparing the curves for the cross sections $\Delta\sigma_\gamma^{\mathrm{TL+SL,D+X}}$ and $\Delta\sigma_\gamma^{\mathrm{TL+SL,D}}$. Furthermore, the TL contribution compared to the SL one in the cross section with distinguishable final-state electrons decreases for increasing beam energy.

The signal cross sections are shown in Fig. 3.24. In order to illustrate the signal cross section over the full experimental mass range, the curves were calculated for a hidden photon mass equal to the central value of each invariant-mass bin, as in Sec. 3.5.4. The expected signal in the experiment of course is not a smooth distribution. Instead, a signal in only one mass bin corresponding to the hidden photon mass is expected. Furthermore, the signal cross sections were divided by ε^2, which corresponds to setting $\varepsilon^2 = 1$. The experimental signature of a γ' would be a peak at a certain mass with the height given in Fig. 3.24 over the smooth QED background presented in Fig. 3.23.

As in the previous section, Eq. (3.37) and the obtained cross sections are used to find a prediction for the reach of a hypothetical experiment in the HPS-type kinematics. For these calculations a constant mass resolution $\delta m = 1\,\mathrm{MeV}$ is assumed, This value is better than the anticipated resolution given in the HPS proposal, which depends on the beam energy and the invariant mass of the lepton pair. Following the HPS proposal, integrated luminosities of of $L = 5\,\mathrm{pb}^{-1}$, $L = 40\,\mathrm{pb}^{-1}$, and $L = 200\,\mathrm{pb}^{-1}$ for the settings with $E_0 = 1.1\,\mathrm{GeV}$, $E_0 = 2.2\,\mathrm{GeV}$, and $E_0 = 6.6\,\mathrm{GeV}$, respectively, are plugged in to estimate the reach of such an experiment. The results are presented in Fig. 3.25, were the solid curve (dashed, dashed-dotted) shows the limit for a beam energy $E_0 = 1.1\,\mathrm{GeV}$ ($2.2\,\mathrm{GeV}$; $6.6\,\mathrm{GeV}$). Note that the individual bands only are shown and there is not a prediction for the summed bins given, which should increase the sensitivity significantly.

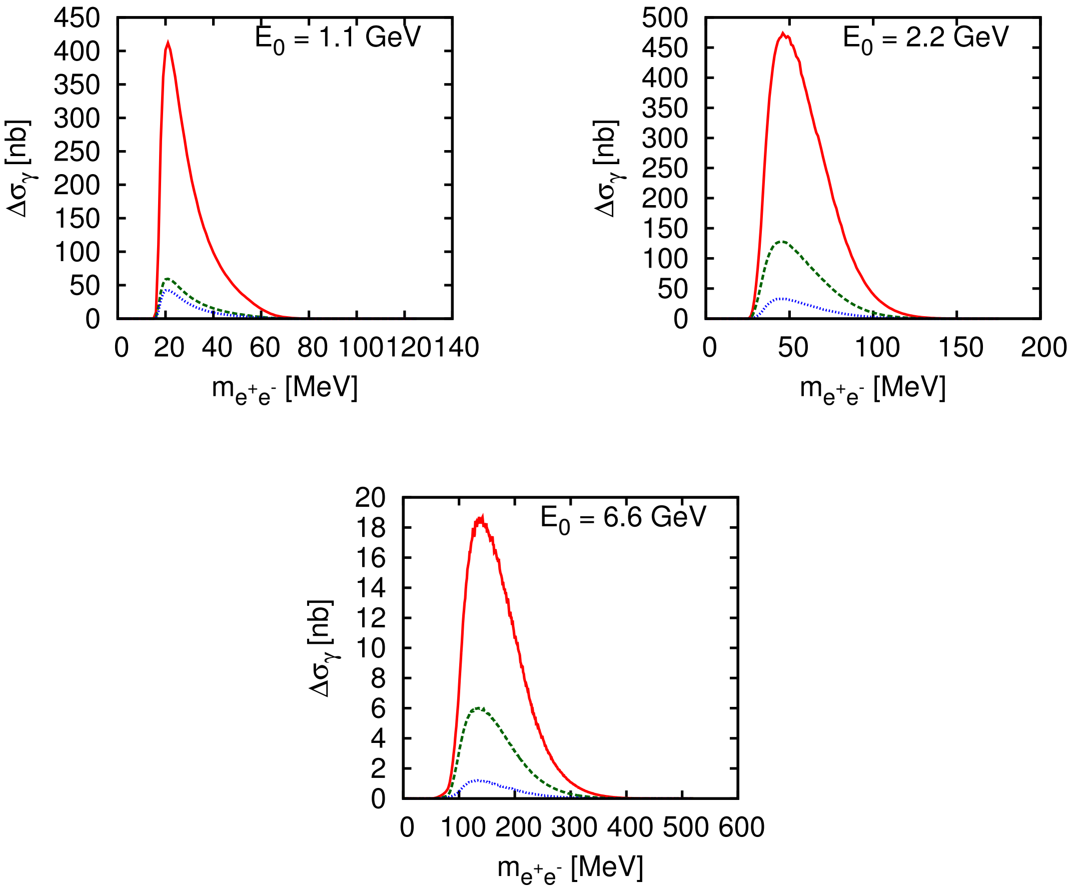

Figure 3.23: Invariant mass distributions of the background cross sections in HPS-type kinematics for selected beam energies. The TL+SL, D+X (TL+SL, D; TL, D) cross section is represented by the solid (dashed; dotted) curve.

3.6 Summary and conclusions of the section

In this section the cross sections which are crucial to describe the existing and planned fixed-target γ' search experiments were studied. A comparison of these calculations with a sample of data taken at MAMI was performed. After applying the leading-order QED radiative corrections for the corresponding elastic electron-hadron scattering process it was found that the data can be described well by the simulation. However, the crude estimate of the radiative corrections can only serve as a first step. To obtain a better agreement between theory and data, the full radiative corrections need to be calculated.

In addition, a calculation of the isolated spacelike and timelike virtual photon exchange cross sections, each for the direct and exchange term, was performed. This allows one to study the dependence of the background cross section on these contributions. Furthermore, it was found that it is necessary to take the exchange term contributing to the irreducible background into account in order to reproduce the data. A refined exclusion limit was calculated from the data taken in the 2010 test run of the A1 experiment.

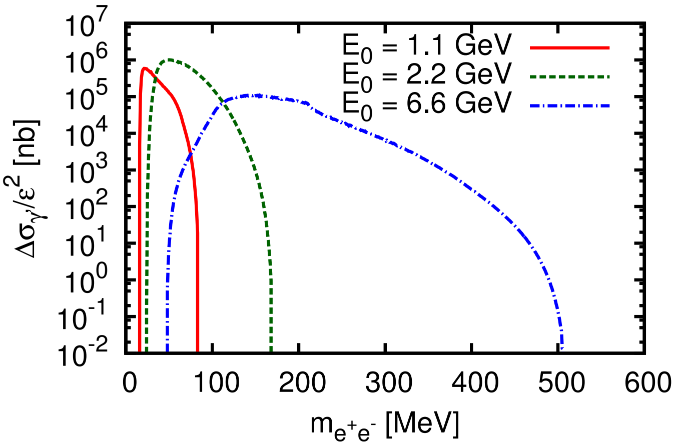

Figure 3.24: Signal cross section normalized by ε^2 in HPS-type kinematics.

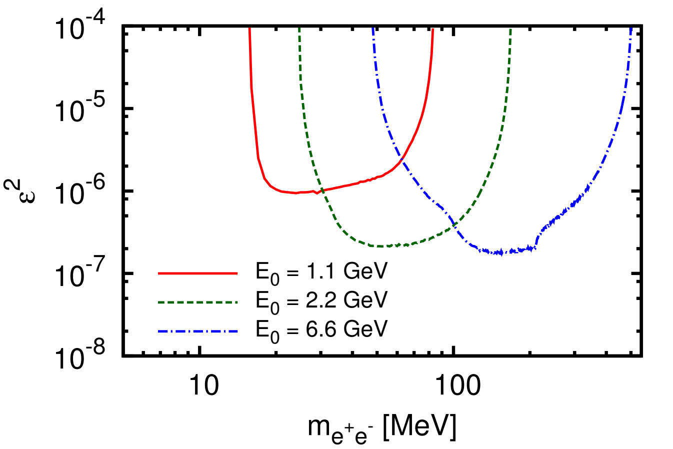

Figure 3.25: Projected exclusion limits for the investigated HPS-type kinematics. Integrated luminosities of $L = 5\,\mathrm{pb}^{-1}$, $L = 40\,\mathrm{pb}^{-1}$, and $L = 200\,\mathrm{pb}^{-1}$ were used for the settings with $E_0 = 1.1\,\mathrm{GeV}$ (solid curve), $E_0 = 2.2\,\mathrm{GeV}$ (dashed), and $E_0 = 6.6\,\mathrm{GeV}$ (dashed-dotted), respectively, to estimate the reach.

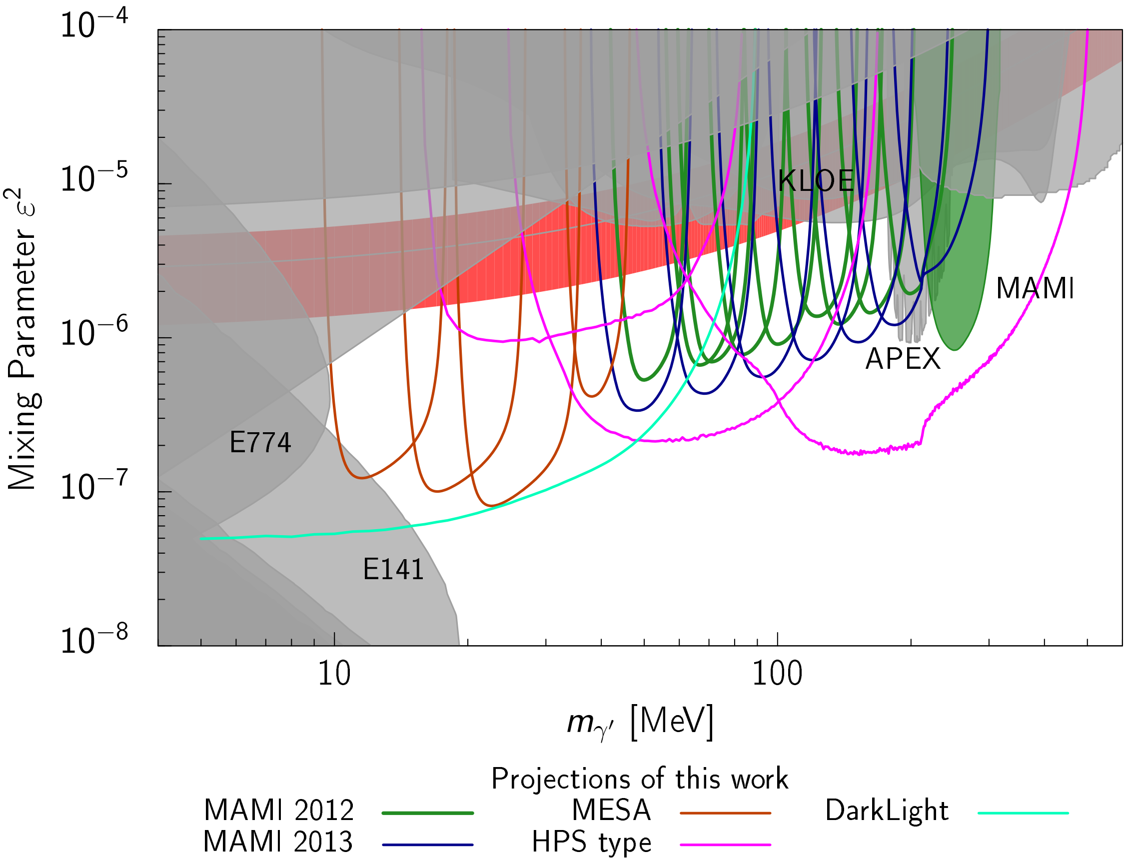

Figure 3.26: Summary of existing exclusion limits for visible γ' decays. Existing limits as published in Refs. [138–140, 144, 147–150, 152, 153] are shown, represented by the shaded regions. The band denoted by $|(g-2)_\mu| < 2\sigma$ is the $(g-2)_\mu$ welcome band, where the existing discrepancy between the experimental and theoretical value of the anomalous magnetic moment of the muon is most likely explained by the γ' contribution to $(g-2)_\mu$. Note that only the region of parameter space is shown, where the investigated experiments have sensitivity. More details about existing limits can be found in Sec. 1.3.4, in particular in Table 1.2 and Fig. 1.19. The reach of the investigated experiments is illustrated by the curves as indicated above.

By means of the cross sections found in this analysis, predictions for the expected exclusion limits can be found. Figure 3.26 shows a summary of exclusion limits and projections. These future bounds for the hidden photon parameter space are valid for γ' decays with purely visible decay products. In this plot only the region of parameter space which is currently accessible in fixed-target experiments is shown. Existing limits are represented by the shaded regions [138–140, 144, 147–150, 152, 153]. The $(g-2)_\mu$ welcome band denoted by $|(g-2)_\mu| < 2\sigma$ corresponds to the region of parameter space in which the current discrepancy between the theoretical and experimental determination of the anomalous moment of the muon can be explained by the contribution of the hidden photon. More details can be found in Sec. 1.3.4, in particular, in Table 1.2 and Fig. 1.19. The results for the setups investigated at MAMI in 2012 and 2013 are illustrated by the green and blue curves, respectively. The red curve indicates the results obtained for the possible experimental setup at MESA. The prediction for DarkLight is shown by the cyan curve. The projected bounds obtained for an HPS-type experiment are illustrated by the magenta curves. The predictions of other works are not shown [188, 189, 202, 205] for a better visualization. Furthermore, during finalizing this work, new limits from the HADES experiment [151] excluding regions of parameter space in the mass range from 20 to 60 MeV down to $\varepsilon^2 = 2.3 \times 10^{-6}$ and from the ν-calorimeter I experiment [145] were released, which are not yet included in Fig. 3.26.

The experimental setups investigated in this work will be conclusive whether or not a hidden photon decaying into a purely visible final state is at the origin of the discrepancy between the experimental and theoretical determination of the anomalous magnetic moment of the muon. Furthermore, each of the investigated experiments will certainly improve the existing current exclusion limit by at least one order of magnitude if no signal of a γ' can be found.

Chapter 4

Rare Kaon Decays as Probe for Additional Light Gauge Bosons

4.1 Introduction

In this section the possibility to study rare kaon decays with regard to signatures of physics beyond the SM is discussed. Starting in the 1970s, when the nature of the electro-weak interaction was not yet fully clarified, meson decays, and in particular kaon decays, served as a versatile probe to find constraints on the weak force. Although these experiments were designed for signals of the weak interaction, their outcome can still be used today to probe models of physics beyond the SM. In this section invisible decays (Sec. 4.2) of the hidden photon as well as reactions in which its decay products can be detected (Sec. 4.3), are investigated. In the case of invisible decays, two different models are used:

Model I: Kinetic mixing of the hidden photon and the SM photon.

Model II: Models in which the new $U(1)$ vector boson couples to the charged lepton field leading to a parity-violating force.

The first model was already discussed in detail in Sec. 1.3. The results of Sec. 4.2 apply for the case that the decay happens outside the detector. This corresponds to a flight length of the hidden photon which is larger than the decay volume of the detector, or a hidden photon decaying dominantly into particles which cannot be detected as Light Dark Matter (LDM). In the discussion of the kinetic mixing model in Sec. 1.3 no assumptions about the sector of dark matter itself were made. Therefore, in the case of decays to LDM, it is assumed that these particles are contained in the dark sector. Besides, no further assumptions are made.

Model II is motivated e.g. by the Proton Radius Puzzle introduced in Sec. 1.2.4. To resolve this puzzle and to reconcile the theoretical and experimental determination of the anomalous magnetic moment of the muon, in Ref. [88] a model was proposed, in which a new $U(1)$ gauge boson V couples to the muon with coupling strength g_R. In this model, gauge anomalies emerge, which can be canceled by the introduction of scalar degrees of freedom at the cost that renormalizability is lost. It was found in Ref. [88] that the validity of this model breaks down above the cut-off

$$\Lambda_{\mathrm{UV}} \sim 700\,\mathrm{GeV}\left(\frac{m_V}{10\,\mathrm{MeV}}\right)\left(\frac{g_R}{e}\right)^{-2},$$

which is consistent with a ultraviolet cut-off above the TeV scale for $m_V \sim 10 - 100\,\mathrm{MeV}$ and $g_R \sim 0.01 - 0.1$. This model was investigated and modified in several works [89, 90, 206]. In Refs. [89, 90] constraints on these parameters were derived from the rare kaon decay

$$K^+ \to \mu^+ + \nu_\mu + V. \tag{4.1}$$

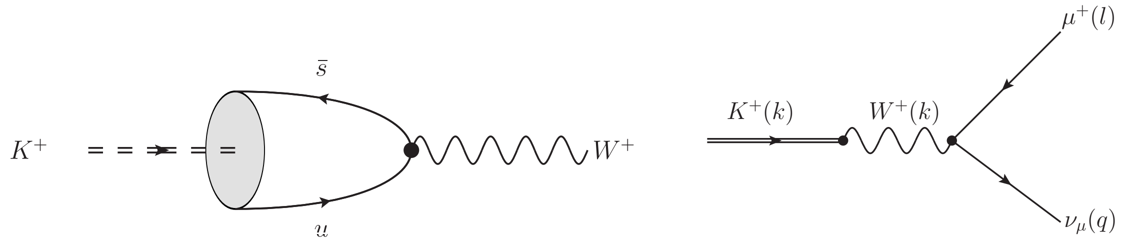

Figure 4.1: Left panel: Feynman diagram for the transition from K^+ to W^+. Right panel: Feynman diagram of the decay $K^+ \to \mu^+\nu_\mu$.

This decay, where the V is invisible, can be constrained by use of experimental data obtained in a pioneering experiment by Pang et al. [207] more than 30 years ago, in which the decay $K^+ \to \mu^+ +$ neutrals was studied. Only the charged muon was detected. Further charged particles or photons in the final state were excluded. Hence, this experiment has sensitivity to the considered process with an invisibly decaying V. The data of Ref. [207] were used to test models with invisible gauge boson decays as introduced above.

In addition, possibilities are investigated to constrain the parameter space of the hidden photon model of Sec. 1.3 by measurements of the reaction

$$K^+ \to \mu^+ + \nu_\mu + (\gamma' \to l^+l^-). \tag{4.2}$$

In particular, the production of an electron-positron pair is of large interest. This decay allows one to probe a wider range of parameter space compared to the decay into a muon pair. Furthermore, all particles in the final state are distinguishable, which simplifies the QED background.

The total decay rate can be obtained easily by the analytical integration over the variables of the lepton pair as demonstrated in Appendix B.3. Therefore, the decay rate can be used for the signal process which was evaluated for invisible decays, as long as the mass of the hidden photon is below the muon production threshold, giving rise to

$$\Gamma_{\gamma'}(K^+ \to \mu^+\nu_\mu\gamma') = N_{\text{eff}} \times \Gamma_{\gamma'}(K^+ \to \mu^+\nu_\mu e^+e^-), \tag{4.3}$$

where $N_{\text{eff}} = 2$ for $m_{\gamma'} < 2 \times m_\mu$. Since predictions for future experiments will be given, which requires an understanding of the irreducible QED background, also the SM process $K^+ \to \mu^+\nu_\mu e^+e^-$ is treated in detail. Furthermore, the same numerical methods as in Chapter 3 are applied to find accurate predictions.

Note that for simplicity, in the following the new gauge boson is always referred to as hidden photon and the coupling is $\varepsilon^2 = {}^{\alpha'}\!/\alpha$. In model II this has to be understood as purely vectorial coupling of the gauge boson V exclusively to the muon with strength g_R.

4.2 Constraints for invisible decays of the hidden photon

4.2.1 Calculation of decay rates

The largest external momentum scale of the considered processes, the kaon mass M_K, is far below the weak gauge boson masses m_W and m_Z. This allows one to approximate the

W- and Z-propagators as ${}^{g^{\mu\nu}}\!/_{M_W^2}$ and ${}^{g^{\mu\nu}}\!/_{M_Z^2}$, respectively. Therefore, one does not have to deal with the transition of the positively charged kaon to a u quark and a $\bar{s}$ quark. This is illustrated in the left panel of Fig. 4.1. Instead, the hadronic weak K^+ decay current is used to describe this interaction, parametrized by

$$\langle 0|\bar{v}_s \gamma_\mu (1-\gamma_5) u_u | K^+(k)\rangle = f_k k_\mu,$$

where f_K is the kaon decay constant.

It is assumed that the K^+ decays at rest. Thus, the calculations for the process

$$K^+(k) \to \mu^+(l) + \nu_\mu(q) + \gamma'(q')$$

will be performed in the K^+-rest frame where the kaon four-vector is given as $k = (M_K, \vec{0})$. The four-momenta are denoted by $l = (E_\mu, 0, 0, |\vec{l}\,|)$ for the muon, $q = E_\nu(1, \sin\theta_\nu, 0, \cos\theta_\nu)$ for the neutrino, and $q' = (k - l - q)$ for the γ'. In addition, $T_\mu = E_\mu - m_\mu$ denotes the kinetic energy of the muon.

Before the process $K^+ \to \mu^+\nu_\mu\gamma'$ is investigated, it is helpful to calculate the rate of the 2-body decay

$$K^+(k) \to \mu^+(l) + \nu_\mu(q),$$

which can be used to normalize the expressions to dimensionless quantities. For the decay into a two-particle final state, the decay width is given by Eq. (A.4). The invariant Feynman amplitude obtained from the diagram in the right panel of Fig. 4.1 is

$$\mathcal{M} = \frac{g^2 \sin\theta_c}{8} \left[\bar{u}(q)\, \gamma^\alpha \,(1-\gamma_5)\, v(l)\right] \frac{-g_{\alpha\beta} + \frac{k^\alpha k^\beta}{M_W^2}}{k^2 - M_W^2}\, j_K^\beta,$$

where G_F is the Fermi constant and θ_c the Cabibbo mixing angle. With $|k^\alpha| \ll M_W$ and $j_K^\beta = f_K\, k^\beta$ one finds

$$\mathcal{M} = \frac{G_F\, f_k\, \sin\theta_c}{\sqrt{2}} \left[\bar{u}(q)\, \not{k}\, (1-\gamma_5)\, v(l)\right].$$

The spin-averaged, squared matrix element is obtained as

$$\begin{aligned}\overline{|\mathcal{M}|^2} &= \frac{G_F^2\, f_k^2\, \sin^2\theta_c}{2}\, 8m_\mu^2 (M_K - E_\mu)(E_\mu + |\vec{l}\,|)\\ &= 2\, G_F^2\, f_k^2\, \sin^2\theta_c\, m_\mu^2\, (M_K^2 - m_\mu^2)\end{aligned}$$

with $E_\mu = {}^{(M_K^2 + m_\mu^2)}\!/_{(2M_K)} \simeq 258\,\mathrm{MeV}$.

Together with Eq. (A.4) the resulting total decay width is

$$\Gamma(K^+ \to \mu^+\nu_\mu) = \frac{(G_F\, f_K\, \sin\theta_c)^2}{8\pi\, M_K^3}\, m_\mu^2\, (M_K^2 - m_\mu^2)^2. \tag{4.4}$$

In order to compare the numerical results with the data of Ref. [207], the differential decay rates have to be folded with the detector efficiency function $D(E_\mu)$. The detector efficiency function $D(E_\mu)$ is given only graphically in Ref. [207]. Hence, the corresponding coordinates were extracted and an interpolation was performed. Figure 4.2 shows D as a function of the kinetic energy T_μ as obtained from Ref. [207]. The differential decay rate reads after folding with $D(E_\mu)$:

$$\Gamma_{\mathrm{exp}}(K^+ \to \mu^+\nu_\mu V) = \int \frac{d\Gamma}{dE_\mu}(K^+ \to \mu^+\nu_\mu V) D(E_\mu) dE_\mu. \tag{4.5}$$

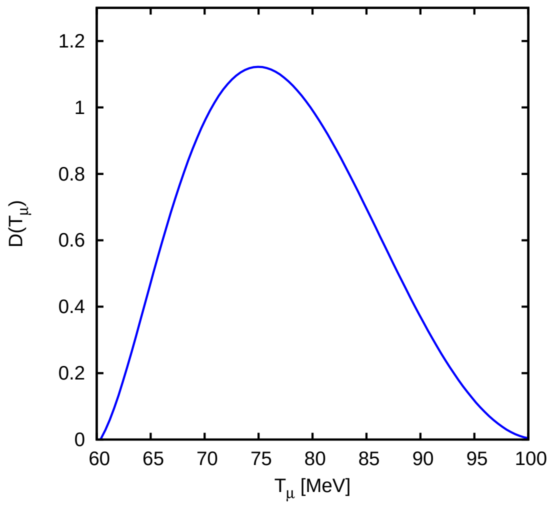

Figure 4.2: The detector efficiency function D depending on the kinetic energy T_μ of the muon as extracted from Ref. [207].

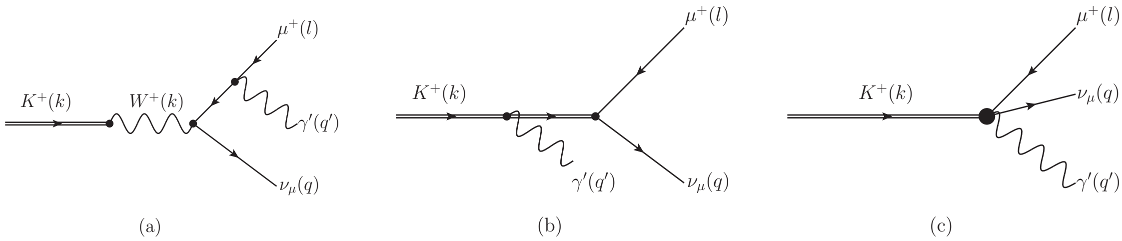

Figure 4.3: Feynman diagrams of the decay $K^+ \to \mu^+\nu_\mu\gamma'$.

4.2.2 Decay width of the signal process

The Feynman amplitudes of the considered type of processes are represented by the diagrams of Fig. 4.3. While in model I the amplitude is given by the sum over all diagrams, in model II it is assumed that the γ' couples only to the muon. Therefore, just diagram (a) contributes in model II and the amplitude simply reads

$$\begin{aligned}\mathcal{M}_{\gamma',a} = {} & \frac{G_F\, f_K\, \varepsilon e\, \sin\theta_c}{\sqrt{2}\left((k-q)^2 - m_\mu^2\right)}\, \varepsilon^*_\alpha(q') \\ & \times \left[\bar{u}(q)(1+\gamma_5)\left(-(k-q)^2 + m_\mu \not{k}\right)\gamma^\alpha v(l)\right] .\end{aligned} \tag{4.6}$$

In model I, on the contrary, one has [208]

$$\mathcal{M}_{\gamma'} = \frac{G_F\, \varepsilon e\, \sin\theta_c}{\sqrt{2}}\, \varepsilon^*_\rho(q')\, \left(f_K\, m_\mu\, L^\rho - H^{\rho\nu} j_\nu\right), \tag{4.7}$$

with

$$L^\rho = \bar{u}(q)(1+\gamma_5)\left\{\frac{2k^\rho - q'^\rho}{2k\cdot q' - q'^2} - \frac{2l^\rho + \not{q}'\gamma^\rho}{2l\cdot q' + q'^2}\right\} v(l), \tag{4.8}$$

$$j_\nu = \bar{u}(q)\gamma_\nu(1-\gamma_5)v(l), \tag{4.9}$$

$$\begin{aligned} H^{\rho\nu} &= -i\, V_1 \varepsilon^{\rho\nu\alpha\beta} q'_\alpha k_\beta - A_1(q'\cdot W - W^\rho q'^\nu) \\ &\quad - A_2(q'^2 g^{\rho\nu} - q'^\rho q'^\nu) - A_4(q'\cdot W q'^\rho - q'^2 W^\rho) W^\nu, \end{aligned} \tag{4.10}$$

with $W = k - q'$, $\varepsilon^{0123} = 1$, and

$$A_4 = \frac{2f_k}{M_K^2 - W^2}\,\frac{F^K_{\mathrm{em}}(q'^2) - 1}{q'^2} + A_3.$$

$F^K_{\mathrm{em}}(q'^2)$ denotes the electromagnetic form factor of the kaon.

The term proportional to f_K is known as inner Bremsstrahlung contribution (IB) and does not contain any structure dependent effects. The contribution proportional to $H^{\rho\nu}$ contains the structure dependent terms, which are parametrized by the form factors V_1, A_1, A_2, and A_4.

The term proportional to the form factor A_4 is neglected in this analysis, since A_4 is a linear combination of the electromagnetic form factor of the K^+ and the form factor A_3, which was set equal zero in this analysis following Ref. [208]. It was found numerically that the influence of the contribution from the electromagnetic form factor is below 0.5% within the range of the considered energies in this analysis and can be neglected. The remaining form factors are parametrized in agreement with Ref. [209] by

$$\begin{aligned} \sqrt{2} M_K A_1(q'^2,\, W^2) &\equiv \frac{-F_A}{\left(1 - {q'^2}/{m_\rho}\right)\left(1 - {W^2}/{m_{K_1}}\right)}, \\ \sqrt{2} M_K A_2(q'^2,\, W^2) &\equiv \frac{-R}{\left(1 - {q'^2}/{m_\rho}\right)\left(1 - {W^2}/{m_{K_1}}\right)}, \\ \sqrt{2} M_K V_1(q'^2,\, W^2) &\equiv \frac{-F_V}{\left(1 - {q'^2}/{m_\rho}\right)\left(1 - {W^2}/{m_{K^*}}\right)}, \end{aligned} \tag{4.11}$$

with $F_A = 0.031$, $R = 0.235$, $F_V = 0.124$, $m_\rho = 770\,\mathrm{MeV}$, $m_{K_1} = 1270\,\mathrm{MeV}$, and $m_{K^*} = 892\,\mathrm{MeV}$.

One obtains the differential decay width by evaluating the general $1 \to 3$ decay formula

$$d\Gamma = \frac{1}{2M_K}\,\frac{d^3\vec{l}}{(2\pi)^3\, 2E_\mu}\,\frac{d^3\vec{q}}{(2\pi)^3\, 2E_\nu}\,\frac{d^3\vec{q}'}{(2\pi)^3\, 2E_{\gamma'}}\,(2\pi)^4\,\delta^{(4)}\left(k - l - q - q'\right)\,\overline{|\mathcal{M}|^2}$$

in the K^+-rest frame, which is equal to the lab frame for an experiment as in Ref. [207]. Using momentum conservation, the integration over the γ' phase space can be eliminated. Furthermore, there is no angular dependence on Ω_μ and ϕ_ν. Thus, also these integrals can be solved trivially. Applying this leads to

$$\begin{aligned} d\Gamma &= \frac{1}{2M_K}\,\frac{1}{(2\pi)^5}\,\frac{d^3\vec{l}}{2E_\mu}\,\frac{d^3\vec{q}}{2E_\nu}\,\frac{1}{2E_{\gamma'}}\,\delta\left(m_{\gamma'} - E_\mu - E_\nu - E_{\gamma'}\right)\,\overline{|\mathcal{M}|^2} \\ &= \frac{1}{2M_K}\,\frac{1}{(2\pi)^5}\,\frac{4\pi\,|\vec{l}|^2\, d|\vec{l}|}{2E_\mu}\,\frac{2\pi\,|\vec{q}|^2\, d|\vec{q}|\, d\cos\theta_\nu}{2E_\nu\, 2E_{\gamma'}}\,\delta\left(m_{\gamma'} - E_\mu - E_\nu - E_{\gamma'}\right)\,\overline{|\mathcal{M}|^2}, \end{aligned} \tag{4.12}$$

where $E_{\gamma'}$ is fixed by the momenta of the remaining particles. In order to compare to the experimental data of Ref. [207] it is valuable—although not necessary—to calculate the differential decay width $d\Gamma/(dE_\mu\, dE_\nu)$. Correspondingly, the energy conserving component of the δ function is used to eliminate the $\cos\theta_\nu$ integration. Exploiting four-momentum conservation leads to

$$\begin{aligned}
q'^2 = m_{\gamma'}^2 &= (k-l-q)^2 \\
\Leftrightarrow 0 &= M_K^2 + (l+q)^2 - 2k\cdot(l+q) - m_{\gamma'}^2 \\
&= M_K^2 + m_\mu^2 - m_{\gamma'}^2 + 2l\cdot q - 2M_K(E_\mu + E_\nu) \\
&= M_K^2 + m_\mu^2 - m_{\gamma'}^2 - 2M_K(E_\mu + E_\nu) + 2E_\mu E_\nu - 2|\vec{l}|E_\nu \cos\theta_\nu,
\end{aligned}$$

and thus

$$\cos\theta_\nu = \frac{M_K^2 + m_\mu^2 - m_{\gamma'}^2 + 2E_\mu E_\nu - 2M_K(E_\mu + E_\nu)}{2E_\nu|\vec{l}\,|}.$$

To transform the δ function into an appropriate form, the derivative of its argument with respect to $\cos\theta_\nu$ has to be calculated, which yields

$$\frac{\partial(E_K - E_\mu - E_\nu - E_{\gamma'})}{\partial\cos\theta_\nu} = \frac{|\vec{l}\,|\,|\vec{q}\,|}{E_{\gamma'}}.$$

Inserting these results into Eq. (4.12), the differential decay width for $K^+ \to \mu^+\nu_\mu\gamma'$ in the K^+-rest frame simply reads

$$\frac{d\Gamma(K^+ \to \mu^+\nu_\mu\gamma')}{dE\mu\, dE_\nu} = \frac{1}{64\pi^3 M_K}\overline{|\mathcal{M}_{\gamma'}|^2}. \tag{4.13}$$

The total decay width is obtained by integrating Eq. (4.13) over E_μ and E_ν within the kinematically allowed limits. The necessary integration must be performed numerically. For that purpose the kinematically allowed regions for E_μ and E_ν have to be found. Obviously the minimal energy carried by the muon is $E_\mu = m_\mu$ when the muon is at rest. The muon carries its maximum energy when the ν_μ is produced at rest, i.e.,

$$\begin{aligned}
m_{\gamma'}^2 &= (k-l-q)^2 \\
&= M_K^2 + m_\mu^2 - 2M_K\,E_\mu + 2\,\underbrace{\left(E_\mu\,E_\nu - E_\nu|\vec{l}\,|\cos\theta_\nu\right)}_{=0,\,\text{since }E_\nu=0} \\
\Leftrightarrow E_\mu &= \frac{M_K^2 + m_\mu^2 - m_{\gamma'}^2}{2M_K}.
\end{aligned}$$

The neutrino energy range can be computed by varying the scattering angle θ_ν using $-1 \le \cos\theta_\nu \le +1$, if the energy of the muon is fixed. One finds

$$\begin{aligned}
\pm 1 &= \frac{M_K^2 + m_\mu^2 - m_{\gamma'}^2 + 2E_\mu E_\nu - 2M_K(E_\mu + E_\nu)}{2E_\nu|\vec{l}\,|} \\
\Leftrightarrow E_\nu &= \frac{M_K^2 + m_\mu^2 - m_{\gamma'}^2 - 2M_K E_\mu}{2\left(M_K - E_\mu \pm |\vec{l}\,|\right)}.
\end{aligned}$$

Thus, the total decay rate for $K^+ \to \mu^+\nu_\mu\gamma'$ is given by

$$\Gamma(K^+ \to \mu^+\nu_\mu\gamma') = \int dE\mu\, dE_\nu \frac{d\Gamma(K^+ \to \mu^+\nu_\mu\gamma')}{dE\mu\, dE_\nu} \tag{4.14}$$

within the kinematical limits

$$m_\mu \leq E_\mu \leq \frac{M_K^2 + m_\mu^2 - m_{\gamma'}^2}{2M_K}$$

for the muon energy, and

$$E_\nu^{\mathrm{min/max}} = \frac{M_K^2 + m_\mu^2 - m_{\gamma'}^2 - 2M_K E_\mu}{2\left(M_K - E_\mu \pm |\vec{l}|\right)}.$$

for the energy of the neutrino.

The underlying experiment of Ref. [207] was performed at a time, when the nature of the weak interaction was still unknown. Neither the weak neutral current nor the weak gauge bosons $W^\pm$ and Z were discovered. Signatures like a neutrino-neutrino interaction or even a 4-neutrino vertex were searched in order to constrain the weak interaction. For this purpose, the experiment was planned in such a way that the background processes could not affect the data. In the case of the background from the 2-body decay $K^+ \to \mu^+\nu_\mu$, the energy of the muon is fixed at $E_\mu \simeq 258\,\mathrm{MeV}$. This corresponds to the kinetic energy $T_\mu \simeq 152\,\mathrm{MeV}$. As Fig. 4.2 shows, only muons in the range of the kinetic energy $60\,\mathrm{MeV} \lesssim T_\mu \lesssim 110\,\mathrm{MeV}$ were accepted. Hence, the background from this process can be separated kinematically.

The largest background within the SM arises from radiative corrections to the 2-body decay $K \to \mu\nu_\mu$. In particular, the soft photon contribution, which accounts for not-detectable, low-energetic photons, is large for a kinetic energy of the muon near the 2-body limit. Due to the applied experimental cuts discussed above, this region lies well outside the experimental acceptance. Therefore, this background does not need to be considered.

4.2.3 Numerical results

A limit for the γ' parameter space can be calculated from the existing data published by Pang et al in Ref. [207]. An upper limit was found for the ratio $\Gamma(K^+ \to \mu^+X)/\Gamma(K^+ \to \mu^+\nu_\mu) < 2 \cdot 10^{-6}$ in this experiment. The state X may contain only undetectable, neutral particles except photons. In the following, the decay rate with applied experimental cuts normalized to the 2-body decay $K^+ \to \mu^+\nu_\mu$ will be used:

$$\tilde{R}(m_{\gamma'}) := \frac{\int \frac{d\Gamma}{dE_\mu}(K^+ \to \mu^+\nu_\mu\gamma')D(E_\mu)dE_\mu}{\Gamma(K^+ \to \mu^+\nu_\mu)}. \tag{4.15}$$

Since the kinetic mixing factor ε is a global factor of the amplitudes in Eqs. (4.6) and (4.7), one can rewrite $\tilde{R}\ (m_{\gamma'}) = \varepsilon^2\ R\ (m_{\gamma'})$. Thus, an upper bound for allowed values of ε^2 is found as:

$$\varepsilon^2 < \frac{2 \cdot 10^{-6}}{R(m_{\gamma'})}. \tag{4.16}$$

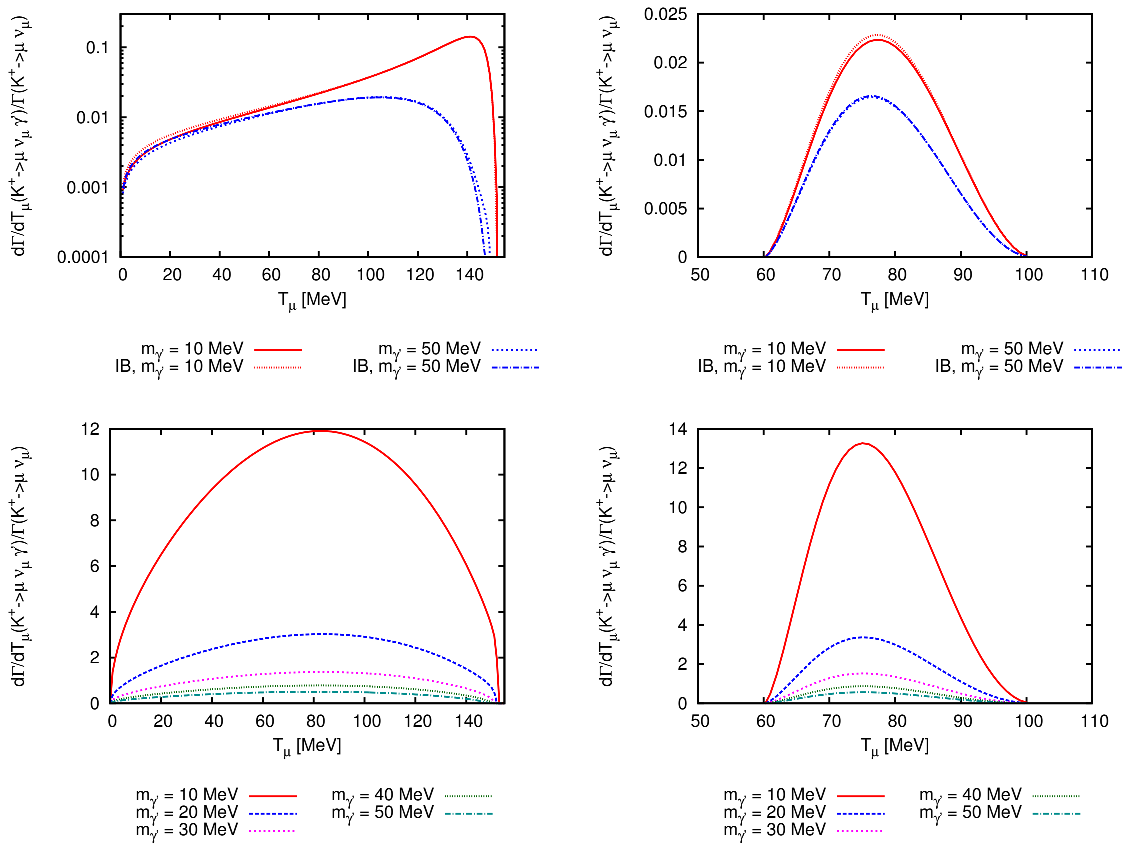

Figure 4.4: Ratio of $\frac{d\Gamma}{dT_\mu}(K^+ \to \mu^+\nu_\mu\gamma')$ and $\Gamma(K^+ \to \mu^+\nu_\mu)$ for various γ' masses for perfect detector efficiency (left panels) and for finite detector efficiency of Ref. [207] (right panels) at $\varepsilon^2 = 1$. Upper panels: kinetic mixing model (model I); lower panels: model II, where the γ' only couples to the μ^+.

In Fig. 4.4 the differential decay rate for the signal process relative to the decay $K^+ \to \mu^+\nu_\mu$ is shown calculated within models I and II for the full phase space (left panels) and with applied corrections due to the given detector acceptance (right panels), according to the experimental set-up of Ref. [207]. One notices that within the kinetic mixing model (upper panels of Fig. 4.4) the IB contribution completely dominates the result for the considered γ' mass parameters. This is illustrated by the comparison between the IB curves and the curves including the form factor dependence which was evaluated according to Refs. [208,209]. Since in model II the gauge invariance is not required, the decay rate is enhanced by a factor of $1/m^2_{\gamma'}$ compared to model I.

4.2.4 Exclusion limit

Figure 4.5 shows the existing exclusion limits for the parameter space of the hidden photon decaying into invisible decay products in comparison with the results of the analysis above. Limits, which require the decay of the hidden photon into SM particles would appear strongly weakened in this plot and thus are not shown. Note that the limit from $K \to \pi^0 X$ [126],

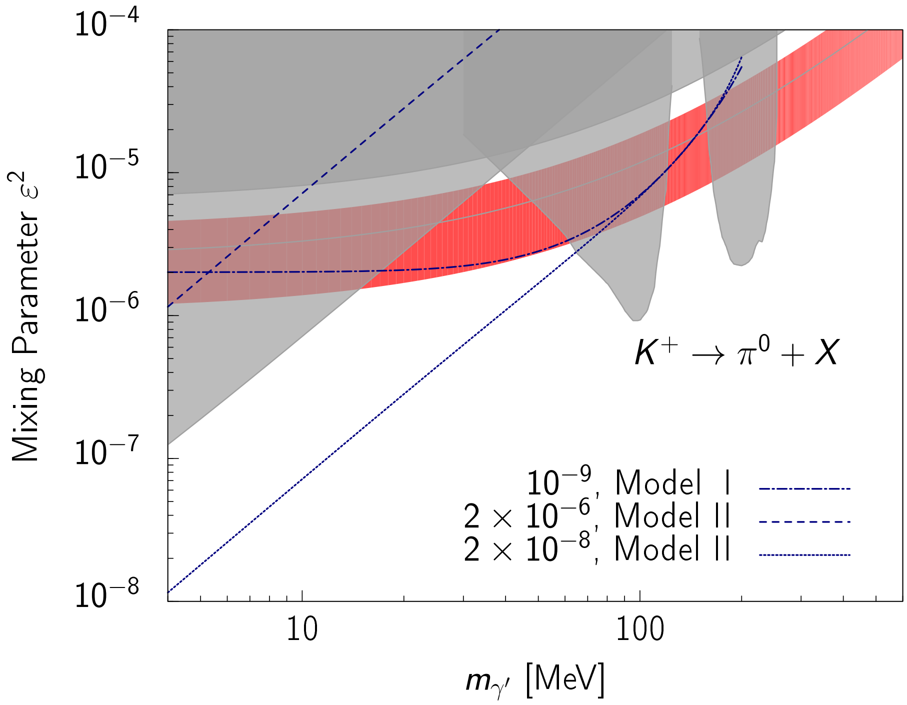

Figure 4.5: Exclusion limits for invisible decays of the hidden photon: The grey shaded regions are excluded from the anomalous magnetic moment of the electron and muon, and the analysis of the decay $K \to \pi^0 X$ [126]. Note that in comparison to Fig. 1.19 the limits which require visible decay products are not applicable and thus are not shown. Dashed-dotted curve: bound calculated in the kinetic mixing model (model I) for an accuracy of the ratio $\Gamma(K^+ \to \mu^+\nu_\mu\gamma')/\Gamma(K^+ \to \mu^+\nu_\mu)$ of 10^{-9}. Dashed curve: result for the 1973 data [207] within model II, where the γ' only couples to the μ^+. Dotted curve: bound calculated in model II for an assumed improvement of the experimental accuracy by two orders of magnitude $(2 \cdot 10^{-8})$.

where X denotes any invisible state, does not apply in model II. In this case the γ' is coupled to the charged lepton only. Therefore, in model II only the bound from $(g-2)$ is relevant.

A possible bound for the kinetic mixing model is represented by the dashed-dotted curve for an assumed experimental accuracy of the ratio $\Gamma(K^+ \to \mu^+\nu_\mu\gamma')/\Gamma(K^+ \to \mu^+\nu_\mu)$ of 10^{-9}. The flight length of the hidden photon is not macroscopic for these parameters. Hence, this bound does not apply for visible decays. Instead, it is only valid, if the hidden photon decay occurs invisibly, such as for the decay into Light Dark Matter. For these processes it is required that a dark-matter particle χ with $2m_\chi < m_{\gamma'}$ exists.

Based on the old $(g-2)_e$ exclusion limit, the 1973 data [207] allow one to slightly improve the bound for the purely vectorial coupling at low masses and large ε (dashed curve) within model II. Due to the refinement of the theoretical determination of $(g-2)_e$ the bound from rare kaon data is already covered by the new $(g-2)_e$ limit. If in a model of the type II, the γ' does not couple to the electron, the bound from $(g-2)_e$ cannot be applied. Thus,

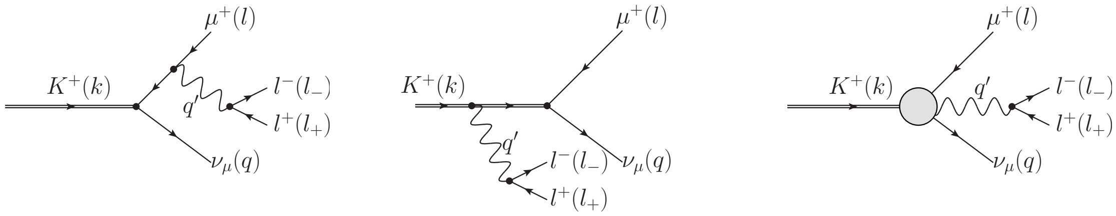

Figure 4.6: Feynman diagrams of the process $K^+ \to \mu^+\nu_\mu l^+ l^-$.

the limit obtained in this work is currently the best in this range. Furthermore, an estimate is given in Fig. 4.5 in which way the exclusion limits change due to an improvement in the experimental accuracy of the ratio $\Gamma(K^+ \to \mu^+\nu_\mu\gamma')/\Gamma(K^+ \to \mu^+\nu_\mu)$ by two orders of magnitude (dotted curve). Obviously, an improvement of the experimental quantities on the right side of Eq. (4.16) will allow for the exclusion of a large region of the parameter space up to masses of about 80 MeV since the bound on ε^2 is depending linearly on the RHS of Eq. (4.16). Larger angular and momentum acceptances and a larger rate of stopped K^+ compared to [207] for example will improve this quantity significantly. Such an improved extraction might be achieved by new facilities, as the NA62 experiment at CERN [210] or rare kaon decay experiments at JPARC [211].

4.3 Constraints for hidden photons decaying into lepton pairs from rare kaon experiments

In this section decays of the type

$$P^\pm \to l^\pm + \nu_l + l'^+ l'^-,$$

where $P^\pm = \pi^\pm, K^\pm$ is a pseudo-scalar meson and l and l' denote charged leptons, are studied with respect to their usage as a probe for hidden photons. Due to the larger mass of the kaon compared to the pion, a much wider range of the hidden photon mass can be probed. Therefore, the following analysis will concentrate on the decay of a K^+. By replacing the parameters associated with the kaon by those of the pion, one can easily obtain the expressions for a decaying pion.

In the signal process, the lepton pair is created by the exchange of a hidden photon, whereas the conversion of a virtual photon into leptons is the SM background. For this purpose, in particular the decay $K^+ \to \mu^+\nu_\mu e^+e^-$ is investigated. The corresponding decay width can be easily calculated by integrating over the lepton pair variables similarly as demonstrated in Appendix B.3.2. In a future experiment at least the lepton pair will be detected and its invariant mass will be reconstructed. Hence, the integration over the lepton pair variables will be performed explicitly. This procedure allows one to include experimental cuts easily and to obtain realistic predictions. Such an experiment could be performed at facilities as JPARC [211].

4.3.1 Calculation of decay rates

The amplitude of the process $K^+(k) \to \mu^+(l) + \nu_\mu(q) + l^+(l_+) + l^-(l_-)$ derived from the Feynman diagrams of Fig. 4.6 reads

$$\mathcal{M} = \frac{G_F \, e \, \sin\theta_c}{\sqrt{2}} \, \bar{\varepsilon}^*_\rho(q') \, \left(f_K \, m_l \, L^\rho - H^{\rho\nu} j_\nu\right), \tag{4.17}$$

where $l^2 = m_l^2$ and

$$\bar{\varepsilon}^*_\rho(q') = \frac{e}{q'^2} \left[\bar{u}(l_-)\gamma_\rho v(l_+)\right] \tag{4.18}$$

for the QED background and

$$\bar{\varepsilon}^*_\rho(q') = \frac{\varepsilon^2 e}{q'^2 - m_{\gamma'}^2 + i m_{\gamma'} \Gamma_{\gamma'}} \left[\bar{u}(l_-)\gamma_\rho v(l_+)\right] \tag{4.19}$$

for the hidden photon signal. Furthermore, the quantities L^ρ, j_ν, and $H^{\rho\nu}$ are given in Eqs. (4.8) to (4.10), respectively. As in Sec. 4.2, the term of the amplitude in Eq. (4.17), which is proportional to the kaon decay constant f_k is referred to as IB contribution, which is independent of structure dependent effects. The SM process with the largest branching fraction is the decay $K^+ \to \mu^+\nu_\mu e^+ e^-$. It was discussed in the literature [208] that the IB contribution dominates the decay rate over a wide range of invariant masses. As can be seen from Eq. (4.17), the IB term is proportional to the mass of the lepton l. Therefore, the decays $K^+ \to e^+\nu_e e^+ e^-$ and $K^+ \to e^+\nu_e \mu^+\mu^-$ are helicity suppressed due to the much smaller mass of the electron. As consequence, the following discussion will concentrate on the decay $K^+ \to \mu^+\nu_\mu e^+ e^-$.

The differential decay rate can be expressed conveniently analogously to Sec. 3.3.1. In general, the 8-fold differential decay rate reads

$$d\Gamma = \frac{1}{2M_K} \frac{d^3\vec{l}}{(2\pi)^3 2E_l} \frac{d^3\vec{q}}{(2\pi)^3 2E_\nu} \frac{d^3\vec{l}_+}{(2\pi)^3 2E_+} \frac{d^3\vec{l}_-}{(2\pi)^3 2E_-} (2\pi)^4 \, \delta^{(4)} \left(k - l - q - l_+ - l_-\right) \overline{|\mathcal{M}|^2}.$$

Following the discussion of Sec. 3.3.1, one finds for the differential decay rate

$$\frac{d\Gamma}{dE_l^L \, d\Omega_l^L \, dm_{ll} \, d\Omega_{q'}^* d\Omega_+^{**}} = \frac{|\vec{l}|^L}{64 M_K} \frac{1}{(2\pi)^8} \frac{|\vec{q}|^* \sqrt{m_{ll}^2 - 4m_l^2}}{\sqrt{s^*}} \overline{|\mathcal{M}|^2}, \tag{4.20}$$

with $q' = l_+ + l_-$. In addition, $*$ and $**$ denote the $(q+q')$- and q'-rest frames, respectively, and the lab frame, where the kaon is at rest, is labeled by L.

To find predictions for the discovery potential of future experiments, one is interested in the decay rate within a certain mass range, which corresponds to the anticipated mass resolution. Hence, Eq. (4.20) has to be integrated over the allowed phase space within the mass range $\delta m = m_{ll,\,\mathrm{max}} - m_{ll,\,\mathrm{min}}$:

$$\Delta\Gamma \equiv \int_{m_{ll,\,\mathrm{max}}}^{m_{ll,\,\mathrm{min}}} dm_{ll} \, \frac{d\Gamma}{dm_{ll}}. \tag{4.21}$$

The SM background decay rate is in the following denoted by $\Delta\Gamma_{\gamma^*}$, where $\bar{\varepsilon}^*_\rho$ entering in Eq. (4.17) can be found in Eq. (4.18). $\Delta\Gamma_{\gamma'}$ is the decay rate of the signal process with $\bar{\varepsilon}^*_\rho$

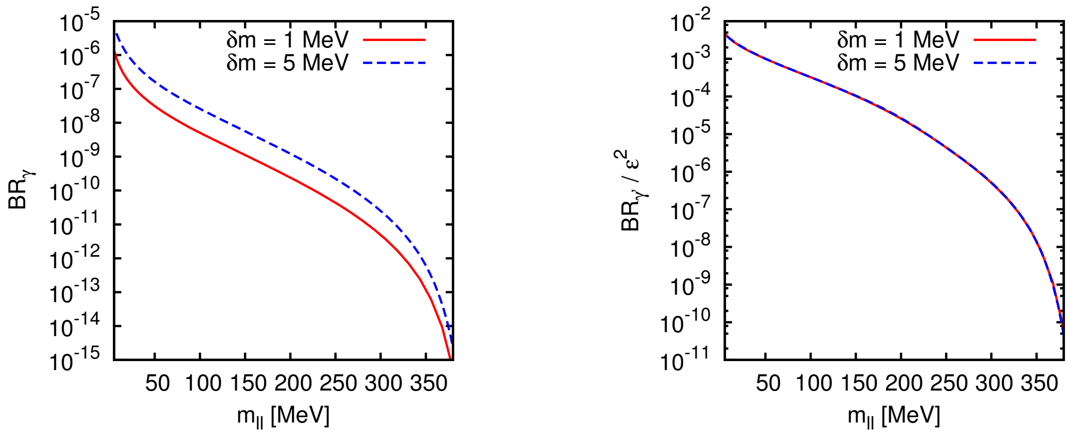

Figure 4.7: The red solid (blue dashed) curve shows the result for $\delta m = 1\,\mathrm{MeV}$ ($\delta m = 5\,\mathrm{MeV}$). Left panel: Calculation of the SM branching fraction from the IB contribution. Right panel: Calculation of the expected branching fraction for the signal process. Note that this curve is drawn for a continuous hidden photon mass $m_{\gamma'} = m_{ll}$ to illustrate the dependence of $\mathrm{BR}_{\gamma'}$ on m_{ll} and δm. In a future experiment, one expects only a signal within one certain mass bin with $m_{ll,\,\mathrm{max}} \leq m_{\gamma'} \leq m_{ll,\,\mathrm{min}}$.

given as in Eq. (4.19). Since the structure of the signal process is equal to the one in Fig. B.2, one can rewrite the $\Delta\Gamma_{\gamma'}$ as

$$\Delta\Gamma_{\gamma'}(\varepsilon^2) = \frac{\Delta\Gamma_{\gamma'}(\widetilde{\varepsilon}^2)}{\widetilde{\varepsilon}^2} \times \varepsilon^2,$$

following the discussion of Sec. 3.5.1. It is convenient to express the results in terms of branching fractions normalized to $\Gamma(K^+ \to \mu^+\nu_\mu) = 0.6355 \times \Gamma_{\mathrm{tot}}$ obtained in Eq. (4.4) to deal with dimensionless quantities. This gives rise to

$$\mathrm{BR}_{\gamma^*/\gamma'} \equiv \frac{\Delta\Gamma_{\gamma^*/\gamma'}}{\Gamma(K^+ \to \mu^+\nu_\mu)} \times 0.6355. \tag{4.22}$$

4.3.2 Numerical results

Since the IB contribution dominates over the structure dependent effects, the investigation of the signal and background process will be restricted to the IB term in the following. It was found in Refs. [208, 209] that the structure dependent terms contribute less than 3% to the decay rate for $m_{ll} \lesssim 150\,\mathrm{MeV}$, which is the mass range of interest in this section. However, to obtain more accurate predictions for $m_{ll} \gtrsim 150\,\mathrm{MeV}$, these contributions need to be taken into account.

As a first step, the findings of this work are compared with the results of the SM background calculation of Ref. [208], which are found to be in excellent agreement. Furthermore, the authors of Ref. [206] obtain the same values for the SM background.

The branching fraction of the background (signal) process is shown in the left (right) panel of Fig. 4.7. The red solid and blue dashed curves illustrate the results for $\delta m = 1\,\mathrm{MeV}$ and

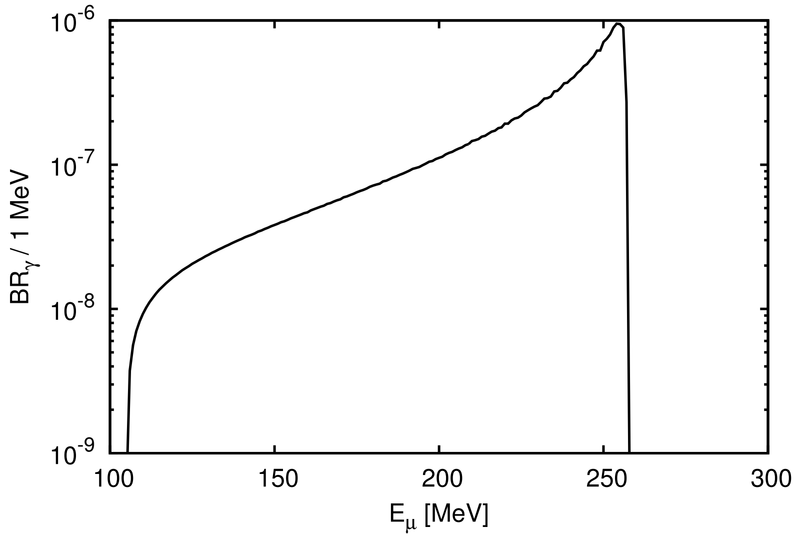

Figure 4.8: Branching fraction BR_{γ^*} as a function of the energy of the μ^+ per 1 MeV.

$\delta m = 5\,\mathrm{MeV}$, respectively. As expected from the structure of the amplitude of the signal process, $\mathrm{BR}_{\gamma'}$ is only slightly affected by δm. The region where the hidden photon is on the mass shell dominates the decay rate. BR_{γ^*}, on the contrary, scales roughly linearly with δm. Figure 4.8 exhibits that the branching ratio strongly increases with the energy of the muon, with a sharp drop at the muon energy of the two-body decay $K^+ \to \mu^+\nu_\mu$. In Sec. 4.2 the kinetic energy of the muon was restricted to the range from 60 MeV to 100 MeV, corresponding to the range $165\,\mathrm{MeV} \lesssim E_\mu \lesssim 205\,\mathrm{MeV}$. This constraint would dramatically reduce the decay rate for the signal as well as the background process. The upper left panel of Fig. 4.4 shows that this constraint would affect in particular the region of low invariant mass m_{ll}, where such decay experiments are most competitive. Therefore, this constraint will not be applied. This will not raise a problem, since in future experiments usually all decay products except neutrinos are planned to be detected. Hence, there is no need for this constraint. This allows for a clear separation between the signal and the reducible background. Predictions for the discovery potential of such an experiment can be obtained by means of the branching fractions of the signal and background processes. One can calculate the minimal coupling ε^2 analogously to Sec. 3.5.1 as

$$\varepsilon^2 = S\,\frac{\widehat{\varepsilon}^2 \times \mathrm{BR}_{\gamma^*}}{\mathrm{BR}_{\gamma'}(\widehat{\varepsilon}^2)}. \tag{4.23}$$

The sensitivity is estimated by following Eq. (3.33) as

$$S = \frac{N_\sigma}{\sqrt{\mathrm{BR}_{\gamma^*} \times N_{K^+}}},$$

with the total number of kaon event N_{K^+}. Figure 4.9 shows the results for the projected bounds. As before, the grey shaded regions in Fig. 4.9 correspond to existing exclusion limits, where details can be found in Sec. 1.3.4. The green and red curves illustrate the projected

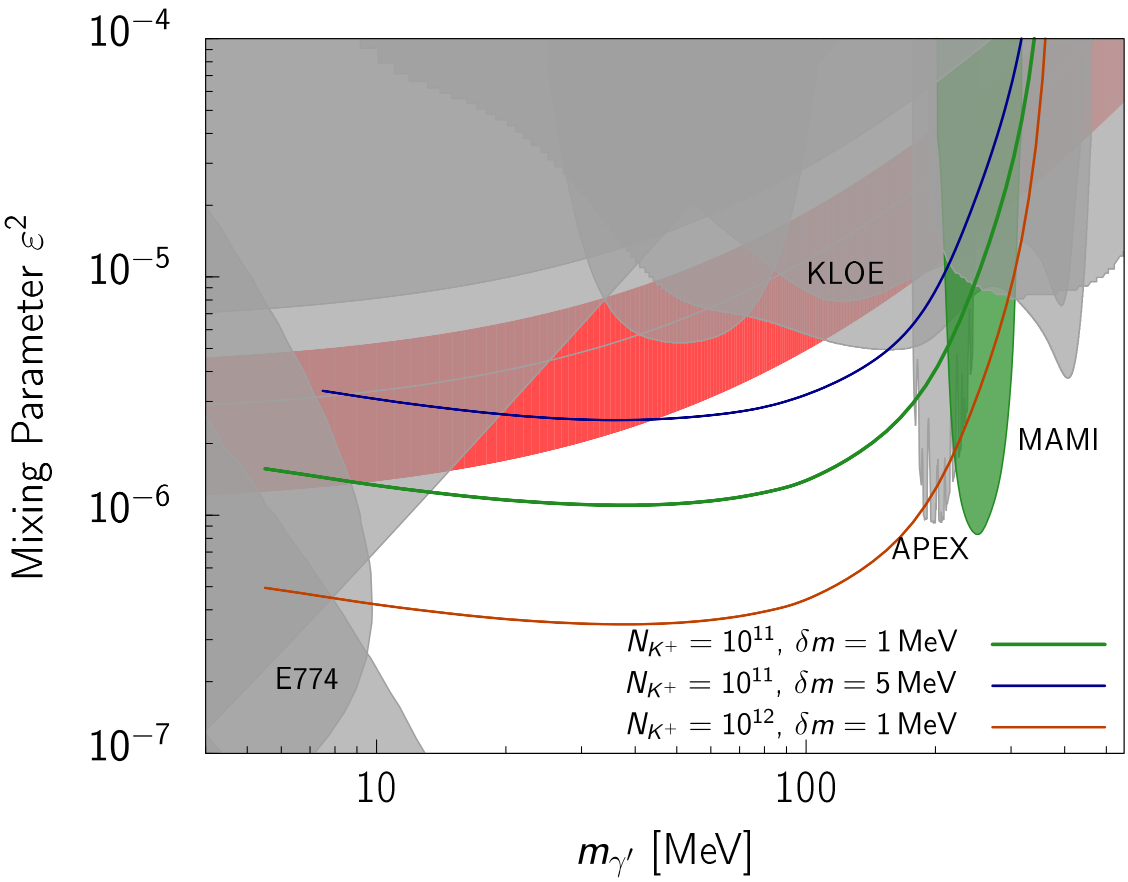

Figure 4.9: Projection of the reach of an experiment searching for an excess from hidden photons in the decay $K^+ \to \mu^+\nu_\mu e^+e^-$. The projected bounds were calculated for a mass resolution $\delta m = 1\,\mathrm{MeV}$ and a total number of kaon events $N_{K^+} = 10^{11}$ and $N_{K^+} = 10^{12}$, shown by the green and red curve, respectively. In addition, the blue curve illustrates the result for $\delta m = 5\,\mathrm{MeV}$ and $N_{K^+} = 10^{11}$. The grey shaded regions correspond to existing bounds, which are explained in detail in Sec. 1.3.4.

bounds for a mass resolution $\delta m = 1\,\text{MeV}$ and total numbers of kaon events $N_{K^+} = 10^{11}$ and $N_{K^+} = 10^{12}$, respectively. The findings for $\delta m = 5\,\text{MeV}$ and $N_{K^+} = 10^{11}$ correspond to the blue curve. It turns out that such an experiment can be used to constrain the low mass region, where presently fixed-target experiments are not sensitive. The findings of Sec. 4.2 indicate that the bound in the region $m_{\gamma'} \gtrsim 150\,\text{MeV}$ will be improved by the structure dependent contribution, which enhances the decay rate strongly. This predicted behavior [208] was proven experimentally in Ref. [209].

4.4 Summary and conclusions of the section

In this chapter rare kaon decays were investigated as a possibility to observe signals from hidden photons, which either decay invisibly or visibly. For this purpose, the processes $K^+ \to \mu^+\nu_\mu\gamma'$ and $K^+ \to \mu^+\nu_\mu(\gamma^*/\gamma' \to l^+l^-)$ for the invisible and visible hidden photon decay, respectively, were analyzed. In the first case, besides the hidden photon model, other types of models, in which the γ' couples to the positively charged muon only, were studied. In the latter case, a feasibility study for future experiments searching for a bump in the invariant-mass distribution of the lepton pair caused by an intermediate hidden photon, was performed. One can find exclusion limits for the parameter space of the corresponding models from the decay rates.

In particular in the case of invisible hidden photon decays, more precise data are necessary. Improving the accuracy compared to that of the forty year old pioneering work of Ref. [207] by two or more orders of magnitude would allow the exclusion of a significantly larger part of the up to now allowed parameter space, which is also containing a considerable part of the $(g-2)_\mu$ welcome band. It was found that future experiments, such as the NA62 experiment at CERN or the TREK experiment at JPARC, will be ideally suited to probe the low mass region of the parameter space in case of a visibly decaying hidden photon.

Conclusions and Outlook

Summary and conclusions

In this work opportunities were studied to search for new, light gauge bosons, weakly coupled to the SM, in laboratory experiments at modest energies. In particular, the hidden photon model was investigated. This model is a $U(1)$ extension of the gauge group of the SM manifesting itself by a light gauge boson γ' with a mass $m_{\gamma'} \sim \mathcal{O}(\text{MeV})$ and a coupling strength $\varepsilon^2 = \alpha'/\alpha \sim \mathcal{O}(10^{-14}) - \mathcal{O}(10^{-2})$ compared to the electromagnetic coupling.

Recently, an intense experimental as well as theoretical program has been started to explore this SM extension. This is motivated by the fact that the hidden photon can be invoked to explain existing discrepancies between theoretical predictions and the corresponding observations in experiments. Such examples are the positron excess in cosmic ray data or the discrepancy between the theoretical and experimental value for the anomalous magnetic moment of the muon. To constrain the parameter space of this model, a large effort is currently ongoing, which requires the interplay between theoretical and experimental physics. The accurate predictions within this model are probed by using existing data sets or by performing new experiments. Some of these, such as the A1 experiment at Mainz, already have taken data. The search for hidden photons in these experiments requires a precise knowledge of the signal as well as background processes.

For this purpose the emission of a hidden photon induced by the scattering of a lepton beam off a hadronic target, i.e. the reaction $e(Z,A) \to e(Z,A)\gamma'$, was investigated. This process was studied from two points of view: The study of the signal process in general as well as the search for invisible hidden photon signatures. The latter requires the precise knowledge of the SM background resulting from the Bethe-Heitler process $e(Z,A) \to e(Z,A)\gamma$. It was found that the signal cross section is dominated by the region of phase space, where nearly the entire beam energy is transferred to the hidden photon and its emission occurs into the beam direction, where the background is comparably low.

As a next step the applicability of the Weizsäcker-Williams (WW) approximation, which is widely used in the existing literature, was studied. It could be shown that for beam energies above 5 GeV the shape of the cross section is well reproduced within the WW approximation, whereas it differs significantly for lower beam energies. This result has a large impact for the actual configuration of experiments. Current experiments are optimized in such a way that the cross section for the emission of a hidden photon is as large as possible. This occurs in the region when the ratio of the γ' energy to the beam energy reaches 1. The two methods show considerably large deviations in this region for beam energies not much larger than the hidden photon mass. Furthermore, the commonly used expressions within the WW approximation overestimate the cross sections of the process $e(Z,A) \to e(Z,A)\gamma'$ found by the analysis of this work. As a consequence, it was pointed out, in which manner the WW expressions need to be modified to reconcile the approximated results with the ones of this thesis. This finding is of high importance, since the studied approximated formulae for the cross sections are widely used for the study of the reach of future experiments as well as to calculate the signal strength. Thus, the approximated cross sections are directly related to exclusion limits.

A large part of the thesis deals with a study of the reaction $e(Z, A) \to e(Z, A)l^+l^-$ which is investigated in fixed-target experiments. In these experiments the lepton pair is detected, which allows one to search for a signal from hidden photons in the invariant-mass distribution of the lepton pair. This requires of course an understanding of the corresponding QED background process. The precise knowledge of the SM background cross section allows one to find realistic predictions for the reach of future experiments and exclusion limits for the parameter space of hidden photons, in case no signal is seen. Therefore, the calculation of the integrated cross section within the actual limits of the particular experiments was discussed. The data taken in the experiment performed by the A1 Collaboration at MAMI in 2010 were compared with corresponding cross section calculation. It was found that the theoretical and experimental values are in very good agreement. Moreover, the signal and background cross sections were studied accounting for the effects from the antisymmetrized diagrams. In addition, the existing limit from the MAMI 2011 experiment was refined.

These results are the basis of the first comprehensive study of existing and future fixed-target experiments searching for hidden photons. The actual chosen kinematic settings for the beam time at MAMI in 2013, which were optimized to be able to probe the largest region of parameter space possible, rely on the calculations of this work. In addition, for the future MESA facility, which is under construction at the University of Mainz, a first detailed feasibility study was performed. Besides the experiments at Mainz, fixed-target experiments are planned at JLAB, which are APEX, HPS, and DarkLight. For two of these experiments, HPS and DarkLight, detailed simulations were performed. It was found that the existing predictions and the results of this analysis are in good agreement.

It was shown that these experiments will improve on the knowledge on the parameter space of hidden photons significantly. In particular, each of the considered experimental programs will extend the knowledge of the parameter region by at least one order of magnitude. Furthermore, the investigated experimental setups will be conclusive whether or not a hidden photon decaying into a purely visible final state is at the origin of the discrepancy between the experimental and theoretical determination of the anomalous magnetic moment of the muon.

In order to obtain cross sections with a numerical precision better than 1%, these calculations were performed on GPUs, which are ideally suited to perform the necessary Monte Carlo integrations. As a byproduct it was found that GPUs and an existing implementation of the widely used VEGAS integration algorithm on GPUs allow one to enhance the speed of the numerical evaluations by orders of magnitude at comparably low cost.

Moreover, rare kaon decays were investigated as a possibility to probe the hidden photon model. For this purpose, reactions which contain invisible as well as visible decays of the hidden photon were studied. In the first case, also additional models were studied. Based on the same methods as in the previous chapter, bounds for the parameter space and predictions for future experiments were obtained.

Outlook

Several dedicated experiments searching for hidden photons are currently underway. The data taken by A1 will be published in the near future. In addition, first data have been taken at APEX, and HPS will start data taking in 2014. Moreover, it is planned that first data will be taken at MESA from 2017 onwards. Further experimental programs are currently proposed, such as a new beam-dump experiment at CERN. These programs will benefit from the results of the analysis of the Weizsäcker-Williams approximation performed in this thesis. In addition, the TREK experiment at J-PARC will investigate rare kaon decays starting in the near future. One of the rare kaon processes studied here can be used for this search.

In addition, the methods of this thesis allow one to easily obtain predictions for any future fixed-target experiment, in which the process $e + (Z, A) \to e + (Z, A) + (\gamma'/\gamma^* \to l^+l^-)$ is investigated. To do so, one needs to calculate the cross sections within the expected acceptances of these experiments requiring only minor adjustments. As an example, this was already performed within the feasibility study for a future experiment at MESA.

Moreover, one can obtain predictions for the beam spin asymmetry

$$\mathcal{A} = \frac{\Delta\sigma(s_e = +) - \Delta\sigma(s_e = -)}{\Delta\sigma(s_e = +) + \Delta\sigma(s_e = -)},$$

where s_e denotes the spin of the lepton in the initial state, which is a further observable which can be probed for a signal resulting from hidden photons. The advantage of this observable results from the fact that $\mathcal{A}$ is vanishingly small for the QED background itself. For this process, a non-vanishing asymmetry can be caused only by the imaginary part of the hidden photon amplitude. As an example, first calculations show that one expects an asymmetry $\mathcal{A} \cong 10^{-4}$ for $m_{\gamma'} = 50\,\text{MeV}$ and $\varepsilon^2 = 10^{-6}$ depending on the kinematics and resolution. Furthermore, the asymmetry $\mathcal{A}$ can be used to investigate a possible signal in one of the data sets in more detail. In addition, $\mathcal{A}$ allows one to probe models of Light Dark Matter, in which the decay of the hidden photon into invisible particles which are not included in the SM is possible. While a bump in the invariant-mass distribution of the SM decay products will be strongly reduced, the asymmetry will be even larger. However, the experimental determination of such a small asymmetry is very challenging and requires a significant effort. Hence, this method does not seem to be applicable to probe a wide range of parameters, but can be used to probe a particular set of parameters $m_{\gamma'}$ and ε to very high accuracy. Of course, further studies are needed to obtain precise predictions.

In addition, other models of new physics can be probed by applying the calculations of this thesis. For example, the process $ep \to ep\mu^+\mu^-$ can be investigated to shed light on the proton radius puzzle. By means of this reaction one can measure the proton radius from μp-scattering without the requirement of a muon beam, e.g. at MAMI. A first study for MAMI indicates that the expected cross sections are far too small to obtain significant results. However, this process allows one to constrain models in which an additional boson couples to the muon, which violates lepton universality or parity. The methods of this work allow one to easily find predictions for possible experiments. However, the exact treatment of radiative corrections is crucial to improve the cross section calculations. Also further interactions such as Z^0 boson exchange need to be included into the amplitude.

Another possibility to utilize the findings of this work, is the determination of the spacelike electromagnetic form factors of the antiproton, which are currently not well known. For this purpose, the scattering of an antiproton beam off a nuclear target (A, Z), from which an electron-positron pair is created, i.e. the process $\bar{p}(A, Z) \to \bar{p}(A, Z)e^+e^-$, can be investigated. The necessary theoretical study can be easily performed by applying the methods of this work.

Appendix

Appendix A

Notation and Conventions

A.1 Kinematical quantities

A.1.1 Kinematical triangle function

The kinematical triangle function λ is defined as

$$\begin{aligned}\lambda(x,\,y,\,z) &\equiv (x-y-z)^2 - 4yz \\ &= \left(s - \left(\sqrt{y}+\sqrt{z}\right)^2\right)\left(s - \left(\sqrt{y}-\sqrt{z}\right)^2\right).\end{aligned} \tag{A.1}$$

The name originates from the fact that the area of a triangle with sides of the length $\sqrt{x}$, $\sqrt{y}$, and $\sqrt{z}$ is defined as $A_\triangle = {}^1\!/_4\sqrt{-\lambda(x,\,y,\,z)}$. Prevalently encountered special cases are:

$$\begin{aligned}\lambda(x,\,y,\,y) &= x\,(x-4y)\,, \\ \lambda(x,\,y,\,0) &= (x-y)^2\,.\end{aligned}$$

A.1.2 Decay rate for 2-body kinematics

In general, for the decay of an unstable particle of mass m and momentum p into a n-body final state, the decay rate reads

$$\Gamma = \frac{1}{\tau} = \frac{1}{2m}\frac{1}{(2\pi)^{3n-4}}\cdot I_n(m^2), \tag{A.2}$$

where

$$I_n(m^2) = \int\prod_{i=1}^{n}\frac{\mathrm{d}^3p_i}{2\,E_i}\,\delta^{(4)}\left(p-\sum_i p_i\right)\,|\langle p_1,\,\ldots,\,p_n|\mathcal{M}|p\rangle|^2\,. \tag{A.3}$$

The phase space integral is treated in detail in Ref. [174]. Since the invariant matrix element $\overline{|\mathcal{M}_{fi}|}^2$ for a 2-body decay only depends on the Mandelstam variable $s = m^2$, the integral in $I_n(m^2)$ is independent of $\overline{|\mathcal{M}_{fi}(s)|}^2$. For such a process one finds

$$\Gamma = \frac{\lambda^{\frac{1}{2}}(s,\,m_1^2,\,m_2^2)}{16\pi\,s^{\frac{3}{2}}}\overline{|\mathcal{M}_{fi}(s)|}^2. \tag{A.4}$$

A.2 Parametrization of the timelike electromagnetic form factor of the pion

The pion form factor F_π can be parametrized within the model of Gounaris and Sakurai [212]. They find

$$F_{\pi,\rho}(q'^2) = \frac{m_\rho^2 + d\, m_\rho \, \Gamma_\rho}{f(q'^2)}, \tag{A.5}$$

where

$$\begin{aligned} f(q'^2) = \left(m_\rho^2 - q'^2\right) + \Gamma_\rho \times \left(\frac{m_\rho^2}{k_{GS}^3(m_\rho^2)}\right) \Bigg(& k_{GS}^2(q'^2) \times \left(h_{GS}(q'^2) - h_{GS}(m_\rho^2)\right) \\ & + k_{GS}^2(m_\rho^2) h'(m_\rho^2) \left(m_\rho^2 - q'^2\right) \Bigg) - i\, m_\rho \, \Gamma_\rho \left(\frac{k_{GS}(q'^2)}{k_{GS}(m_\rho^2)}\right)^3 \left(\frac{m_\rho}{\sqrt{q'^2}}\right) \end{aligned}$$

with

$$k_{GS}(s) = \sqrt{\frac{s}{4} - m_{\pi^\pm}},$$

and

$$\begin{aligned} h_{GS}(s) &= \frac{2}{\pi} \frac{k_{GS}(s)}{\sqrt{s}} \times \log \frac{\sqrt{s} + 2k_{GS}(s)}{2m_{\pi^\pm}}, \\ h'_{GS}(s) &= \partial h_{GS}(s)/\partial s, \\ d &= \frac{3}{\pi} \frac{m_{\pi^\pm}}{k_{GS}^2(m_\rho^2)} \times \log \frac{m_\rho + 2k_{GS}(m_\rho^2)}{2m_{\pi^\pm}} + \frac{m_\rho}{2\pi k_{GS}(m_\rho^2)} - \frac{m_{\pi^\pm}^2 m_\rho}{\pi k_{GS}^3(m_\rho^2)}. \end{aligned}$$

Furthermore, $m_\rho = 776.3\,\mathrm{MeV}$ is the mass of the neutral ρ meson and $\Gamma_\rho = 150.5\,\mathrm{MeV}$ is the total decay width. Since the contribution of ω meson to the pion form factor interferes with the ρ meson contribution, it is helpful to include this effect to the pion form factor. In addition, the contribution of the ρ' meson is included in the parametrization as well. For this purpose, the mass and width of the ρ meson are replaced by the corresponding quantities of the ω and ρ' meson in the above expressions, i.e.

$$\begin{aligned} m_\omega &= 783\,\mathrm{MeV}, \quad & \Gamma_\omega &= 8.4\,\mathrm{MeV}, \\ m_{\rho'} &= 1370\,\mathrm{MeV}, \quad & \Gamma_{\rho'} &= 350\,\mathrm{MeV}. \end{aligned}$$

The pion form factor can be written as linear combination of the three contributions [213–216]

$$F_\pi(q'^2) = \frac{F_{\pi,\rho}(q'^2)}{1 + 1.95 \times 10^{-3}} \left(1 + 1.95 \times 10^{-3} F_{\pi,\omega}(q'^2)\right) - \frac{0.083 \times F_{\pi,\rho'}(q'^2)}{1 - 0.083}. \tag{A.6}$$

A.3 List of frequently used acronyms

Acronym	Meaning	Explanation
APEX	A prime experiment	Fixed-target experiment searching for the γ' at JLAB
D	direct term	corresponds to the Feynman diagrams of Fig. 3.1 on page 80
GPU	graphics processing unit	see Appendix C
HPS	Heavy Photon Search	Fixed-target experiment searching for the γ' at JLAB
IB	inner bremsstrahlung	structure independent part of the amplitude of the analyzed kaon decays, e.g. Eq. (4.7) on page 126
λCDM	Standard Model of Cosmology	see Sec. 1.1.1
MAMI	Mainz Microtron	see Secs. 3.4.3 and 3.5.2
MESA	Mainz Energy-recovering Superconducting Accelerator	see Sec. 3.5.3
JLAB	Jefferson Lab	Thomas Jefferson National Accelerator Facility at Newport News, USA
SL	spacelike	spacelike V, e.g. in the Feynman diagrams in the central panel of Fig. 3.1 on page 80
SM	Standard Model of particle physics	see Sec. 1.1.3
TL	timelike	timelike V, e.g. in the Feynman diagrams in the upper panel of Fig. 3.1 on page 80
VVCS	doubly virtual Compton scattering	see the Feynman diagrams in the lower panel of Fig. 3.1 on page 80
WW	Weizsäcker–Williams approximation	see Sec. 2.3
X	exchange term	corresponds to the Feynman diagrams of Fig. 3.2 on page 81

Appendix B

Auxiliary calculations

B.1 Approximation of the γ' to direct timelike γ ratio $\frac{d\sigma_{\gamma'}}{d\sigma_{\gamma^*}}$

In this Section, the derivation of Eq. (19) of Ref. [140] is presented, which allows one to easily relate the cross section of γ' production in the reaction

$$e + (Z,\, A) \to e + (Z,\, A) + (\gamma' \to l^+ l^-)$$

to the direct TL background cross section of the process

$$e + (Z,\, A) \to e + (Z,\, A) + (\gamma^* \to l^+ l^-)$$

defined in Eq. (3.27a). The cross sections of these two processes are nearly identical and only differ in the propagator of the intermediate vector boson. Within the small mass window, where the pure γ' production cross section is not negligible, which is the region where the denominator of the γ' propagator is approximating zero, it is sufficient to compute the integrals over the invariant mass of the lepton pair. All other quantities entering in the cross section can be considered as constants within this small region. These constants will cancel each other when the ratio of the two cross sections is taken. Furthermore, one can exploit that due to the very narrow width, the squared propagator in the signal cross sections in Eqs. (3.25) and (3.26) can be rewritten by using the definition of the Dirac δ distribution $\delta_\epsilon(x) = \frac{1}{\pi}\frac{\epsilon}{x^2+\epsilon^2}$ for sufficient small ϵ, which leads to

$$\lim_{m_{\gamma'}\Gamma_{\gamma'}\to 0} \left(\frac{1}{(q'^2 - m_{\gamma'}^2)^2 + m_{\gamma'}^2 \Gamma_{\gamma'}^2} \right) \to \frac{\pi}{m_{\gamma'}\Gamma_{\gamma'}} \delta_{(m_{\gamma'}\Gamma_{\gamma'})}(q'^2 - m_{\gamma'}^2). \tag{B.1}$$

Since the total decay width of the hidden photon $\Gamma_{\gamma'}$ given in Eq. (1.34) is by several orders of magnitude smaller than the γ' mass in the non-excluded regions of the parameter space, the approximate treatment by use of the Dirac δ function is possible.

Starting with the integral of the squared γ' propagator with $q'^2 = (l_+ + l_-)^2$ leads to

$$\begin{aligned}
\int dq'^2 \left| \frac{\varepsilon^2}{q'^2 - m_{\gamma'}^2 + i m_{\gamma'}\Gamma_{\gamma'}} \right|^2 &= \int d(q'^2 - m_{\gamma'})^2 \left| \frac{\varepsilon^2}{(q'^2 - m_{\gamma'}^2) + i m_{\gamma'}\Gamma_{\gamma'}} \right|^2 \\
&= \int d(q'^2 - m_{\gamma'}^2)\, \frac{\varepsilon^4}{(q'^2 - m_{\gamma'}^2)^2 + m_{\gamma'}^2\Gamma_{\gamma'}^2} \\
&= \int d(q'^2 - m_{\gamma'}^2)\, \frac{\varepsilon^4 \pi}{m_{\gamma'}\Gamma_{\gamma'}}\, \delta(q'^2 - m_{\gamma'}^2) \\
&= \frac{\varepsilon^4\, \pi}{m_{\gamma'}\Gamma_{\gamma'}}
\end{aligned} \tag{B.2}$$

The authors of Ref. [140] parametrize this width by the partial decay width into an electron-positron pair $\Gamma_{\gamma'\to e^+e^-}$ derived in Eq. (1.31) and the factor N_{eff}, which accounts for additional degrees of freedom within the decay of the hidden photon into SM particles. The effective degrees of freedom can be parametrized by

$$N_{\text{eff}} = \frac{\Gamma_{\gamma'}}{\Gamma_{\gamma'\to e^+e^-}} = 1 + \frac{\Gamma_{\gamma'\to\mu^+\mu^-}}{\Gamma_{\gamma'\to e^+e^-}}(1 + R(m_{\gamma'})),$$

where as in Sec. 1.3.3 R is the SM ratio $\sigma(e^+e^- \to \text{hadrons})/\sigma(e^+e^- \to \mu^+\mu^-)$ of the hadron to muon production cross sections. Therefore, the total γ' width reads

$$\begin{aligned}\Gamma_{\gamma'} &= \Gamma_{\gamma'\to e^+e^-} \times N_{\text{eff}}\\ &= \frac{\alpha\varepsilon^2}{3m_{\gamma'}^2}\sqrt{m_{\gamma'}^2 - 4m_l^2}\,(m_{\gamma'}^2 + 2m_l^2) \times N_{\text{eff}} = \frac{\varepsilon^2\alpha}{3}m_{\gamma'} \times N_{\text{eff}},\end{aligned}$$

where in the last step Eq. (1.32) was used.

Inserting these expressions for $\Gamma_{\gamma'}$ into Eq. (B.2), one finds

$$\int dq'^2 \left|\frac{\varepsilon^2}{q'^2 - m_{\gamma'}^2 + im_{\gamma'}\Gamma_{\gamma'}}\right|^2 = \frac{3\pi}{N_{\text{eff}}}\frac{\varepsilon^2}{\alpha}\frac{m_{\gamma'}}{(m_{\gamma'}^2 + 2m_e^2)\sqrt{m_{\gamma'}^2 - 4m_e^2}} \tag{B.3}$$

$$\simeq \frac{3\pi}{N_{\text{eff}}}\frac{\varepsilon^2}{\alpha}\frac{1}{m_{\gamma'}^2}, \tag{B.4}$$

where the last step is only possible for $m_{\gamma'} \gg m_e$.

The result for the corresponding Bethe-Heitler process is obtained by integrating the virtual photon propagator within the limits of one mass bin, which is taken in this calculation as the interval

$$\left[m_{\gamma'} - \frac{\delta m}{2}, m_{\gamma'} + \frac{\delta m}{2}\right],$$

where δm is the mass resolution of the experiment, which is typically much less than $m_{\gamma'}$. One finds

$$\int_{(m_{\gamma'}-\frac{\delta m}{2})^2}^{(m_{\gamma'}+\frac{\delta m}{2})^2} dq'^2 \frac{1}{q'^4} = \frac{1}{(m_{\gamma'} - \frac{\delta m}{2})^2} - \frac{1}{(m_{\gamma'} + \frac{\delta m}{2})^2}$$

$$= \frac{2\,\delta m\, m_{\gamma'}}{(m_{\gamma'}^2 - \frac{\delta m^2}{4})^2} \tag{B.5}$$

$$\simeq \frac{2\,\delta m}{m_{\gamma'}^3}, \tag{B.6}$$

where for the last step $\delta m \ll m_{\gamma'}$ is required.

From the ratio of Eqs. (B.3) and (B.5) one obtains

$$\frac{d\sigma_{\gamma'}}{d\sigma_{D,\gamma^*}^{\text{TL}}} = \frac{3\pi}{N_{\text{eff}}}\frac{\varepsilon^2}{\alpha}\frac{\left(m_{\gamma'}^2 - {}^{\delta m^2}/_4\right)^2}{\delta m\,(m_{\gamma'}^2 + 2m_e^2)\sqrt{m_{\gamma'}^2 - 4m_e^2}}. \tag{B.7}$$

Taking the ratio of Eqs. (B.4) and (B.6) finally leads to the approximate expression

$$\frac{d\sigma_{\gamma'}}{d\sigma^{\mathrm{TL}}_{D,\gamma^*}} \simeq \frac{3\pi}{2N_{\mathrm{eff}}} \frac{\varepsilon^2}{\alpha} \frac{m_{\gamma'}}{\delta m}, \tag{B.8}$$

which is valid for $m_l \ll m_{\gamma'}$ and $\delta m \ll m_{\gamma'}$.

B.2 Detector coordinates

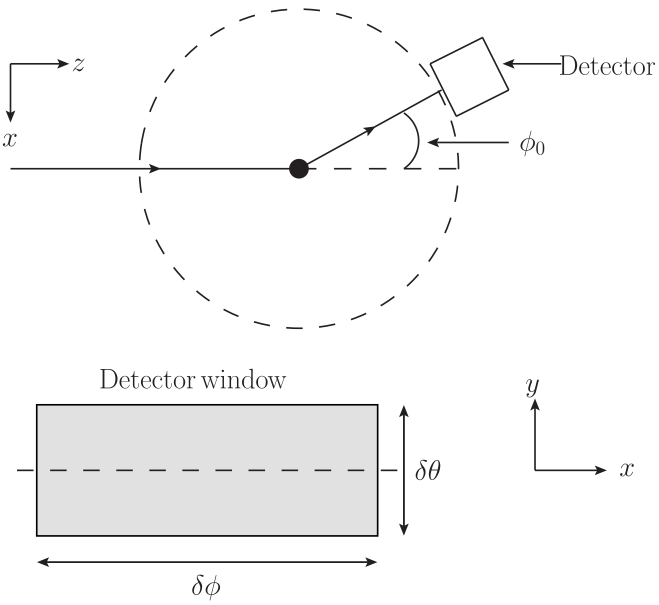

Figure B.1: Definition of angles in detector coordinates: The detector is centered at the scattering angle ϕ_0 measured with respect to the z-axis. The size of the detector window is parametrized by the horizontal and vertical angles, the scattering angle $\delta\phi$ and the out-of-plane angle $\delta\theta$, each measured from the center of the detector. Note that the detector is assumed to be centered in the same plane as the beam, i.e. for the central out-of-plane angle one has $\theta_0 = 0°$.

To parametrize the angular acceptances of detectors in terms of two angles, which describe the opening window of the detector, the so-called Cartesian detector coordinates are used. A sketch of a detector and the definition of the angles describing its acceptances can be found in Fig. B.1. In these coordinates the detector is centered at the scattering angle ϕ_0 measured with respect to the z-axis. Furthermore, it is assumed that the detector is centered in the same plane as the beam, i.e. for the central out-of-plane angle one has $\theta_0 = 0°$. The size of the detector window is parametrized by the horizontal and vertical angles, where $\delta\phi$ is the deviation from the horizontal scattering angle and $\delta\theta$ is the deviation from the vertical out-of-plane angle, each measured from the center of the detector.

The lab frame three-momenta in terms of coordinates directly related to the detector geometry can be parametrized as

$$\vec{l_\pm} = \frac{|\vec{l_\pm}|}{\sqrt{1+\tan^2\delta\theta+\tan^2\delta\phi}}\begin{pmatrix}\tan\delta\phi\,\cos\phi_0+\sin\phi_0\\ \tan\delta\theta\\ \cos\phi_0-\tan\delta\phi\,\sin\phi_0\end{pmatrix}. \tag{B.9}$$

For $\phi_0 = 0°$ it becomes clear that the angles $\delta\phi$ and $\delta\theta$ are directly related to the Cartesian coordinates x and y, respectively. Integrating over the angles $\delta\phi$ and $\delta\theta$ within the limits of the experimental acceptances leads to the cross section $\Delta\sigma$.

To account for this geometry, the cross section has to be multiplied by a Jacobian, which relates the momentum components of a momentum $\vec{p}$ in Cartesian coordinates p_x, p_y and p_z to the detector coordinates, i.e.

$$dp_x\,dp_y\,dp_z = J(\delta\phi,\,\delta\theta)\,|\vec{p}|^2\,d|\vec{p}|\,d\delta\phi\,d\delta\theta,$$

where

$$J(\delta\phi,\,\delta\theta) = \left|\frac{1}{\cos^2\delta\phi\,\cos^2\delta\theta\,(1+\tan^2\delta\theta+\tan^2\delta\phi)^{3/2}}\right|. \tag{B.10}$$

B.3 Factorization of lepton pair production

B.3.1 Factorization of matrix element and phase space

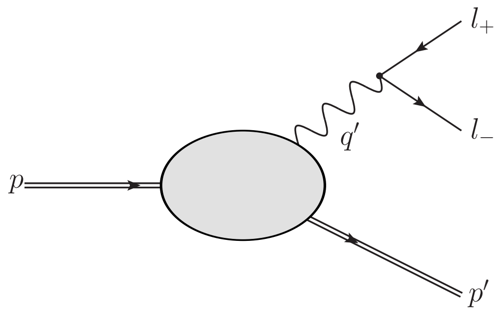

Figure B.2: Sketch of lepton pair production by exchange of a virtual vector boson.

In this Section expressions for the analytical integration over the variables of a lepton pair, which is created from the annihilation of a timelike vector boson, are derived. This allows one to relate the cross section or decay width for lepton pair production from hidden photon bremsstrahlung and the emission of a hidden photon easily. The underlying process is sketched in Fig. B.2. Let $d\sigma$ denote either the differential decay width or the differential cross section, if the initial state consists of one particle with momentum p or two particles with momenta p_1 and p_2, $p = p_1 + p_2$, respectively. The label s refers to any spin of the initial state particles, i.e. s is the spin of the decaying particle in case of the calculation of a decay width and $s = (s_1,\, s_2)$ for the cross section calculation, where s_1 and s_2 are the spins of the two initial state particles. The final state consists of N particles, where the lepton and antilepton of the created pair carry the momenta l_- and l_+, respectively, and $q' = l_+ + l_-$ is the momentum of the intermediate vector state. The sum of the momenta of the remaining

$N-2$ particles is $p' = \sum_{i_1}^{N-2} p'_i = p - q'$. Analogous to the initial state, $s' = (s'_1, \ldots, s'_{N-2})$ refers to the $(N-2)$-tuple of spins of the unspecified final state particles. For the discussion of this Section there is no need to specify their properties in more detail.

For any process as shown in Fig. B.2 with I particles in the initial state and N final state particles, the Feynman amplitude can in general be decomposed as

$$\mathcal{M}_{\mathcal{I}\to\mathcal{N}} = \mathcal{M}_0^\mu D_{\mu\nu}\, l^\nu,$$

where

$$D_{\mu\nu} = (-\varepsilon e)\frac{-g_{\mu\nu} + \frac{q'_\mu q'_\nu}{q'^2}}{q'^2 - m_{\gamma'}^2 + i m_{\gamma'}\Gamma_{\gamma'}}$$

for an intermediate hidden photon and

$$D_{\mu\nu} = (-e)\frac{-g_{\mu\nu}}{q'^2}$$

for a virtual ordinary photon, and $l^\nu = [\bar{u}(l_-,\, s_-)\gamma^\nu v(l_+,\, s_+)]$ is the electromagnetic current of the lepton pair. Due to gauge invariance of the electromagnetic current one has $q'_\nu l^\nu = 0$. The spin averaged, squared matrix element can be written as

$$\overline{|\mathcal{M}|^2}_{I\to N} = \underbrace{\overline{\sum_s}\sum_{s'} \mathcal{M}_0^\mu \mathcal{M}_0^{*\nu} D_{\mu\alpha} D^*_{\nu\beta}}_{=:\overline{|\mathcal{M}_{0,\alpha\beta}|^2}} \sum_{s_+,\, s_-} l^\alpha l^{*\beta}. \tag{B.11}$$

The Lorentz invariant phase space for a process with I and N particles in the initial and final state, respectively, reads

$$d\mathrm{Lips}_{I\to N} = \frac{1}{f(I)}\Pi_{i=1}^N \frac{d^3\vec{p_i}\,'}{(2\pi)^3 2p_i'^0}(2\pi)^4\delta^{(4)}\left(p - \sum_{i=1}^N p'_i\right),$$

where $f(I=1) = 2p^2$ and $f(I=2) = 4\sqrt{(p_1\cdot p_2)^2 - p_1^2 p_2^2}$. The phase space of the considered type of processes can always be factorized as

$$d\mathrm{Lips}_{I\to N} = \frac{1}{f(I)}\Pi_{i=1}^{N-2}\frac{d^3\vec{p_i}\,'}{(2\pi)^3 2p_i'^0}\frac{d^3\vec{l_+}}{(2\pi)^3 2E_+}\frac{d^3\vec{l_-}}{(2\pi)^3 2E_-}(2\pi)^4\delta^{(4)}\left(q' - l_+ - l_-\right),$$

where $q' = p - p'$ was used. Therefore, one finds

$$\begin{aligned}
d\sigma_{I\to N} &= d\mathrm{Lips}_{I\to N}\overline{|\mathcal{M}|^2}_{I\to N} \\
&= \frac{1}{f(I)}\Pi_{i=1}^{N-2}\frac{d^3\vec{p_i}\,'}{(2\pi)^3 2p_i'^0}\overline{|\mathcal{M}_{0,\alpha\beta}|^2} \\
&\quad\times \frac{d^3\vec{l_+}}{(2\pi)^3 2E_+}\frac{d^3\vec{l_-}}{(2\pi)^3 2E_-}(2\pi)^4\delta^{(4)}\left(q' - l_+ - l_-\right)\sum_{s_+,\, s_-} l^\alpha l^{*\beta} \\
&= \frac{1}{f(I)}\Pi_{i=1}^{N-2}\frac{d^3\vec{p_i}\,'}{(2\pi)^3 2p_i'^0}\overline{|\mathcal{M}_{0,\alpha\beta}|^2}\times\frac{1}{(2\pi)^2}\times\frac{d^3\vec{l_+}}{2E_+}\frac{d^3\vec{l_-}}{2E_-}\delta^{(4)}\left(q' - l_+ - l_-\right)\sum_{s_+,\, s_-} l^\alpha l^{*\beta}.
\end{aligned} \tag{B.12}$$

B.3.2 Analytical integration over the variables of the lepton pair

As the next step, the integration over the variables of the lepton pair particles will be performed analytically. One finds

$$
\begin{aligned}
L^{\alpha\beta} &= \int \frac{d^3\vec{l_+}}{2E_+}\frac{d^3\vec{l_-}}{2E_-}\delta^{(4)}\left(q' - l_+ - l_-\right) \sum_{s_+,\, s_-} l^{\alpha} l^{*\beta} \\
&= \int \frac{d^3\vec{l_+}}{2E_+}\frac{d^3\vec{l_-}}{2E_-}\delta^{(4)}\left(q' - l_+ - l_-\right) \mathrm{Tr}\left((\not{l}_- + m_l)\gamma^{\alpha}(\not{l}_+ - m_l)\gamma^{\beta}\right) \\
&= \int \frac{d^3\vec{l_+}}{2E_+}\frac{d^3\vec{l_-}}{2E_-}\delta^{(4)}\left(q' - l_+ - l_-\right) 4\left(l_+^{\alpha} l_-^{\beta} + l_-^{\alpha} l_+^{\beta} - g^{\alpha\beta}(l_- \cdot l_+ + m_l^2)\right),
\end{aligned}
$$

where $m_l^2 = l_+^2 = l_-^2$ is the mass of the lepton pair particles. Since $L^{\alpha\beta}$ may not depend on the four-momenta l_+ and l_- or any of their components after the integration and the Lorentz structure needs to be conserved, the result must be of the form

$$
L^{\alpha\beta} = a g^{\alpha\beta} + b\frac{q'^{\alpha} q'^{\beta}}{q'^2}.
$$

The evaluation of the integral is performed in the rest frame of the lepton pair, i.e.

$$
\vec{l_+} = -\vec{l_-} \Rightarrow E_+ = E_-.
$$

In this frame one has $\vec{q}' = \vec{0}$ and thus, $q'^2 = (q'^0)^2$, which leads to $E_+ = {q'^2}/2$ and $|\vec{l_+}| = \sqrt{q'^2 - 4m_l^2}/2$. For the four-vector scalar products one has $l_+ \cdot l_- = 1/2(q'^2 - 2m_l^2)$, and $q' \cdot l_- = q' \cdot l_+ = {q'^2}/2$. In the following the invariant mass of the lepton pair is denoted by $m_{ll} = \sqrt{q'^2}$. Contracting $L^{\alpha\beta} = a g^{\alpha\beta} + b(q'^{\alpha} q'^{\beta})/q'^2$ with the metric tensor $g_{\alpha\beta}$ leads to

$$
\begin{aligned}
4a + b &= \int \frac{d^3\vec{l_+}}{2E_+}\frac{d^3\vec{l_-}}{2E_-}\delta^{(4)}\left(q' - l_+ - l_-\right) 4\left(2\, l_+ \cdot l_- - 4\, l_+ \cdot l_- - 4m_l^2\right) \\
&= \int \frac{d^3\vec{l_+}}{2E_+}\frac{d^3\vec{l_-}}{2E_-}\delta^{(4)}\left(q' - l_+ - l_-\right)(-4)\left(m_{ll}^2 + 2m_l^2\right) \\
&= \int \frac{d^3\vec{l_+}}{4E_+E_-}\delta\left(q'^0 - E_+ - E_-\right)(-4)\left(m_{ll}^2 + 2m_l^2\right) \\
&= \int \frac{|\vec{l_+}|dE_+ d\Omega_+}{4E_-}\frac{1}{2}\delta\left(E_+ - \frac{q'^0}{2}\right)(-4)\left(m_{ll}^2 + 2m_l^2\right) \\
&= \int d\Omega_+\left(-\frac{|\vec{l_l}|}{2E_+}\right)\left(m_{ll}^2 + 2m_l^2\right) \\
&= -\frac{1}{2}\frac{\sqrt{m_{ll}^2 - 4m_l^2}}{m_{ll}}\left(m_{ll}^2 + 2m_l^2\right)\Omega_+.
\end{aligned}
$$

The contraction of $L^{\alpha\beta} = a g^{\alpha\beta} + b(q'^{\alpha} q'^{\beta})/q'^2$ with $(q_{\prime\alpha} q_{\prime\beta})$ yields

$$
(a + b)q'^2 = 0,
$$

since $L^{\alpha\beta}$ is gauge invariant. Hence, one has

$$a = -b,$$

and

$$a = -\frac{1}{6}\frac{\sqrt{m_{ll}^2 - 4m_l^2}}{m_{ll}}\left(m_{ll}^2 + 2m_l^2\right)\Omega_+ .$$

Thus, the integral over the variables of the lepton pair gives

$$L^{\alpha\beta} = \frac{\Omega_+^{\mathrm{cm}_{l^+l^-}}}{6}\frac{\sqrt{m_{ll}^2 - 4m_l^2}}{m_{ll}}\left(m_{ll}^2 + 2m_l^2\right)\left(-g^{\alpha\beta} + \frac{q'^{\alpha}q'^{\beta}}{m_{ll}^2}\right), \tag{B.13}$$

and for $\Omega_+^{\mathrm{cm}_{l^+l^-}} = 4\pi$

$$L^{\alpha\beta} = \frac{2\pi}{3}\frac{\sqrt{m_{ll}^2 - 4m_l^2}}{m_{ll}}\left(m_{ll}^2 + 2m_l^2\right)\left(-g^{\alpha\beta} + \frac{q'^{\alpha}q'^{\beta}}{m_{ll}^2}\right).$$

B.3.3 Relation between the cross sections of the processes $I \to (N-2) + (\gamma'^* \to l^+l^-)$ and $I \to (N-2) + \gamma'$

To obtain a relation between the cross sections for the processes of lepton pair production by the exchange of an intermediate hidden photon $I \to (N-2) + (\gamma'^* \to l^+l^-)$ and real hidden photon emission $I \to (N-2) + \gamma'$, it is helpful to insert a unity into the cross section for lepton pair production $d\sigma_{I\to N}^{\gamma'\to l^+l^-}$ written in Eq. (B.12) in terms of

$$1 = \int dq'^4 \delta^{(4)}(q' - (p - p')) = \int \frac{dq'^2}{2\pi}\frac{d^3\vec{q}'}{(2\pi)^3 2q'^0}(2\pi)^4\delta^{(4)}(p - p' - q'),$$

which allows one to rewrite Eq. (B.12) as

$$\begin{aligned} d\sigma_{I\to N}^{\gamma'\to l^+l^-} &= \frac{1}{f(I)}\Pi_{i=1}^{N-2}\left(\frac{d^3\vec{p}_i{}'}{(2\pi)^3 2p_i'^0}\right)\frac{d^3\vec{q}'}{(2\pi)^3 2q'^0}(2\pi)^4\delta^{(4)}(p - p' - q')\frac{dq'^2}{2\pi}\overline{|\mathcal{M}_{0,\alpha\beta}|^2} \\ &\times \frac{1}{(2\pi)^2} \times \frac{d^3\vec{l_+}}{2E_+}\frac{d^3\vec{l_-}}{2E_-}\delta^{(4)}\left(q' - l_+ - l_-\right)\sum_{s_+,\,s_-} l^{\alpha}l^{*\beta}. \end{aligned}$$

After applying the analytical integration over the lepton pair variables one finds

$$\begin{aligned} d\sigma_{I\to N}^{\gamma'\to l^+l^-} &= \frac{1}{f(I)}\Pi_{i=1}^{N-2}\left(\frac{d^3\vec{p}_i{}'}{(2\pi)^3 2p_i'^0}\right)\frac{d^3\vec{q}'}{(2\pi)^3 2q'^0}(2\pi)^4\delta^{(4)}(p - p' - q')\frac{dq'^2}{2\pi}\overline{|\mathcal{M}_{0,\alpha\beta}|^2} \\ &\times \frac{1}{6\pi}\frac{\sqrt{m_{ll}^2 - 4m_l^2}}{m_{ll}}\left(m_{ll}^2 + 2m_l^2\right)\left(-g^{\alpha\beta} + \frac{q'^{\alpha}q'^{\beta}}{m_{ll}^2}\right). \end{aligned} \tag{B.14}$$

Because in the hidden photon model gauge invariance needs to be fulfilled, the terms $\propto q'^{\alpha}q'^{\beta}$ vanish after contracting with $\overline{|\mathcal{M}_{0,\alpha\beta}|^2}$. Rewriting the propagators in the squared amplitude of Eq. (B.11) as

$$
\begin{aligned}
g^{\alpha\beta} D_{\mu\alpha} D^*_{\nu\beta} &= (\varepsilon e)^2 g_{\mu\alpha} g^{\alpha}_{\nu} \frac{1}{q'^2 - m_{\gamma'} + i m_{\gamma'}\Gamma_{\gamma'}} \frac{1}{q'^2 - m_{\gamma'} - i m_{\gamma'}\Gamma_{\gamma'}} \\
&= (\varepsilon e)^2 g_{\mu\nu} \frac{1}{\left(q'^2 - m^2_{\gamma'}\right)^2 - m^2_{\gamma'}\Gamma^2_{\gamma'}},
\end{aligned}
$$

allows one to use Eq. (B.1) to perform the q'^2-integration easily by approximating this structure by a Dirac δ-distribution. Within this work it was proven numerically that this approximation is valid to high accuracy for the allowed parameter space. Therefore, one finds from Eq. (B.14)

$$
\begin{aligned}
d\sigma^{\gamma'\to l^+l^-}_{I\to N} &= \frac{1}{f(I)} \Pi_{i=1}^{N-2} \left(\frac{d^3\vec{p}_i{}'}{(2\pi)^3 2p'^0_i} \right) \frac{d^3\vec{q}'}{(2\pi)^3 2q'^0} (2\pi)^4 \delta^{(4)}(p - p' - q') \frac{\varepsilon^2 e^2}{2m_{\gamma'}\Gamma_{\gamma'}} \\
&\times \frac{1}{6\pi} \frac{\sqrt{m^2_{\gamma'} - 4m_l^2}}{m_{\gamma'}} \left(m^2_{\gamma'} + 2m_l^2\right) \overline{\sum_s} \sum_{s'} \mathcal{M}_0^{\mu} \mathcal{M}_0^{*\nu} (-g_{\mu\nu}),
\end{aligned}
\tag{B.15}
$$

where Eq. (B.4) was used and after performing the integration over the invariant mass of the lepton pair one has $q'^2 = m^2_{\gamma'}$. Identifying terms in Eq. (B.15) with the decay width of a hidden photon into a lepton antilepton pair given in Eq. (1.31) leads to

$$
d\sigma^{\gamma'\to l^+l^-}_{I\to N} = \frac{1}{f(I)} \Pi_{i=1}^{N-2} \left(\frac{d^3\vec{p}_i{}'}{(2\pi)^3 2p'^0_i} \right) \frac{d^3\vec{q}'}{(2\pi)^3 2q'^0} (2\pi)^4 \delta^{(4)}(p - p' - q') \frac{\Gamma_{\gamma'\to l^+l^-}}{\Gamma_{\gamma'}} \overline{|\mathcal{M}_0^{\mu\nu}|^2} (-g_{\mu\nu}).
\tag{B.16}
$$

The cross section for the process of hidden photon emission can be obtained analogously to the derivation for the lepton pair production process. One finds

$$
\begin{aligned}
d\sigma^{\gamma'}_{I\to N-1} &= \frac{1}{f(I)} \Pi_{i=1}^{N-2} \left(\frac{d^3\vec{p}_i{}'}{(2\pi)^3 2p'^0_i} \right) \frac{d^3\vec{q}'}{(2\pi)^3 2q'^0} (2\pi)^4 \delta^{(4)}(p - p' - q') \\
&\times \overline{\sum_s} \sum_{s'} \sum_{\lambda,\lambda'} \mathcal{M}_0^{\mu} \varepsilon^*_{\mu}(\vec{q}', \lambda) \mathcal{M}_0^{*\nu} \varepsilon_{\nu}(\vec{q}', \lambda'),
\end{aligned}
$$

where $\varepsilon_\mu(\vec{q}', \lambda)$ denotes the polarization vector of a hidden photon with momentum q' and polarization λ. The sum over polarization states can be replaced using

$$
\sum_{\lambda,\lambda'} \varepsilon^*_{\mu}(\vec{q}', \lambda) \varepsilon_{\nu}(\vec{q}', \lambda') = -g_{\mu\nu} + \frac{q'_\mu q'_\nu}{m^2_{\gamma'}}.
$$

Due to gauge invariance only the term proportional to the metric tensor contributes and the cross section can be rewritten as

$$
d\sigma^{\gamma'}_{I\to N-1} = \frac{1}{f(I)} \Pi_{i=1}^{N-2} \left(\frac{d^3\vec{p}_i{}'}{(2\pi)^3 2p'^0_i} \right) \frac{d^3\vec{q}'}{(2\pi)^3 2q'^0} (2\pi)^4 \delta^{(4)}(p - p' - q') \overline{|\mathcal{M}_0^{\mu\nu}|^2} (-g_{\mu\nu}).
\tag{B.17}
$$

By comparison of Eqs. (B.16) and (B.17) one easily sees

$$
d\sigma^{\gamma'\to l^+l^-}_{I\to N} = d\sigma^{\gamma'}_{I\to N-1} \times \frac{\Gamma_{\gamma'\to l^+l^-}}{\Gamma_{\gamma'}},
\tag{B.18}
$$

after the integration over the variables of the lepton pair has been performed.

Appendix C

Calculations on the GPU

In this Section a description is given, how programming code which is written to be operated on the ordinary CPU can be ported to the execution on graphics processing units. For this purpose, a short introduction to the NVIDIA CUDA programming framework is given. Furthermore, the most relevant steps are outlined, which were necessary for the porting to graphics processing units.

C.1 The CUDA programming model

Graphics processing units (GPUs) were developed for the fast creation of output for computer displays. While in the 1980s, when the use of personal computers started, GPUs were only utilized to link the text based graphical output of operating systems to the display, nowadays the demand on GPUs is much larger. Due to the high demand placed on the appearance of computer graphics, the rendering of three dimensional moving images is every day work of GPUs. The calculations necessary for that require a high level of parallelization and GPUs fulfill much more tasks than only linking to the display. Therefore, one nowadays also speaks of “General Purpose Graphics Processing Units (GPGPU).”[1] This fact can be used for calculations of elementary particle physics.

It was shown in Ref. [187] that GPUs are ideally suited for the calculation of Monte Carlo integrals. It is discussed that for the calculation of integrated cross sections or samples of events, the most time consuming step is the calculation of the spin-summed amplitude $\overline{|\mathcal{M}|^2}$. Therefore, the calculation of $\overline{|\mathcal{M}|^2}$ was performed in parallel in Ref. [187], which is exactly the need of parallelization for this work. It is further pointed out that the performance on the GPU is getting worse, the more diagrams are contained in the amplitude and the more complicated the amplitude is.

In order to perform these calculations on the GPU, one has to understand the differences between GPUs and the well-known central processing units (CPUs). Since CPUs are designed to perform any kind of operation, programming on them is straightforward. For GPUs the situation is different: One has to understand that these devices are developed for the execution of particular operations as fast as possible. This is achieved by the aforementioned large number of parallel computing units, which in contrast to CPUs are specialized for these operations. Therefore, code for GPUs must be optimized to account for this structure. In Table C.1 selected properties of the NVIDIA “Tesla M 2070” GPU are shown, which was employed for the calculations of this work. These properties are utilized to point out the differences between CPUs and GPUs, which in the following are referred to as host and device, respectively.

[1] In the following the terms GPGPU and GPU are used equivalently.

Property	Number
Number of streaming multiprocessors	14
Number of cores per multiprocessors	32
Number of cores	448
GPU Clock Speed	1.15 GHz
Memory Clock rate	1.57 GHz
Total amount of global memory	6 GB
Total amount of constant memory	64 kB
Total amount of shared memory per thread block	48 kB
Total amount of registers per thread block	32768
Maximum number of threads per block	1024

Table C.1: Parameters of the "Tesla M 2070."

A program on the CPU is run within one threads or several threads, if the code is suited for parallel execution. Each of the threads is executed on a single CPU core independently. The memory is assigned automatically, whereas one has to take care that the program is thread safe. Thread safe means that variables are only modified by the thread they belong to.

A CUDA program in general is executed in "blocks" of threads, which are independently run on the multiprocessors. The number of blocks is shared between the multiprocessors. Table C.1 reveals that the used device offers 14 of the multiprocessors, where each of them consists of 32 cores. The threads contained in the block are grouped by the multiprocessors into so-called "warps," where 32 threads are contained in a warp. The execution of each warp is scheduled independently of the other warps. However, maybe the most important feature one has to take care of, is that each warp executes one common operation at the same time. This means that the best performance can only be reached, if all 32 threads perform the same operations. If the execution diverges, e.g. due to a particular condition the execution of some threads differ, the distinct paths are executed one after the other.

From Table C.1 one can see that different kinds of memory are existing on GPUs. Of course, also on CPUs different kinds of memory are available, which will not be discussed here in detail. In general, a variable is stored within a register. If the number of registers is not sufficient to store all variables, which is usually the case for the calculation of $\overline{|\mathcal{M}|^2}$, the so-called local memory is used to store variables, which is much slower.

Furthermore, the device cannot access the host memory directly and vice versa. Hence, the data necessary for the operations on the device have to be copied from the host too the device and back. While for rendering movies or textures the process of copying is a bottleneck, in this work, where only a small amount of data needs to be copied, one does not have to take it into account. However, one needs to understand the usage of the different kinds of memory to obtain the best performance.

For the numerical calculations in this work, libraries and parts of the code developed by the authors of Refs. [175, 217] were used. Based on this code, which was also applied to check the results for consistency, the programs for the calculations were written. Since the original code was developed for the usage on CPUs, large parts of it had to be rewritten for

Memory	Speed	Lifetime	Writing	Reading
register	fastest	Thread	D	D
local	slow	Thread	D	D
shared	fast	Block	D	D
constant	fast	Program	H	D

Table C.2: Different kinds of memory on CUDA enabled GPUs: Access from the host (GPU device) is denoted by H (D).

the execution on GPUs.

In Appendix C.2 it is described, in which way the employed code had to be modified to be executed on GPUs. Selected optimizations, in which properties of physics are applied in order to obtain a more efficient code for the program, are discussed in Appendix C.3

C.2 Porting from CPU to GPU

Although it is possible to port a code written for the execution on CPUs to GPUs, it is worthwhile spending some time to understand the different types of memories on GPUs and their properties. Therefore, a short introduction on this topic is given.

In Table C.2 the most important properties of the different types of memory on GPUs are summarized. Registers are the fastest type of memory. They can be accessed by the thread on the device, by which they were created. Unfortunately, for the Tesla M 2070 GPU, with properties shown in Table C.1, only 63 registers per thread are available, consequently for the calculation of cross sections one must make use of the slower memory in any way.

Since the shared memory resides on the chip itself as well as the Registers, this type of memory should be preferred as next choice. The shared memory can be accessed by all threads in a block. As a consequence, variables stored in it will be modified, as long as they are not defined in a thread safe way. In this work, the shared memory was used to store variables, which are not modified during the program execution, such as initial state quantities. Hence, it does not require that the definition of variables in the code developed for the CPU needs to be changed. As a consequence this means that all other variables defined on the device must be stored in the slower local memory, since the device cannot write data into the fast constant memory.

To enhance the speed of the Local memory access, it is employed that on GPUs as the one applied in this work the shared memory can be reduced to allow for improved caching of the local memory. The constant memory is used to store initial values as physical constants or input variables which are not changed as the hidden photon mass.

The only way to reduce the amount of local memory needed is reducing the number of necessary operations for calculating the cross section. Selected optimizations are presented in Appendix C.3.

Another complication entering is the fact that with the GPU devices available for this work, not more than around 32 000 registers may be used in total (see Table C.1). This limits the length of a program strictly, which makes it crucial to perform as few operations as possible. While on CPUs programs can be easily written to choose from different ways of operation, e.g. the choice of different contributions to the amplitude, this is not preferable for GPUs. Therefore, only the necessary parts of the original code have been calculated on the GPU. As a consequence, instead of obtaining one program in which the path of execution is chosen during the execution, several, highly specialized programs were created. The time required to build these executables is vanishingly small compared to the time which can be saved by performing the numerical integration.

To account for the fact that only one common operation is performed by a warp at the same time, one has to calculate the cross section which offers the best coverage of the integration volume. One needs to find the cross section parametrization, in which only small regions of the phase space have to be excluded due to unphysical solutions or experimental cuts. The cross section was calculated in terms of the recursive variables as in Sec. 3.3.1 or in terms of detector coordinates which is presented in Sec. 3.3.2. The first method is well suited for the calculation of total cross sections, where the integration is performed over the full phase space. The latter one is necessary to obtain a high performance for the case that the acceptance integrated cross section is calculated within the particular kinematical limits of experiments as done in Secs. 3.4 and 3.5.

In this study, the efficiency of the calculation of the acceptance integrated cross section was compared for these two methods. It was found that the calculation of the cross section in detector coordinates leads to a much larger performance on the GPU. Since the parametrization in terms of the coordinates is directly related to the detector geometry only those regions of the phase space are taken into account for the numerical integration, which are within the acceptance of the experiment. On the contrary, for the other method the integration regime needs to be restricted manually to the experimentally allowed region, which is much less accurate. Therefore, although only physically allowed events are generated, most of these have to be rejected, since they are not allowed by the experiment. Thus, in most cases different execution paths have to be followed and the efficiency on the GPU drops. Of course, a fraction of the generated events which is allowed by the detector geometry corresponds to unphysical configurations, but these are much less than the rejected events which are not allowed by the geometry. It turned out that for the experiments at MAMI, around 90 % of the events generated by the second method are within the regions allowed by the physical as well as the geometry constraints and only around 25 % for the first one.

C.3 Optimizations by physical relations

In this Section selected examples of optimization steps resulting from rewriting the expressions into a more appropriate form for the fast numerical evaluation are introduced. Moreover, optimizations are presented, which make use of physical relations to simplify the expressions, such as the Dirac equation. To make sure that no mistakes enter during the optimization process, the results of the improved code and of the primary version were compared after each step.

In the original libraries, the Feynman slash operator

$$\not{p} = \sum_{\mu=0}^{3} \gamma^{\mu} p_{\mu} \tag{C.1}$$

is calculated by performing the multiplications and summation in Eq. (C.1) with every call of the function $\not{p}$. By this method the definition of $\not{p}$ does not depend on the actual choice of the representation of the Dirac matrices. As a consequence, this operator does not need to be modified, if the Dirac matrix representation is changed. This generality comes together with the cost of more than 60 necessary operations each time $\not{p}$ is called. The only representation of Dirac matrices used is the one as defined in Ref. [198]. The result of Eq. (C.1) can be obtained analytically. One finds

$$\not{p} = \begin{pmatrix} p^0 & 0 & -p^3 & -p^1 + ip^2 \\ 0 & p^0 & -p^1 - ip^2 & p^3 \\ p^3 & p^1 - ip^2 & -p^0 & 0 \\ p^1 + ip^2 & -p^3 & 0 & -p^0 \end{pmatrix}. \tag{C.2}$$

Obviously, significantly less operations are needed. In particular the number of multiplications of complex numbers is strongly reduced. Furthermore, the operator $(\not{p}\,\not{q})$ was defined in an analogous way, which allows one to slightly reduce the number of performed operations.

Another reduction of operations is illustrated by use of the following example. The straightforward calculation of an amplitude as in Eq. (3.5) is to compute

$$\mathcal{M}^{\mathrm{TL}}_{\gamma^*} \propto \sum_{\mu=0}^{3} \left(\sum_{\alpha=0}^{3} \left[J^{\mu}_N \, \mathcal{I}_{\mu\alpha} \, j^{\alpha\mathrm{pair}} \right] \right) \tag{C.3}$$

in the order as emphasized by the parentheses. In the original version of the code this was done by evaluating the quantity in the squared brackets within two nested `for` loops for the summations over μ and α. Since in general the tensor $\mathcal{I}_{\mu\alpha}$ is a product of Dirac matrices the effort for this calculation is large, for example in case of Eq. (3.5) it is a structure containing products of 3 of them. Therefore, in this work the currents J^{μ}_N and $j^{\alpha\mathrm{pair}}$ are treated as four-vectors, which can be contracted with the γ-matrices contained in $\mathcal{I}_{\mu\alpha}$. For this example one finds

$$\begin{aligned} \mathcal{M}^{\mathrm{TL}}_{\gamma^*} \propto \overline{u}_e(k', s'_k) \Bigg(& (\gamma \cdot J_N) \frac{\not{k} - \not{q}' + m}{(k - q')^2 - m^2} (\gamma \cdot j^{\mathrm{pair}}) \\ & + (\gamma \cdot j^{\mathrm{pair}}) \frac{\not{k}' + \not{q}' + m}{(k' + q')^2 - m^2} (\gamma \cdot J_N) \Bigg) u_e(k, s_k). \end{aligned} \tag{C.4}$$

The great simplification that the most complicated structure $\mathcal{I}_{\mu\alpha}$ has to be calculated only once because the sums over μ and α can be dropped, comes at the expense of a worse readability of the code.

By means of the anti-commutation relations for Dirac matrices [183] and the Dirac equation, one can rewrite Eq. (C.4):

$$\begin{aligned} & \overline{u}_e(k', s'_k) \Bigg((\gamma \cdot J_N) \frac{2k \cdot j^{\mathrm{pair}} - (\gamma \cdot j^{\mathrm{pair}})\not{k} - \not{q}'(\gamma \cdot j^{\mathrm{pair}}) + m(\gamma \cdot j^{\mathrm{pair}})}{(k - q')^2 - m^2} \\ & \qquad + \frac{2k' \cdot j^{\mathrm{pair}} - \not{k}'(\gamma \cdot j^{\mathrm{pair}}) + (\gamma \cdot j^{\mathrm{pair}})\not{q}' + (\gamma \cdot j^{\mathrm{pair}})m}{(k' + q')^2 - m^2} (\gamma \cdot J_N) \Bigg) u_e(k, s_k) \\ & = \overline{u}_e(k', s'_k) \Bigg((\gamma \cdot J_N) \left(\frac{2k \cdot j^{\mathrm{pair}}}{(k - q')^2 - m^2} + \frac{2k' \cdot j^{\mathrm{pair}}}{(k' + q')^2 - m^2} \right) \\ & \qquad - \frac{(\gamma \cdot J_N)\not{q}'(\gamma \cdot j^{\mathrm{pair}})}{(k - q')^2 - m^2} + \frac{(\gamma \cdot j^{\mathrm{pair}})\not{q}'(\gamma \cdot J_N)}{(k' + q')^2 - m^2} \Bigg) u_e(k, s_k). \end{aligned} \tag{C.5}$$

Although at first glance this expression looks more complicated, in fact it is easier to compute numerically than Eq. (C.4) and less registers are needed.

For protons one has to take their electromagnetic structure parametrized by the two form factors F_1 and F_2 into account, which means that for the electromagnetic proton current one has

$$\overline{u}_N(p', s_p')\Gamma_\mu u_N(p, s_p) = \overline{u}_N(p', s_p')\left(F_1(Q^2)\,\gamma_\mu + F_2(Q^2)\,i\,\sigma_{\mu\nu}\frac{q^\nu}{2M}\right)u_N(p, s_p),$$

where $q = (p' - p)$, $Q^2 = -q^2 > 0$, and $\sigma_{\mu\nu} = {}^{i}\!/\!{}_{2}\,(\gamma^\mu\gamma^\nu - \gamma^\nu\gamma^\mu)$. In this representation, each call of the proton vertex requires the evaluation of a product of Dirac matrices. One can get rid of the tensor $\sigma_{\mu\nu}$ by using the Gordon identity

$$\overline{u}_N(p', s_p')\gamma^\mu u_N(p, s_p) = \overline{u}_N(p', s_p')\left(\frac{(p+p')^\mu}{2M} + \frac{i\sigma^{\mu\nu}q_\nu}{2M}\right)u_N(p, s_p).$$

Hence, one finds

$$\Gamma_\mu(Q^2) = G_M(Q^2)\gamma_\mu - \frac{(p+p')^\mu}{2M}F_2(Q^2),$$

where $G_M = F_1 + F_2$ is the magnetic Sachs form factor defined in Eq. (1.19). Note that this transformation is only possible, if both fermion lines of the vertex correspond to particles on the mass shell. On this account, one cannot simplify the Compton tensor $\mathcal{H}_{\mu\alpha}$ appearing e.g. in Eqs. (3.2) and (3.7) in this way.

In addition, since the electromagnetic interaction is parity conserving, one of the spin-summations needed to calculate $\overline{|\mathcal{M}|^2}$ can be omitted. This was used, as far as no polarization observables are taken into account.

Bibliography

[1] T. Beranek and M. Vanderhaeghen, "Study of the discovery potential for hidden photon emission at future electron scattering fixed target experiments," (2013), arXiv:1311.5104 [hep-ph].

[2] T. Beranek, H. Merkel, and M. Vanderhaeghen, Phys.Rev. **D88**, 015032 (2013).

[3] T. Beranek and M. Vanderhaeghen, Phys.Rev. **D87**, 015024 (2013).

[4] J. Beringer *et al.* (Particle Data Group), Phys.Rev. **D86**, 010001 (2012).

[5] S. M. Carroll, *Spacetime and geometry: An introduction to general relativity* (Addison-Wesley, San Francisco, 2004).

[6] G. F. Smoot, C. Bennett, A. Kogut, E. Wright, J. Aymon, *et al.*, Astrophys.J. **396**, L1 (1992).

[7] N. Jarosik, C. Bennett, J. Dunkley, B. Gold, M. Greason, *et al.*, Astrophys.J.Suppl. **192**, 14 (2011).

[8] D. Larson, J. Dunkley, G. Hinshaw, E. Komatsu, M. Nolta, *et al.*, Astrophys.J.Suppl. **192**, 16 (2011).

[9] E. Komatsu *et al.* (WMAP Collaboration), Astrophys.J.Suppl. **192**, 18 (2011).

[10] C. Bennett *et al.* (WMAP), Astrophys.J.Suppl. **208**, 20 (2013).

[11] G. Hinshaw *et al.* (WMAP), Astrophys.J.Suppl. **208**, 19 (2013).

[12] P. Ade *et al.* (Planck Collaboration), "Planck 2013 results. I. Overview of products and scientific results," (2013), arXiv:1303.5062 [astro-ph.CO].

[13] P. Ade *et al.* (Planck Collaboration), "Planck 2013 results. XVI. Cosmological parameters," (2013), arXiv:1303.5076 [astro-ph.CO].

[14] F. Zwicky, Helv.Phys.Acta **6**, 110 (1933).

[15] F. Zwicky, Astrophys.J. **86**, 217 (1937).

[16] G. Bertone, D. Hooper, and J. Silk, Phys.Rept. **405**, 279 (2005).

[17] V. C. Rubin and J. Ford, W. Kent, Astrophys.J. **159**, 379 (1970).

[18] V. Rubin, N. Thonnard, and J. Ford, W.K., Astrophys.J. **238**, 471 (1980).

[19] K. Begeman, A. Broeils, and R. Sanders, Mon.Not.Roy.Astron.Soc. **249**, 523 (1991).

[20] Y. Sofue, Y. Tutui, M. Honma, A. Tomita, T. Takamiya, *et al.*, "Central rotation curves of spiral galaxies," (1999), arXiv:astro-ph/9905056 [astro-ph].

[21] Y. Sofue and V. Rubin, Ann.Rev.Astron.Astrophys. **39**, 137 (2001).

[22] H. Leutwyler, "On the history of the strong interaction," (2012), arXiv:1211.6777 [physics.hist-ph].

[23] H. Yukawa, Proc.Phys.Math.Soc.Jap. **17**, 48 (1935).

[24] J. J. O'Connor and E. F. Robertson(2008), `http://www-history.mcs.st-andrews.ac.uk/Biographies/Stueckelberg.html`.

[25] L. M. Brown, Phys.Today **31N9**, 23 (1978).

[26] E. Fermi, Z.Phys. **88**, 161 (1934).

[27] M. Gell-Mann, "The Eightfold Way: A Theory of Strong Interaction Symmetry," (1961).

[28] Y. Ne'eman, Nucl.Phys. **26**, 222 (1961).

[29] M. Gell-Mann, Phys.Lett. **8**, 214 (1964).

[30] G. Zweig, "An SU(3) Model for Strong Interaction Symmetry and its Breaking. Pt. 2," (1964).

[31] M. Han and Y. Nambu, Phys.Rev. **139**, B1006 (1965).

[32] D. Gross and F. Wilczek, Phys.Rev.Lett. **30**, 1343 (1973).

[33] H. D. Politzer, Phys.Rev.Lett. **30**, 1346 (1973).

[34] H. Weyl, Z.Phys. **56**, 330 (1929).

[35] J. Guttmann, *Nucleon electromagnetic structure studies in the spacelike and timelike regions*, Ph.D. thesis, Johannes Gutenberg-Universität (2013).

[36] H. Spiesberger, M. Spira, and P. Zerwas, "The Standard model: Physical basis and scattering experiments," (2000), arXiv:hep-ph/0011255 [hep-ph].

[37] A. Metz, "Lecture on: Introduction to electroweak theory," (2008).

[38] M. Kobayashi and T. Maskawa, Prog.Theor.Phys. **49**, 652 (1973).

[39] F. Hasert *et al.* (Gargamelle Neutrino Collaboration), Phys.Lett. **B46**, 138 (1973).

[40] S. Glashow, J. Iliopoulos, and L. Maiani, Phys.Rev. **D2**, 1285 (1970).

[41] J. Augustin *et al.* (SLAC-SP-017 Collaboration), Phys.Rev.Lett. **33**, 1406 (1974).

[42] J. Aubert *et al.* (E598 Collaboration), Phys.Rev.Lett. **33**, 1404 (1974).

[43] F. Abe *et al.* (CDF Collaboration), Phys.Rev.Lett. **74**, 2626 (1995).

[44] M. L. Perl, G. Abrams, A. Boyarski, M. Breidenbach, D. Briggs, *et al.*, Phys.Rev.Lett. **35**, 1489 (1975).

[45] K. Kodama *et al.* (DONUT Collaboration), Phys.Lett. **B504**, 218 (2001).

[46] G. Aad *et al.* (ATLAS Collaboration), Phys.Lett. **B716**, 1 (2012).

[47] S. Chatrchyan *et al.* (CMS Collaboration), Phys.Lett. **B716**, 30 (2012).

[48] D. Kazakov, "Beyond the standard model: In search of supersymmetry," (2000), arXiv:hep-ph/0012288 [hep-ph].

[49] A. Arbey, M. Battaglia, A. Djouadi, F. Mahmoudi, and J. Quevillon, Phys.Lett. **B708**, 162 (2012).

[50] "Summary plots from the ATLAS Supersymmetry physics group," `https://atlas.web.cern.ch/Atlas/GROUPS/PHYSICS/CombinedSummaryPlots/`.

[51] G. Charpak, F. Farley, R. Garwin, T. Muller, J. Sens, *et al.*, Phys.Rev.Lett. **6**, 128 (1961).

[52] G. Bennett *et al.* (Muon g-2 Collaboration), Phys.Rev.Lett. **92**, 161802 (2004).

[53] G. Bennett *et al.* (Muon G-2 Collaboration), Phys.Rev. **D73**, 072003 (2006).

[54] M. Davier, A. Hoecker, B. Malaescu, and Z. Zhang, Eur.Phys.J. **C71**, 1515 (2011).

[55] T. Aoyama, M. Hayakawa, T. Kinoshita, and M. Nio, Phys.Rev.Lett. **109**, 111807 (2012).

[56] T. Aoyama, M. Hayakawa, T. Kinoshita, and M. Nio, Phys.Rev.Lett. **109**, 111808 (2012).

[57] K. Fujikawa, B. Lee, and A. Sanda, Phys.Rev. **D6**, 2923 (1972).

[58] A. Czarnecki, B. Krause, and W. J. Marciano, Phys.Rev.Lett. **76**, 3267 (1996).

[59] M. Knecht, S. Peris, M. Perrottet, and E. De Rafael, JHEP **0211**, 003 (2002).

[60] A. Czarnecki, W. J. Marciano, and A. Vainshtein, Phys.Rev. **D67**, 073006 (2003).

[61] F. Jegerlehner, Acta Phys.Polon. **B44**, 2257 (2013).

[62] J. Jaeckel and A. Ringwald, Ann.Rev.Nucl.Part.Sci. **60**, 405 (2010).

[63] M. Kawasaki and K. Nakayama, Ann.Rev.Nucl.Part.Sci. **63**, 69 (2013).

[64] C. Baker, D. Doyle, P. Geltenbort, K. Green, M. van der Grinten, *et al.*, Phys.Rev.Lett. **97**, 131801 (2006).

[65] R. Peccei and H. R. Quinn, Phys.Rev.Lett. **38**, 1440 (1977).

[66] S. Weinberg, Phys.Rev.Lett. **40**, 223 (1978).

[67] F. Wilczek, Phys.Rev.Lett. **40**, 279 (1978).

[68] J. E. Kim, Phys.Rev.Lett. **43**, 103 (1979).

[69] M. A. Shifman, A. Vainshtein, and V. I. Zakharov, Nucl.Phys. **B166**, 493 (1980).

[70] K. Baker, G. Cantatore, S. Cetin, M. Davenport, K. Desch, *et al.*, Ann. Phys. **525**, A93 (2013).

[71] E. Riordan, M. Krasny, K. Lang, P. De Barbaro, A. Bodek, *et al.*, Phys.Rev.Lett. **59**, 755 (1987).

[72] J. Bjorken, S. Ecklund, W. Nelson, A. Abashian, C. Church, *et al.*, Phys.Rev. **D38**, 3375 (1988).

[73] A. Bross, M. Crisler, S. H. Pordes, J. Volk, S. Errede, *et al.*, Phys.Rev.Lett. **67**, 2942 (1991).

[74] J. Hewett, H. Weerts, *et al.*, "Fundamental Physics at the Intensity Frontier," (2012), arXiv:1205.2671 [hep-ex].

[75] R. Pohl, R. Gilman, G. A. Miller, and K. Pachucki, Ann.Rev.Nucl.Part.Sci. **63**, 175 (2013).

[76] J. Bernauer *et al.* (A1 Collaboration), Phys.Rev.Lett. **105**, 242001 (2010).

[77] M. O. Distler, J. C. Bernauer, and T. Walcher, Phys.Lett. **B696**, 343 (2011).

[78] P. J. Mohr, B. N. Taylor, and D. B. Newell, Rev.Mod.Phys. **84**, 1527 (2012).

[79] R. Pohl, A. Antognini, F. Nez, F. D. Amaro, F. Biraben, *et al.*, Nature **466**, 213 (2010).

[80] A. Antognini, F. Nez, K. Schuhmann, F. D. Amaro, FrancoisBiraben, *et al.*, Science **339**, 417 (2013).

[81] A. De Rujula, Phys.Lett. **B697**, 26 (2011).

[82] C. E. Carlson and M. Vanderhaeghen, Phys.Rev. **A84**, 020102 (2011).

[83] C. E. Carlson, V. Nazaryan, and K. Griffioen, Phys.Rev. **A83**, 042509 (2011).

[84] G. Miller, A. Thomas, J. Carroll, and J. Rafelski, Phys.Rev. **A84**, 020101 (2011).

[85] J. Jaeckel and S. Roy, Phys.Rev. **D82**, 125020 (2010).

[86] V. Barger, C.-W. Chiang, W.-Y. Keung, and D. Marfatia, Phys.Rev.Lett. **106**, 153001 (2011).

[87] D. Tucker-Smith and I. Yavin, Phys.Rev. **D83**, 101702 (2011).

[88] B. Batell, D. McKeen, and M. Pospelov, Phys.Rev.Lett. **107**, 011803 (2011).

[89] V. Barger, C.-W. Chiang, W.-Y. Keung, and D. Marfatia, Phys.Rev.Lett. **108**, 081802 (2012).

[90] C. E. Carlson and B. C. Rislow, Phys.Rev. **D86**, 035013 (2012).

[91] J. Chang, J. Adams, H. Ahn, G. Bashindzhagyan, M. Christl, *et al.*, Nature **456**, 362 (2008).

[92] O. Adriani *et al.* (PAMELA Collaboration), Nature **458**, 607 (2009).

[93] M. Ackermann *et al.* (Fermi LAT Collaboration), Phys.Rev.Lett. **108**, 011103 (2012).

[94] G. L. Kane, L.-T. Wang, and T. T. Wang, Phys.Lett. **B536**, 263 (2002).

[95] D. Hooper, J. E. Taylor, and J. Silk, Phys.Rev. **D69**, 103509 (2004).

[96] I. Cholis, D. P. Finkbeiner, L. Goodenough, and N. Weiner, JCAP **0912**, 007 (2009).

[97] I. Cholis, L. Goodenough, D. Hooper, M. Simet, and N. Weiner, Phys.Rev. **D80**, 123511 (2009).

[98] M. Cirelli, M. Kadastik, M. Raidal, and A. Strumia, Nucl.Phys. **B813**, 1 (2009).

[99] N. Arkani-Hamed, D. P. Finkbeiner, T. R. Slatyer, and N. Weiner, Phys.Rev. **D79**, 015014 (2009).

[100] E. A. Baltz, J. Edsjo, K. Freese, and P. Gondolo, Phys.Rev. **D65**, 063511 (2002).

[101] P. Jean, J. Knoedlseder, V. Lonjou, M. Allain, J.-P. Roques, *et al.*, Astron.Astrophys. **407**, L55 (2003).

[102] J. Knodlseder, V. Lonjou, P. Jean, M. Allain, P. Mandrou, *et al.*, Astron.Astrophys. **411**, L457 (2003).

[103] G. Weidenspointner, C. Shrader, J. Knoedlseder, P. Jean, V. Lonjou, *et al.*, Astron.Astrophys. **450**, 1012 (2006).

[104] C. Boehm, P. Fayet, and J. Silk, Phys.Rev. **D69**, 101302 (2004).

[105] P. Fayet, Phys.Rev. **D70**, 023514 (2004).

[106] D. P. Finkbeiner and N. Weiner, Phys.Rev. **D76**, 083519 (2007).

[107] D. J. Thompson, D. L. Bertsch, and J. R. H. O'Neal, Astrophys.J.Suppl. **157**, 324 (2005).

[108] R. Bernabei *et al.* (DAMA Collaboration), Eur.Phys.J. **C56**, 333 (2008).

[109] A. Sommerfeld, Ann. Phys. **403**, 257–330 (1931).

[110] P. Meade, M. Papucci, A. Strumia, and T. Volansky, Nucl.Phys. **B831**, 178 (2010).

[111] D. Hooper, N. Weiner, and W. Xue, Phys.Rev. **D86**, 056009 (2012).

[112] M. Aguilar *et al.* (AMS Collaboration), Phys.Rev.Lett. **110**, 141102 (2013).

[113] S. Coutu, Physics **6**, 40 (Apr 2013).

[114] D. P. Finkbeiner, L. Goodenough, T. R. Slatyer, M. Vogelsberger, and N. Weiner, JCAP **1105**, 002 (2011).

[115] C.-R. Chen, M. M. Nojiri, F. Takahashi, and T. Yanagida, Prog.Theor.Phys. **122**, 553 (2009).

[116] Q. Yuan, X.-J. Bi, G.-M. Chen, Y.-Q. Guo, S.-J. Lin, *et al.*, "Implications of the AMS-02 positron fraction in cosmic rays," (2013), arXiv:1304.1482 [astro-ph.HE].

[117] I. Cholis and D. Hooper, Phys.Rev. **D88**, 023013 (2013).

[118] P.-F. Yin, Z.-H. Yu, Q. Yuan, and X.-J. Bi, Phys.Rev. **D88**, 023001 (2013).

[119] P. Langacker, Rev.Mod.Phys. **81**, 1199 (2009).

[120] P. Langacker, Phys.Rept. **72**, 185 (1981).

[121] P. Fayet, Phys.Lett. **B69**, 489 (1977).

[122] P. Fayet, Phys.Lett. **B84**, 416 (1979).

[123] P. Fayet, Nucl.Phys. **B347**, 743 (1990).

[124] M. Pospelov, A. Ritz, and M. B. Voloshin, Phys.Lett. **B662**, 53 (2008).

[125] M. Pospelov and A. Ritz, Phys.Lett. **B671**, 391 (2009).

[126] M. Pospelov, Phys.Rev. **D80**, 095002 (2009).

[127] L. Okun, Sov.Phys.JETP **56**, 502 (1982).

[128] B. Holdom, Phys.Lett. **B166**, 196 (1986).

[129] P. Fayet, Nucl.Phys. **B187**, 184 (1981).

[130] C. Boehm and P. Fayet, Nucl.Phys. **B683**, 219 (2004).

[131] J.-H. Huh, J. E. Kim, J.-C. Park, and S. C. Park, Phys.Rev. **D77**, 123503 (2008).

[132] R. Essig, J. A. Jaros, W. Wester, *et al.*, "Dark Sectors and New, Light, Weakly-Coupled Particles," (2013), arXiv:1311.0029 [hep-ph].

[133] N. Arkani-Hamed and N. Weiner, JHEP **0812**, 104 (2008).

[134] R. Essig, P. Schuster, and N. Toro, Phys.Rev. **D80**, 015003 (2009).

[135] M. Goodsell, J. Jaeckel, J. Redondo, and A. Ringwald, JHEP **0911**, 027 (2009).

[136] M. Cicoli, M. Goodsell, J. Jaeckel, and A. Ringwald, JHEP **1107**, 114 (2011).

[137] M. Goodsell, S. Ramos-Sanchez, and A. Ringwald, JHEP **1201**, 021 (2012).

[138] H. Davoudiasl, H.-S. Lee, and W. J. Marciano, Phys.Rev. **D86**, 095009 (2012).

[139] M. Endo, K. Hamaguchi, and G. Mishima, Phys.Rev. **D86**, 095029 (2012).

[140] J. D. Bjorken, R. Essig, P. Schuster, and N. Toro, Phys.Rev. **D80**, 075018 (2009).

[141] J. Blumlein and J. Brunner, Phys.Lett. **B701**, 155 (2011).

[142] S. Gninenko, Phys.Rev. **D85**, 055027 (2012).

[143] S. Gninenko, Phys.Lett. **B713**, 244 (2012).

[144] S. Andreas, C. Niebuhr, and A. Ringwald, Phys.Rev. **D86**, 095019 (2012).

[145] J. Blümlein and J. Brunner, "New Exclusion Limits on Dark Gauge Forces from Proton Bremsstrahlung in Beam-Dump Data," (2013), arXiv:1311.3870 [hep-ph].

[146] B. Echenard, Mod.Phys.Lett. **A27**, 1230016 (2012).

[147] F. Archilli, D. Babusci, D. Badoni, I. Balwierz, G. Bencivenni, *et al.*, Phys.Lett. **B706**, 251 (2012).

[148] D. Babusci *et al.* (KLOE-2 Collaboration), Phys.Lett. **B720**, 111 (2013).

[149] S. Gninenko, Phys. Rev. **D87**, 035030 (2013).

[150] P. Adlarson *et al.* (WASA-at-COSY Collaboration), Phys.Lett. **B726**, 187 (2013).

[151] G. Agakishiev *et al.* (HADES Collaboration), "Searching a Dark Photon with HADES," (2013), arXiv:1311.0216 [hep-ex].

[152] H. Merkel *et al.* (A1 Collaboration), Phys.Rev.Lett. **106**, 251802 (2011).

[153] S. Abrahamyan *et al.* (APEX Collaboration), Phys.Rev.Lett. **107**, 191804 (2011).

[154] D. Hanneke, S. Fogwell, and G. Gabrielse, Phys.Rev.Lett. **100**, 120801 (2008).

[155] R. Bouchendira, P. Clade, S. Guellati-Khelifa, F. Nez, and F. Biraben, Phys.Rev.Lett. **106**, 080801 (2011).

[156] A. Konaka, K. Imai, H. Kobayashi, A. Masaike, K. Miyake, *et al.*, Phys.Rev.Lett. **57**, 659 (1986).

[157] M. S. Turner, Phys.Rev.Lett. **60**, 1797 (1988).

[158] J. Blumlein, J. Brunner, H. Grabosch, P. Lanius, S. Nowak, *et al.*, Z.Phys. **C51**, 341 (1991).

[159] J. Blumlein, J. Brunner, H. Grabosch, P. Lanius, S. Nowak, *et al.*, Int.J.Mod.Phys. **A7**, 3835 (1992).

[160] M. Davier and H. Nguyen Ngoc, Phys.Lett. **B229**, 150 (1989).

[161] P. Astier *et al.* (NOMAD Collaboration), Phys.Lett. **B506**, 27 (2001).

[162] P. Astier *et al.* (NOMAD Collaboration), Phys.Lett. **B527**, 23 (2002).

[163] C. Kullenberg *et al.* (NOMAD Collaboration), Phys.Lett. **B706**, 268 (2012).

[164] G. Bernardi, G. Carugno, J. Chauveau, F. Dicarlo, M. Dris, *et al.*, Phys.Lett. **B166**, 479 (1986).

[165] G. Bernardi, G. Carugno, J. Chauveau, F. Dicarlo, M. Dris, *et al.*, Phys.Lett. **B203**, 332 (1988).

[166] F. Bergsma *et al.* (CHARM Collaboration), Phys.Lett. **B128**, 361 (1983).

[167] F. Bergsma *et al.* (CHARM Collaboration), Phys.Lett. **B166**, 473 (1986).

[168] R. Meijer Drees *et al.* (SINDRUM I Collaboration), Phys.Rev.Lett. **68**, 3845 (1992).

[169] G. Agakishiev *et al.* (HADES Collaboration), Eur.Phys.J. **A48**, 64 (2012).

[170] G. Agakishiev *et al.* (HADES COllaboration), Phys.Lett. **B715**, 304 (2012).

[171] G. Agakishiev *et al.* (HADES Collaboration), Phys. Rev. C **88**, 024904 (2013).

[172] M. Reece and L.-T. Wang, JHEP **0907**, 051 (2009).

[173] B. Batell, M. Pospelov, and A. Ritz, Phys.Rev. **D79**, 115008 (2009).

[174] E. Byckling and K. Kajantie, *Particle Kinematics* (John Wiley and Sons, 1973).

[175] M. Vanderhaeghen, J. Friedrich, D. Lhuillier, D. Marchand, L. Van Hoorebeke, *et al.*, Phys.Rev. **C62**, 025501 (2000).

[176] L. I. Schiff, Phys.Rev. **83**, 252 (1951).

[177] Y.-S. Tsai, Rev.Mod.Phys. **46**, 815 (1974).

[178] P. A. Guichon, G. Liu, and A. W. Thomas, Nucl.Phys. **A591**, 606 (1995).

[179] J. Roche *et al.* (VCS Collaboration, A1 Collaboration), Phys.Rev.Lett. **85**, 708 (2000).

[180] G. von Gehlen, Phys.Rev. **118**, 1455 (1960).

[181] S. Drell and J. Walecka, Annals Phys. **28**, 18 (1964).

[182] F. Halzen and A. D. Martin, *Quarks and Leptons: an introductory course in modern particle physics* (John Wiley and Sons, 1984).

[183] M. E. Peskin and D. V. Schroeder, *An Introduction to quantum field theory* (Addison-Wesley, Reading, 1995).

[184] J. Friedrich and N. Voegler, Nucl.Phys. **A373**, 192 (1982).

[185] E. Moniz, I. Sick, R. Whitney, J. Ficenec, R. D. Kephart, *et al.*, Phys.Rev.Lett. **26**, 445 (1971).

[186] G. P. Lepage, J.Comput.Phys. **27**, 192 (1978).

[187] J. Kanzaki, Eur.Phys.J. **C71**, 1559 (2011).

[188] R. Essig, P. Schuster, N. Toro, and B. Wojtsekhowski, JHEP **1102**, 009 (2011).

[189] J. Jaros, M. Holtrop, S. Stepanyan, *et al.* (HPS Collaboration), Proposal to JLAB **PAC 38** (2011), `http://www.jlab.org/exp_prog/proposals/12/C12-11-006.pdf`.

[190] P. Fisher, R. Milner, and others. (DarkLight Collaboration), Proposal to JLAB **PAC 38** (2011), `http://www.jlab.org/exp_prog/proposals/12/C12-11-008.pdf`.

[191] E. Fermi, Z.Phys. **29**, 315 (1924).

[192] C. von Weizsacker, Z.Phys. **88**, 612 (1934).

[193] E. Williams, Phys.Rev. **45**, 729 (1934).

[194] K. J. Kim and Y.-S. Tsai, Phys.Rev. **D8**, 3109 (1973).

[195] Y.-S. Tsai, Phys.Rev. **D34**, 1326 (1986).

[196] J. C. Bernauer, *Measurement of the elastic electron-proton cross section and separation of the electric and magnetic form factor in the Q 2 range from 0.004 to 1 (GeV/c) 2*, Ph.D. thesis, Johannes Gutenberg-Universität (2010).

[197] D. Yennie, S. C. Frautschi, and H. Suura, Annals Phys. **13**, 379 (1961).

[198] J. D. Bjorken and S. D. Drell, *Relativistic Quantum Mechanics* (McGraw-Hill, New York, 1964).

[199] `http://www.nvidia.com/object/cuda_home_new.html`.

[200] K. Blomqvist, W. Boeglin, R. Bohm, M. Distler, R. Edelhoff, *et al.*, Nucl.Instrum.Meth. **A403**, 263 (1998).

[201] L. Maximon and J. Tjon, Phys.Rev. **C62**, 054320 (2000).

[202] M. Freytsis, G. Ovanesyan, and J. Thaler, JHEP **1001**, 111 (2010).

[203] K. Aulenbacher, M. Dehn, H.-J. Kreidel, R. Heine, and R. Eichhorn, ICFA Beam Dyn.Newslett. **58**, 145 (2012).

[204] K. Aulenbacher, AIP Conference Proceedings **1563**, 5 (2013).

[205] Y. Kahn and J. Thaler, Phys.Rev. **D86**, 115012 (2012).

[206] C. E. Carlson and B. C. Rislow, "Constraints to new physics models for the proton charge radius puzzle from the decay $K^+ \to \mu^+ + \nu + e^- + e^+$," (2013), arXiv:1310.2786 [hep-ph].

[207] C. Pang, R. Hildebrand, G. Cable, and R. Stiening, Phys.Rev. **D8**, 1989 (1973).

[208] J. Bijnens, G. Ecker, and J. Gasser, Nucl.Phys. **B396**, 81 (1993).

[209] A. Poblaguev, R. Appel, G. Atoyan, B. Bassalleck, D. Bergman, *et al.*, Phys.Rev.Lett. **89**, 061803 (2002).

[210] F. Ambrosino (NA48/2, NA62), Nucl.Phys.Proc.Suppl. **245**, 223 (2013).

[211] M. Kohl and T. Collaboration, AIP Conference Proceedings **1563**, 147 (2013).

[212] G. Gounaris and J. Sakurai, Phys.Rev.Lett. **21**, 244 (1968).

[213] L. Barkov, A. Chilingarov, S. Eidelman, B. Khazin, M. Y. Lelchuk, *et al.*, Nucl.Phys. **B256**, 365 (1985).

[214] J. H. Kuhn and A. Santamaria, Z.Phys. **C48**, 445 (1990).

[215] C. Bruch, A. Khodjamirian, and J. H. Kuhn, Eur.Phys.J. **C39**, 41 (2005).

[216] J. Lees *et al.* (BaBar Collaboration), Phys.Rev. **D86**, 032013 (2012).

[217] M. Guidal and M. Vanderhaeghen, Phys.Rev.Lett. **90**, 012001 (2003).